Measurements of Quantum Interference of Two Identical Particles with respect to the Event Plane in Au+Au Collisions at $\sqrt{sNN}$ = 200GeV at RHIC-PHENIX

著者	新井田 貴文
year	2013
その他のタイトル	RHIC-PHENIX 実験200GeV 金+金衝突における同種2粒子を用いた量子力学的干渉効果の反応平面依存性の測定
学位授与大学	筑波大学 (University of Tsukuba)
学位授与年度	2013
報告番号	12102甲第6719号
URL	http://hdl.handle.net/2241/00122770

Measurements of Quantum Interference of Two Identical Particles with respect to the Event Plane in Au+Au Collisions at $\sqrt{s_{\rm NN}} = 200$ GeV at RHIC-PHENIX

Takafumi NIIDA

October 2013

Measurements of Quantum Interference of Two Identical Particles with respect to the Event Plane in Au+Au Collisions at $\sqrt{s_{\mathrm{NN}}} = 200$ GeV at RHIC-PHENIX

Takafumi NIIDA
Doctoral Program in Physics

Submitted to the Graduate School of
Pure and Applied Sciences
in Partial Fulfillment of the Requirements
for the Degree of Doctor of Philosophy in
Science

at the
University of Tsukuba

Abstract

Quark-gluon plasma (QGP) is known as a state of nuclear matter in which the quarks and gluons are deconfined. The Relativistic Heavy Ion Collider (RHIC) at Brookhaven National Laboratory allows us to study the QGP though relativistic nucleus-nucleus collisions. Experimental observables measured at RHIC so far indicate that these nucleus-nucleus collisions lead to the formation of the QGP. The formed QGP expands and cools rapidly, and goes back to a hadronic system as predicted by Quantum Chromodynamics (QCD). The characteristics of the QGP, and the detailed picture of its space-time evolution is emerging by extensive measurements at RHIC. Studies of the final space-time distribution of hadrons and an understanding of its dependence on the initial collision geometry are needed to complete the picture of the space-time evolution of the QGP.

The quantum mechanical interferometry of two identical particles, also known as Hanbury Brown and Twiss (HBT) interferometry, provides us information on the space-time extent of the particle emitting source. Its technique was used to measure the stellar size through the intensity of interference between two photons in the field of astronomy. The same technique have been developed in the field of particle and nuclear physics. In heavy ion collisions, hadron interferometry provides us the space-time extent of hadronic system at the time of last scattering, referred to as kinetic freeze-out. In non-central collisions, it is thought that the collision area is like almond shape at initial state. Then a reaction plane is defined as the plane that the beam axis and the vector connecting the centers of two nuclei make. The larger pressure gradient in the direction of reaction plane due to such a spatial anisotropy leads to the momentum anisotropy called elliptic flow, which is stronger expansion of the source toward the direction of the reaction plane than to the perpendicular direction of that. One may expect the source at kinetic freeze-out change to the shape extended to the direction of the reaction plane. To study the source shape at kinetic freeze-out would be one of the key observables to investigate how and how long the system evolves.

The initial density distribution in the collision area has a spatial fluctuation due to the finite number of participating nucleons in addition to the elliptical source shape. Therefore higher order components, such as triangular (3^{rd}-order) flow, or quadrangular (4^{th}-order) flow, etc may be present in both spatial and momentum distribution at kinetic freeze-out. Higher order collective flow have been recently measured, which is thought to primarily come from the initial spatial fluctuations. The initial spatial fluctuations may be preserved until the freeze-out, depending on the strength of the initial fluctuations, flow profile, and expansion time as well as the system temperature, a viscosity, and the source opacity. Therefore the measurement of HBT interferometry with respect to different order event planes, which corresponds to the axes of higher order flows, would be a unique probe of the magnitude of the spatial state fluctuations and the subsequent space-time of a heavy ion collision.

We have performed HBT measurement with respect to 2^{nd}-order event plane in Au+Au collisions at $\sqrt{s_{\text{NN}}} = 200$ GeV at the PHENIX experiment. The Gaussian source radii (HBT radii) have been measured for charged pions and kaons as functions of collision centrality and the transverse mass (m_T). Azimuthal angle dependence of the HBT radii have been observed for both species. Final eccentricities calculated by the pion HBT radii increase with centrality going from central to peripheral collisions and are less than the initial eccentricities in all centralities, which is consistent with the result from STAR experiment. This result indicates that the source strongly expands to the direction of the reaction plane due to the elliptic flow, but is still elliptical and also oriented in the same vertical direction with respect to the reaction plane. On the other hand, the final

eccentricity of kaons is larger than that of pions in peripheral events. Because heavier particles get larger momentum by the collective expansion, the emission region of particles will be different even if they have the same momentum. To take into account the effect, the transverse mass (m_T) scaling needs to be considered in the comparison of both species. However the final eccentricity of kaons still shows larger value than that of pions even at the same m_T. It have also been found that azimuthally average HBT radii of kaons are slightly larger than those of pions, and the difference increases with centrality going from peripheral to central collisions. These difference may indicate that pions and kaons have different freeze-out mechanism, and it may be difficult to explain them only by the hadronic rescattering with different cross sections before the freeze-out because positive kaons with less cross section does not show any significant difference compared to negative kaons.

In order to study the details of features at kinetic freeze-out and the difference between particle species, the Blast-wave model fit have been performed for measured HBT radii with the results of the transverse momentum distribution and elliptic flow measured at PHENIX. The Blast-wave model is a kind of hydrodynamics inspired fitting model parameterized by the freeze-out conditions. The obtained parameters corresponding the flow anisotropy and source shape agrees with what we intuitively expect from the results of the elliptic flow and final eccentricity. The extracted freeze-out time (τ) and the emission duration $\Delta\tau$ increase with centrality going from peripheral to central collisions (τ=6-8 fm/c, $\Delta\tau$=1.5-2.0 fm/c). The extracted freeze-out time shows a similar value obtained by the result from 3D-source imaging analysis with the comparison of a theoretical calculation based on a hydrodynamic expansion including the effect of resonance decays. The result is also closer to a prediction by the hydrodynamic calculation without the hadronic rescattering than the hydrodynamic calculation with the hadronic rescattering. That may suggest that the stage of the hadronic rescattering before the freeze-out is much shorter than expected. The Blast-wave model assumes that the freeze-out of all hadrons takes place at the same time. Therefore the HBT radii of pions and kaons should be explained by the same freeze-out parameters. However the difference between pions and kaons could have not been explained although the transverse momentum distribution and elliptic flow can be explained well for both species. These results may imply that pions and kaon have different freeze-out time or different emission duration during the freeze-out.

We have also performed a first measurement of HBT radii as a function of azimuthal angle with respect to 3^{rd}-order event plane for charged pions. As well as 2^{nd}-order event plane, the angle dependence have been observed although the oscillation amplitudes are smaller than those for 2^{nd}-order. The result in central collisions appears to be qualitatively consistent with a picture that the angle dependence of HBT radii is driven by a finite triangular flow, not a spatial triangular anisotropy, suggested by a recent hydrodynamic model for 3^{rd}-order event plane dependence.

It is known that the dynamical correlation between momentum and spatial distribution affects the HBT radii. For the 3^{rd}-order event plane dependence, both effects of the triangular flow and spatial anisotropy would make the oscillation of HBT radii. In order to disentangle the contributions of spatial and flow anisotropy to azimuthal angle dependence of HBT radii, we have performed a Monte-Carlo simulation including both effects. The simulation results indicate that the initial triangular shape is significantly reduced in central collisions and also implies that initial triangularity may be flipped to have an opposite sign at the end of freeze-out by the triangular expansion in peripheral collision. These result would provide important constraints on the dynamics of the QGP, especially for the time scale of the system evolution.

Acknowledgment

I would like to express the deepest appreciation to Prof. Yasuo Miake, who gave me great opportunities for learning not only physics but also a lot of things and had me various experience in my campus life. He also gave me a lot of sound advice on my analysis. My deepest appreciation goes to Prof. ShinIchi Esumi. He gave me insightful comments and useful advice which led to accomplish this thesis. He is always willing to have a discussion about my analysis. I appreciate Prof. Tatsuya Chujo for his useful advice and support which is not only for my research but also life at BNL. I would like to thank Prof. M. Inaba for his professional advice about detectors and electronics. I also would like to express my thanks to Prof. H. Masui for his insightful advice and careful reading of my thesis. I received generous support from Mr. S. Kato, who arranged computer system at Tsukuba.

I would like to express my gratitude to Prof. Akira Ozawa for his careful reading of my thesis. My thesis effectively improved thanks to his useful comments and suggestions.

I want to thank all the members of High Energy Nuclear Physics Group at University of Tsukuba. I express my thanks to Ms. H. Sakai, Mr. Y. Ikeda, Mr. D. Sakata, Mr. M. Sano, Mr. T. Todoroki, Ms. J. Bhom, Mr. S. Mizuno, Mr. H. Nakagomi, Mr. D. Watanabe, Mr. K. Kihara, Mr. T. Kobayashi, Mr. K. Oshima, Ms. H. Ozaki, Mr. N. Tanaka, Mr. T. Nonaka, Mr. R. Hosokawa, Mr. W. Sato for their friendship, advice, and encouragement. I want to thank many other colleague including those who already graduated for their advice and discussions. Especially, special thanks to Ms. T. Nakajima for her friendly and humorous encouragement.

I am very grateful to the PHENIX-J group for their financial support. I would like to thank Prof. K. Ozawa for his arrangement for my stay at BNL. I want to thank colleagues in Tokyo University and Hiroshima University, especially thank Mr. M. Nihashi for his many help and friendship. I also would like to express my thanks to Dr. M. Shimomura and Dr. T. Hachiya for their many useful advice, suggestions, and kind help at BNL.

I am deeply grateful to the PHENIX Collaboration. I am grateful to the spokesperson Prof. B. V. Jacak, Prof. J. L. Nagle, and Prof. D. Morrison for their various arrangement and advices. I express my appreciation to Dr. R. Soltz for his many help and useful discussion in writing a paper. I also would like to thank Prof. A. Enokizono for his useful advice on the HBT analysis. I would like to thank the conveners of PLHF (Photons, Light Vector Mesons, Hadrons, and Flow) Physics Working Group, Prof. A. Drees, Prof. K. Shigaki, Dr. T. Sakaguchi, Dr. P. Stankus, and Prof. R. Seto. I express my thanks to Dr. J. S. Haggerty, Dr. M. Chiu. for their many support for the detector works in my stay at BNL. My appreciation also goes to the computing team, especially Dr. C. H. Pinkenburg, Dr. J. Seele. for their support about the data analysis.

I would like to express my thanks to Prof. M. A. Lisa, Prof. S. A. Voloshin, Prof. U. Heinz, and Prof. T. Hirano for their useful advice and valuable discussions on the HBT analysis.

Finally, I would like to thank my family, Toshiko, Keigo, Miwako and Hanae for their continuous support and encouragement. I could never finished this work without their understanding and help.

Contents

List of Figures

List of Tables

Chapter 1

Introduction

It is well known that the matter existing around us consists of various kinds of atoms and molecules. The atom have a nuclei in the center and electrons exist around the nuclei like a cloud. Furthermore the nuclei is composed of protons and neutrons called the nucleon. Protons and neutrons are composed of three quarks. Thus the matter is composed of smaller particles hierarchically, which is called hierarchical structure of the matter.

At present, the most fundamental particles composing the matter are believed to be quarks, leptons, gauge bosons that are photon, gluon, and W and Z bosons and mediate the interactions between particles, and Higgs boson that gives particles the mass and have been discovered in July 2012. Quarks and gluons, which are one of gauge bosons and mediates the strong force between quarks, are confined in "hadrons" in ordinary state. Hadrons is a generic name of baryons (made of three quarks) and mesons (made of one quark and one anti-quark). Here several questions may arise to you. Can't quarks and gluons move freely? Doesn't such a state exist? The quantum chromodynamics (QCD) which is the fundamental theory describing the strong interaction between quarks and gluons can answer the questions. The QCD theory predicts such an ultimate state called quark-gluon plasma (QGP) would have existed in the early universe or within neutron star.

In this chapter, we introduce the QCD theory which predicts the existence of the QGP, and the relativistic heavy ion collisions which is a unique way to create the QGP on earth and its features.

1.1 Quantum Chromodynamics

Quantum chromodynamics is a gauge field theory that describes the strong interaction between quarks and gluons. QCD is analogous to the quantum electrodynamics (QED), which describes electro-magnetic interaction between charged particles. In QED, the electro-magnetic force is mediated by the exchange of photons, while the strong interaction between quarks is mediated by the exchange of gauge bosons called gluons. The photon is electrically neutral and therefore carry no charge, while gluons carry color charge. In QCD, a quark can take one of three color charges and an anti-quark can take one of three anti-color charges. To make it possible for quarks with different colors to interact, it is required that there are eight gluons, which are mixtures of a color and an anti-color. Since gluons carry color, they can interact among themselves, and this makes the strong force unlike in QED.

The classical Lagrangian density of a quark with mass m is given by

$$\mathcal{L} = \bar{q}^{\alpha}\left(i\gamma^{\mu}(D_{\mu})_{\alpha\beta} - m\delta_{\alpha\beta}\right)q^{\beta} - \frac{1}{4}F^{a}_{\mu\nu}F^{\mu\nu}_{a}, \tag{1.1}$$

where q^α is the quark field with color index α, γ^μ is a Dirac matrix, and $F^a_{\mu\nu}$ is the gluon field strength tensor with color index a. The index α runs from 1 to 3, and a runs from 1 to 8 which corresponds to 8 gluons and repeated indices are summed over. The D_μ is a covariant derivative acting on the color-triplet quark field defined as:

$$D_\mu = \partial_\mu + igt^a A^a_\mu, \tag{1.2}$$

where t^a is the fundamental representation of SU(3) Lie algebra and A^a_μ is the gluon field. The gluon field strength tensor is defined as:

$$F^a_{\mu\nu} = \partial_\mu A^a_\nu - \partial_\nu A^a_\mu - g f_{abc} A^b_\mu A^c_\nu, \tag{1.3}$$

where f_{abc} is the structure constants of SU(3) and g is the dimensionless coupling constant in QCD, which is related to the coupling strength α_s by $g^2 = 4\pi\alpha_s$. The third term in Eq. (1.3) is non-Abelian term, which gives rise to triplet and quartic gluon self-interactions. The gauge boson self-interactions are a features of non-Abelian theories and their existence distinguishes QCD from QED.

QCD provides us two important properties of quark-gluon dynamics: **Confinement** and **Asymptotic freedom**. As a result of the gluon self-interactions, QCD implies that the coupling strength α_s becomes large at large distance or at low momentum transfers (Q). The large coupling constant at large distance means that quarks exist as bound states of quarks forming hadrons, which is known as confinement of quarks and gluons inside hadrons. On the other hand, the coupling constant becomes small at short distance or $Q \to \infty$, where the interaction between quarks becomes asymptotically weak, which is known as the asymptotic freedom.

The coupling strength can be calculated by perturbative QCD [2]:

$$\alpha_s(Q^2) = \frac{1}{\beta_0 \ln(Q^2/\Lambda^2)}. \tag{1.4}$$

Here Λ is called the QCD scale parameter and β_0 is given by

$$\beta_0 = \frac{33 - 2N_f}{12\pi}, \tag{1.5}$$

and N_f is the number of active quark flavors. Perturbative QCD teaches us how α_s varies with Q, but we must determine the absolute value from experiment. The value of the coupling at $Q = M_Z$ is usually chosen as the fundamental parameter, where M_Z is the mass of Z boson (M_Z=91.2 GeV). Figure 1.1 shows the running coupling strength α_s as a function of momentum transfer Q. Equation (1.4) indicates that α_s diverges to infinity at small Q. It means that perturbative QCD is not applicable for small Q region. Therefore non-perturbative methods must be used in that case.

Lattice QCD is one of the most developed non-perturbative methods and has successfully provided the predictions of proton mass with an error less than 2%. The key concept of this method is to define QCD on a space-time lattice. In Lattice QCD, field operators are applied on a discrete, four-dimensional Euclidean space-time of hypercubes with side length a. Increasing finite lattice size and decreasing lattice space a, the continuum QCD is recovered. Lattice QCD allows us to study the properties of non-perturbative QCD, such as the confinement and phase transition.

Figure 1.2 shows the energy density over the temperature, ϵ/T, as a function of T scaled by the critical temperature T_c calculated by Lattice QCD [3]. Lattice QCD calculation shows that large jumps of ϵ/T_4 are seen around $T \approx T_c$. The extrapolated critical temperatures are $T_c \simeq 175$ MeV for $N_f = 2$ and $T_c \simeq 155$ MeV for $N_f = 3$. The corresponding critical energy density ϵ_c is

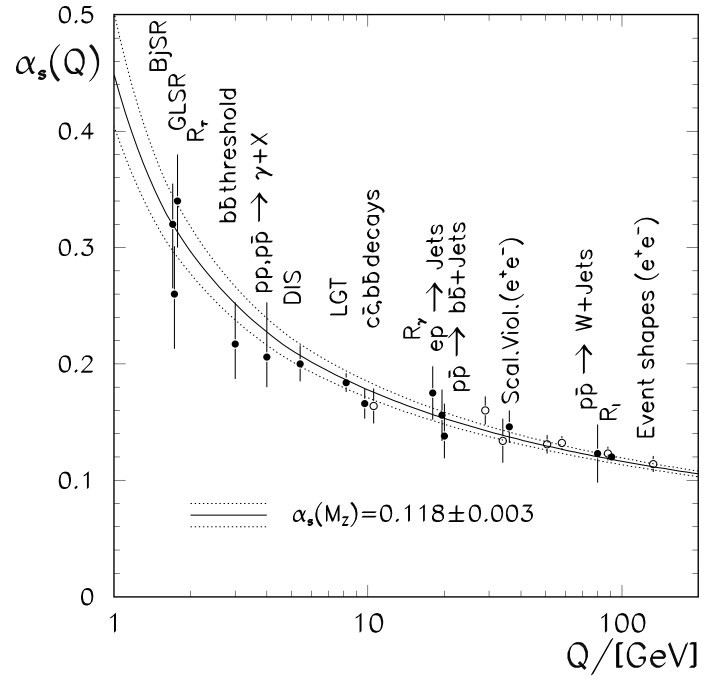

Figure 1.1: Running coupling constant as a function of momentum transfer Q by the various types of measurements at different scales [2]. The curve is the QCD prediction.

$\epsilon \simeq 0.5 - 1.0$ GeV/fm^3. This large jump indicates that a first order phase transition to new state called **quark-gluon plasma (QGP)** takes place around T_c because ϵ/T^4 reflects the number of degrees of freedom or the entropy density. However the order of the phase transition is still not clear for realistic case.

Here we consider the massless pions for simplicity. At extremely low temperature, the interactions among pions are weak, while at the extremely high temperature, the momenta of quarks and gluons are high, and so that the running coupling strength α_s becomes weak due to asymptotic freedom. Therefore at extremely low or high temperature, we can assume a free pion gas or a free quark-gluon gas and apply the general statistical mechanics for them. In the above assumption, energy density and entropy density of the massless pion gas are expressed as the followings:

$$\epsilon_H = 3d_\pi \frac{\pi^2}{90} T^4, \tag{1.6}$$

$$s_H = 4d_\pi \frac{\pi^2}{90} T^3, \tag{1.7}$$

where d_π is the number of massless Nambu-Goldstone bosons in N_f flavors, which is given by:

$$d_\pi = N_f^2 - 1. \tag{1.8}$$

In a free quarks and gluons gas, that is QGP, energy density and entropy density are given by:

$$\epsilon_{QGP} = 3d_{QGP} \frac{\pi^2}{90} T^4 + B, \tag{1.9}$$

$$s_{QGP} = 4d_{QGP} \frac{\pi^2}{90} T^3, \tag{1.10}$$

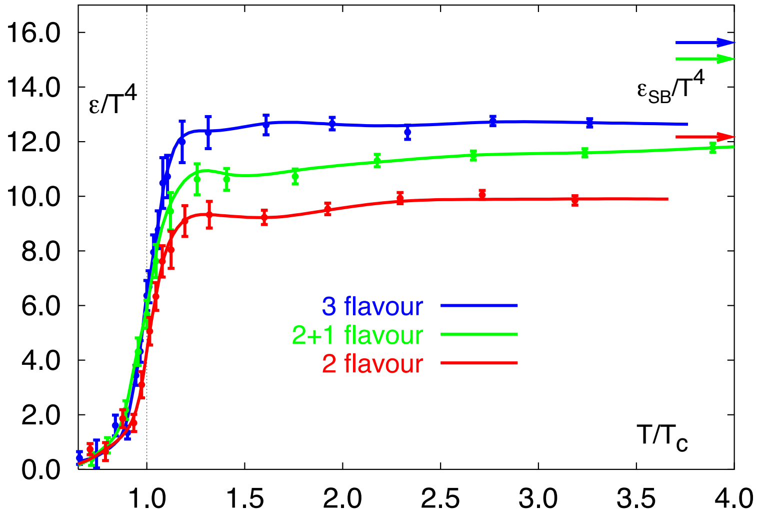

Figure 1.2: The energy density over T^4 as a function of the temperature T scaled by the critical temperature T_c calculated in Lattice QCD [3]. The arrows indicate the Stefan-Boltzmann limit of ϵ/T^4.

where B is called the bag constant and d_{QGP} is the number of degrees of freedom in QGP phase:

$$\begin{aligned} d_{QGP} &= d_g + \frac{7}{8} d_q \\ &= 2_{spin} \cdot (N_f^2 - 1) + \frac{7}{8} \cdot 2_{spin} \cdot 2_{q\bar{q}} \cdot N_c \cdot N_f, \end{aligned} \tag{1.11}$$

where the degrees of freedom of spin and color are summed over for gluons, and the degrees of spin, color, quark/anti-quark, flavor are summed over for quarks. The factor 7/8 is derived from the Fermi statistics. In case of $N_c = 3$, $N_f = 2$, the degrees of freedom of pion gas and QGP are 3 and 37 respectively. Therefore the energy density in QGP phase is about twelve times larger than that in hadron state, which leads to the discontinuous change of the energy density around T_c.

1.2 Relativistic Heavy Ion Collisions

As predicted by the QCD theory descrbed in the previous section, the phase transition from normal nuclear matter to the QGP state is expected to take place at the extremely high temperature or density. A unique way to achieve such a state on the earth is the relativistic heavy ion collisions. Various experiments have been carried out so far at Brookhaven National Laboratory (BNL) located in the suburb of New York, USA, and the European Organization for Nuclear Research (CERN) in Switzerland as listed in Table. 1.1. In this section, the overview of the heavy ion collisions is decrbed in terms of the time history and the geometry of the collisions.

1.2.1 Space-Time Evolution

Let us consider the spec-time evolution in a heavy ion collision. Figure 1.3 shows a schematic diagram of space-time evolution of a relativistic heavy ion collision, where the "space" axis (hor-

Accelerator	Location	Beam	$\sqrt{s_{\mathrm{NN}}}$	Year
SPS	CERN	^{16}O,^{32}S	19.4	1986
		^{208}Pb	17.4	1994
AGS	BNL	^{16}O,^{28}Si	5.4	1986
		^{197}Au	4.8	1992
RHIC	BNL	^{197}Au	130	2000
		^{197}Au	200	2001
		d+^{197}Au	200	2003
		^{197}Au	200, 62.4	2003/2004
		$^{63.5}$Cu	200, 62.4	2005
		^{197}Au	200	2007
		d+^{197}Au	200	2008
		^{197}Au	200, 62.4, 39	2010
		^{197}Au	200, 27, 19.6	2011
		^{238}U	193	2012
		$^{63.5}$Cu+^{197}Au	200	2012
LHC	CERN	^{208}Pb	2760	2010
		p+^{208}Pb	5020	2012

Table 1.1: Summary of heavy ion collider facilities with the ion beams and the center of mass energy.

izontal axis) represents the longitudinal (beam) direction. In this picture, two nuclei which are Lorentz-contracted like pancakes in the beam direction collide at $z = 0$ and $t = 0$ in the center of mass frame. The picture of the space-time evolution of the overlap of two nuclei after the collision is supposed by Bjorken [4] as the following stages:

- Pre-equilibrium
- Partonic thermalization and QGP phase
- Phase transition to hadron state
- Chemical and Kinetic Freeze-out

Pre-equilibrium

Parton-parton hard scatterings occur in the initial overlap of two nuclei and a large number of patrons are created then. However its mechanism is not well understood. Several models, such as the color-string model [5], the color glass condensate (CGC) [6, 7], and perturbative QCD models [8], are proposed to describe the initial pre-equilibrium stage.

Partonic thermalization and QGP phase

With the multiple scatterings of partons and the process of the parton production, parton density increases in the central region of the collision, so that the partonic matter reaches the local thermal equilibrium and the QGP phase is formed before a proper time τ_0. The proper time is expected to be about 1 fm/c or less.

Phase transition to hadron state

Once the local thermal equilibrium is achieved, the system expands rapidly due to the internal pressure. The system cools down with the expansion and the QCD phase transition takes place at the critical temperature T_c. At T_c, partons start to be reconfined into hadrons, which is called "hadronization". If the first order phase transition takes place, the system becomes a mixture of the QGP and hadronic matter during the phase transition.

If the mean free path of constituent particles is much shorter than the length scale of the system, the evolution of the system until freeze-out is described by the relativistic hydrodynamics. The basic equations of the relativistic hydrodynamics are the conservation laws of the energy-momentum tensor and the baryon number:

$$\partial_\mu T^{\mu\nu} = 0, \tag{1.12}$$

$$\partial_\mu j_B^\mu = 0, \tag{1.13}$$

where $T^{\mu\nu}$ is the energy-momentum tensor, and j_B^μ is the baryon number current, which are given by the following equations for perfect fluid:

$$T^{\mu\nu} = (\varepsilon + P)u^\mu u^\nu - g^{\mu\nu}P, \tag{1.14}$$

$$j_B^\mu = n_B u^\mu, \tag{1.15}$$

where ε is the local energy density, P is the local pressure, n_B is the baryon number density, and u^μ is a fluid four-velocity defined as $u^\mu = \gamma(1, \mathbf{v})$. Equation (1.12) and (1.13) contain five independent equations. By solving these equations in addition to an extra equation which is provided by the equation of state relating ε and P, unknown variables, ε, P, n_B, and the flow vector u_x, u_y, u_z, are determined.

Chemical and Kinetic Freeze-out

The hadronic matter expands with hadron-hadron interaction, and the temperature of the system decreases. The number of each species is fixed at the temperature T_{ch}, which is called the "chemical freeze-out". Then, the hadron interaction stops and the "kinetic freeze-out" happens at the temperature T_f and $t = \tau_f$ where the kinetic equilibrium is no longer maintained. Eventually, the mean free path of hadrons exceeds the system size, so that hadrons freely move away from the system and are measured by experimental detectors.

1.2.2 Collision Geometry

The collision geometry in relativistic heavy ion collisions is characterized by a degree of the overlap of two nuclei. The impact parameter b, which is the distance between the center of nuclei, is usually used to show a quantity of the overlap. If $b \approx 0$, it represents a head-head (central) collision. The collision with $b > 0$ is called a mid-central or a peripheral collision. In the peripheral collision, the geometrical treatment of the nucleus-nucleus collision is explained by a participant-spectator picture as shown in Figure 1.4, where the region participating in the collision is called as the "participant" and the rest that do not participate in the collision is called as the "spectator". This picture is held by the following characteristics in relativistic heavy ion collisions:

- The de Broglie wavelength of the nucleons is much shorter than the size of the nucleus, so that the nucleus-nucleus collision can be described by the nucleon-nucleon collision.

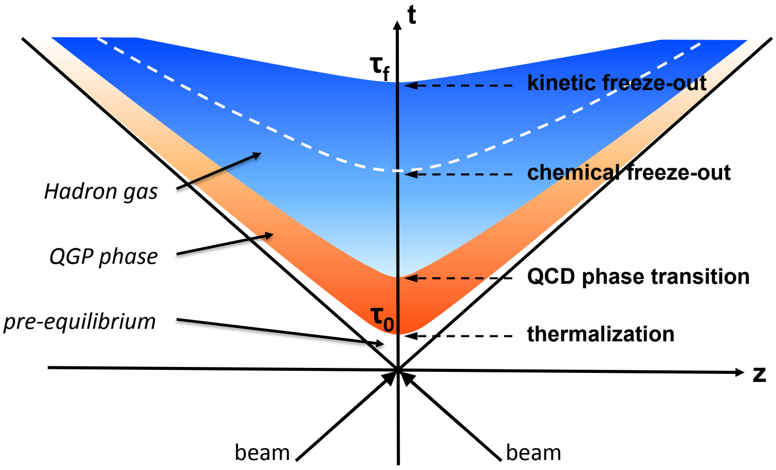

Figure 1.3: Space-time diagram of a relativistic heavy ion collision

- The mean free path of the nucleon-nucleon collision is shorter than the radius of the nuclei.
- As the velocity of the Lorentz-boosted nuclei is much faster than the Fermi motion of nucleons in the nucleus, the move of nucleons by the Fermi motion during the crossing time is negligible.

It is difficult to measure the impact parameter directly in the experiment. Therefore the "centrality" is defined and measured instead of the impact parameter, which is explained in Section 4.1.1.

The number of participant nucleons (N_{part}) and the spacial eccentricity (ε) for a given impact parameter b are evaluated by Glauber model [9]. The Glauber model is semi-classical model, where the nucleus-nucleus collisions are treated as multiple nucleon-nucleon interactions, and nucleons are assumed to travel in straight lines and are not deflected after the collisions. The nuclear thickness function is defined as:

$$T_A(\mathbf{s}) = \int dz\ \rho_A(z, \mathbf{s}), \tag{1.16}$$

where ρ_A is the nucleon density normalized to mass number A and the vector $\mathbf{s}$ is in the transverse plane with respect to the beam direction z. The nuclear thickness function T_A represents the number of nucleons per a unit transverse area and is related to the mass number by the following equation:

$$\int d\mathbf{s}\ T_A(\mathbf{s}) = A. \tag{1.17}$$

The Woods-Saxon parameterization is used as the density distribution for a heavy nucleus such as Au:

$$\rho_A(r) = \frac{\rho_0}{1 + \exp((r - R_A)/a)}, \tag{1.18}$$

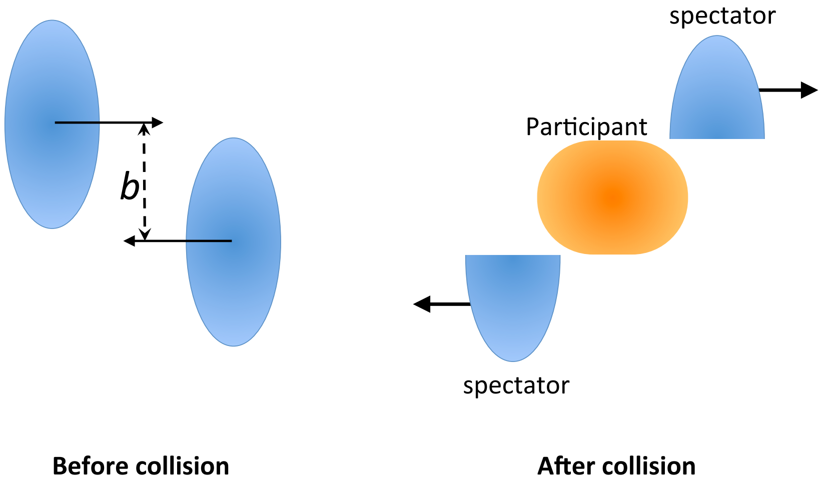

Figure 1.4: Participant-spectator picture in relativistic heavy ion collision.

where R_A is the nuclear radius and a is the surface diffuseness. Then the number of participant nucleons N_{part} is given by

$$\begin{aligned} N_{part} &= \int d\mathbf{s}\, T_A(\mathbf{s}) \left(1 - \exp(-\sigma_{\rm NN}^{in} T_B(\mathbf{s}))\right), \\ &+ \int d\mathbf{s}\, T_B(\mathbf{s}-\mathbf{b}) \left(1 - \exp(-\sigma_{\rm NN}^{in} T_A(\mathbf{s}))\right), \end{aligned} \tag{1.19}$$

where $\sigma_{\rm NN}^{in}$ is the nucleon-nucleon inelastic cross section. In this study, Monte Carlo calculations of the Glauber model have been carried out to estimate the number of participant and the spatial eccentricity and triangularity in the initial state. The detail is described in Sec. 4.6 and Appendix C.

1.3 Experimental Observables

In this section, we mainly introduce the experimental results measured at RHIC which indicate the formation of the QGP and are related to the motivation of this thesis.

1.3.1 Energy Density

The energy density achieved in the relativistic heavy ion collisions can be estimated by Bjorken picture [4], where two nuclei penetrate each other leaving particles behind at very high energy and the expansion is treated as one-dimensional expansion in the longitudinal direction. Here the number density of particles in the region with collision overlap area A and minimal longitudinal direction dz at $z = 0$ and at a proper time τ is given by

$$n = \frac{dN}{Adz} = \frac{dN}{Ady}\frac{dy}{dz}, \tag{1.20}$$

where y is rapidity defined as:

$$y = \frac{1}{2}\left(\frac{E+p_z}{E-p_z}\right) = \frac{1}{2}\left(\frac{t+z}{t-z}\right). \tag{1.21}$$

We can connect 2nd formula with 3rd formula in the above equation by the relation of $\beta_z = p_z/E = z/t$, and E, p_z are expressed as the followings:

$$\begin{aligned} E &= m_T \cosh y, \\ p_z &= m_T \sinh y, \\ m_T &= \sqrt{E^2 - p_z^2}, \end{aligned} \tag{1.22}$$

where m_T is called the transverse mass. As well as the above equations, t and z are expressed as:

$$\begin{aligned} t &= \tau \cosh y, \\ z &= \tau \sinh y, \\ \tau &= \sqrt{t^2 - z^2}. \end{aligned} \tag{1.23}$$

Therefore Eq. (1.20) can be rewritten as:

$$n = \frac{1}{A\tau \cosh y}\frac{dN}{dy}. \tag{1.24}$$

The Bjorken energy density is given by

$$\epsilon_{Bj} = n\langle E\rangle, \tag{1.25}$$

$$= \frac{\langle m_T\rangle}{A\tau}\frac{dN}{dy}, \tag{1.26}$$

$$= \frac{1}{\pi R^2 \tau}\frac{dE_T}{dy}, \tag{1.27}$$

where R is the nucleus radius used in a Woods-Saxon model and E_T is the transverse energy, which is obtained as the sum of all clusters energies deposited in the Electromagnetic calorimeter. Figure 1.5 shows the measured Bjorken energy density as a function of the number of participants calculated by Glauber model for three RHIC energies. For most central collisions, $\varepsilon_{Bj}\tau$ reaches about 5.4 GeV·fm$^{-2}c^{-1}$ at the RHIC top energy $\sqrt{s_{\rm NN}} = 200$ GeV. If we assume the nominal value τ =1 fm/c, the estimated energy density ε_{Bj} is larger than the critical energy density ε_c predicted by the Lattice QCD. Therefore it is expected that the formation of QGP is achieved at RHIC.

1.3.2 Radial Flow

As described in Sec. 1.2.1, the produced hadrons fly away through a stage of the kinetic freeze-out. Therefore transverse momentum (p_T) distributions known as p_T spectra reflect the conditions of a late stage in the collision as well as the integrated effects of expansion from the initial stage of the collision. The transverse momentum (mass) distribution is expressed in terms of an invariant cross-section:

$$E\frac{d^3\sigma}{d^3p} = \frac{1}{2\pi p_T}\frac{d^2\sigma}{dp_T dy} \tag{1.28}$$

$$= \frac{1}{2\pi m_T}\frac{d^2\sigma}{dm_T dy} \tag{1.29}$$

$$\propto \exp(-\frac{m_T}{T}), \tag{1.30}$$

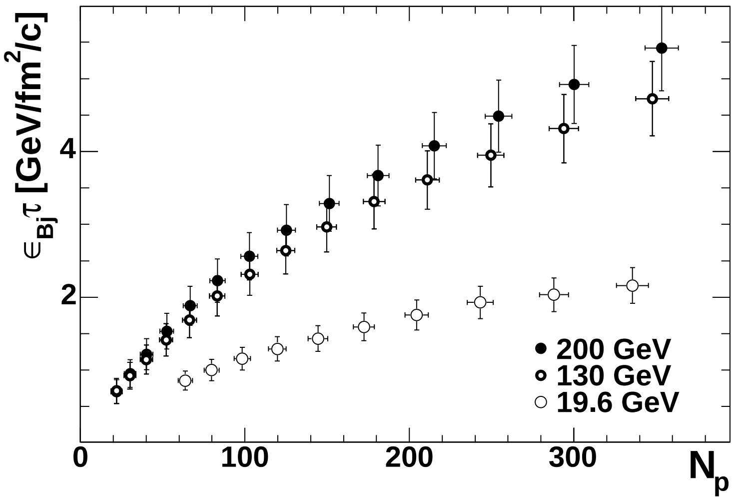

Figure 1.5: The Bjorken energy density multiplied by the formation time τ for three RHIC energies [11].

where T is the inverse slope parameter, which is interpreted as the temperature at the kinetic freeze-out. Figure 1.6 shows transverse mass distributions for identified particles for different centrality selections in Au+Au collisions [12]. The m_T spectra are well described by the exponential function at low m_T ($p_T < 2$ GeV/c).

It is found that the inverse slope parameter T is common to various particles, such as pions, kaons and protons, in high energy pp/pA collisions, which is called m_T scaling [13]. On the other hand, in nucleus-nucleus collisions it is observed that the inverse slope parameter is proportional to the mass of the particles. Figure 1.7 shows the inverse parameter T as a function of the mass for charged hadrons obtained by the fit of exponential function for the m_T spectra shown in Fig. 1.6. The inverse slope parameters increase with increasing particles mass in all centrality bins. This increase in central collisions is steeper than that in peripheral collisions. This result indicates the collective expansion of particles, that is all particles have a common transverse velocity in addition to their thermal motion. Then the inverse slope parameter is represented as:

$$T = T_f + \frac{1}{2}m\langle v\rangle^2, \tag{1.31}$$

where T_f is the temperature at freeze-out, m is the particle mass, and $\langle v\rangle$ is the average of collective flow velocity. The extracted T_f is $\sim$ 177 MeV for most central collisions. It is known that the effect of the radial flow in the spectra is well described by the phenomenological hydrodynamical model called **blast-wave model** in low m_T region [14].

1.3.3 Elliptic Flow

Azimuthal anisotropy of emitting particles in momentum space has been studied as a probe to access the early stage of collisions. In non-central collisions, the initial overlap of two nuclei has a spatial anisotropy like an almond shape as illustrated in Fig. 1.8 (a). If the local thermal equilibrium is established, where the mean free path of particles is much shorter than the system size, the

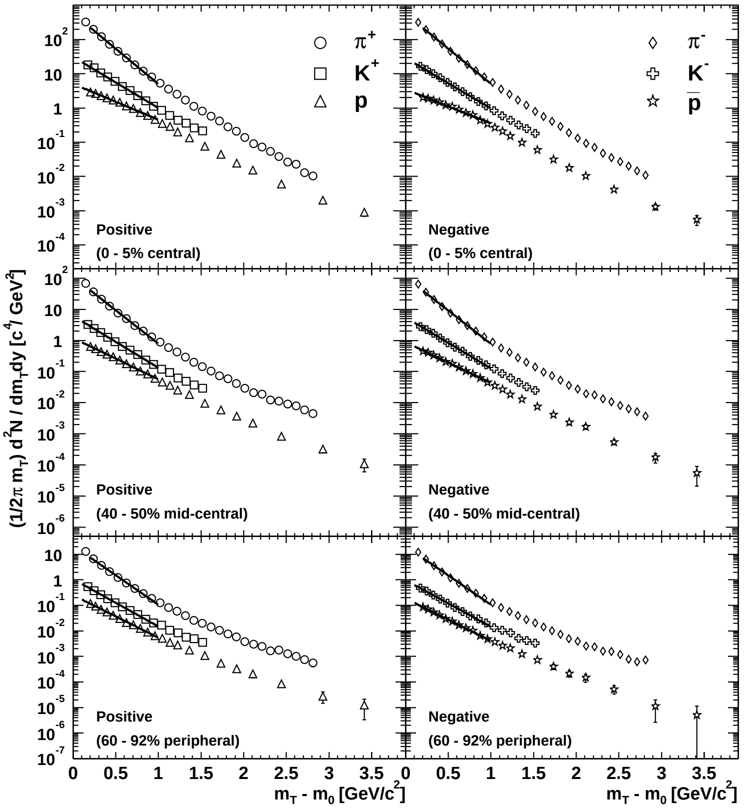

Figure 1.6: Transverse mass m_T distributions for $\pi^{\pm}$, $K^{\pm}$, $p(\bar{p})$ for 3 centrality bins in Au+Au collisions at $\sqrt{s_{\mathrm{NN}}}$=200 GeV [12]. The solid lines on each spectra represent fitting results with m_T exponential function.

hydrodynamics can be applied to describe the space-time evolution of the system. In the hydrodynamical picture, a collective flow is generated by the pressure gradient. In case of the overlap region with an almond shape, the pressure gradient is steeper in the direction of the short axis than in the direction of the long axis. Therefore more particles are emitted to the direction of the short axis. In other words, the spatial anisotropy makes an anisotropy in momentum space as shown in Fig. 1.8 (b).

Azimuthal distribution of emitted particles is represented in the form of Fourier expansion and by taking up to the 2$^{\mathrm{nd}}$-order, it is expressed as

$$\frac{dN}{d\phi} \propto 1 + 2\left(v_1 \cos[\phi - \Psi_r] + v_2 \cos[2(\phi - \Psi_r)]\right), \tag{1.32}$$

$$v_2 = \langle \cos[2(\phi - \Psi_r)] \rangle, \tag{1.33}$$

where ϕ is the azimuthal angle of the emitted particle, Ψ_r is the azimuthal angle of the reaction plane in the laboratory frame respectively. The Fourier coefficient v_1 and v_2 represent the strength of directed flow and elliptic flow.

Left panel in Fig. 1.9 shows v_2 for charged hadrons as a function of p_T in Au+Au collisions [15]. Solid lines show the result of a hydrodynamical calculation including a first-order phase transition with a freeze-out temperature of 120 MeV. In the low p_T region ($p_T < 2$ GeV/c), the mass ordering is seen, that is v_2 for a particle with a lighter mass is larger, and the data is well reproduced by

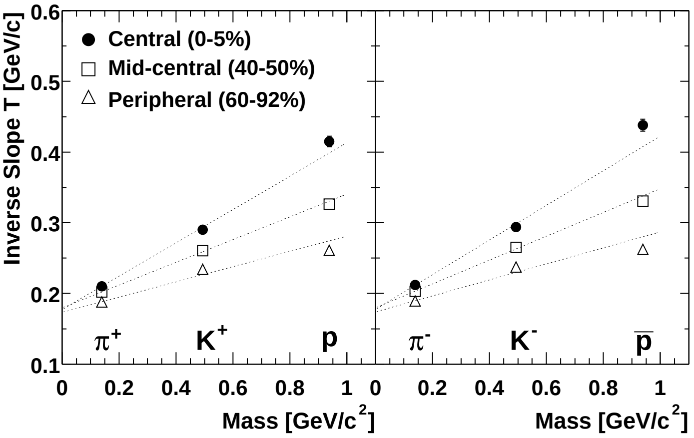

Figure 1.7: Mass and centrality dependence of inverse slope parameter T obtained by the fit of exponential function in Fig. 1.6 [12]. The dotted lines are a linear fit of the results with Eq. (1.31).

the hydrodynamic calculation. On the other hand, v_2 saturates at high p_T ($p_T > 2$ GeV/c) and v_2 for π, K is smaller than that for (anti)proton unlike the behavior in the low p_T region. Such a behavior is understood by the quark recombination model.

Quark recombination model

A mechanism of quark recombination [16] dominates the hadron production at intermediate p_T in heavy ion collisions. In this picture, quarks and anti-quarks of thermal origin combine to form mesons and baryons. Although partons have to be close to each other in phase space to hold this picture, we expect a densely populated phase space in central heavy ion collisions. In a simplified case, the momentum distribution of mesons (M) and baryons (B) are given by

$$\begin{aligned} E\frac{d^3N_M}{d^3p} &\approx C_M \int_\Sigma d\sigma \int dx\, w(r;xp)\, w(r;(1-x)p)\, |\phi_M(x)|^2, & (1.34) \\ E\frac{d^3N_B}{d^3p} &\approx C_B \int_\Sigma d\sigma \int_0^1 dx_1 dx_2 dx_3 \delta(x_1+x_2+x_3-1) \\ &\times\ w(r;x_1p)\, w(r;x_2p)\, w(r;x_3p)\, |\phi_B(q,s)|^2, & (1.35) \end{aligned}$$

where $C_{M(B)}$ is the coalescence probabilities for meson (baryons), $d\sigma$ measures the volume of the hypersurface Σ and $r \in \Sigma$, $\phi_{M(B)}$ is the effective wave function of mesons (baryons) and $w(r;xp)$ is a phase space distribution of quarks. If we take an equal fraction of $x = 1/2$ (1/3) for mesons (baryons), which means the momentum of the hadon is distributed equally among the valence quarks, we can rewrite Eq. (1.34) and Eq. (1.35) as

$$E\frac{d^3N_M}{d^3p} \simeq C_M w^2(p_T/2), \tag{1.36}$$

$$E\frac{d^3N_B}{d^3p} \simeq C_B w^3(p_T/3). \tag{1.37}$$

In this recombination model, the azimuthal anisotropy of the produced hadrons reflects the anisotropy of the constituent quarks and anti-quarks. If we assume the quarks and anti-quarks

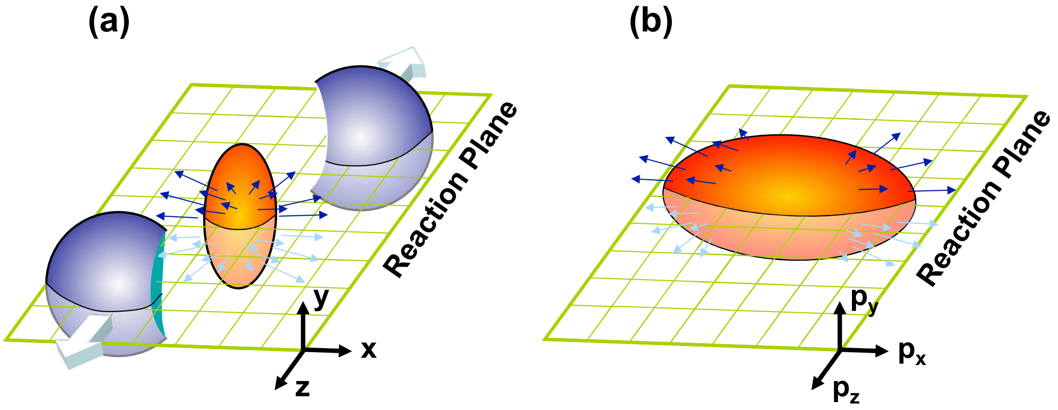

Figure 1.8: (a)Initial overlap of two nuclei in non central collisions in coordinate space. (b)Collective flow into the direction of reaction plane in momentum space.

have a elliptic flow $v_{2,q}$, the azimuthal distribution of mesons is given by

$$\frac{d^2N_M}{d\phi p_T dp_T} \approx (1+2v_{2,q}\cos 2\phi)^2 \simeq 1+4v_{2,q}. \tag{1.38}$$

Therefore the elliptic flow for the meson and baryon have the following relation to the elliptic flow of quarks and anti-quarks.

$$v_{2,M}(p_T) \simeq 2v_{2,q}(p_T/2), \quad v_{2,B}(p_T) \simeq 3v_{2,q}(p_T/3). \tag{1.39}$$

If these relations are true for experimental observables, it would indicate the collective flow at par tonic level, that is the existence of quark-gluon plasma.

Right two panels in Fig. 1.9 show v_2 for identified particles with and without the scaling by the number of constituent quarks n_q as functions of KE_T and KE_T/n_q, where KE_T is the transverse energy defined as $KE_T = m_T - m$. Unscaled v_2 in the left panel a) shows clearly distinction between mesons and baryons although the mass ordering vanishes by KE_T scaling. When the number of constituent quarks scaling is applied for them, v_2 for all particle species show good agreement as shown in the right panel b) of Fig. 1.9.

1.3.4 Higher-order Harmonic Flow

The initial geometry of the overlap region in heavy ion collisions has been treated as the collisions of nuclei with smooth density profile so far. In recent study, it is considered that the spatial density distribution of the participating nucleons fluctuates geometrically and it leads to higher-order harmonic deformation. This spatial fluctuation is converted to momentum space by the collective expansion and then higher-order harmonic flow v_n is created.

Azimuthal distribution of emitted particles is rewritten as the following:

$$\frac{dN}{d\phi} \propto 1+\sum_{n=1} 2v_n\cos(\mathrm{n}(\phi-\Psi_\mathrm{n})), \tag{1.40}$$

$$v_n = \langle\cos(\mathrm{n}(\phi-\Psi_\mathrm{n}))\rangle, \tag{1.41}$$

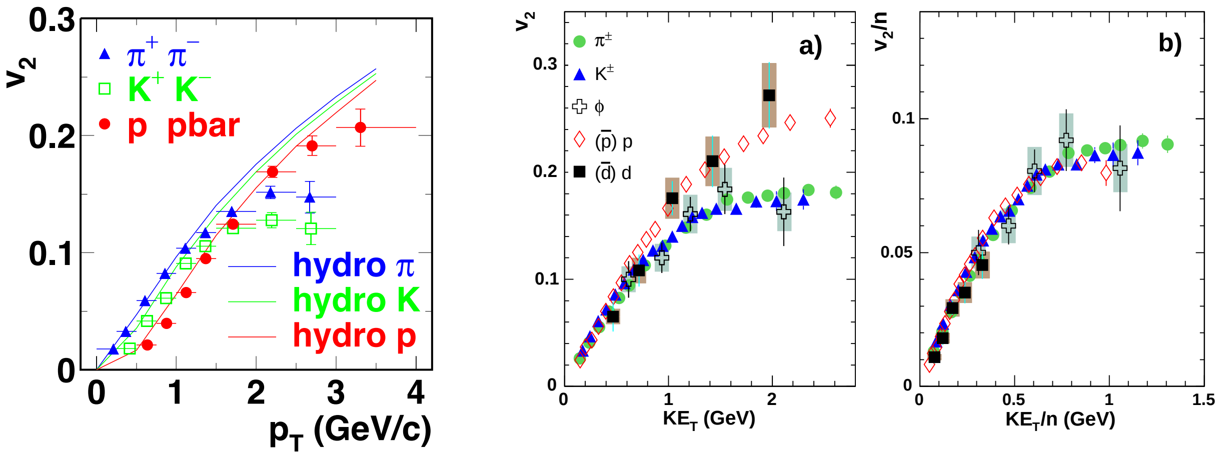

Figure 1.9: (Left)v_2 for charged hadrons, π, K, p as a function of p_T in Minimum bias events in Au+Au collisions at $\sqrt{s_{\rm NN}}$ = 200 GeV [15]. (Right)Unscaled and scaled v_2 as functions of KE_T and KE_T/n_q [17] in 20-60% centrality in Au+Au collisions [17].

where n indicates the harmonic order, ϕ and Ψ_n denote the azimuthal angle of emitted particles and event plane angle for $n^{\rm th}$ harmonic order. The $2^{\rm nd}$-order event plane is the estimate of the reaction plane in the experiment, but it is not necessarily the same because of the density fluctuation. Basically the event plane represents the direction to which more particles are emitted with certain modulation. The detail is described in Sec. 4.2. The Fourier coefficient v_n represents the flow strength, where v_2, v_3, v_4 correspond to the elliptic flow, triangular flow and quadrangular flow. Charged hadron v_n have been measured at PHENIX [18] as shown in Fig. 1.10, where v_2 increases from central to peripheral collisions, while v_3 doesn't show such a strong centrality dependence. It indicates that v_3 mainly comes from the initial fluctuation. Though some theoretical models with different initial conditions can explain v_2 well, some of them fail to explain v_3 as shown in Fig. 1.11, where v_3 seems to prefer lower viscosity. Therefore v_3 provides the new constraints on the theoretical models. Besides, it is expected that v_n for identified particles will provide more constraints on the theoretical models.

1.3.5 Hanbury-Brown and Twiss Interferometry

As mentioned in Sec. 1.2.1, the phase transition is expected to takes place from the QGP state to hadronic matter after heavy ion collisions. During the phase transition the total amount of the entropy S_{total} is conserved for a perfect fluid [1]:

$$S_{total} = s_{QGP}V_{QGP} = s_H V_H, \tag{1.42}$$

where s_{QGP} and s_H are the entropy density of the QGP and the hadron gas, and V_{QGP} and V_H are the volume of those one respectively. As shown in Eq. (1.7) and Eq.(1.10), the entropy density is proportional to the number of degrees of freedom. In case of N_f=2, the degree of freedom of the QGP is about twelve larger than that of hadron gas. Therefore we expect larger volume of hadron gas ($V_H \gg V_{QGP}$) if the QGP is created in heavy ion collisions. The entropy density for the perfect fluid is written by

$$s(\tau, y) = \frac{s(\tau_0, y)\tau_0}{\tau}, \tag{1.43}$$

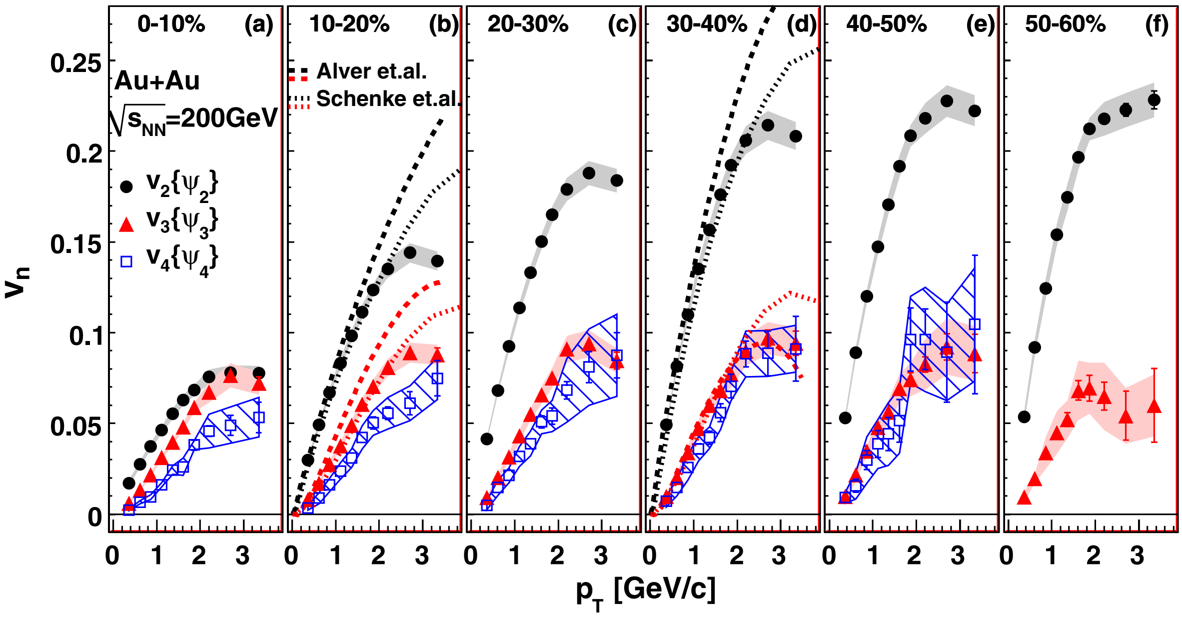

Figure 1.10: v_2, v_3 and v_4 as a function of p_T for different centrality bins measured with PHENIX.

where τ_0 is the proper time and y is rapidity. We can obtain the following relation:

$$\frac{\tau_H}{\tau_c} = \frac{s_{QGP}}{s_H} = \frac{d_{QGP}}{d_\pi}, \tag{1.44}$$

where τ_c is the time when the QCD phase transition take places and τ_H is the time when the phase transition is over. The ratio τ_H/τ_c provides the lifetime of the mixed phase of the QGP and the hadron gas. Important consequence of the QCD phase transition is a time-consuming expansion of the system or a large volume of a hadron gas in order to conserve the total entropy. Those features are not limited to the first order transition and are qualitatively true as long as the entropy density rapidly changes in a small interval of the temperature.

A useful tool to study the space-time extent of the matter created by heavy ion collisions is two identical particle interferometry called “HBT interferometry” or “femtoscopy”. The detail is described in Chapter 2. Here we show the experimental results and theoretical calculations of HBT interferometry.

Transverse momentum dependence

Size of static source measured by HBT interferometry is the same as the whole source size. However in case of expanding source, it is known that the HBT interferometry does not measure the whole source size but the “length of homogeneity region” [19]. In heavy ion collisions, produced particles strongly expands to outgoing direction with finite flow velocity, like the radial flow, where particle momenta correlate strongly with the emission points. Under the assumption of the radial flow, particles with higher momentum are emitted from the region near a surface of the source, which result in smaller source size measured by HBT interferometry. In other words, the transverse momentum dependence of the measured size indicates the expansion of the particle emitting source.

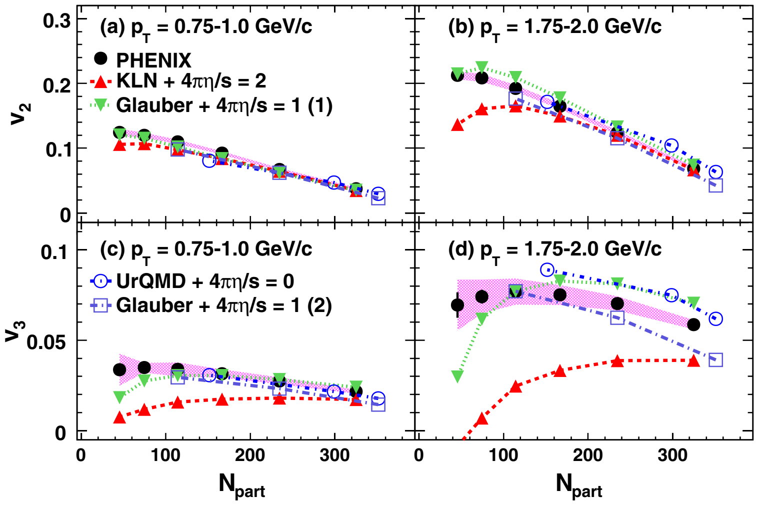

Figure 1.11: v_2 and v_3 as a function of N_{part} for two p_T ranges with the theoretical predictions, which are hydrodynamic calculations with the Glauber-MC or MC-KLN initial condition and different viscosities ($4\pi\eta/s$) and the UrQMD transport model.

Left figure in Fig. 1.12 shows the three-dimensional source radii as a function the transverse momentum of pair particles measured at RHIC [20], where R_{side}, R_{out}, R_{long} called "HBT radius" denote the three-dimensional radii of the source and R_{out}/R_{side} carrys the temporal information like the emission duration of particles (The detail is explained in Chap. 2). Each HBT radius clearly decrease with increasing the transverse momentum k_T, which implies the strong expansion of the source.

HBT puzzle

As explained in the previous sections, hydrodynamics reproduces the transverse momentum distribution and elliptic flow at low p_T. Therefore it is natural that one would like to test whether the hydrodynamics also can reproduce the observables of HBT interferometry dominated by two particles with low momentum. A variety of hydrodynamic models have been calculated and compared to the experimental results as shown in the left of Fig. 1.12. For example, a three-dimensional hydrodynamic calculation by Hirano *et al.* [21] assumes the early chemical freeze-out and a first-order phase transition which leads to a long lifetime of the system. Since it is known that the ratio R_{out}/R_{side} is sensitive to the emission duration (see Chapter 2), the model calculations show much larger value than unity as discussed in the above, but the data almost shows unity. The compared models significantly overpredict the ratio of R_{out}/R_{side}. Although the hydrodynamic models successfully reproduce the transverse momentum distribution (p_T spectra) and the elliptic flow v_2, large discrepancies between the models and data still remain in HBT measurements, which is called "HBT puzzle".

In order to solve this puzzle, some improvements have been preformed in the hydrodynamic model. The hydrodynamic models shown in the left of Fig. 1.12 didn't take account for the real situation, such as the order of phase transition, the equation of state, viscosity and so on. Recent Lattice QCD [24] suggests the crossover at the baryon chemical potential μ=0 which determines

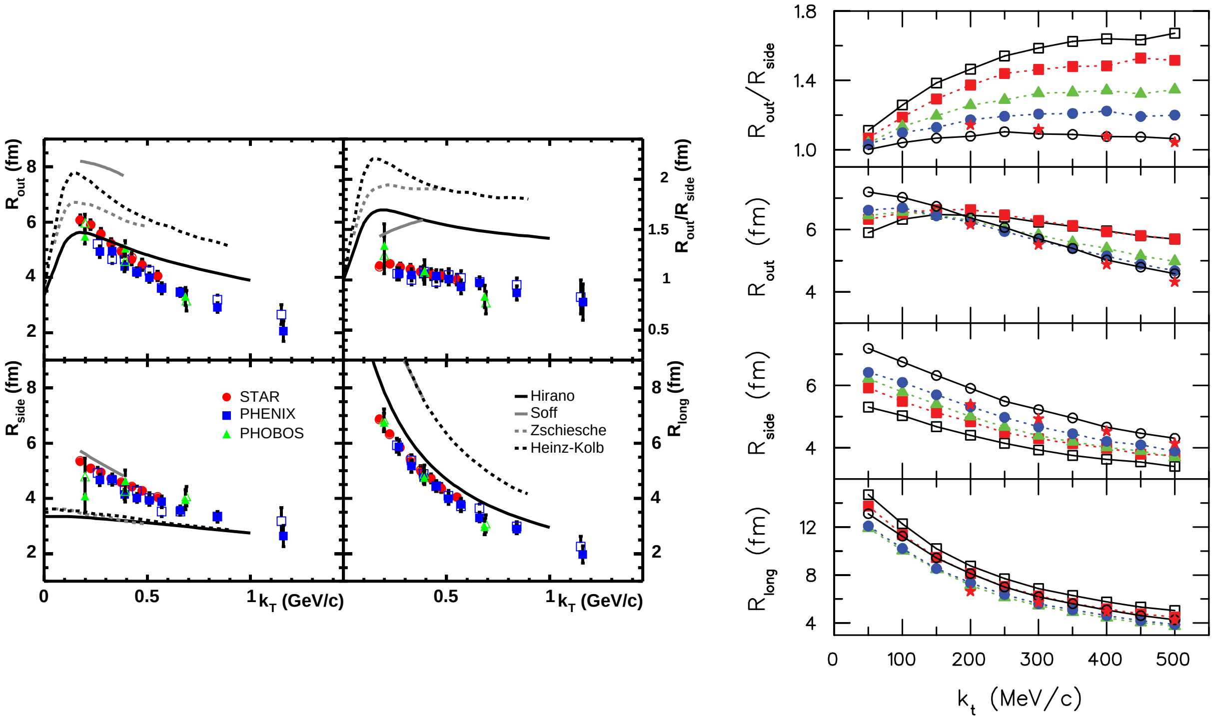

Figure 1.12: (Left)Source radii in Bertcsh Pratt parameterization measured with charged pions as a function of the mean transverse momentum of pair particles k_T [20]. Hydrodynamic (Hirano [21], Kolb [22], and Zschiesche [23]) and hybrid hydrodynamic/cascade (Soff) model calculation are compared. (Right)Source radii calculated by the improved hydrodynamic model with several conditions (symbols with lines), where experimental data from STAR (red star) are compared [25].

the nature of phase transition at RHIC, while early studies used a soft equation of state with a first-order phase transition. Right figure in Fig. 1.12 shows one of the recent improved hydrodynamic calculations with changing such conditions [25]. Red star symbols show the data from STAR experiment, and other symbols with lines show the hydrodynamic calculations with different conditions. Open square symbols show the calculation with a first-order phase transition as a benchmark. Red squares, green triangles, and blue circles show the calculations of adding pre-thermal acceleration (initial flow), stiffer equation of state, and viscosity to the benchmark condition respectively. Open circles show the calculation including more compact profile for initial energy density in addition to all the above features. Data reproduction becomes well though there still remain discrepancy in low k_T region.

Spatial Anisotropy at Freeze-out

In non central collisions, the source shape is expected to be an elliptical shape as shown in Fig. 1.8 (a). If the source keeps the initial shape until freeze-out, the extracted transverse size of the source by HBT measurement depends on azimuthal angle with respect to the reaction plane. The initial spatial anisotropy creates the momentum anisotropy called elliptic flow v_2 because the pressure gradient is different between the direction of short axis (in-plane) and long axis (out-of-plane) of ellipticity, and then the source strongly expands to in-plane direction. One may expect that the source shape may be extended to in-plane direction at the end of the time evolution as shown in

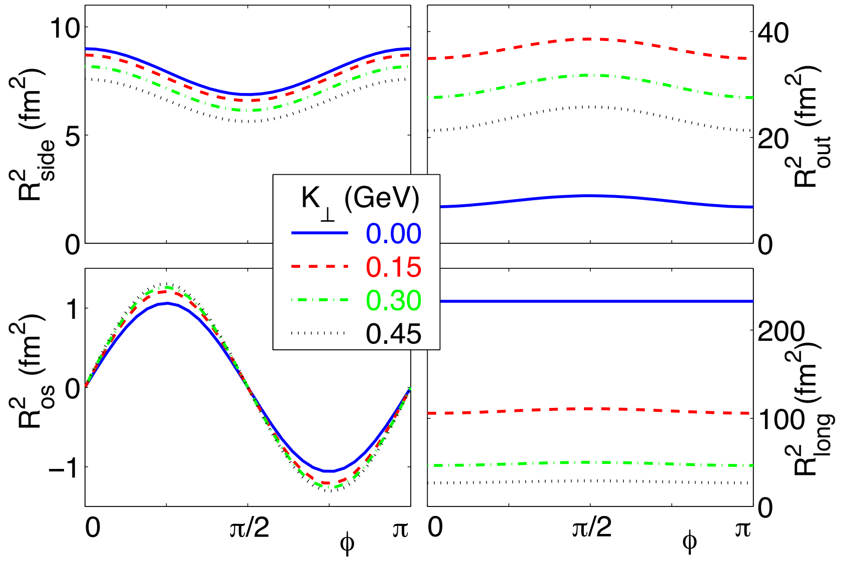

Figure 1.13: Azimuthal angle dependence of HBT radii calculated by the hydrodynamic model [26], assuming the impact parameter b=7 fm and Au+Au collisions at $\sqrt{s_{\rm NN}}$=130 GeV.

Fig. 1.14 if the expansion is much strong or long to change the shape. Hydrodynamic calculation with RHIC energy [26] shown in Fig. 1.13 clearly shows the azimuthal angle dependence of HBT radii in non central collisions. In the limit of the transverse pair momentum $K_\perp$=0, the source size obtained via HBT is almost corresponds to the whole source size, which means pions pairs with $K_\perp$=0 are emitted from the entire source. The calculation in Fig. 1.13 indicates that the source is still elongated to the in-plane direction at freeze-out in RHIC energy.

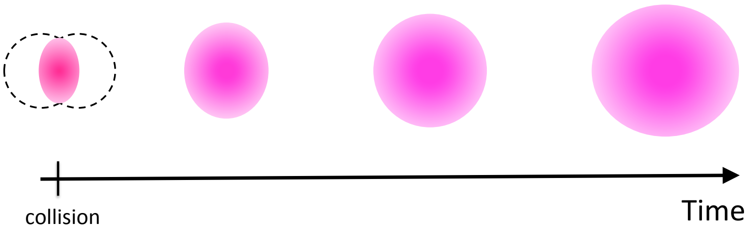

Figure 1.14: A sketch of the evolution of the system shape in coordinate space after the collision.

As described in the previous section, higher harmonic flows result primarily from spatial fluctuations of the initial density across the collision area. If the shape caused by initial fluctuations still exists at freeze-out, the HBT measurement relative to higher order event plane may show these features. A hydrodynamic model calculation reports that the shape of the initial fluctuations resulting in a triangular component of the initial shape may be preserved until freeze-out [27]. Triangular flow v_3 has a weak centrality dependence as shown in Fig. 1.10, while the initial triangularity calculated within a Glauber model has a pronounced centrality dependence (see Sec. 4.6). Triangularity at freeze-out will be determined by the initial triangularity, v_3, the expansion time, and so on. Therefore the HBT measurement relative to higher order event plane provides strong constraints on theoretical models and will be a key observable to reveal the space-time evolution in detail.

1.4 Thesis Motivation

Experimental results to indicate the signature of the QGP have been observed at RHIC so far. In order to study the characteristics of the QGP, further study is in progress in both experiment and theory. The QGP formed by the nucleus-nucleus collisions expands and cools down rapidly and go back to the hadronic state. Although a space-time picture of the evolution of the QGP is emerging with extensive measurements, there are still questions about the collision dynamics and the system evolution. Studies of the final space-time distribution of hadrons and an understanding of its dependence on the initial collision geometry are needed to complete the picture of the space-time evolution of the QGP.

The quantum interference of two identical particles, also known as HBT interference, provides information on the space-time extent of the particle emitting source. Especially the HBT measurement for hadrons with respect to the event plane can provide not only the source size but also the source shape at freeze-out (final eccentricity). In non-central collisions, the collision area is elliptic like an almond shape at initial state (initial eccentricity). Therefore the comparison of the source shape at initial state and freeze-out provides us information on the space-time evolution of the system. Because the final eccentricity is determined by the strength of collective flow, expansion time, velocity profile and so on.

In this thesis, we present the azimuthal HBT measurements with respect to the 2^{nd}-order event plane for charged pions and kaons in Au+Au collisions at $\sqrt{s_{\mathrm{NN}}} = 200$ GeV at RHIC-PHENIX. It is known that charged kaons have less cross section and are less affected by a long-lived resonance decay than charged pions. Therefore we examine HBT radii and final eccentricities of charged pions and kaons, and discuss about the space-time evolution for different particle species.

As introduced in Section 1.3.4, higher harmonic flow have been recently measured, which is considered to originate from the spatial fluctuation of participicting nucleons. A theoretical model based on hydrodynamics predicts that such spatial fluctuation like triangular shape, may be preserved until freeze-out and may be observed by azimuthal HBT measurement with respect to higher-order event planes. Since the signal of the initial fluctuation at initial state is small unlike the initial eccentricity, the magnitude of spatial fluctuation at freeze-out is more sensitive to the expansion time of the system. Therefore that measurement will provide us more detailed information on the space-time evolution of the system. Azimuthal HBT measurement with respect to 3^{rd}-order event plane for charged pions is presented in this thesis.

Besides, the blast wave model is compared to the results of azimuthal HBT measurements to extract the features at freeze-out like the temperature T_f, the velocity profile, and especially temporal information such as the freeze-out time and the emission duration.

Chapter 2

Hanbury-Brown and Twiss Interferometry

In this chapter, we introduce the basics of quantum interference of two identical particles also known as Hanbury-Brown and Twiss (HBT) interferometry.

2.1 History

In the early 1950s, Robert Hanbury Brown and Richard Q. Twiss developed the technique to measure the stellar size through the intensity interference of light in the field of astronomy [28]. They collected the light from the star Sirius onto two photo-multiplier tubes using two mirrors and observed an interference effect between the two intensities. They succeeded in the determination of the angular diameter of Sirius by the interference. This technique is named after names of the pioneers and called “HBT” interferometry.

Also, in the 1960s, the same technique was applied in particle physics by G. Goldhaber, S. Goldhaber, W. Lee, and A. Paris independently of H. Brown and R. Twiss. They observed an unexpected angular correlation between identical pions in proton and anti-proton collisions and successfully reproduced the empirical angular distribution using the symmetrized wave function for identical particles. They concluded the effect originated from the quantum statistical effect called “Bose-Einstein correlation”. Afterwards this technique have been developed in the filed of high energy nuclear experiment and used to determine the space-time extent of the particle emission in a heavy ion collision.

2.2 Theoretical Formalism

2.2.1 Quantum Interference of Two Identical Particles

Here we consider a simple example that two identical particles emits at spatial positions x_1 and x_2 in a certain source as shown in Fig. 2.1. The two particles with four-momentum p_1 and p_2 are observed by two detectors located at x'_1 and x'_2. Then there are two possible routes to reach detectors shown as solid lines and dashed lines in Fig. 2.1. If the particles are identical, the routes cannot be distinguished in quantum mechanics.

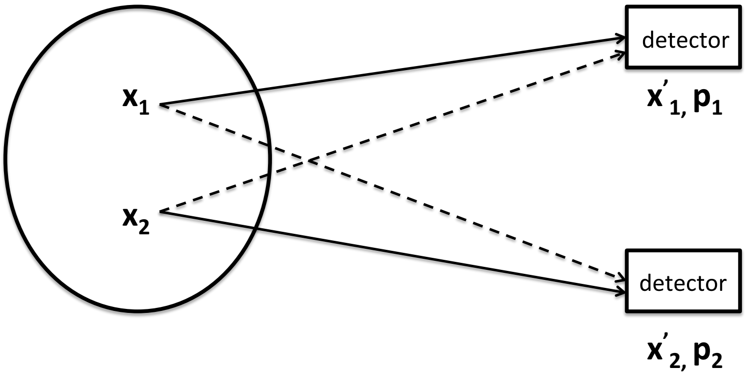

Figure 2.1: Conceptual diagram of quantum interference between two identical particles.

The wave function of two identical particles with plane wave assumption is described as:

$$\begin{aligned}\Psi_{12}(x_1,x_2) &= \frac{1}{\sqrt{2}}\left[\Psi_1(x_1)\Psi_2(x_2) \pm \Psi_1(x_2)\Psi_2(x_1)\right], \\ &= \frac{1}{\sqrt{2}}\left\{A_1A_2e^{-ip_1(x'_1-x_1)}e^{-ip_2(x'_2-x_2)} \pm A_1A_2e^{-ip_1(x'_1-x_2)}e^{-ip_2(x'_2-x_1)}\right\},\end{aligned} \tag{2.1}$$

where $\Psi_i(x)$ is a wave function for a single particle emitted from a point x with momentum p_i and A_i is its amplitude. The upper (lower) sign corresponds to the case of bosons (fermions). The wave function of bosons (fermions) must be symmetric (antisymmetric) under the exchange of two particles. Then the probability density is written as the following equation:

$$|\Psi_{12}(x_1,x_2)|^2 = \frac{1}{2}|A_1|^2|A_2|^2\left[2 \pm e^{-ix_1(p_2-p_1)}e^{ix_2(p_2-p_1)} \pm e^{ix_1(p_2-p_1)}e^{-ix_2(p_1-p_2)}\right], \tag{2.2}$$

$$= |A_1|^2|A_2|^2\left[1 \pm \cos(\Delta x \cdot q)\right], \tag{2.3}$$

where $\Delta x = x_2 - x_1$ and $q = p_2 - p_1$. Second term in Eq. (2.3) represents the strength of the correlation in HBT effect. Therefore the correlation becomes strong when the relative difference Δx or relative momentum q are small.

Here we define the correlation function C_2 as the following equation:

$$C_2 = \frac{P(p_1,p_2)}{P(p_1)P(p_2)}, \tag{2.4}$$

where $P(p_1,p_2)$ is the probability to observe two particles with momentum p_1, p_2 and $P(p)$ is the probability to observe a single particle with momentum p. Using Eq. (2.2) and assuming a normarized spatial distribution of the particle emitting source $\rho(x)$, $P(p_1,p_2)$ is described as:

$$P(p_1,p_2) = \int d^4x_1d^4x_2\rho(x_1)\rho(x_2)|\Psi_{12}(x_1,x_2)|^2, \tag{2.5}$$

$$= |A_1|^2|A_2|^2\left[1 \pm \left|\int d^4x\rho(x)e^{ix(p_2-p_1)}\right|^2\right]. \tag{2.6}$$

A probability to observe a single particle $P(p)$ is written as the following:

$$P(p) = \int d^4x\rho(x)\left|\Psi(p)\right|^2 = \left|A\right|^2. \tag{2.7}$$

Therefore the correlation function C_2 is described as:

$$\begin{aligned} C_2 &= 1 \pm \left|\int d^4x\rho(x)e^{ixq}\right|^2, & (2.8)\\ &= 1 \pm \left|\tilde{\rho}(x)\right|^2, & (2.9)\end{aligned}$$

where $\tilde{\rho}(x)$ is the Fourier transform of the spatial distribution $\rho(x)$. Here we assume that the spatial distribution is the Gaussian distribution:

$$\rho(x) = \frac{1}{4\pi R^2}\exp\left(-\frac{x^2}{2R^2}\right), \tag{2.10}$$

where R is the standard deviation. Since the Fourier transform of Gaussian distribution is also Gaussian distribution, the correlation function C_2 can be expressed as:

$$C_2 = 1 \pm \exp\left(-R^2q^2\right). \tag{2.11}$$

Thus the correlation function C_2 is written as functions of the relative momentum q and the standard deviation of a Gaussian distribution of the particles emitting source. In other words, the source size is obtained as the standard deviation by measuring the relative momentum of two identical particles experimentally. The obtained source size R is usually called "HBT radius". In case of the data analysis, λ parameter is introduced in Eq. (2.11), which is known as the "chaoticity" or "incoherence" factor.

$$C_2 = 1 \pm \lambda\exp\left(-R^2q^2\right). \tag{2.12}$$

The λ takes from 0 to 1. In a fully chaotic source, the λ takes 1, but in the experimentally measured correlation function the λ could be below 1 because particles coming from long-lived decay are included in measuring the correlation function. The contamination of mis-identified particles and the detector efficiency also reduce the λ.

In the 1-dimensional analysis, the correlation function is written as a function of a Lorenz-invariant relative momentum (q_{inv}):

$$C_2 = 1 \pm \lambda\exp\left(-R_{inv}^2q_{inv}^2\right), \tag{2.13}$$

where R_{inv} represents 1-dimensional source size and q_{inv} is defined as:

$$\begin{aligned} q_{inv} &= \sqrt{q_x^2 + q_y^2 + q_z^2 - q_0^2}, & (2.14)\\ q_0 &= E_1 - E_2, & (2.15)\end{aligned}$$

where q_i is the relative momentum in each direction of the coordinate space. The q_0 is the energy difference between two particles, where the energy is defined as $E = \sqrt{p^2 + m^2}$ with the particle mass m. This 1-dimensional analysis is usually performed in case of limited statistics.

2.2.2 Bertsch-Pratt Parameterization

In order to obtain more detailed spatial information on the particle emitting source, 1-dimensional correlation function is expanded to three-dimensional function. In this analysis, we use the Bertsch-Pratt parameterization [31, 32], where the relative momentum is decomposed into sideward (q_{side}), outward (q_{out}) and longitudinal direction (q_{long}). The longitudinal direction denotes the beam direction, and the outward direction is parallel to the pair transverse momentum $k_T = (p_{T1}+p_{T2})/2$, and the sideward direction is perpendicular to both longitudinal and outward directions. In the Bertsch-Pratt parameterization, the correlation function C_2 is written as:

$$\begin{aligned} C_2 &= 1 + \lambda \exp(-R^2 q^2), & (2.16) \\ &= 1 + \lambda \exp(-R_x^2 q_x^2 - R_y^2 q_y^2 - R_z^2 q_z^2 - \sigma_t^2 q_0^2), & (2.17) \\ &= 1 + \lambda \exp(-R_{side}^2 q_{side}^2 - R_{out}^2 q_{out}^2 - R_{long}^2 q_{long}^2 - \sigma_t^2 q_0^2). & (2.18) \end{aligned}$$

The Longitudinal Center of Mass System (LCMS) is also adopted as the analysis frame, where $p_{z1} + p_{z2} = 0$. Therefore q_0 is rewritten as the following:

$$q_0 = E_1 - E_2 = \frac{p_1 + p_2}{E_1 + E_2}(p_1 - p_2) = \beta_{pair} q \overset{LCMS}{\approx} \beta_T q_{out}, \tag{2.19}$$

where β_{pair} is the velocity of pair particles and β_T is the transverse velocity of pair particles. The correlation function is rewritten using Eq. (2.19) as:

$$\begin{aligned} C_2 &= 1 + \lambda \exp(-R_{side}^2 q_{side}^2 - (R_{out}^2 + \beta_T^2 \sigma_t^2) q_{out}^2 - R_{long}^2 q_{long}^2), & (2.20) \\ &= 1 + \lambda \exp(-R_{side}^2 q_{side}^2 - R_{out}^{exp2} q_{out}^2 - R_{long}^2 q_{long}^2). & (2.21) \end{aligned}$$

Feature of this parameterization is that the term of the emission duration σ_t is included only in the experimentally measured R_{out}^{exp}. After here, we write R_{out}^{exp} simply as R_{out}, and HBT radii are sometimes expressed with an omission as R_s, R_o, and R_l.

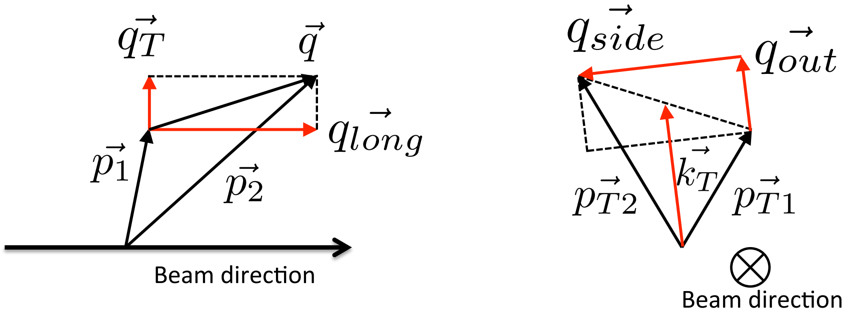

Figure 2.2: Schematic figure of Bertsch-Pratt parameterization. The relative momentum of pair particles is decomposed into a longitudinal, sideward and outward direction.

In general, the correlation function of two identical bosons for a Gaussian source is expressed as:

$$C_2 = 1 + \lambda \exp\left(-q^\mu q^\nu R_{\mu\nu}^2\right), \tag{2.22}$$

where μ and ν take $side, out, long$. $R^2_{\mu\nu}$ denotes the six HBT radii parameters, R^2_{side}, R^2_{out}, and R^2_{long} including the cross term between each q_μ, R^2_{os}, R^2_{ol}, and R^2_{sl}. The cross term R^2_{ol} and R^2_{sl} contain information on the extent to which the main axis the emission ellipsoid is tilted relative to the beam direction [20]. For a boost invariant source, these terms vanish by symmetry. In azimuthally sensitive analysis using data measured at mid-rapidity with the PHENIX detectors, the following correlation function is used.

$$C_2 = 1 + \lambda \exp(-R^2_{side}q^2_{side} - R^2_{out}q^2_{out} - R^2_{long}q^2_{long} - 2R^2_{os}q_{out}q_{side}). \tag{2.23}$$

In azimuthally integrated analysis, R^2_{os}=0.

2.3 Final State Interaction

In the introduction of the correlation function in the previous section, it is assumed that there is no final state interaction between two particles. However there are the Coulomb and strong interaction among actual charged hadrons. Especially the Coulomb repulsion for like sign pairs affects the correlation function at low relative momentum. Therefore the correction is needed in the data analysis. In this section, we explain the contribution from those final interaction to the correlation function.

2.3.1 Coulomb Interaction

As mentioned in the previous section, the HBT effect shows up at low relative momentum. However, the Coulomb interaction is not negligible in case of dealing with charged particles. Since the Coulomb force is repulsive for like sign pairs, the number of pair particles decrease at low relative momentum.

To evaluate the strength of the Coulomb interaction, we consider the Schrödinger equation containing the Coulomb potential. Such a equation is written as Eq. (2.24) using two particle wave function in relative coordinate space of two particles:

$$\left[-\frac{\hbar^2\nabla^2}{2\mu} + \frac{Z_1Z_2e^2}{r}\right]\Psi_c(\vec{q},\vec{r}) = E\Psi_c(\vec{q},\vec{r}), \tag{2.24}$$

where r is the relative distance between two particles, μ is the reduced mass defined as $m_1m_2/(m_1+m_2)$, Z_1e and Z_2e are the charge of two particles, and E is the energy in the center of mass frame.

Solution of Eq. (2.24) is obtained as:

$$\begin{aligned} \Psi_c(\vec{q},\vec{r}) &= \Gamma(1+i\gamma)e^{-\pi\gamma/2}e^{i\vec{q}\cdot\vec{r}}F(-i\gamma;1;iqr - i\vec{q}\cdot\vec{r}), && (2.25) \\ \gamma &= \frac{me^2}{\hbar^2 q}Z_1Z_2, && (2.26) \end{aligned}$$

where Γ is the Gamma function, F is the confluent hypergeometric function. The function F is defined by the power series expansion as:

$$F(a;b;x) = 1 + \frac{ax}{b\cdot 1!} + \frac{a(a+1)x^2}{b(b+1)\cdot 2!} + \cdots . \tag{2.27}$$

In the limit of $-ix \to \infty$, the function F is rewritten as the following:

$$F(-i\gamma;1;x) \overset{-ix\to\infty}{\approx} \frac{e^{\pi\gamma/2}}{\Gamma(1+i\gamma)}\left[e^{i\gamma\ln(-ix)}\left(1-\frac{\gamma^2}{x}+\cdots\right) + \frac{\Gamma(1+i\gamma)}{\Gamma(-i\gamma)}\frac{e^x}{x}e^{-i\gamma\ln(-ix)}\right]. \tag{2.28}$$

Also, Γ function satisfies the following equation:

$$\Gamma(1+i\gamma)\Gamma^*(1+i\gamma) = \frac{\pi\gamma}{\sinh(\pi\gamma)}. \tag{2.29}$$

In the limit of reducing the distance between two particles ($r \to 0$ in Eq. (2.25)), the Coulomb wave function can be rewritten as:

$$\Psi_c(r=0) = e^{-\pi\gamma/2}\Gamma(1+i\gamma). \tag{2.30}$$

Also, the probability density is written as:

$$\begin{aligned} |\Psi_c(r=0)|^2 &= e^{-\pi\gamma}\Gamma(1+i\gamma)\Gamma^*(1+i\gamma) \qquad (2.31)\\ &= \frac{2\pi\gamma}{e^{2\pi\gamma}-1}. \qquad (2.32)\end{aligned}$$

This value is known as the Gamow factor, which assume that the particle emitting source is a point. Since the actual source in a heavy ion collision has finite size, the approximation by the Gamow factor overestimates the strength of the Coulomb interaction.

The symmetrized Coulomb wave function is written as:

$$\Psi_{c,sym}(\vec{q},\vec{r}) = \frac{1}{\sqrt{2}}\left(\Psi_c(\vec{q},\vec{r}) + \Psi_c(\vec{q},\vec{-r})\right). \tag{2.33}$$

Therefore the strength of the Coulomb interaction F_c is calculated as the following:

$$\begin{aligned} F_c &= \frac{P_c(\vec{p_1},\vec{p_2})}{P_{12}(\vec{p_1},\vec{p_2})}, \qquad (2.34)\\ P_c(\vec{p_1},\vec{p_2}) &= \int d^3r\rho(\vec{r})\left|\Psi_{c,sym}\right|^2, \qquad (2.35)\end{aligned}$$

where $\rho(r)$ is the spatial distribution of the relative distance between two particles.

2.3.2 Other Final State Interaction

Strong Interaction

The correlation function is affected by a strong interaction between hadrons. However the system scale of hadron gas created by the heavy ion collisions is much larger than the range of the strong interaction. For example, the range that the s-wave interaction with isospin $I = 2$ for pion pair acts is expected to be about 0.2 fm, which is much shorter than the typical size of interaction region in heavy ion collisions. Therefore since the effect by the strong interaction is negligible [33], we don't treat it in this analysis.

External Coulomb interaction

The particle emitting source has positive charges of nuclear protons. Therefore charged particles emitted from the source feel not only the Coulomb interaction between two particles but also the Coulomb interaction between the emitted particle and the source itself. The past study [34] shows that the effect is much small and negligible. Therefore we don't apply any correction for this effect in this analysis.

2.4 Characteristics in Heavy Ion Collisions

In heavy ion collisions, the measured HBT radii is thought to depend on the following quantities:

- Transverse pair momentum
- System Size
- Reaction Plane

When we extract information on the space-time extent of particle emitting source in the heavy ion collisions, we need to carefully deal with the above items. In this section, we briefly introduce those characteristics.

2.4.1 Dynamical System

As we already described in Sec. 1.3.5, the HBT radii measured in the heavy ion collisions strongly depend on the transverse pair momentum (k_T). This appears for a dynamically expanding source, where the particle momenta are strongly correlated with the particle spatial emission points. Figure 2.3 shows a sketch of the emission region for a static source and a dynamical expanding source. In a static source shown in Fig.2.3 (a), the constituent particles emit from the source with their thermal momenta toward random directions, where there is no correlation between the spatial and momentum distributions. In a expanding source shown in Fig. 2.3 (b), we assume that the particles are emitted to radial direction from the center of the source with a velocity $\vec{\beta}_T(\vec{r})$ like a radial flow, where the particles around the surface of the source get larger momentum. Therefore the emission region measured as the HBT radius would correspond to a smaller region around the surface for higher k_T, and a larger region for lower k_T, and it would become closer to the whole size of the source in the limit of $k_T = 0$. In other words, the presence of the k_T dependence of the HBT radii indicates the dynamical expansion of the source.

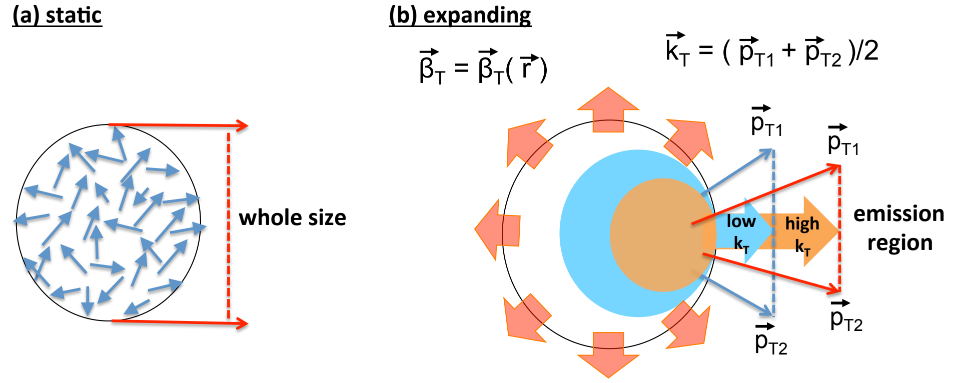

Figure 2.3: A sketch of the emission region for a static source (a) and a dynamical expanding source (b). In the expanding source, it is assumed that the transverse velocity β_T of particles is proportional to the distance from the center of the source to their particle positions.

Within a simple model with a Gaussion source approximation based on the hydrodynamics, the HBT radii are explicitly written as a function of $k_T(m_T)$ as follows [35]:

$$R_s^2(m_T) = \frac{R_{geom}^2}{1 + m_T\eta_f^2/T}, \tag{2.36}$$

$$R_o^2(m_T) = R_s^2(m_T) + \frac{1}{2}(\frac{T}{m_T})^2\beta_T^2\tau_0^2, \tag{2.37}$$

$$R_l^2(m_T) = \tau_0^2\frac{T}{m_T}\frac{K_2(m_T/T)}{K_1(m_T/T)}, \tag{2.38}$$

where R_{geom} is the actual source size, η_f is the flow rapidity, T is the temperature, β_T is the transverse pair velocity, and τ_0 denotes the freeze-out time. The above aproximation assumes a longitudinal boost-invariance and a sharp freeze-out at the time τ_0 ($\Delta\tau = 0$). One can see that the HBT radii decrease with m_T. In the limit of $m_T \to 0$, the R_s agrees with the R_{geom}.

2.4.2 System Size Dependence

As described in the previous section, the HBT radii represent the standard deviation of the source size assuming Gaussian function as the spatial density distribution. In case of hadron-hadron correlation, the extracted source size corresponds to the spatial extent of particle emitting source at kinetic freeze-out. Therefore the extracted HBT radii should depend the quantity which represents the system size, such as centrality and multiplicity. It is known that HBT radii are linearly scaled well by the 1/3 power of the number of participants N^{part} calculated by Glauber model as shown in Fig. 2.4 [36], where the value of N_{part} corresponds to the volume of the source and $N_{part}^{1/3}$ corresponds to the radius of the source.

2.4.3 Azimuthal Angle Dependence

In non central collisions, the source shape is expected to be an elliptical shape. If the source keep the initial shape until freeze-out, the extracted transverse size of the source by HBT measurement depends on azimuthal angle with respect to the reaction plane. The initial spatial anisotropy creates the momentum anisotropy called elliptic flow v_2, and the source strongly expands to in-plane direction. As a result, the source may change the shape extended to in-plane direction shown in Fig. 1.14. Therefore this measurement provides us information of the expansion strength and time.

Right panel in Fig. 2.4 shows the results of squared HBT radii with respect to 2^{nd}-order event plane measured at the STAR experiment [64]. The HBT radius R_s and R_o representing the transverse source size have a clear event plane angle dependence and the strength of oscillation increases with centrality going from central to peripheral collisions. This result indicates that the final distribution still retains the initial elliptical orientation upon freeze-out.

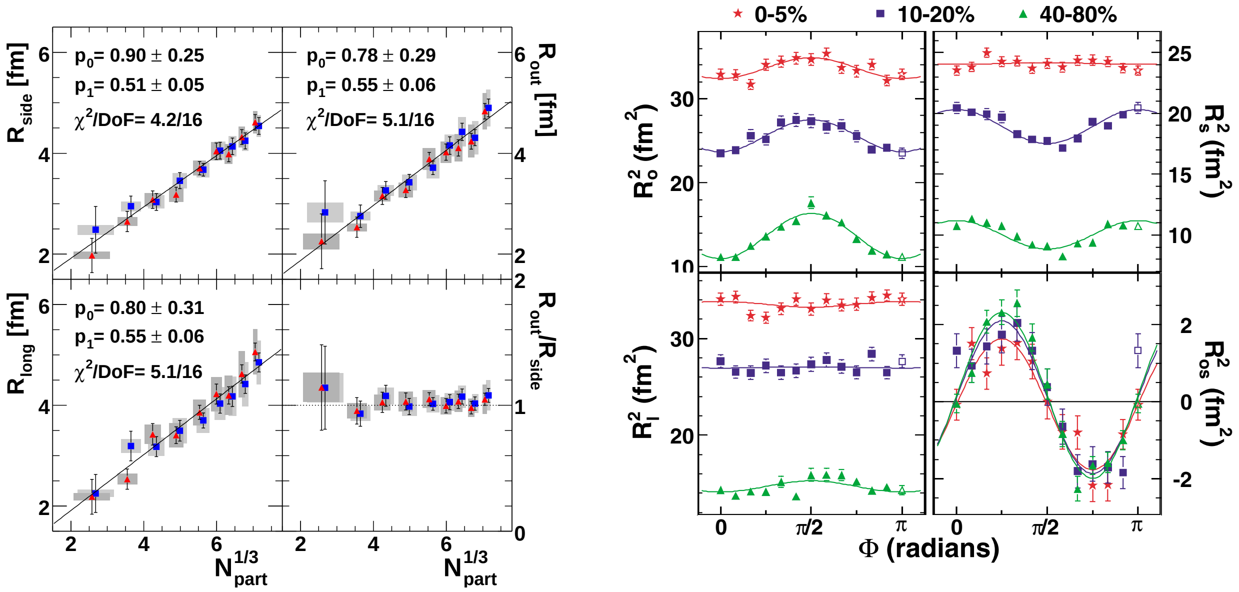

Figure 2.4: (Left)The HBT radii and the ratio of R_s and R_o for positive (blue square) and negative (red triangle) pion pairs as a function of $N_{part}^{1/3}$ in Au+Au collisions at $\sqrt{s_{\mathrm{NN}}} = 200$ GeV, measured at the PHENIX experiment [36]. (Right)Squared HBT radii with respect to 2^{nd}-order event plane for three centrality bins measured at the STAR experiment [64].

Chapter 3

Experiment

In this chapter, we introduce the Relativistic Heavy Ion Collider and the PHENIX experiment.

3.1 Relativistic Heavy Ion Collider

Relativistic Heavy Ion Collider (RHIC) is a unique heavy ion accelerator and collider, which is at Brookhaven National Laboratory in the United States of America. RHIC consists of two circular rings of superconducting magnets that are 3.8 km in circumstance, which can accelerate various ions such as proton and gold nuclei, and can collide them at several crossing points around rings. The top energy ranges from 100 GeV to 250 GeV per nucleon, which depends on the ion accelerated and is 100 GeV for gold ions and 250 GeV for proton. The designed luminosity is 2×10^{26} cm^{-2} s^{-1} for gold ions and 1.4×10^{31} cm^{-2} s^{-1} for protons.

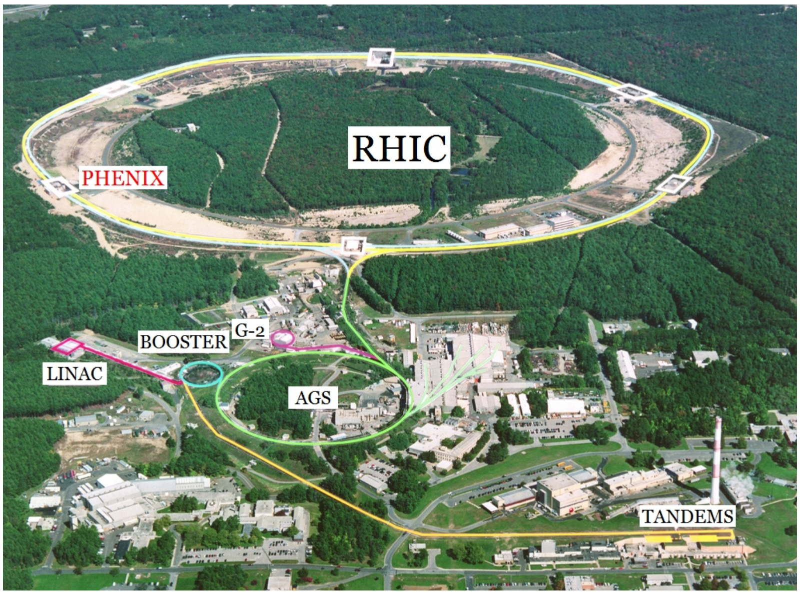

Figure 3.1: Aerial photograph of the RHIC facility

To accelerate heavy ion to relativistic energy, a chain of particle accelerators are used to pre-accelerate and inject ions into the collider rings, which are the Tandem Van de Graaff, the Booster

Synchrotron, and the Alternating Gradient Synchrotron (AGS). Here, we explain the steps to accelerate gold ions to 200 GeV per nucleon.

First, ions created by sputter ion source are accelerated to 1 MeV per nucleon by the Tandem Van de Graaff, where some of electrons around nuclei are removed. These positive ions enter the Tandem-to-Booster line, which carries them to the Booster Synchrotron through a vacuum via a magnetic field. Ions have about 5% the speed of light at this point. The Booster Synchrotron accelerates ions up to 95 MeV per nucleon by an radio frequency (RF) electric filed, and the ions are stripped to the charge state of +77 at the exit of the Booster and injected to the AGS. The AGS accelerates the bunch of ions to the required injection energy for the RHIC, which is 10.8 GeV per nucleon. The ions from the AGS, which are stripped to the charge state of +79, go through the AGS-To-RHIC transfer line and are injected to the two RHIC rings by a switching magnet. The two rings are called the blue and yellow rings where the ions travel to opposite directions. Finally, the ions are accelerated to 100 GeV per nucleon by electric field in an RF cavity as in the Booster and AGS.

RHIC ring has six intersection points where the ion beams from two rings collide to each other. PHENIX detector locates in one of the intersection points. The detail of PHENIX detector is described in the next section.

3.2 PHENIX Experiment

3.2.1 Overview of PHENIX

The Pioneering High Energy Nuclear Interacting eXperiment (PHENIX) is one of the largest experiments at RHIC. PHENIX has more than 450 collaborators representing 56 institutions in 12 countries. A prime goal for the PHENIX experiment is to produce a deconfined state of nuclear matter called the Quark Gluon Plasma and study its properties with heavy ion beams. A second major goal is to measure the spin structure of the nucleon with polarized proton beams. In order to perform such a broad study of physics, the PHENIX detectors are designed to measure many different particles produced by a nucleus-nucleus collision with good resolution, including photons, electrons, muons, and hadrons. They can carry information about processes or action within the collisions. Therefore, PHENIX provides the information of the inside hot and dense matter produced by the heavy ion collision as x-ray or MRI provides imaging information about the inside of human body. Figure 3.2 shows the layout of PHENIX detectors in 2007 RHIC-run configuration. The PHENIX detectors consist of magnet systems, global detectors, central arm detectors, and muon arm detectors. In the next section, we introduce the detectors related to this study.

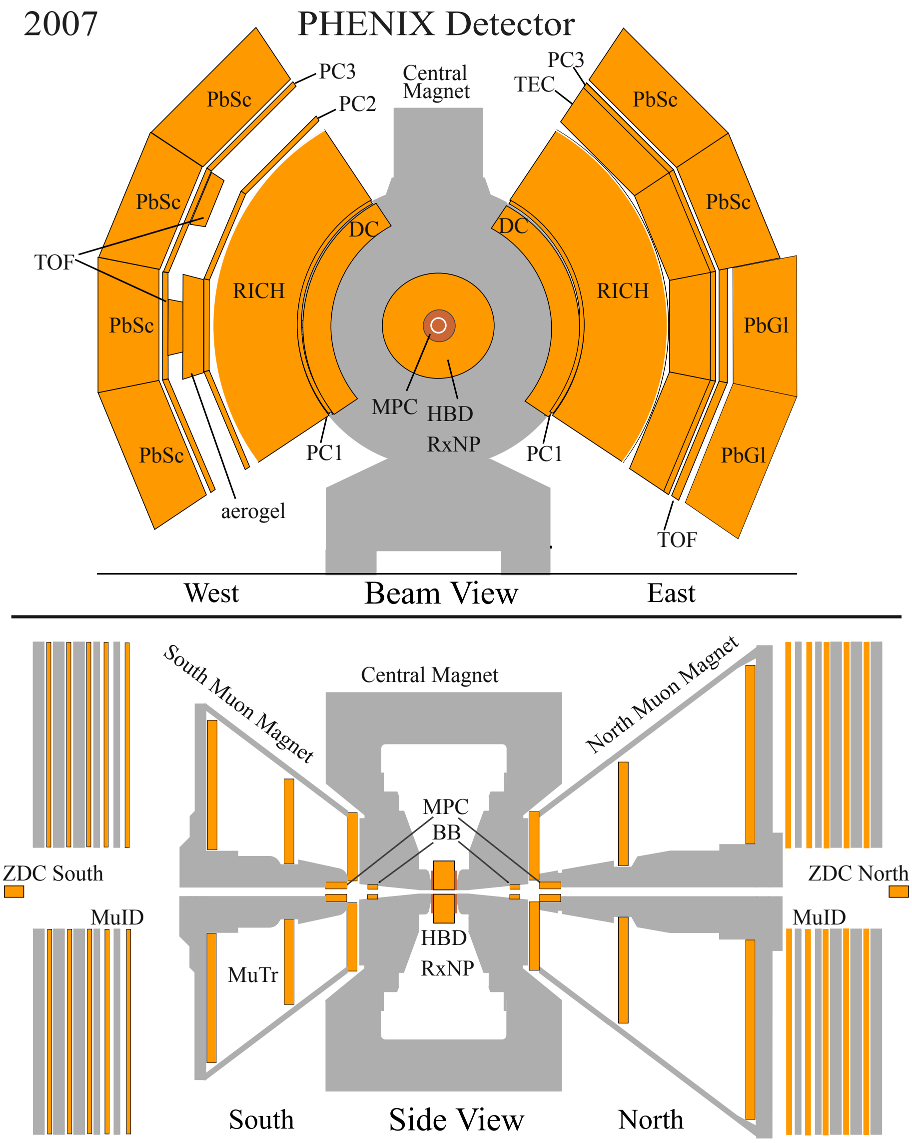

Figure 3.2: The layout of PHENIX detectors in 2007 RHIC-run configuration. Top figure is the central arm detectors viewed from the beam axis. Bottom figure is side view of the global detectors and muon arm detectors.

3.2.2 Magnet System

PHENIX magnet system [37] consists of three spectrometer magnets with warm iron yokes and water-cooled copper coils, which are Central Magnet and Muon Magnets in north and south side. A schematic of the PHENIX magnet system is shown in Fig. 3.3. The Central Magnet is energized by two pairs of concentric coils and provides a field around the interaction vertex that is parallel to the beam, which allows to create zero field region near R = 0 (R is the radial distance from the beam axis). It is also designed to satisfy such requirements that the magnetic filed should be minimal in the region of photomultiplier tubes of the Ring Image Cherenkov Counter and the Electromagnetic Calorimeter. The north and south Muon Magnets (MMN and MMS) use solenoid coils to produce a radial magnetic filed for muon analysis. Each of the three magnets provides a field integral of about 0.8 $T \cdot m$.

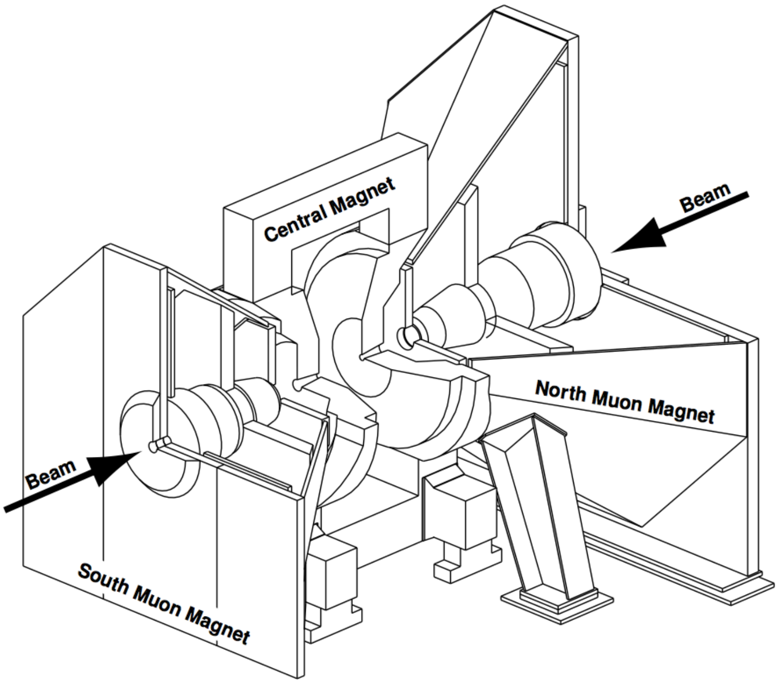

Figure 3.3: Line drawings of the PHENIX magnets, shown in perspective and cut away to show the interior structures. Arrows indicate the line of the colliding beams in RHIC.

3.2.3 Global Detectors

The global detectors aim to characterize the global properties of an heavy ion collision like the collision vertex along beam direction, the collision time, the collision centrality, and the event plane, which are installed around the beam line. In this subsection, we explain the detail of the Beam-Beam Counter, the Zero-Degree Calorimeter and the Reaction Plane Detector used in this analysis.

Beam-Beam Counters

The main role of the Beam-Beam Counters (BBC) [38] is to measure the collision time, the collision point along the beam axis and to produce the PHENIX Level-1 trigger that inform the PHENIX data acquisition system of the occurrence of the collision. The BBC consists of two identical sets of counters installed on both side of the collision point along the beam axis. They are located at 144 cm from the collision point and surround the beam pipe, which corresponds to a pseudo rapidity range from 3.0 to 3.9 over the full azimuth. Each counter is composed of 64 mesh-dynode photomultiplier tubes (PMT) of 1 inch in diameter equipped with 3 cm quartz on their head as a Cherenkov radiator. Figure 3.4 shows a element of the BBC in the left, a set of BBC with the assembled 64 elements in the middle, and a set of the BBC installed around the beam pipe behind the Central Magnet.

Figure 3.4: (Left)An element of the BBC composed of a mesh-dynode photomultiplier with a quartz radiator. (Middle)A BBC composed of 64 elements. (Right)The BBC installed around the beam pipe behind the Central Magnet.

The collision time T_0 and the collision vertex position Z_{vtx} along the beam axis are calculated by the average arrival time at the two BBCs and the timing difference between each counter as defined the following:

$$T_0 = \frac{T_S + T_N - 2L/c}{2}, \tag{3.1}$$

$$Z_{vtx} = \frac{(T_S - T_N) \cdot c}{2}, \tag{3.2}$$

where T_S and T_N are the arrival time at each counter in the south and north side and c is the speed of light and L is the distance from the center of beam axis to each BBC. The time resolution of a single BBC element is 52 ps.

Zero-Degree Calorimeters

The Zero-Degree Calorimeters (ZDC) are Cherenkov light sampling calorimeters placed on the both side of the collision point, at 18 m from the collision point along the beam axis, behind DX dipole magnet as shown in Fig. 3.5 (A). The purpose of the ZDC is to detect the neutrons included in the rest nucleons that did not participated in the heavy ion collisions and measure their total energy, when protons and other charged particles are swept away by the DX dipole magnet as shown in Fig. 3.5. The ZDC coincidence of the two beam directions is a minimum bias selection of heavy ion collisions. This makes it useful as an event trigger and a luminosity monitor.

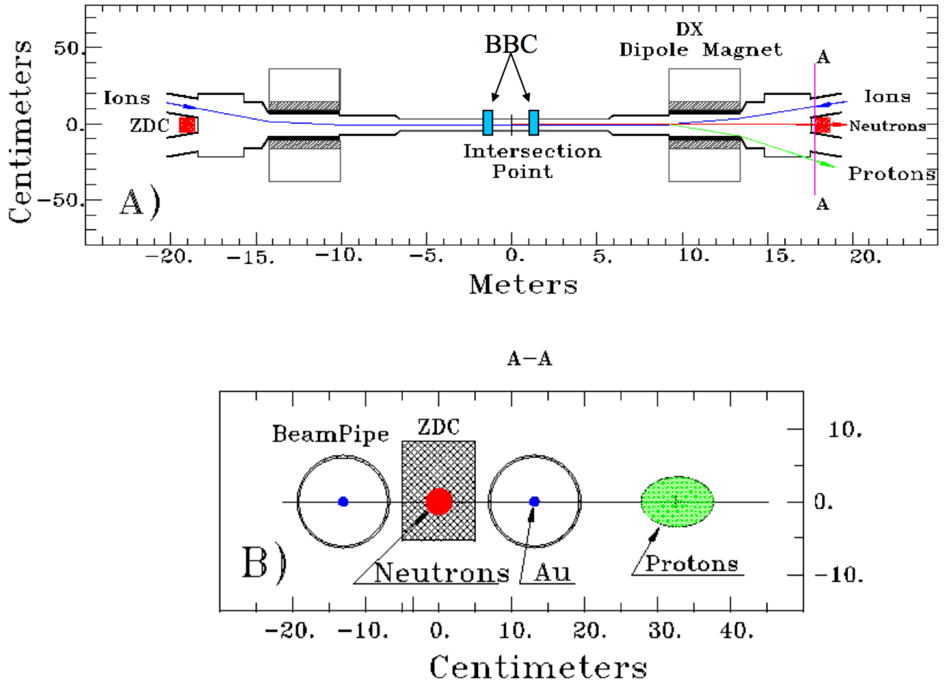

Figure 3.5: (A)Plain view along the beam axis indicating the location of the BBC, the DX dipole magnet and the ZDC. (B)Cross-section view of Figure (A) along the A-A line.

A ZDC is subdivided into 3 identical modules with 2 interaction length each. The active medium is clear PMMA fibers (ϕ=0.5 mm) interleaved with tungsten plates of 5 mm thickness with threaded mounting holes (Fig. 3.6). This sandwich structure is tilted at 45 degree to the beam to align the optical fibers with the Cherenkov angle for forward particles in the shower. The energy resolution of the ZDC for 100 GeV neurons is 21%. The timing resolution is $\sim$120 ps for 100 GeV neutrons which corresponds to vertex position resolution $\sim$2.5 cm.

Reaction Plane Detector

The Reaction Plane Detector (RXNP) [41] was installed prior to the 2007 RHIC run with the aim of accurately measuring the reaction plane angle of the heavy ion collision. Although the BBC have mainly played a role in the measurement of the reaction plane angle, the resolution of the reaction plane angle was poor for the detailed study of the flow and other measurements related to the reaction plane. The RXNP provides better resolution by a factor of two compared to the BBC.

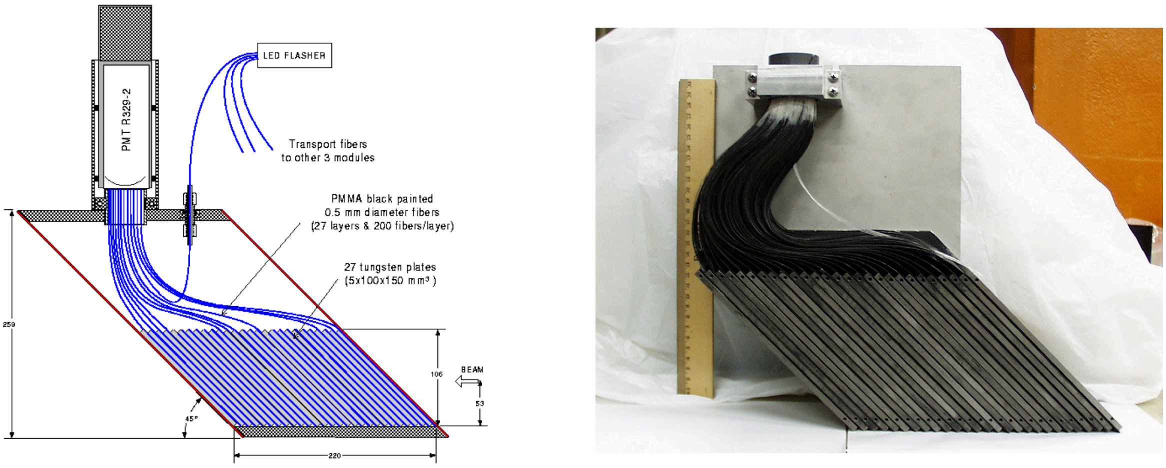

Figure 3.6: (Left)Schematic of a ZDC module. (Right)A photo of a ZDC module.

The RXNP is composed of two sets of 24 scintillators in the north and south side, located at 39 cm from the vertex position. The scintillators are arranged around the beam pipe in two concentric rings (inner and outer rings) composing 12 segments in azimuthal direction as shown in Fig. 3.7. Each ring covers the pseudo rapidity range $1.0 < |\eta| < 1.5$, $1.5 < |\eta| < 2.8$ respectively. To enhance the observed signal, a lead converter of 2 cm thickness is located in front of the scintillator. Each scintillator is embedded with optical fiber connected to the photomultipliers through the cookie which bends the light by a 45° reflective surface. The resolution of 2^{nd}-order event plane $\langle\cos[2(\Psi_2 - \Psi_R)]\rangle$ is approximately 0.75 at mid-central collisions.

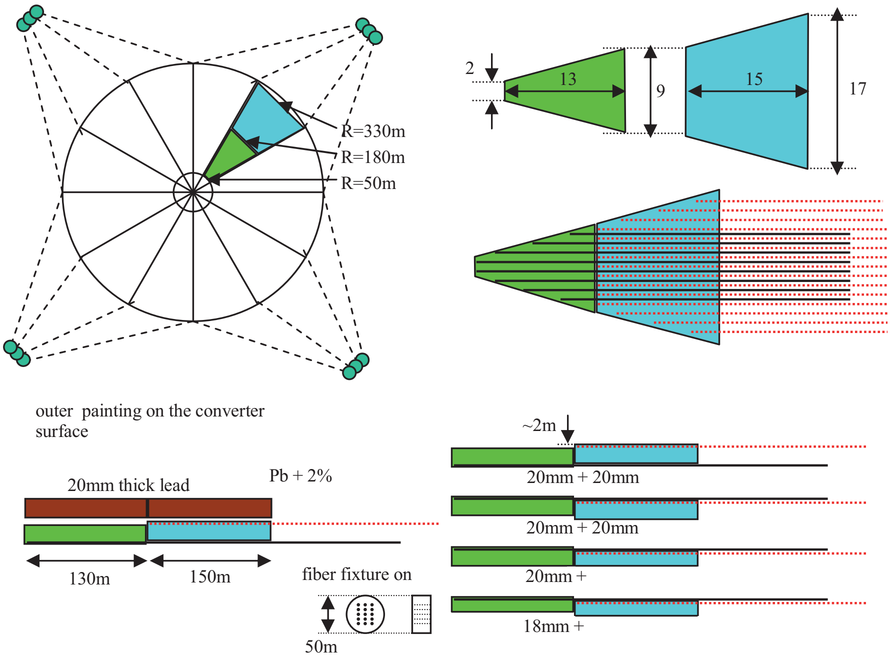

Figure 3.7: Schematic view of the Reaction Plane Detector

Figure 3.8: Photo of the RXNP installed on the nosecone of the PHENIX central magnet in north side, where four quadrants surround the beam pipe.

3.2.4 Central Arm Detectors

PHENIX central arm detectors consist of a pair of arms located in west and east side. Each arm covers 90° in azimuth direction and $|\eta| < 0.35$. In this section, we explain the main detectors used in this analysis.

Drift Chamber

The Drift Chambers (DC) [49] are located in the region from 2.02 to 2.46 m from the beam axis in east and west arms and cover the azimuthal angle of 90° and 2 m length along the beam axis. The DC measures trajectories of charged particles in the r-ϕ direction to determine the transverse momentum p_T of each particle. In order to achieve the determination of p_T with high momentum resolution and the good tracking efficiency for the highest multiplicities at RHIC, the DC is needed to satisfy the following requirements:

- Single wire resolution better than 150 μm in the r-ϕ.
- Single wire two track separation better than 1.5 mm.
- Single wire efficiency better than 99%.
- Spatial resolution in the z direction better than 2 mm.

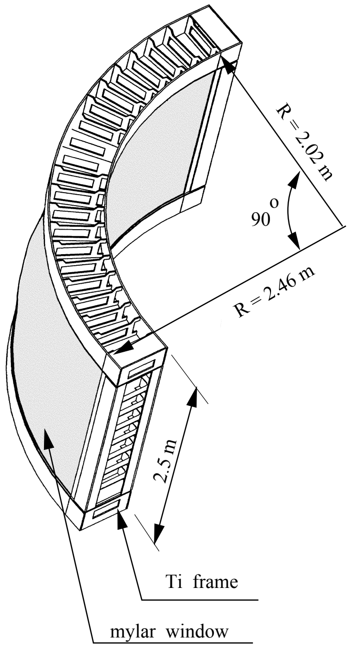

Figure 3.9: The frame of the Drift Chambers

The DC volume is defined by a cylindrical titanium frame as shown in Fig. 3.9. The frame is filled with drift chamber modules and is divided in 20 equal sectors covering 4.5° in azimuth. There are six types of wire modules stacked radially in each sector: X1, U1, V1, X2, U2 and V2. Each module contains 4 sense (anode) planes and 4 cathode planes forming cells with a 2-2.5 cm drift space in azimuthal direction. The X1 and X2 wire cells run in parallel to the beam axis to perform precise track measurements in the r-ϕ. These wire cells are followed by two sets of small angle U, V wire planes used in the pattern recognition. U1, V1, U2 and V2 wires have stereo angles of about 6° relative to the X wires and measure the z coordinate of the track. The X-stereo cell contains 12 anode wires, and each of U and V-stereo cells contains 4 anode wires respectively. As a result, there are 40 drift cells in the DC located at different radii. The layout of wires within one DC sector is shown in Fig. 3.10. The DC works being filled with a gas mixture of 50% Ar and 50% C_2H_5.

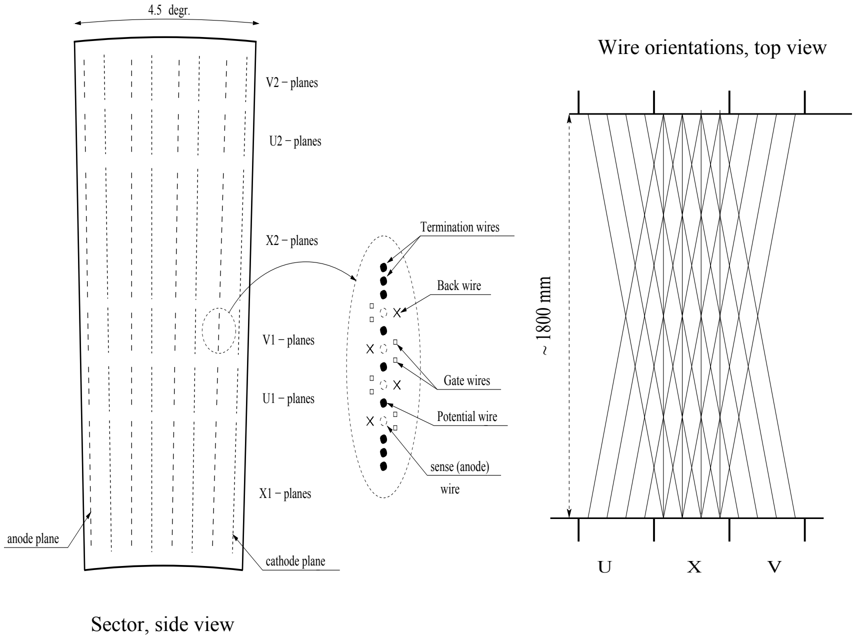

Figure 3.10: (Left)The layout of wire position within one DC sector and inside the anode plane. (Right)Top view of the stereo wire orientation.

Pad Chamber

The Pad Chambers (PC) [49, 43] are multi-wire proportional chambers that consists of three separate chambers (PC1, PC2, PC3) in both central arms as shown in Fig. 3.2. The three chambers are located at the radial distances of 2.5 m (PC1), 4.2 m (PC2) and 4.9 m (PC3) from the interaction region. The PC1 is placed between the DC and the Ring Image Cherenkov Counter (RICH) and the PC3 is placed in front of the Electromagnetic Calorimeter (EMCal) in the both east and west arms. The PC2 is present behind the RICH only in the west arm. The PC system determines space points along the particle trajectories of the straight line outside the magnetic field. The PCs are the only non-projective detectors in the central tracking system and thus critical elements of the pattern recognition. The PC1 is essential for determining the three dimensional momentum vector by providing the z coordinate at the exit of the DC. The PC2 and the PC3 are needed to resolve ambiguities in the outer detectors where about 30% of the particles striking the EMCal are produced by either secondary interactions and particle decays outside the aperture of the DC and the PC1 or low momentum primary tracks that curves around PC1 in the magnetic field and strike the PC2 and the PC3.

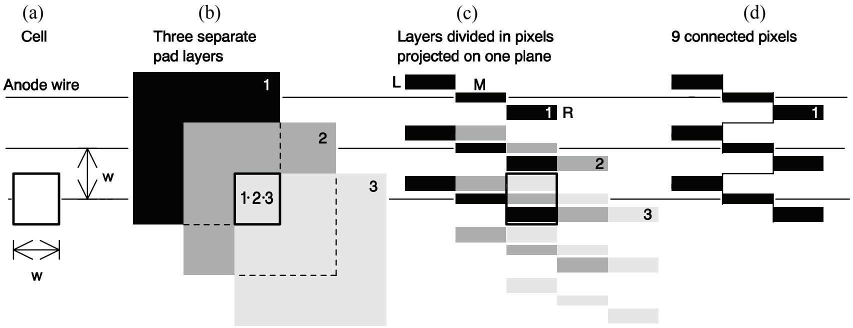

Figure 3.11: The principle of the pad geometry

Two dimensional readout of wire chambers is done by using a cathode segmented into readout pads. Figure 3.11 shows the principle of the pad geometry. The readout pad is composed of three separate layers of pads. One pad consists of 3 × 3 cells (8.4 × 8.4 mm^2 for one cell in PC1) with an electronic readout channel. The three layers are arranged being shifted by one cell relative to each other in both dimensions (Fig. 3.11 (b)). Each cell contains three pixels and an avalanche must be sensed by all three pixels to form a valid hit in the cell. The three pixels in a cell are always connected to different but neighboring channels and each cell is defined by its unique triplet. This system saves a factor of nine in readout channels compared to readout of every pixel and a factor of three compared to a readout pad geometry where a cell is the actual electrode connected to an electronics channel. Figure 3.12 shows a an exploded view of the individual parts of a PC1 chamber. Each chamber is made of two flat panels, the pixel panel and the cathode panel, and an anode wire electrode between them. The anode wires are made of a tungsten-rhenium alloy with gold coating with a diameter of 25 μm. The field wires are gold-coated copper-beryllium of 75 μm diameter.

The position resolution in the z direction is ±1.7 mm which is better than the design goals. The PC2 and PC3 have the same angular resolution as the PC1. Thus the cells on the PC3 have 4 times the area of the PC1 cells since the PC3 is at twice the distance from the crossing beams as compared to the PC1.

Time-Of-Flight Counter

The Time-Of-Flight (TOF) system makes it possible to identify charged hadrons by measuring the time of flight of charged particles. There are two types of TOF detectors in PHENIX, which are the TOF.East of plastic scintillation counter in the east arm and the TOF.West of Multi-gap Resistive Plate Chamber in the west arm.

The **TOF.East** (TOF.E) [44] is located at a distance of 5.1 m from the collision point and between the PC3 and Electromagnetic calorimeter (EMCal) in the east arm. It is designed to cover the η range of the central arm ($70° \leq \theta \leq 100°$) over 30° in azimuth. The TOF.E consists of 10 panels, and one panel consists of 96 slats of plastic scintillators with PMTs and light guides which are at both ends of scintillators. Scintillators with two different length (637.7 and 433.9 mm)

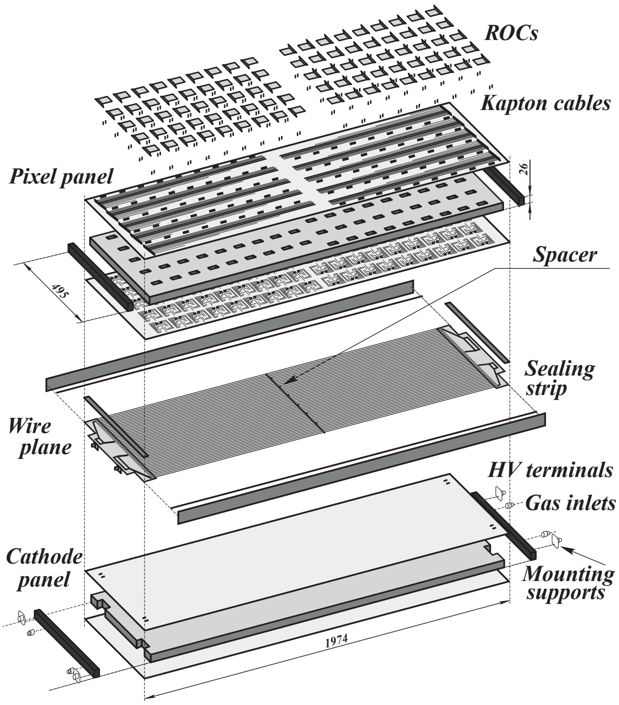

Figure 3.12: Exploded view of a PC1 chamber

are assembled in an alternating fashion in order to avoid geometrical conflicts between the PMTs neighboring slats. Total 10 TOF.E panels, 960 slats of scintillators and 1920 channels of PMTs were installed and operated in the first year of PHENIX operation.

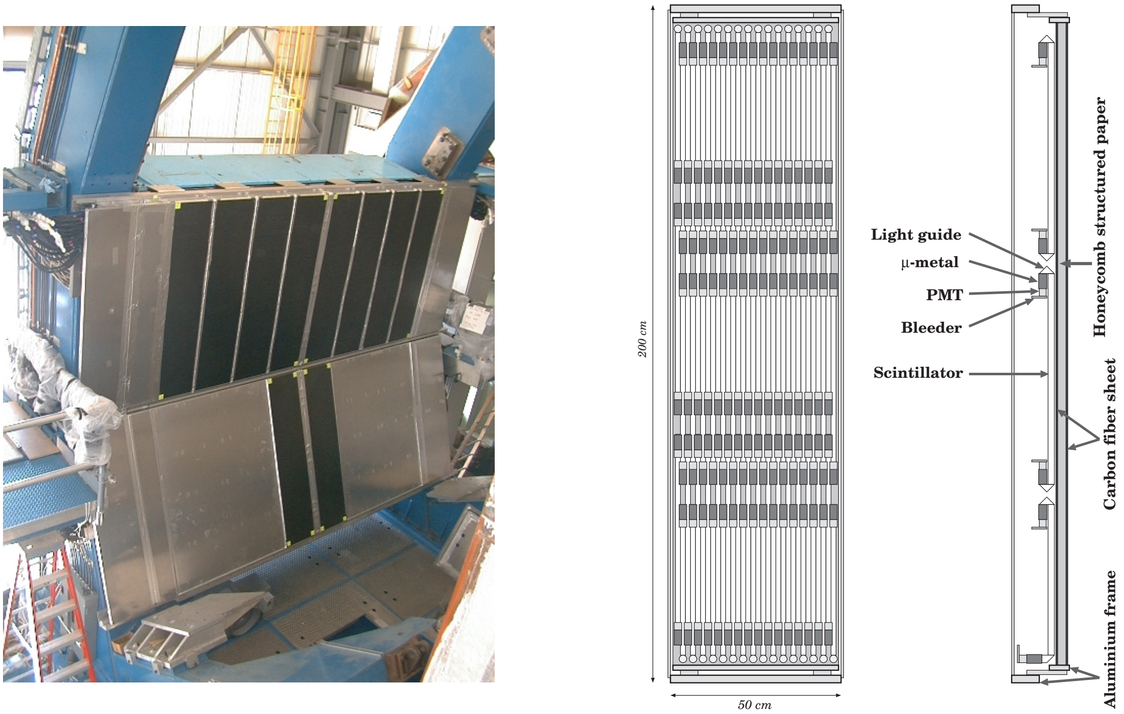

Figure 3.13: (Left) Photo of the TOF.E detector mounted on the PHENIX east arm. (Right) Schematic diagram of the components of a single TOF.E panel.

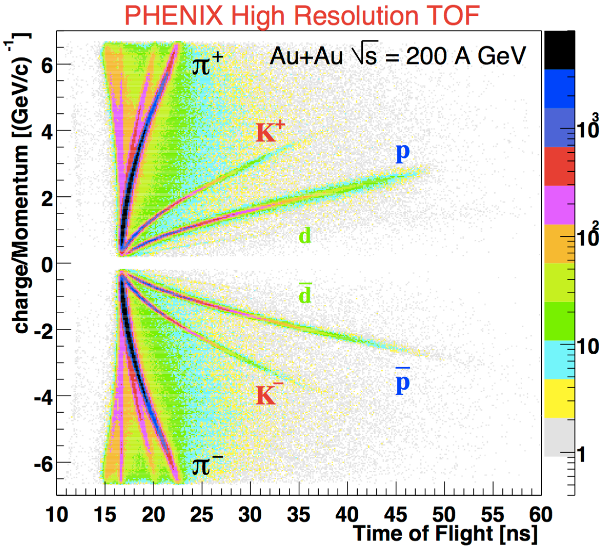

Figure 3.14: Contour plot of the time of flight versus reciprocal momentum in minimum bias Au+Au collisions.

Particle identification for charged hadrons is performed by combining the information from the DC, PC1, BBC and the TOF.E. The designed time of flight resolution is about 100 ps, which allows us to achieve a 4σ π/K separation at momenta up to 2.4 GeV/c. Figure 3.14 shows a 2-dimensional contour plot of the time of flight versus reciprocal momentum in minimum bias Au+Au collisions. The figure demonstrates that particle identification was achieved by the TOF detector. The timing resolution was about 133 ps for the momentum range of $1.0 < p_T < 1.7$ in Au+Au collisions in year 2007 (Run7).

The **TOF.West** (TOF.W) [45] is time-of-flight counters consisting of the Multi-gap Resistive Plate Chamber (MRPC) installed in the west arm prior to the 2007 RHIC run. The TOF.W is located at the two sectors of the west arm in front of the PC3, where the detector in the bottom sector is placed to be overlapped with the Aerogel Cherenkov Counter (ACC) in order to extend the particle identification capability for charged hadrons together with the ACC and the Ring Image Cherenkov Counter. The MRPC is characterized by the high timing resolution, the good detection efficiency and much lower cost compared to the scintillation counter with PMTs. It also has the advantage of a simple structure and being easy to construct it.

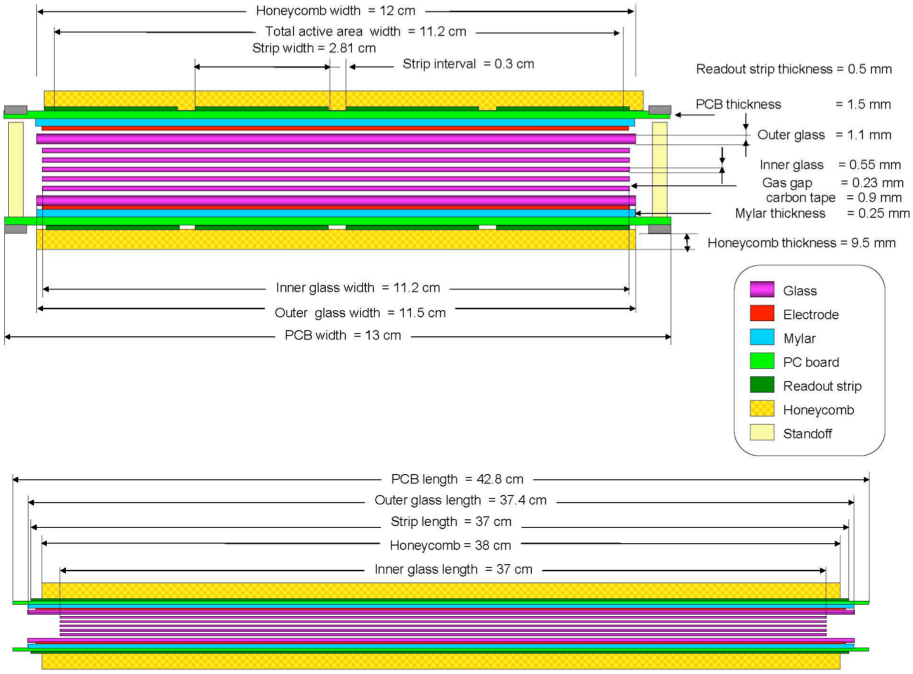

Figure 3.15: Cross sectional view of the TOF.W MRPC.

The MRPC consists of a stack of plates with high electrical conductivity (resistive plates) which are spaced from one another with equal sized spacers creating a series of gas gap (multi-gap). Figure 3.15 shows the cross sectional view of the TOF.W MRPC. The MRPC configuration of a single stack with 6 gap is adopted as the TOF.W with outer glass thickness 1.1 mm, inner glass thickness 0.55 mm and gap size 0.23 mm. Monofilament fishing line is used as spacers. Electrodes (carbon tape) are connected to the outer surfaces of the stack of resistive plates, while internal plates are left electrically floating. Copper strips for the readout are placed outside the stack of resistive plates. Each MRPC contains 4 strips with double ended readout. The TOF.W consists of 4 panels and one panel contains 32 MRPC modules and have a total of 1024 channels. Figure 3.16 shows photos of the MRPC. Left figure shows side view of a MRPC chamber. RIght figure shows one panel consisting of 32 MRPC modules. The MRPC works with a gas mixture of R143A 95% and isobutane 5%. The timing resolution was about 90 ps for the momentum range of $1.3 < p_T < 1.7$ in Au+Au collisions in year 2007.

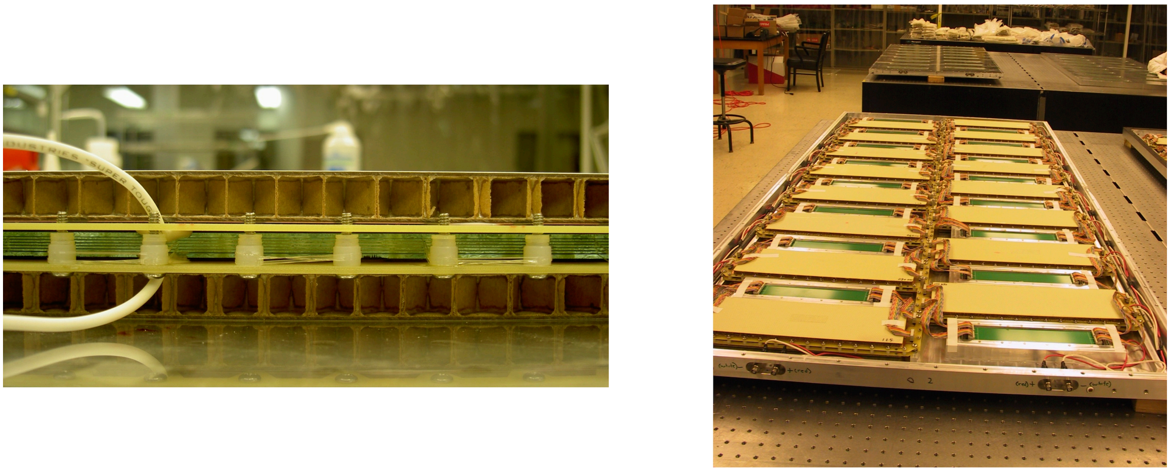

Figure 3.16: (Left)Side view of a MRPC chamber (Right)A panel of TOF.W consisting of 32 MRPC chambers.

Ring Image Cherenkov Counter

The Ring Image Cherenkov Counter (RICH) [44] is one of the primary devices for separation of electrons from the large number of the produced charged pions. The working principle of the RICH is based on a physical phenomena of Cherenkov radiation. When a charged particle exceeds the speed of light in a certain medium, electromagnetic radiation is emitted, which is called Cherenkov radiation. The threshold of Cherenkov radiation is given by the following equation:

$$\beta > \frac{1}{n}, \tag{3.3}$$

where β is the ratio of the speed of the particle in a certain medium and the speed of light, n is the refractive index of the medium. Emission angle of the radiation is $\cos(\theta)=(\beta n)^{-1}$ Therefore it is possible to identify particles by the different threshold of Cherenkov radiation.

Each of the PHENIX central arms contains a RICH detector, which has a volume of 40 m^3, with an entrance window area of 8.9 m^2 and an exit window area of 21.6 m^2. Each detector contains 48 composite mirror panels, forming two interesting spherical surfaces, with a total reflecting area of 20 m^2. The spherical mirrors focus Cherenkov light onto two arrays of 1280 PMTs located on either side of the RICH entrance window. Figure 3.17 shows a cutaway view of a RICH detector. CO_2 (n=1.00041) is used as the radiator gas. It has a pion Cherenkov threshold of 4.65 GeV/c and produces an average of 12 photons per ring for a β=1 particle for a path length of 1.2 m. The ring diameter on PMT plane for CO_2 gas is about 11.8 cm.

Electromagnetic Calorimeter

The Electromagnetic Calorimeter (EMCal) [46] is located at a radial distance of 5.1m from the beam axis, which is the outermost region of the PHENIX central arms. It covers the full central detectors

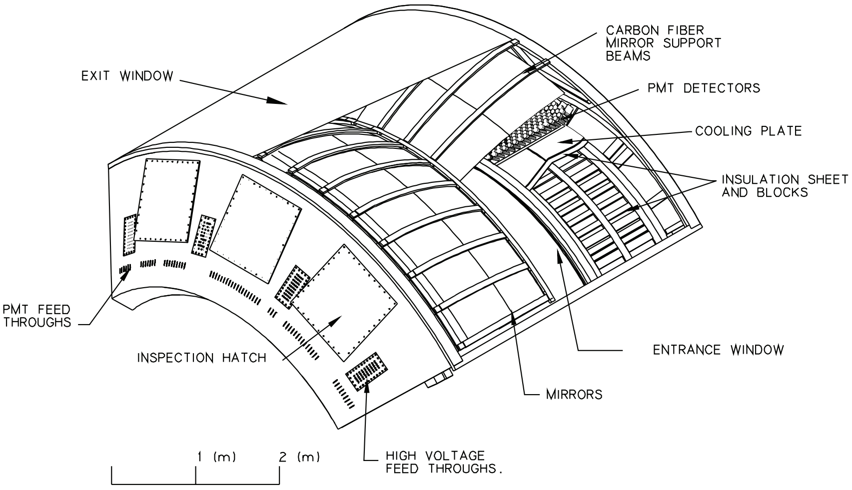

Figure 3.17: A cutaway view of a RICH detector showing the spherical mirrors and PMTs inside.

acceptance of $70^\circ \leq \theta \leq 110^\circ$ and 90° in azimuth in both east and west arms. The primary role of the EMCal is to measure the spatial position and energy of electrons and photons produced in heavy ion collisions. It is also used as the detector for particle identification and an important part of PHENIX trigger system. There are two types of the EMCal in the PHENIX central arms. One is lead-scintillator sampling calorimeters (PbSc) and the other is lead-glass Cherenkov calorimeters (PbGl). Although they have good energy, spatial and timing resolution, especially the PbSc has better timing and the PbGl has better energy resolution. The PbSc is located at 4 sectors of the west arm and the lower half of the east arm, and the PbGl is at the upper half of the east arm. In this part, we introduce the design and properties of the PbSc which is mainly used in this analysis. The details of the PbGl is described in [46].

The basic readout unit of the PbSc is called "tower", which is 5.535 cm × 5.535 cm × 37.5 cm size. Each tower contains 66 sampling cells consisting of alternating tiles of Pb (1.5 mm) and scintillator (4 mm) These cells are optically connected by 36 longitudinally penetrating wavelength shifting fibers for light collection. Light is read out by PMTs at the back of the towers. Four towers are mechanically grouped together into a single structural entity called a "module" as shown in Figure 3.18. Thirty six modules are attached to a backbone and held together by welded stainless-steel skins on the outside to form a "supermodule". Eighteen super modules make a "sector".

The nominal energy resolution of the PbSc is given by

$$\sigma(E)/E = 8.1\%/\sqrt{E} \oplus 2.1\%, \tag{3.4}$$

and an intrinsic timing resolution is better than 200 ps for electromagnetic showers. For real data, π/K separation is achieved up to $p_T \sim 1$ GeV/c, and K/p separation up to $p_T \sim 2$ GeV/c.

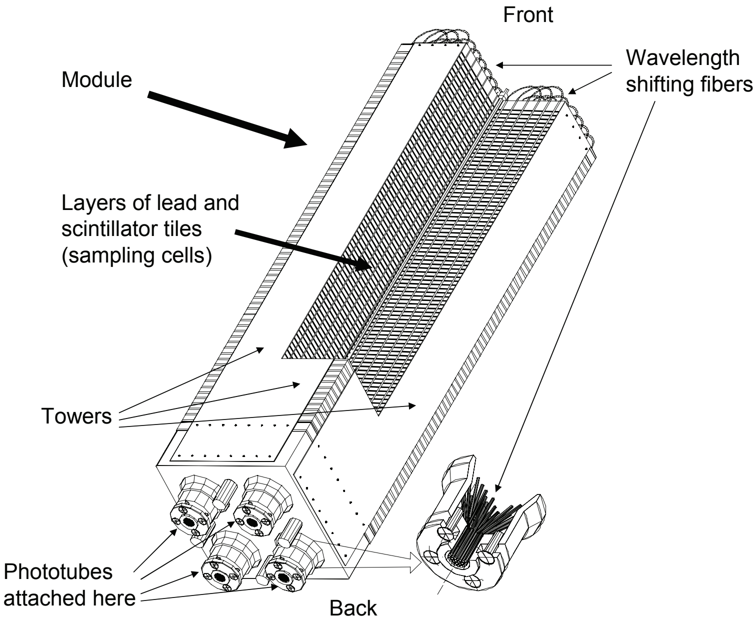

Figure 3.18: Interior view of a Pb-scintillator calorimeter module showing a stack of scintillator and lead plates, wavelength hitting fiber readout and leaky fiber inserted in the central hole.

3.2.5 Summary of PHENIX detectors

Element	$\Delta\eta$	$\Delta\phi$	Purpose and Special Features
Magnet: central	$\pm$ 0.35	360°	Up to 1.15 T·m
muon (south)	-1.1~-2.2	360°	0.72 T·m for $\eta = 2$
muon (north)	1.1~2.4	360°	0.72 T·m for $\eta = 2$
BBC	$\pm 3.1 \sim 3.9$	360°	Start timing, fast vertex
ZDC	$\pm$2 mrad	360°	Minimum Bias trigger
DC	$\pm$0.35	90°×2	Good momentum and mass resolution
PC	$\pm$0.35	90°×2	Pattern recognition, tracking for non-bend direction
RICH	$\pm$0.35	90°	Electron identification
TOF	$\pm$0.35	45°	Good hadron identification, $\sigma < 100ps$
PbSc EMCal	$\pm$0.35	$90° + 45°$	For both calorimeter, photon and electron detection
PbGl EMCal	$\pm$0.35	45°	Good $e^{\pm}/\pi^{\pm}$ separation at $p > 1GeV/c$ by EM shower and $p < 0.35$ GeV/c by TOF. $K^{\pm}/\pi^{\pm}$ separation up to 1 GeV/c by TOF.
μ tracker	-1.15~-2.25	360°	Tracking for muons
	1.15~2.44	360°	
μ Identifier	-1.15~-2.25	360°	Steel absorbers and Iarocci tubes for muon/hadron separation
	1.15~2.44	360°	

Table 3.1: Summary of PHENIX detector subsystems

3.2.6 Data Acquisition System

The PHENIX Data Acquisition System (DAQ) [47] is designed to accomplish the data taking in a variety of colliding system from p+p to Au+Au collisions. The number of the measured particles ranges from a few tracks in p+p collisions to several hundred tracks in central Au+Au collisions. The interaction rate varies from a few kHz for Au+Au collisions to about 500 kHz for p+p collisions. The PHENIX DAQ makes it possible to seamlessly deal with the wide range of event size and rate through the pipelined and deadtimeless features of the detector front ends and the ability to accommodate higher level triggers. Figure 3.19 shows the schematic diagram of the PHENIX DAQ system.

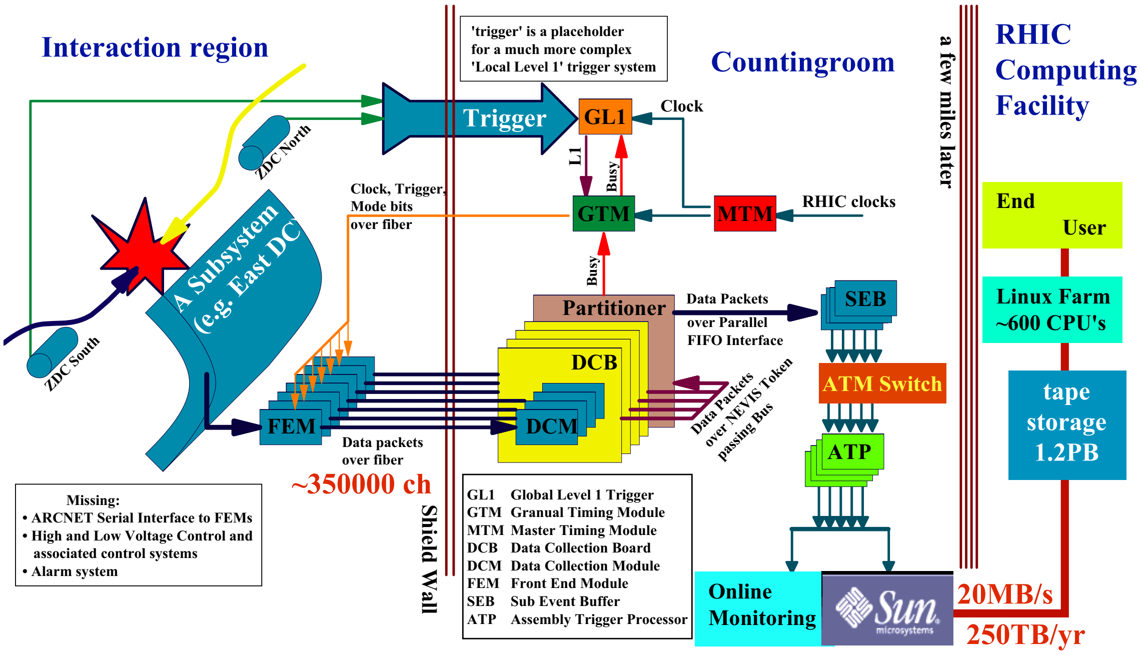

Figure 3.19: Schematic diagram of the PHENIX DAQ system.

Signals from the PHENIX detectors are processed by Front End Electronics (FEE) that convert analog signals into digital data involving the processing of analog signal with amplification and shaping to extract the optimum time and/or amplitude information. All the FEMs have distribution of the RHIC beam clock for the synchronization of data taking by the Master Timing Module (MTM). The data is buffered up to 40 beam crossings to allow for the time needed to make the Level-1 trigger (LVL1) decision and digitization.

The LVL1 trigger selects potentially interesting events and provides event rejection to reduce the data rate to a level that the PHENIX DAQ system can handle. The PHENIX LV1 trigger consists of the Local Level-1 (LL1) system which processes detector information into reduced bit data and the Global Level-1 (GL1) system which makes trigger decisions by receiving and combining data from the LL1 and manages busy signals.

If the LVL1 trigger accepts an event, a signal is transmitted to the Granule Timing Module (GTM) which generates an ACCEPT signal that is transmitted to the Front End Modules (FEM). The FEM processes the data from the individual detectors and sends it to the Data Collection

Modules (DCM) via fiber-optic cable. The DCMs perform zero suppression, error checking, and data formatting and output the compressed data to the Event Builder (EvB) which perform the final stage of event assembly. In the EvB, the data from the DCM are buffered in a set of the Sub Event Buffers (SEB). The SEB transfers the data on request to a set of Assembly/Trigger Processors (ATPs) by the Asynchronous Transfer Mode (ATM) switch. Assemble data are transmitted to the Online Control System (ONCS) for lodging and distribution to monitoring processes. The final data format is called PHENIX Raw Data Format (PRDF).

Chapter 4

Analysis

In this study, the data of Au+Au collisions at $\sqrt{s_{\rm NN}} = 200$ GeV taken at the PHENIX experiment in year 2007 (Run7) are analyzed. In this chapter, we present the data reduction and the analysis method. Event and track selections are described in Sec. 4.1, 4.3 and the event plane determination in Sec 4.2. The analysis method for the HBT measurement is described in Sec 4.5.

4.1 Event Selection

The following event selection is required in this analysis.

- minimum bias trigger determined by the BBC and ZDC
- vertex position is within ±30 cm

The minimum bias trigger is defined as a coincidence of both hit information in the BBC and ZDC. It requires at least 2 fired PMTs in each BBC and at least the detection of one forward neutron in each ZDC at $\sqrt{s_{\rm NN}} = 200$ GeV in Au+Au collisions. A total number of events used in this analysis are ∼4.18 billion events, where a centrality described in the next section is required to be $< 92\%$.

4.1.1 Centrality Determination

The "centrality" is used to classify the initial collision geometry between two nuclei since it is difficult to measure the true impact parameter experimentally. The nucleus-nucleus collisions can be explained by the participant-spectator picture as described in Sec. 1.2.2. In case of central collisions, a number of particles are created by the collision and few neutrons is included in the spectator. On the other hand, in case of peripheral collisions, the number of particles created in the collisions decreases and the rest neutrons in the spectator increases. Therefore the centrality can be determined by using the charge sum information measured by the BBC which is originated from the participants and the energy measured by the ZDC which is originated from the spectators.

Left panel in Fig. 4.1 shows the correlation between the charge sum (Q_{BBC}) deposited in the BBC and the total energy (E_{ZDC}) measured in the ZDC, where Q_{BBC} and E_{ZDC} are normalized by their measured maximum values Q^{max}_{BBC} and E^{max}_{ZDC}. The boundary lines of centrality classes are shown in the figure.

As shown in Table. 1.1, various run have been performed with lower energy and using different nucleus beam. However, in those case the efficiency of the ZDC significantly decreases and insufficient for the determination of the centrality. Therefore the only total charge deposited in

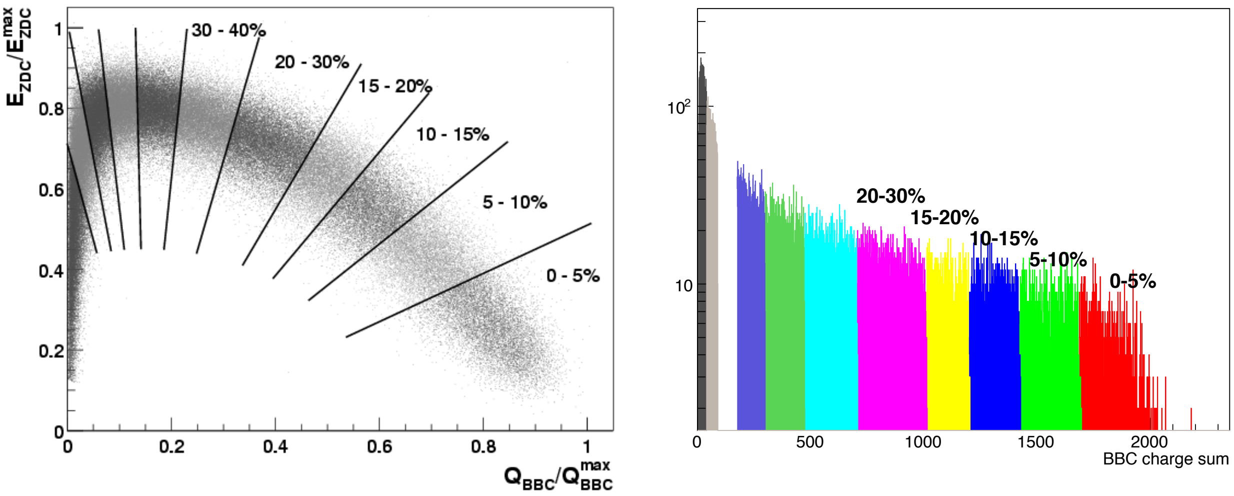

Figure 4.1: (Left) Correlation between the total energy measured in the ZDC and the charge sum deposited in the BBC. (Right) Distribution of the charge sum deposited in the BBC.

the BBC have been used since Year-2005. Right panel in the Fig. 4.1 shows the total BBC charge distribution with the boundary lines with centrality classes. Centrality is determined each z-vertex of 5cm step and divided into 93 bins. Centrality is represented as a percentile where 0-1% refers to the most central (head-on) collision and 93% refers to the most peripheral (grazing) collision.

4.2 Event Plane Determination

In this section, we introduce the method to determine the event plane which is an estimate of the true reaction plane determined by the azimuthal distribution of emitted particles.

4.2.1 Azimuthal Distribution of Emitted Particles

The azimuthal distribution $r(\phi)$ of emitted particles is written with the Fourier-expansion of the periodic function with a 2π period:

$$r(\phi) = \frac{x_0}{2\pi} + \frac{1}{\pi}\sum_{n=1}^{\infty}(x_n \cos(n\phi) + y_n \sin(n\phi)), \tag{4.1}$$

$$x_n = \int_0^{2\pi} d\phi\ r(\phi)\cos(n\phi) = \sum_i r_i(\phi)\cos(n\phi), \tag{4.2}$$

$$y_n = \int_0^{2\pi} d\phi\ r(\phi)\sin(n\phi) = \sum_i r_i(\phi)\sin(n\phi), \tag{4.3}$$

where ϕ is an azimuthal angle of emitted particles in laboratory frame and x_n, y_n are the Fourier coefficients. In experiment, the integral is rewritten by the summation of the number of particles due to a finite number of particles in an event.

Here particles are emitted with respect to the reaction plane and the azimuthal distribution of emitted particles should be symmetric in symmetric nucleus-nucleus collisions, therefore sine term in the Fourier expansion becomes zero. Using the azimuthal angle of reaction plane Ψ_r, Eq. (4.1) is rewritten as the following:

$$\begin{aligned}
r(\phi) &= \frac{x_0}{2\pi} + \frac{1}{\pi}\sum_{n=1}^{\infty}\left(x'_n\cos(n[\phi-\Psi_r]) + y'_n\sin(n[\phi-\Psi_r])\right),\\
&= \frac{x_0}{2\pi} + \frac{1}{\pi}\sum_{n=1}^{\infty}x'_n\cos(n[\phi-\Psi_r]),\\
&= \frac{x_0}{2\pi}\left(1+2\sum_{n=1}^{\infty}\frac{x'_n}{x_0}\cos(n[\phi-\Psi_r])\right),\\
&= \frac{x_0}{2\pi}\left(1+2\sum_{n=1}^{\infty}v_n\cos(n[\phi-\Psi_r])\right), \qquad (4.4)
\end{aligned}$$

where the coefficients $v_n = \langle\cos(n[\phi-\Psi_r])\rangle$ is the strength of azimuthal anisotropy, where $\langle\rangle$ means an average over all particles in all events. Since the impact parameter cannot be determined in the experiment, the reaction plane is estimated by the azimuthal anisotropy of emitted particles, which is called "event plane". Here we introduce the variables v_n^{obs} and Ψ_n defined as:

$$\begin{aligned}
v_n^{obs} &= \frac{\sqrt{x_n^2+y_n^2}}{x_0}, \qquad (4.5)\\
\Psi_n &= \frac{1}{n}\tan^{-1}\left(\frac{y_n}{x_n}\right), \quad 0\le\Psi_n\le\frac{2\pi}{n}. \qquad (4.6)
\end{aligned}$$

Using Eq. (4.5), (4.6), the azimuthal distribution Eq. (4.1) can be given by

$$\begin{aligned}
r(\phi) &= \frac{x_0}{2\pi}\left(1+2\sum_{n=1}^{\infty}\left(\frac{x_n}{x_0}\cos(n\phi)+\frac{y_n}{x_0}\sin(n\phi)\right)\right),\\
&= \frac{x_0}{2\pi}\left(1+2\sum_{n=1}^{\infty}v_n^{obs}\cos(n\Psi_n)\cos(n\phi)+v_n^{obs}\sin(n\Psi_n)\sin(n\phi)\right),\\
&= \frac{x_0}{2\pi}\left(1+2\sum_{n=1}^{\infty}v_n^{obs}\cos(n[\phi-\Psi_n])\right), \qquad (4.7)
\end{aligned}$$

where Ψ_n is the event plane for n^{th} harmonic and v_n^{obs} is the observed azimuthal anisotropy with respect to Ψ_n.

$$\begin{aligned}
v_n^{obs} &= \langle\cos(n[\phi-\Psi_n])\rangle,\\
&= \langle\cos(n[\phi-\Psi_r]-\cos(n[\Psi_n-\Psi_r])\rangle,\\
&= \langle\cos(n[\phi-\Psi_r])\rangle\langle\cos(n[\Psi_n-\Psi_r])\rangle+\langle\sin(n[\phi-\Psi_r])\rangle\langle\sin(n[\Psi_n-\Psi_r])\rangle,\\
&= \langle\cos(n[\phi-\Psi_r])\rangle\langle\cos(n[\Psi_n-\Psi_r])\rangle,\\
&= v_n\langle\cos(n[\Psi_n-\Psi_r])\rangle \qquad (4.8)
\end{aligned}$$

where the event average of sine terms vanish due to the reflection symmetry of ϕ and Ψ_n distribution with respect to the reaction plane with large multiplicity. The observed azimuthal anisotropy v_n^{obs} is represented as the true one v_n multiplied by $\langle\cos(n[\Psi_n-\Psi_r])\rangle$. The term $\langle\cos(n[\Psi_n-\Psi_r])\rangle$ is called the event plane resolution.

4.2.2 Event Plane Determination

In this analysis, the RXNP is used to determine event planes each event. The RXNP covers the full azimuth and consists of 24 scintillator segments as explained in Sec. 3.2.3. The event plane is calculated based on Eq. (4.6).

$$\begin{aligned} \Psi_n^{obs} &= \frac{1}{n}\tan^{-1}\left(\frac{Q_y}{Q_x}\right), && (4.9)\\ Q_x &= \sum_{i=1}^{n_{ring}} w_i \cos(n\phi_i), && (4.10)\\ Q_y &= \sum_{i=1}^{n_{ring}} w_i \sin(n\phi_i), && (4.11) \end{aligned}$$

where Ψ_n^{obs} is the azimuthal angle of the measured event plane for the n^{th} harmonic, Q_x, Q_y are the event flow vectors, w_i is the weight, ϕ_i is the azimuthal angle of each segment and n_{ring} is the number of segments. If we determine the event plane using segments only in inner or outer, n_{ring} is 12. In case of using both inner and outer segments, n_{ring} is 24. The weight w_i is the charge output of each PMT for each segment, which is normalized by the total charge of all segments.

4.2.3 Event Plane Calibration

The azimuthal angle distribution of the event plane should be flat because the relative collision positions of two nuclei are taken randomly in laboratory frame. However the actual distribution is not flat due to several effects such as dead PMTs, unequal PMT's gains, the offset of beam position, and the imperfect detector acceptance. Therefore some calibration steps are needed to remove these effects. As a first step, each PMT's gain is calibrated to have the same mean ADC value. The second step is re-centering calibration which recenters the average of the event flow vector Q_x, Q_y and normalizes the width of their distribution.

$$\begin{aligned} \Psi_n^{corr} &= \frac{1}{n}\tan^{-1}\left(\frac{Q_y^{corr}}{Q_x^{corr}}\right), && (4.12)\\ Q_x^{corr} &= \frac{Q_x - \langle Q_x\rangle}{\sigma_x}, && (4.13)\\ Q_y^{corr} &= \frac{Q_y - \langle Q_y\rangle}{\sigma_y}, && (4.14) \end{aligned}$$

where $\langle Q_x\rangle$, $\langle Q_y\rangle$ are the average over many events, and σ_x, σ_y are the standard deviation of Q_x, Q_x distribution, which are obtained by the Gaussian fit.

The third step is flattening calibration to remove the remaining non-flatness of event planes [48]. A new event plane is defined as:

$$\begin{aligned} n\Psi_n^{flat} &= n\Psi_n^{rec} + n\Delta\Psi, && (4.15)\\ n\Delta\Psi &= \sum_k \left(A_k \cos(kn\Psi_n^{rec}) + B_k \sin(kn\Psi_n^{rec})\right). && (4.16) \end{aligned}$$

The coefficients A_k and B_k can be obtained by requiring the vanishing of the n^{th} Fourier moment of the new distribution,

$$A_k = \frac{-2}{k}\langle\sin(nk\Psi_n^{rec})\rangle, \tag{4.17}$$

$$B_k = \frac{2}{k}\langle\cos(nk\Psi_n^{rec})\rangle. \tag{4.18}$$

In this analysis, k runs up to 8.

4.2.4 Event Plane Resolution

The event plane resolution can be expressed analytically as:

$$\langle\cos[km(\Psi_m - \Psi_r)]\rangle = \frac{\sqrt{\pi}}{2\sqrt{2}}\chi_m \exp(-\chi_m^2/4)\ [I_{(k-1)/2}(\chi_m^2/4) + I_{(k+1)/2}(\chi_m^2/4)], \tag{4.19}$$

where I_n is the modified Bessel function. The parameter $\chi_m = v_m\sqrt{2N}$, where N is the number of particles used to determine the event plane.

Experimentally we can estimate the event plane resolution by the correlation between the event plane angles determined from two same detectors, the North and South RXNP.

$$\langle\cos(n[\Psi_n^N - \Psi_n^S])\rangle = \langle\cos(n[\Psi_n^N - \Psi_r])\rangle\langle\cos(n[\Psi_n^S - \Psi_r])\rangle, \tag{4.20}$$

where Ψ_n^N and Ψ_n^S are event planes determined by the North and South RXNP. If we assume that two subdetectors have equal v_n and multiplicity, both event plane resolutions are same:

$$\langle\cos(n[\Psi_n^N - \Psi_r])\rangle = \langle\cos(n[\Psi_n^S - \Psi_r])\rangle = \sqrt{\langle\cos(n[\Psi_n^N - \Psi_n^S])\rangle} \tag{4.21}$$

Under the above assumption, the parameter for each event plane resolution of subdetectors is taken as:

$$\chi^{NS} = \sqrt{2}\chi^N = \sqrt{2}\chi^S \tag{4.22}$$

where $\chi^N(\chi^S)$ are the parameter χ for the North (South) RXNP, and χ^{NS} is that for the combined both subdetectors. Using Eq. (4.19) and (4.21), we can obtain the values of χ^N and χ^S. After that, the event plane resolution for the combined subdetectors can be obtained by Eq. (4.19) and (4.22). Figure 4.22 shows 2^{nd} and 3^{rd}-order event plane measured with the North (South) and both combined RXNP. The resolution of Ψ_n has a maximum of 0.75 (0.32) at mid-central (most-central) collisions for the 2^{nd} (3^{rd})-order event planes.

4.3 Track Selection

4.3.1 Track Reconstruction

A huge number of particles are produced in heavy ion collisions and measured with PHENIX detectors introduced in Sec. 3.2. Before the data analysis, the hit information at each detectors needs to be reconstructed as tracks. In this section, the track reconstruction for charged particles are explained.

The produced charged particles at the collision point pass through the DC, the PC1 and the outer detector such as the TOF and EMC, where the trajectories are bent to the direction perpendicular to the beam axis because of the magnetic field parallel to the beam axis. The track can

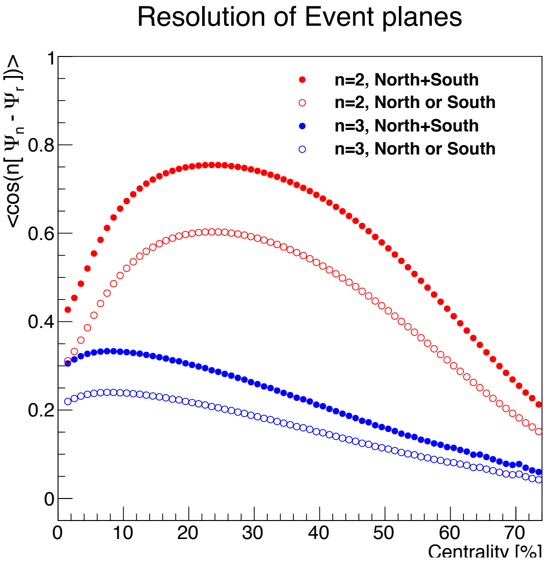

Figure 4.2: Event plane resolution as a function of centrality in Au+Au collisions at $\sqrt{s_{\mathrm{NN}}} = 200$ GeV. The resolution for the North or South RXNP and the combined subdetectors are shown.

be reconstructed by combining the hit information at each detectors. Track reconstruction within the DC is performed using a combinatorial Hough transform technique [49]. In this technique, the hit information at the DC is mapped to the azimuthal angle ϕ and the inclination of the track α at the intersection of track with a reference radius which is the mid-point of the DC as illustrated in the left of Fig. 4.3. Figure 4.4 shows the example of the DC hits from a simulated HIJING Au+Au collisions and the Hough transform feature space for this region. Tracks appear as peaks in the Hough space. After tracks are reconstructed in $\phi - \alpha$ plane, the straight line projections of tracks are made to the PC1 as shown in the right panel of Fig. 4.3. The z coordinates of tracks are determined by Hough transform using reconstructed PC1 clusters and hit information in the U and V wires of the DC. Eventually the reconstructed tracks are associated with the vertex position determined by the BBC.

4.3.2 Momentum Determination

The curvature of a charged particle is proportional to the momentum of the particle for a fixed magnetic field and the charge of the particle. Therefore the relation of the inclination angle α and the transverse momentum p_T is expressed as:

$$\alpha \simeq \frac{K}{p_T}, \tag{4.23}$$

where $K = 101$ mrad$\cdot$GeV$/c$ is the field integral along the track trajectory. Because of the complicated and non-uniform shape of the magnetic field along the path length of charged particles, an analytic solution cannot be obtained for momentum determination. Therefore a four-dimensional field-integral grid, where the variables are the z coordinate of the event vertex, the polar angle of the particle at the vertex, the total momentum p, and the radius r, is constructed for momentum reconstruction [49].

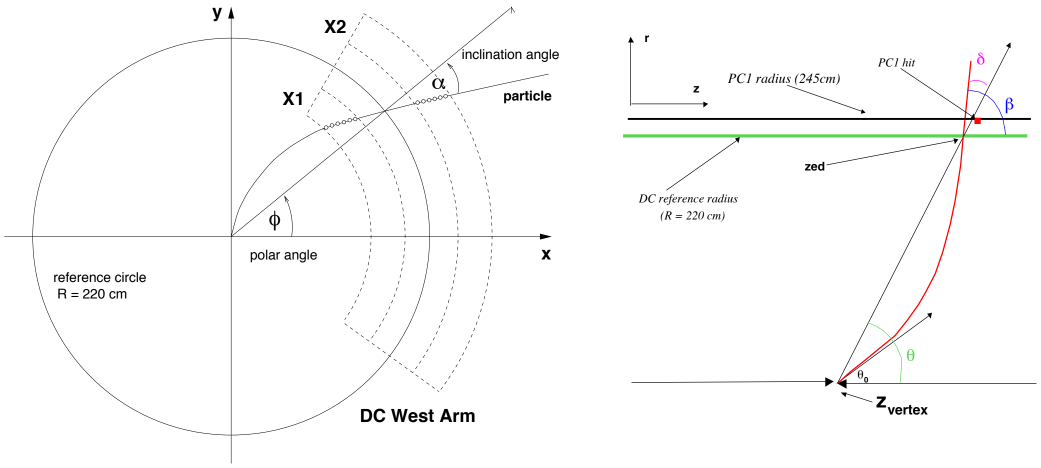

Figure 4.3: The schematic view of a reconstructed track by the DC in $x - y$ plane (Left) and $r - z$ plane (Right).

The momentum resolution is determined by the contributions from multiple scattering and angular resolution of the DC:

$$\frac{\delta p}{p} = \frac{\delta \alpha}{\alpha} = \frac{1}{K}\sqrt{\left(\frac{\sigma_{ms}}{\beta}\right)^2 + (\sigma_\alpha p)^2}. \tag{4.24}$$

The momentum resolution in Run7 dataset is estimated to be $\delta p/p \sim 1.3\% \oplus 1.2\% \times p$ GeV/c [50].

4.3.3 Track Selection

In this section, the conditions applied for track selection in this analysis are explained.

Track Quality Requirement

Track quality is given for every reconstructed track, which expresses the hit information of the DC wires and PC1 with a 6 bit number. Good tracks are typically required to have a hit in both X1 and X2 wires and one of the UV layers of the DC as well as a hit in the PC1, which corresponds to 31 or 63 of the quality number. For the quality value of 63, the hit in the UV layers and PC1 is unique match, for the value of 31 there are multiple PC1 hits though the hit in the UV layers is unique.

In this analysis, we require the track quality of 31 and 63.

Track Matching

The tracks reconstructed by the DC and PC1 are extended as straight lines and associated with hits at the outer detectors such as the TOF and EMC. The closest hit from the intersection of the projected track and outer detectors is identified as the associated hit.

There is a difference between the projected point of the track and the associated hit point because of imperfect detector resolution and the wrong track reconstruction. The differences in ϕ

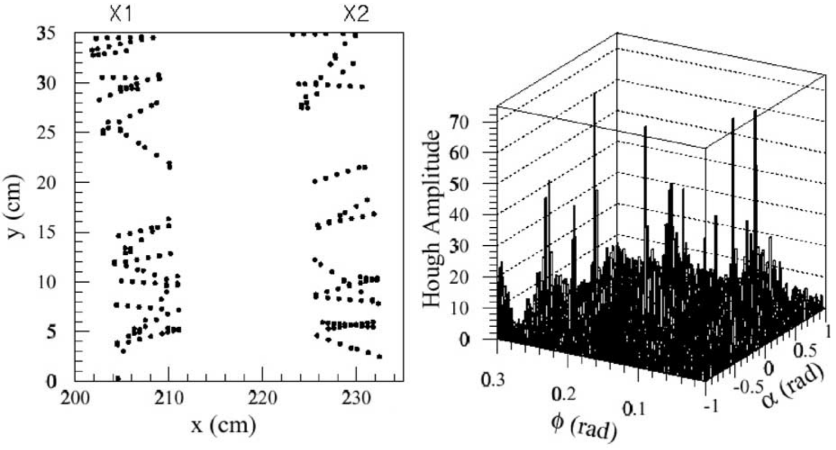

Figure 4.4: (Left)The DC hits in $x-y$ plane. (Right)The hit distribution in Hough space [49].

and z direction are approximately expressed by Gaussian with a width as

$$\sigma_{macth} = \sqrt{\sigma^2_{detector} + \left(\frac{\sigma_{ms}}{p\beta}\right)^2}, \tag{4.25}$$

where $\sigma_{detector}$ is the finite detector resolution and σ_{ms} is the contribution from multiple scattering. Multiple scattering dominates at low momentum, and the detector resolution become worse at higher momentum. Therefore the width σ_{match} of the residual distribution depends on a momentum. The residual distributions in ϕ and z directions are normalized by σ_{match} for each momentum. Then tracks within a required standard deviation are selected, which is called "track matching cut".

In this analysis, the following track matching cuts are required:

- $\sqrt{d\phi^2 + dz^2} < 2\sigma$ at PC3
- $\sqrt{d\phi^2 + dz^2} < 2\sigma$ at EMC

Other Requirements

- Momentum cut : $p < 2.0$ GeV/c
- Transverse momentum cut
  - $p_T > 0.2$ GeV/c for π
  - $p_T > 0.3$ GeV/c for K
  - $p_T > 0.3$ GeV/c for p
- DC hit position cut : $|zed| < 75$ cm
- EMC energy cut for a cluster : $ecent > 0.1$ GeV
- Cut for arrival time of the hit in the EMC : $temc < 50$ ns
  This cut is applied to remove the background particles which takes too much time to reach to the EMC after the collisions.

- Require the veto of the hit in the RICH : $n0 < 4$
  RICH veto is required to remove electrons as background for charged hadrons. The $n0$ is the number of fired PMTs. As described in Sec. 3.2.4, charged hadrons don't emit Cherenkov light in the above momentum range. Therefore RICH veto cut is usually applied to remove electrons in the analysis of charged hadrons.

4.4 Particle Identification

Particle Identification (PID) of charged particles is performed by using the information of their Time-Of-Flight. The mass of the particles is given by the following equation:

$$m^2 = E^2 - p^2 = p^2\left(\frac{1}{\beta^2} - 1\right), \tag{4.26}$$

$$= p^2\left(\left(\frac{ct}{L}\right)^2 - 1\right), \tag{4.27}$$

where p is the particle momentum, β is the velocity which is given by the time of flight, t, the flight path length, L, and the speed of light, c. The momentum is measured by the DC, the time of flight is measured as a timing difference between BBC and EMCal or TOF, the flight path length corresponds to the reconstructed track trajectory between vertex position and EMCal or TOF wall.

Figure 4.5 show squared mass distribution of positive particles calculated by using the EMC information. Three peaks correspond to pions, kaons, and protons. Solid lines show Gaussian fit functions for each particle, where triple Gaussian fit is performed for those particles. Dashed lines show each component of the single Gaussian functions.

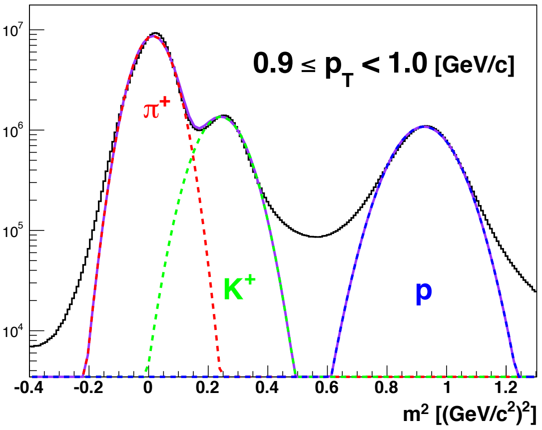

Figure 4.5: Squared mass distribution in the p_T region of $0.9 \le p_T < 1.0$ GeV/c. Solid lines show triple Gaussian fit functions and dashed lines show each component of them.

The mean and standard deviation obtained by the Gaussian fit are plotted as a function of momentum in Fig. 4.6. The width of each peak in squared mass distibution is given by the following parameterization:

$$\begin{aligned}
\sigma^2_{m^2} &= \left(\frac{\partial m^2}{\partial p}\right)^2 \delta p^2 + \left(\frac{\partial m^2}{\partial t}\right)^2 \delta t^2, && (4.28)\\
&= 4m^4 \left(\frac{\delta p}{p}\right)^2 + 4p^2\left(m^2+p^2\right)\left(\frac{c}{L}\delta t\right)^2, && (4.29)\\
&= \frac{\sigma^2_\alpha}{K^2}\left(4m^4p^2\right) + \frac{\sigma^2_{ms}}{K^2}\left[4m^4\left(1+\frac{m^2}{p^2}\right)\right] + \left(\frac{c\delta t}{L}\right)^2\left[4p^2(m^2+p^2)\right], && (4.30)
\end{aligned}$$

where δp is momentum and δt is timing resolution and the 3$^{\mathrm{rd}}$ equation is obtained by the relation of Eq. (4.24). We have performed the fit with Eq. (4.30) for the width of each particle setting parameters except momentum as free parameters. The mean value of squared mass distribution is fitted by constant or linear function only for anti-proton. Using the obtained parameters, we have selected each particles within 2σ width from the mean of its particle and 2σ away from the means of other particles.

Figure 4.7 shows a scatter plot of momentum multiplied by a sign of charged track vs mass square calculated by Eq.(4.30) using the EMC after applying the PID cut.

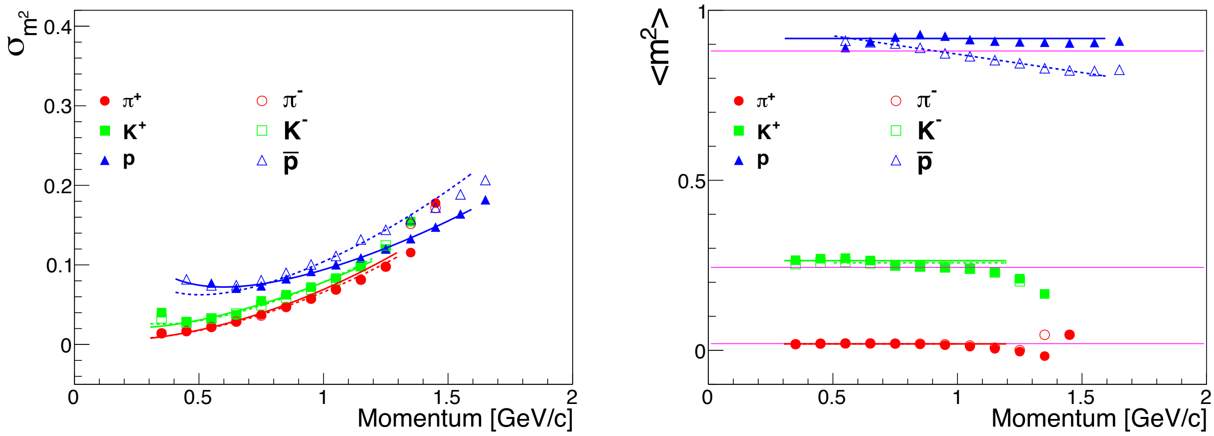

Figure 4.6: Mean (left) and width (right) of squared mass distribution as a function of momentum for $\pi/K/p$. Filled (open) symbols represent positive (negative) particles.

4.5 HBT Analysis Method

4.5.1 Construction of Correlation Function

HBT radii are obtained by fitting the experimentally measured correlation function by the fitting function. The correlation function is defined as C_2.

$$C_2 = \frac{A(q)}{B(q)}, \tag{4.31}$$

where $A(q)$ is the pair distribution with relative momentum q in the same event (real pairs) and $B(q)$ is that in the different event (mixed pairs). Mixed pairs are made by event mixing technique, where several different events with similar global variables are selected, and then particle pairs are

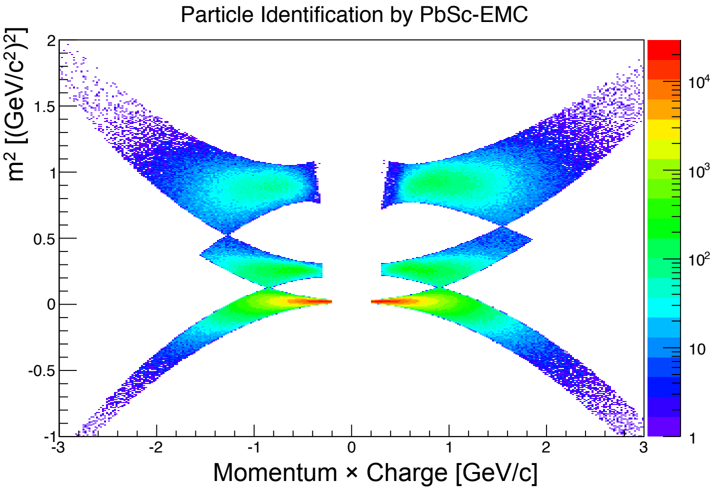

Figure 4.7: Momentum multiplied by a sign of charged track vs mass square for Particle Identification by EMCal.

made by one particle selected from a event and one particle selected from other event. Therefore the mixed pairs doesn't include the HBT effect, while the real pairs includes the HBT effect and Coulomb interaction.

In this analysis, events are classified by the global variables, zvertex, centrality and 2$^{\mathrm{nd}}$-order event plane. we make the pion pairs from the similar events with the following conditions:

- within 2 cm for zvertex position
- within 5% for centrality
- within 6° for 2$^{\mathrm{nd}}$-order event plane

Conditions for kaon is changed a little because the binning of centrality and the event plane in kaon analysis is coarser than that in pion analysis. The following are applied for the event mixing of kaon pairs:

- within 2 cm for zvertex position
- within 10% for centrality
- within 9° for 2$^{\mathrm{nd}}$-order event plane

In case of analysis with respect to 3$^{\mathrm{rd}}$-order event plane, events are also classified by 3$^{\mathrm{rd}}$-order event plane in addition to the above conditions in order to make the mixed pairs with similar condition with the real pairs.

- within 6° for 3$^{\mathrm{rd}}$-order event plane

Figure 4.8 shows the relative momentum q distribution for real and mixed pairs (upper panel) and correlation function obtained by the ratio of the real and mixed pairs shown in upper panel

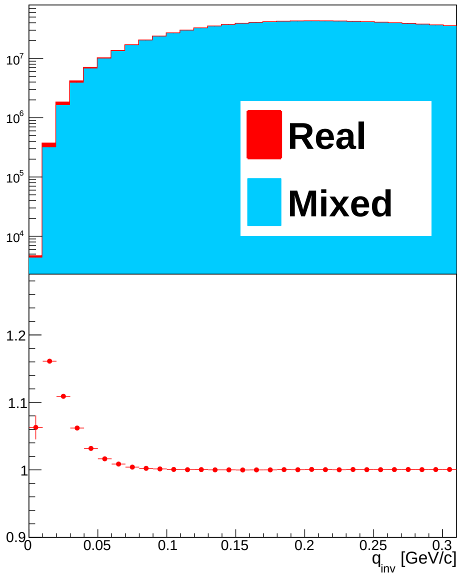

Figure 4.8: Relative momentum distributions for real and mixed pairs (Upper panel) and a correlation function obtained by the ratio of real and mixed pair q-distributions in upper panel (Lower Panel).

(lower panel), where the mixed pair distribution is normalized. A subtle difference between real and mixed pairs can be seen at low q, which leads to the enhancement of correlation function in lower panel.

As shown in Fig. 4.8, correlation function is dominated by pairs with similar relative momentum and with similar trajectories. Therefore we need to consider the effects of the detector efficiency and the Coulomb interaction for like sign pairs described in next sections.

4.5.2 Pair Selection

Particle pairs with similar momenta and spatially close to each other are affected by the wrong reconstruction and detector inefficiency, which are called “ghost track” and “merged track”. The ghost track means that a single particle is reconstructed by mistake as two tracks being spatially close, which leads to the enhancement of pairs at low relative momentum. The merged track means that two particles are reconstructed as a single track because of detector inefficiency, which leads to the reduction of pairs at low relative momentum. Therefore pair selection cuts is applied to remove ghost tracks and pair tracks in the inefficient region of the detector. In this analysis, we have applied the pair cuts at the DC and the EMC. In case of the EMC, there are tracks sharing the same cluster because the hit positions of particles are very close, which leads to the wrong track reconstruction. So pairs that hits on the same tower are first removed.

Figure 4.9 shows the ratio of real and mixed distribution of the relative difference of hit positions for pion pairs at the DC. The horizontal and vertical axis show dz_{dc} and $d\phi_{dc}$ which are defined as the followings:

$$dz_{dc} = |z_{dc,1} - z_{dc,2}|, \tag{4.32}$$
$$d\phi_{dc} = |\phi_{dc,1} - \phi_{dc,2}|, \tag{4.33}$$

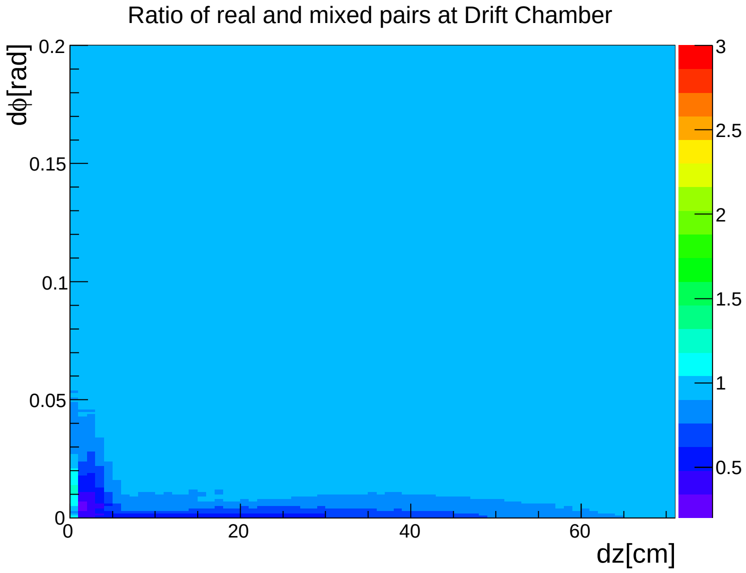

Figure 4.9: Ratio of real and mixed pion pairs as functions of the relative difference in dz-$d\phi$ plane at the DC in 0-10% centrality, where mixed pairs is normalized so that the total number of pair over 50< dz <100 cm and 0.1< $d\phi$ <0.2 rad. should be equal between real and mixed pairs.

where z_{dc} and ϕ_{dc} are the z-coordinate and the azimuthal angle at the intersection of the track at a reference radius of the DC. Since there is no significant difference between positive and negative pairs, both charge pairs are merged to determine the pair cut conditions.

The ratio of real and mixed pairs should be unity. However the effect by ghost tracks is seen at small $d\phi_{dc}$ and dz. Inefficiency region of the detector is also seen at wide dz_{dc} and small $d\phi_{dc}$. To see the effect in detail, we have projected Fig. 4.9 to $d\phi_{dc}$ direction by 1 cm step of dz_{dc} for different centralities.

In the most left top panel, the ratio at small $d\phi_{dc}$ over unity because of the ghost tracks. In other dz_{dc} regions, the ratio is lower than unity because of the detector inefficiency. In low $d\phi_{dc}$, the centrality dependence can be slightly seen because the effects of the ghost track and the detector inefficiency depend on the multiplicity. In order to remove these effects, the following regions are used for the analysis. Since the applied cuts are enough strict compared to the difference of the centrality, the same cuts are applied for different centrality classes.

- $dz_{dc} < 5$ cm and $d\phi_{dc} > 0.07$ rad
- 5 cm $\leq dz_{dc} <$ 70 cm and $d\phi_{dc} > 0.02$ rad
- $dz_{dc} \geq 70$ cm

After removing the pairs in the inefficiency region at the DC, we have checked the relative difference between the reconstructed pair tracks at the EMC. Figure 4.10 shows the ratio of real and mixed pion pairs as a function of the relative difference of two tracks. The relative difference dr_{emc} is defined as:

$$dr_{emc} = \sqrt{(x_{emc,1} - x_{emc,2})^2 + (y_{emc,1} - y_{emc,2})^2 + (z_{emc,1} - z_{emc,2})^2}, \tag{4.34}$$

where $x_{emc}, y_{emc}, z_{emc}$ are the projected positions of the reconstructed track to the EMC. Inefficiency region is still seen at small dr. Therefore the following pair cut is applied at the EMC.

- $dr_{emc} \geq 17$ cm

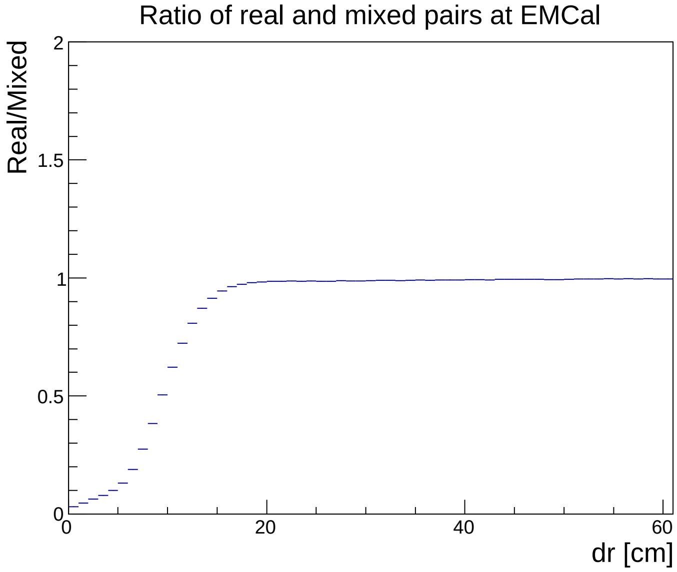

Figure 4.10: Ratio of real and mixed pairs as functions of the relative difference at the EMC in 0-10% centrality, where mixed pairs are normalized, so that the total number of pair over 50< dr <100 cm should be equal between real and mixed pairs.

Pair cut study was also performed for charged kaon pairs. Figure 4.12 shows the ratio of real and mixed pairs as functions of dz_{dc} and $d\phi_{dc}$. Figure 4.14 shows the slice of Fig. 4.12 every dz_{dc}. Figure 4.13 shows the 2-dimensional plot of the relative difference of kaon pairs in a space of dz_{emc} and $d\phi_{emc}$ at the EMC for real, mixed, and the ratio of real and mixed pairs. In real and mixed distributions, a grid structure can be seen, which step corresponds to the size of a module of the EMCal. In the ratio of real and mixed pair distribution, the structure is cancelled. A radial cut shown as a red line in the right panel of Fig. 4.13 is applied at the EMC for kaons in order not to reduce the statistics as much as possible. Finally, pair cuts for kaon pairs is determined as the followings:

- $dz_{dc} < 4$ cm and $d\phi_{dc} > 0.04$ rad
- 4 cm $\leq dz_{dc} < 65$ cm and $d\phi_{dc} > 0.01$ rad
- $dz_{dc} \geq 65$ cm
- $\sqrt{(d\phi_{emc}/0.06)^2 + (dz_{emc}/19)^2} < 1.5$

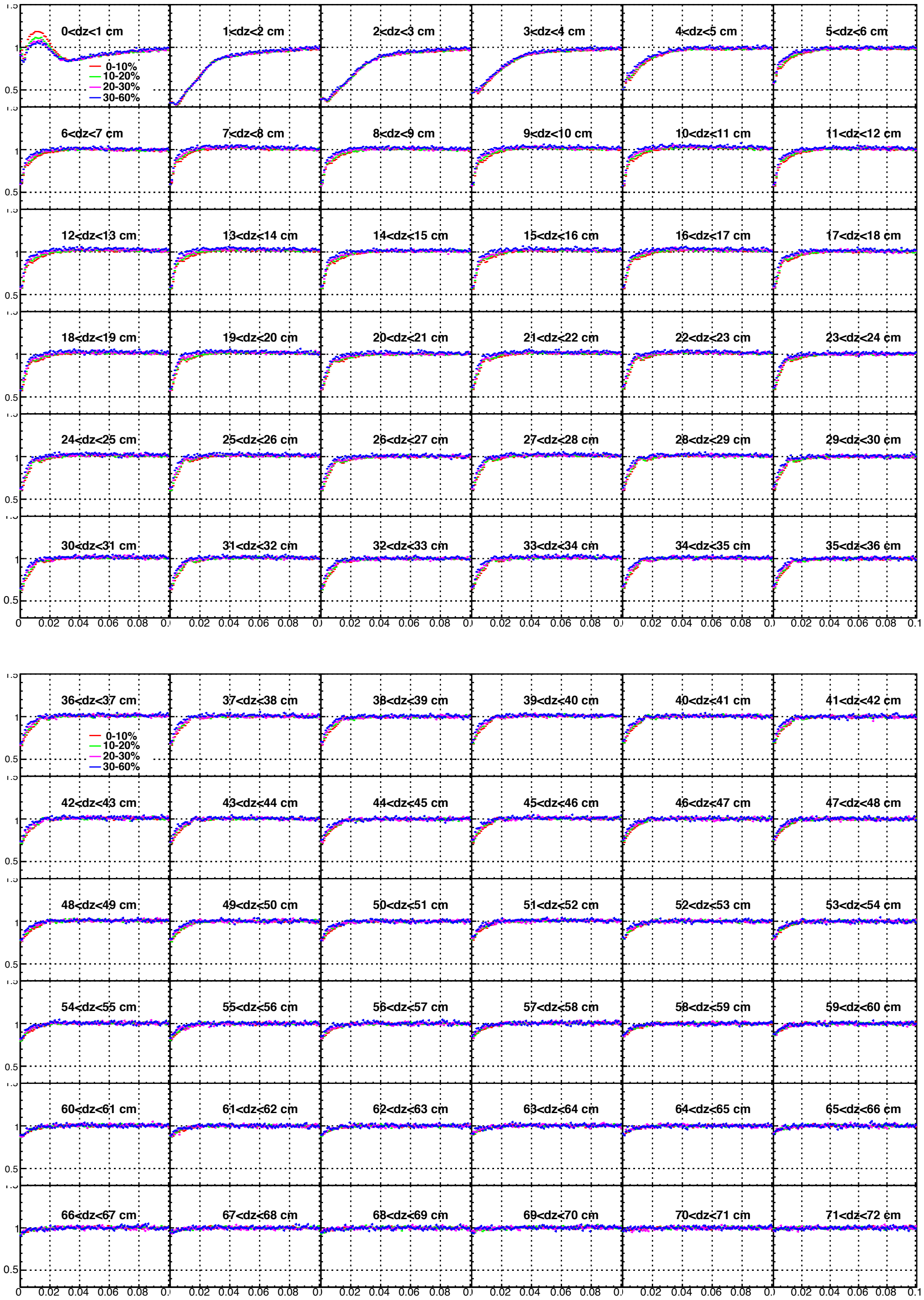

Figure 4.11: Ratio of real and mixed pion pairs as a function of the relative angular difference $d\phi$ every dz with 1 cm step. This plot is a slice of Fig. 4.9.

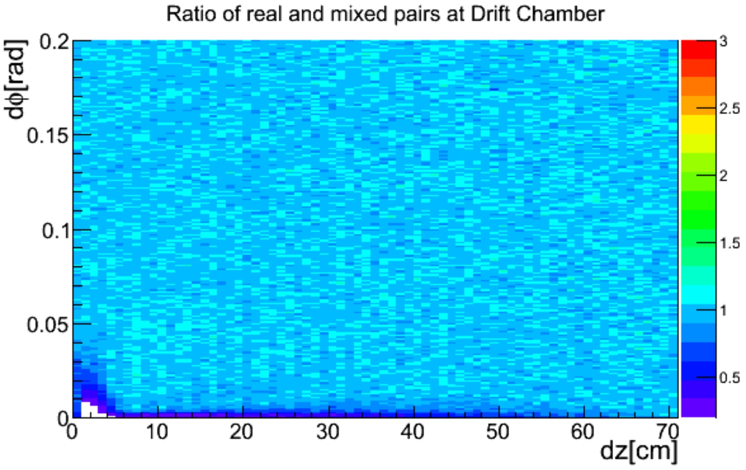

Figure 4.12: Ratio of real and mixed kaon pairs as functions of the relative difference in dz-$d\phi$ plane at the DC in 0-60% centrality, where mixed pairs is normalized, so that the total number of pair over 50< dz <100 cm and 0.1< $d\phi$ <0.2 rad. should be equal between real and mixed pairs.

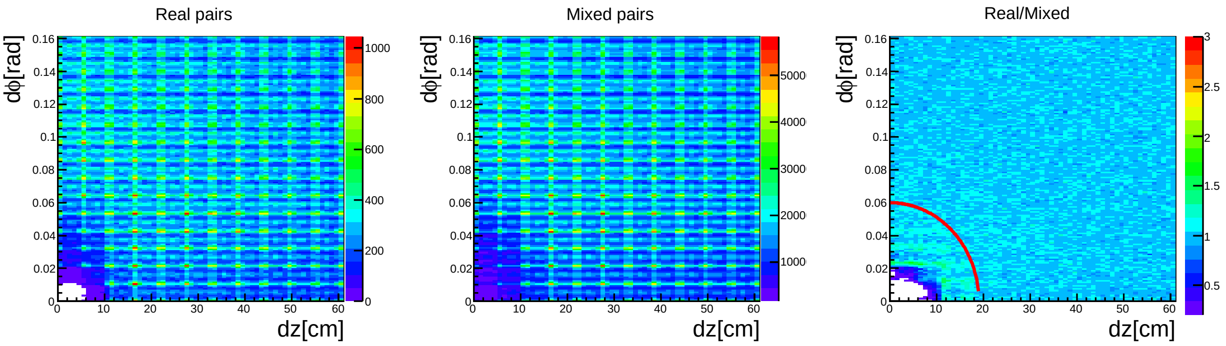

Figure 4.13: Real pairs, mixed pairs, and the ratio of real and mixed pairs for charged kaons as functions of dz and $d\phi$ at the EMC in 0-60%.

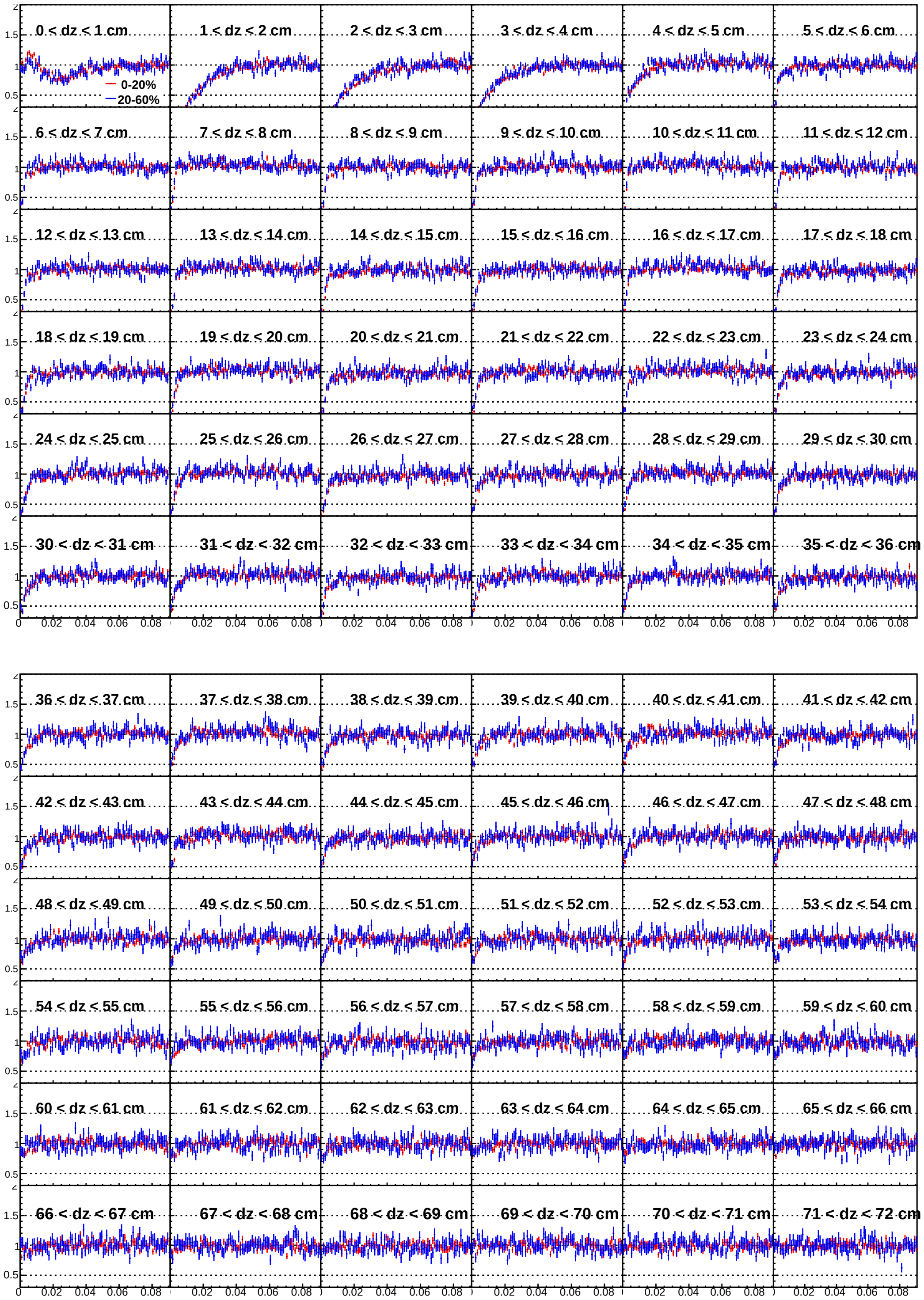

Figure 4.14: Ratio of real and mixed kaon pairs as a function of the relative angular difference $d\phi_{dc}$ every dz_{dc} with 1 cm step.

4.5.3 Correction of Coulomb Interaction

The Coulomb force between two chared particles is calculated by using the Coulomb wave function given by Eq. (2.25). Since Eq. (2.25) includes the relative distance between two particles, "r", we need to assume the source size to calculate the Coulomb strength.

In this analysis, Gaussian distribution is assumed as the spatial distribution of the input source for the Coulomb calculation. The spatial positions of particles following Gaussian distribution are determined randomly, the Coulomb strength is calculated with the relative difference and momentum every particle pairs. Integral in Eq. (2.35) is performed for 20 points of the spatial positions generated by random number to speed up the calculation [51]. The calculated strength is averaged using real pairs each the relative momentum.

The actual procedure to correct the Coulomb effect has been developed in the past experiments [52, 53]. It is known that the correction of correlation function by the calculated Coulomb strength itself will be a overcorrection because it assumes that all pairs interact with each other.

There are two types of methods to apply the Coulomb correction to the measured correlation function. One is the way to correct the correlation function itself directly [52, 53, 36]. Another one is that the Coulomb correction factor is included in the fit function, which is based on the Core-Halo picture of emitting source [54, 55, 36, 62]. Charged pions used in this analysis come from not only the produced matted by heavy ion collisions (Core part) but also the decay of long-lived particles such as η, η', ω, which decay into pions around more than ~10 fm away from the core part (Halo part). Since HBT interference from these particles appears at very low relative momentum, the Halo part cannot be resolved experimentally. Although these particles also have the Coulomb interaction, the interaction with a particle in the core part is negligible [54, 36]. Therefore the Coulomb correction should be taken into account for pairs which contribute HBT interference. Fit function consisting of the core and halo parts is given by

$$\begin{aligned} C_2 &= C_2(core) + C_2(halo), && (4.35) \\ &= N[(\lambda(1+G) \cdot F_{coul}) + (1-\lambda)], && (4.36) \end{aligned}$$

where N is a normalization factor, F_{coul} is the Coulomb correlation function calculated by Coulomb wave function and applied only for the Core part, and G is the Gaussian component of the correlation function given by

$$G = \exp(-R_{inv}^2 q_{inv}^2), \tag{4.37}$$

for 1-dimensional C_2 and given by

$$G = \exp(-R_{side}^2 q_{side}^2 - R_{out}^2 q_{out}^2 - R_{long}^2 q_{long}^2 - 2R_{os} q_{side} q_{out}), \tag{4.38}$$

for 3-dimensional C_2.

Figure 4.15 shows the measured 1-dimensinal correlation function for charged pion pairs with fit function of Eq. (4.36), where F_{coul} is also plotted. The strength of applied Coulomb correction is scaled by the parameter λ.

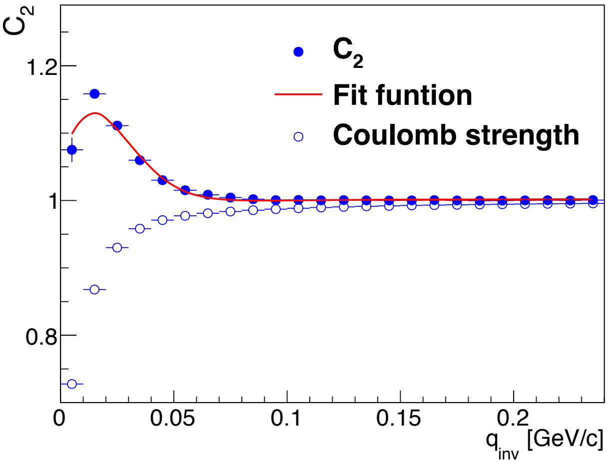

Figure 4.15: Measured 1-dimensional correlation function (filled circles) of charged pion pairs as a function q_{inv} with the fit function (solid line) of Eq.(4.36). Coulomb correction factor $F_{coul}(q_{inv})$ calculated by the Coulomb wave function is shown as open symbols.

4.5.4 Correction of Momentum Resolution

Finite momentum resolution of the detector leads to the broadening of the correlation function and results in the underestimate of the HBT radii. In this section, we estimate the momentum resolution by Monte-Carlo simulation and explain the way to correct the effect.

In order to estimate the momentum resolution, single particles Monte-Carlo simulation have been performed. Single particles are generated by EXODUS, which is a phenomenological single particle event generator in PHENIX and allows us to simulate the hadronic decay [56]. EXODUS generates particles with given phase-space distributions, the transverse momentum p_T and rapidity distributions. In this study, single particles are generated with flat distributions in p_T, rapidity and azimuth. The generated particles go through a GEANT simulation of PHENIX detectors to simulate the interactions of the particles with the detectors and the secondary particle generation, which is called PISA (PHENIX Integrated Simulation Application). Then the hit information of the detectors in the PISA simulation are reconstructed by the usual track reconstruction. Finally, these simulated tracks can be analyzed in the same way as real data.

Figure 4.16 shows the differences of p_T, azimuthal and elevation angle between the original particles generated by the EXODUS and the reconstructed tracks after the PISA simulation as a function of momentum. To evaluate the resolutions, the Gaussian fit is applied for each distributions every momentum. The standard deviation and means of the fit results are shown in Fig. 4.17, Fig. 4.18. There is no significant difference between the charge of particles and the orientation of magnetic field for the standard deviation, while the mean of $\Delta p_T/p_T$ shows a little difference between the same charged particles with different magnetic field and seems to depend on the orientation of the track curvature. The resolution of $\Delta p_T/p_T$ is less than about 1.5% in the momentum range we use in the analysis. To evaluate these values, we have fitted them with the polynomial function as shown in Fig. 4.19. The same study have been done for charged kaons as shown in Fig. 4.20. The momentum resolution of kaons is worse than that of pions at low momentum because of different effect from multiple scattering.

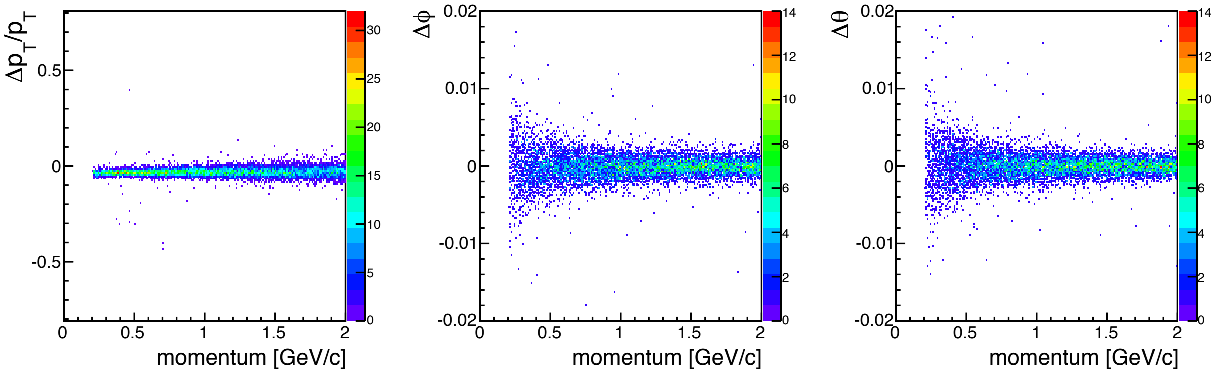

Figure 4.16: Difference of p_T, ϕ, θ between the generated particles and reconstructed tracks in the simulation as a function of momentums.

Momentum resolution correction is taken into account by applying the correction factor to the measured correlation function. In this study, we use the similar way to the method used in STAR experiment [62].

$$C_2 = \frac{A(\vec{q})}{B(\vec{q})} F_{mom}(\vec{q}), \tag{4.39}$$

where F_{mom} is the correction factor for momentum resolution and defined as the following equation:

$$\begin{aligned} F_{mom}(\vec{q}) &= \frac{C_2(\vec{q}_{ideal})}{C_2(\vec{q}_{smear})}, & (4.40)\\ &= \frac{A(\vec{p}_{1,ideal}, \vec{p}_{2,ideal})}{B(\vec{p}_{1,ideal}, \vec{p}_{2,ideal})} \Big/ \frac{A(\vec{p}_{1,smear}, \vec{p}_{2,smear})}{B(\vec{p}_{1,smear}, \vec{p}_{2,smear})}, & (4.41) \end{aligned}$$

where p_{ideal} and p_{smear} are the ideal and smeared momenta of the single particle. The correction factor of the momentum resolution is calculated as the ratio of the ideal and smeared correlation functions. The ideal C_2 is made by the numerator and denominator using the mixed pairs, where we assume the particles of those pairs have the real momenta. The histogram for the numerator is weighted with the fit function C_2 defined as Eq. (4.36). To calculate the weight, HBT radii and the Coulomb correction factor are needed as the input. The smeared C_2 is also made by the same procedure as the ideal C_2, where the weight of the numerator is the same one in making the ideal C_2. The momenta of each particles of pairs are smeared according to the estimated momentum resolution, where the random number following the Gaussian distribution is used.

Since the extracted HBT radii are needed to calculate the correction factor of the momentum resolution, the iterative procedure have been applied as the followings:

1. Fit the measured C_2 without the momentum resolution correction and extract the HBT radii.

2. Make the correction factor of the momentum resolution using the HBT radii extracted in the above step.

3. Fit the measured C_2 with the correction factor of the momentum resolution and extract the HBT radii.

4. Iterate the step.2 and step.3 until the difference of the input parameters and the extracted parameters as the output becomes negligibly small.

Figure 4.21 shows the comparison of 3D HBT radii for charged pions with and without the momentum resolution correction. Since the momentum resolution estimated by the PISA simulation have less effect than 1% on the extracted HBT radii for both pions and kaons and doesn't change the oscillation amplitudes more than statistical error, the resolution correction is not applied to the final result.

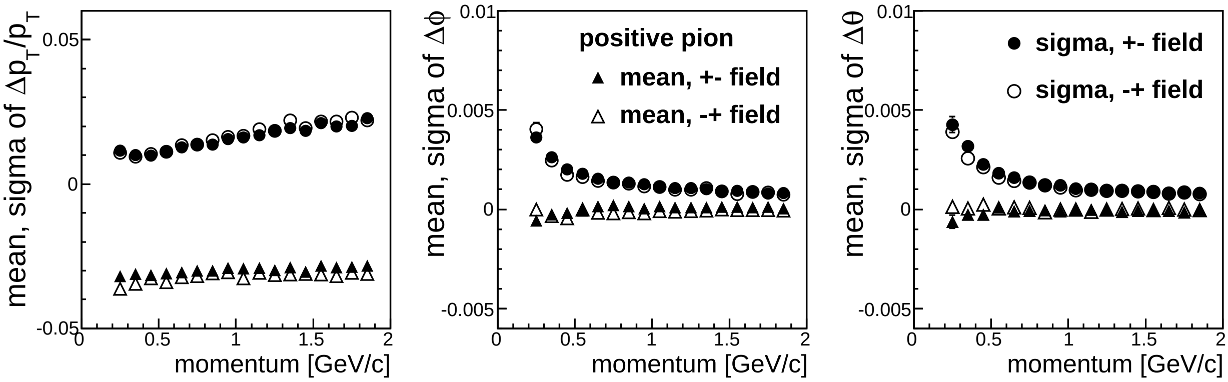

Figure 4.17: Momentum resolution for positive pions in the different magnetic fields. The standard deviations and means of $\Delta p_T/p_T$, $\Delta\phi$, $\Delta\theta$ distribution obtained by the Gaussian fit are plotted as a function momentum.

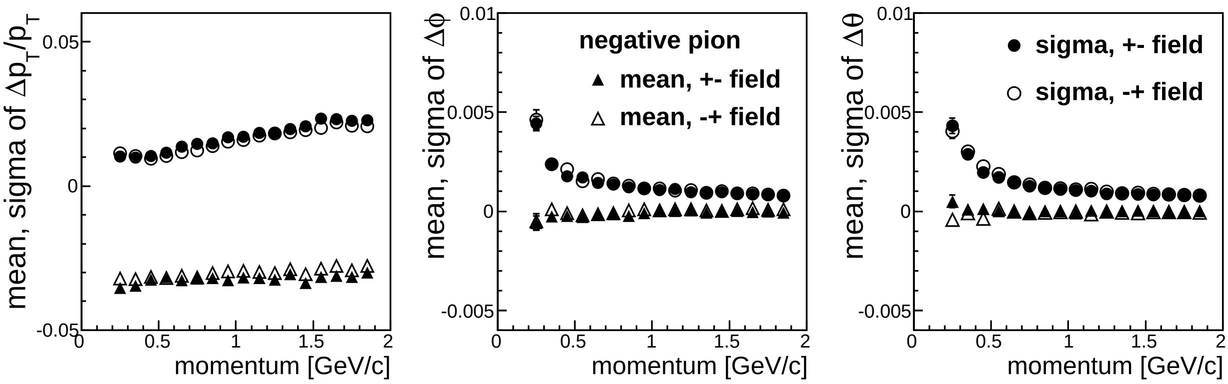

Figure 4.18: Momentum resolution for negative pions in the different magnetic fields. The standard deviations and means of $\Delta p_T/p_T$, $\Delta\phi$, $\Delta\theta$ distribution obtained by the Gaussian fit are plotted as a function momentum.

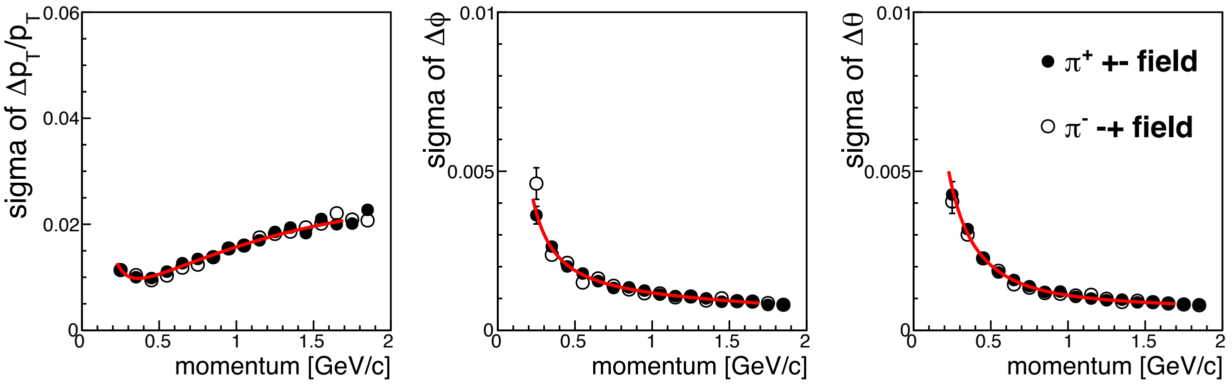

Figure 4.19: Momentum resolution for charged pions with polynomial fit. The standard deviations of $\Delta p_T/p_T$, $\Delta\phi$, $\Delta\theta$ distribution obtained by the Gaussian fit are plotted as a function momentum.

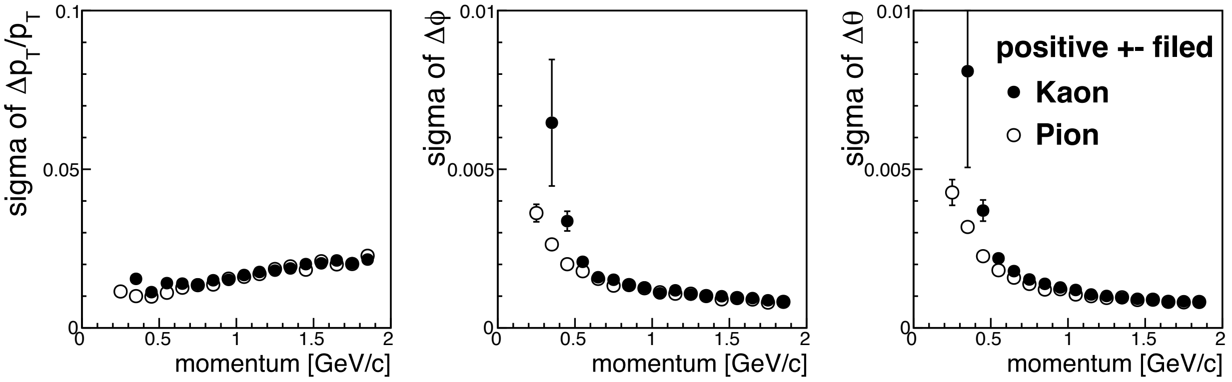

Figure 4.20: Momentum resolution for positive kaons in $+-$ magnetic field. The standard deviations of $\Delta p_T/p_T$, $\Delta\phi$, $\Delta\theta$ distribution obtained by the Gaussian fit are plotted as a function momentum, where the result of pions are compared.

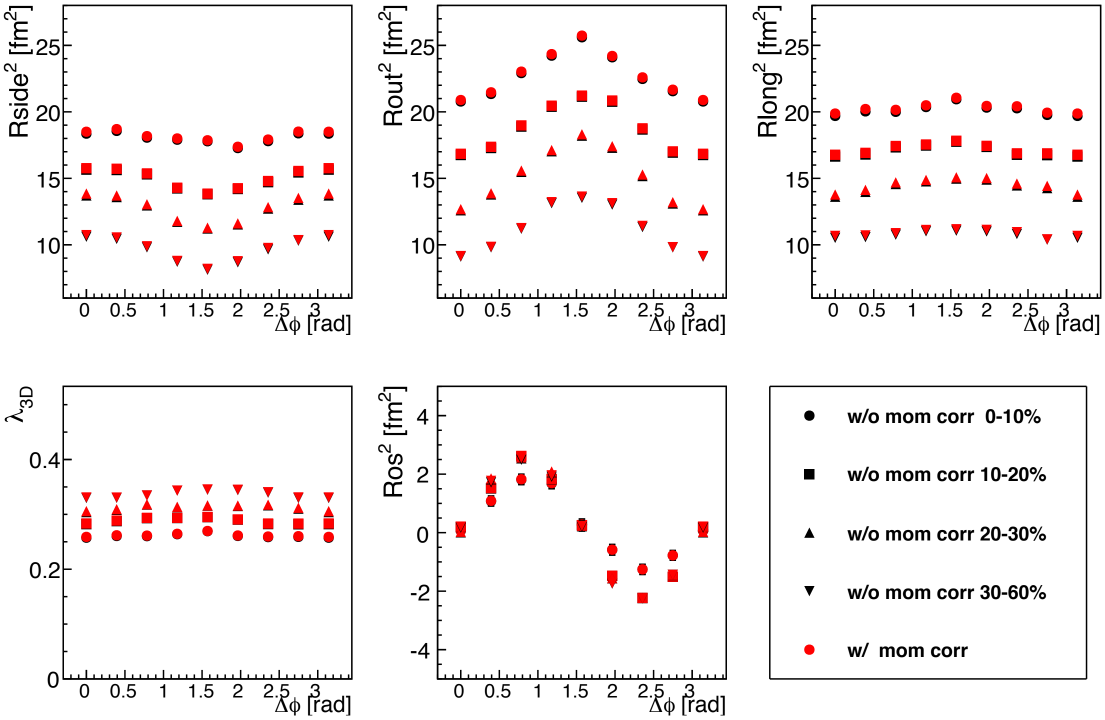

Figure 4.21: Extracted 3D-HBT radii with and without momentum resolution correction

4.5.5 Correction of Event Plane Resolution

Finite event plane resolution reduces the oscillation amplitude of HBT radii as a function of pair angle with respect to the measured event plane as shown in Fig. 4.22.

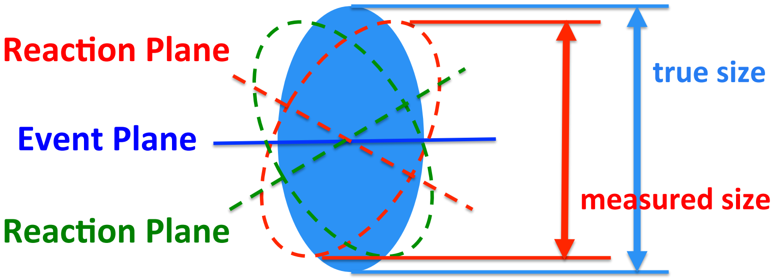

Figure 4.22: Illustration of the smearing effect for the measured source size by the finite event plane resolution.

A model independent correction is applied in this analysis as described in [57]. This method also corrects the effect of azimuthal angular binning. The following equation is applied to real q-distribution and mixed q-distribution.

$$N(q,\Phi_j) = N_{exp}(q,\Phi_j) + 2\sum_{n=m,2m,\cdots}^{n_{bin}/2} \zeta_{n,m}(\Delta)[N^{exp}_{c,n}(q)\cos(n\Phi_j) + N^{exp}_{s,n}(q)\sin(n\Phi_j)], \tag{4.42}$$

where $N_{exp}(q,\Phi_j)$ denotes the measured relative momentum distribution of real and mixed pairs, n_{bin} is the number of azimuthal angular bins, and m is the order of the measured event plane, and Φ_j denotes the center of j_{th} angular bin which corresponds to the azimuthal angle of pair with respect to the measured event plane. And $N^{exp}_{c,n}(q)$, $N^{exp}_{c,n}(q)$, $\zeta_{n,m}(\Delta)$ are given by the followings.

$$N^{exp}_{c,n}(q) = \langle N_{exp}(q,\Phi)\cos(n\Phi)\rangle = \frac{1}{n_{bin}}\sum_{j=1}^{n_{bin}} N_{exp}(q,\Phi_j)\cos(n\Phi_j), \tag{4.43}$$

$$N^{exp}_{s,n}(q) = \langle N_{exp}(q,\Phi)\sin(n\Phi)\rangle = \frac{1}{n_{bin}}\sum_{j=1}^{n_{bin}} N_{exp}(q,\Phi_j)\sin(n\Phi_j), \tag{4.44}$$

$$\zeta_{n,m}(\Delta) = \frac{n\Delta/2}{\sin(n\Delta/2)\langle\cos(n(\Psi_m - \Psi_R))\rangle} - 1, \tag{4.45}$$

where the factor $\langle\cos(n(\Psi_m - \Psi_R))\rangle$ is the well-known correction factors for the measured event plane resolution. Δ denotes the width of azimuthal angular bins. Here, when pair particles are measured relative to 2^{nd} or 3^{rd}-order event plane, only even or odd values of n which is 2 or 3 and above are summed over. Equation (4.42) corrects the smearing effect of the oscillation amplitude of azimuthal HBT radii caused by finite resolution of event plane and finite width of azimuthal angular binning.

In Eq. (4.42), the coefficients defined as Eq. (4.43), (4.44) fluctuates in case of low statistics. Besides, the factor $\zeta_{n,m}$ in the correction term is proportional to the reciprocal of the event plane resolution. Therefore if the event plane resolution is low, this correction method amplifies the fluctuation. In order to make sure the validity of this method in current situation, we have performed a simple simulation. The detailed setup of the simulation is explained in Appendix D.

Figure 4.23 shows the result of corrected and uncorrected HBT radii with a bad event plane resolution in simulation, where Gaussian distribution is assumed as the spatial density of the source and the standard deviation σ in y-direction is set to be larger than that in x-direction to make the elliptical shape. Here we assume the difference of event plane and reaction plane follows Gaussian distribution. The extracted radii with the correction of event plane resolution shows a good agreement with the original radii measured with respect to ideal reaction plane even in a bad resolution. The differences of amplitudes of corrected and original radii are about 3% in R_{side} and R_{out}.

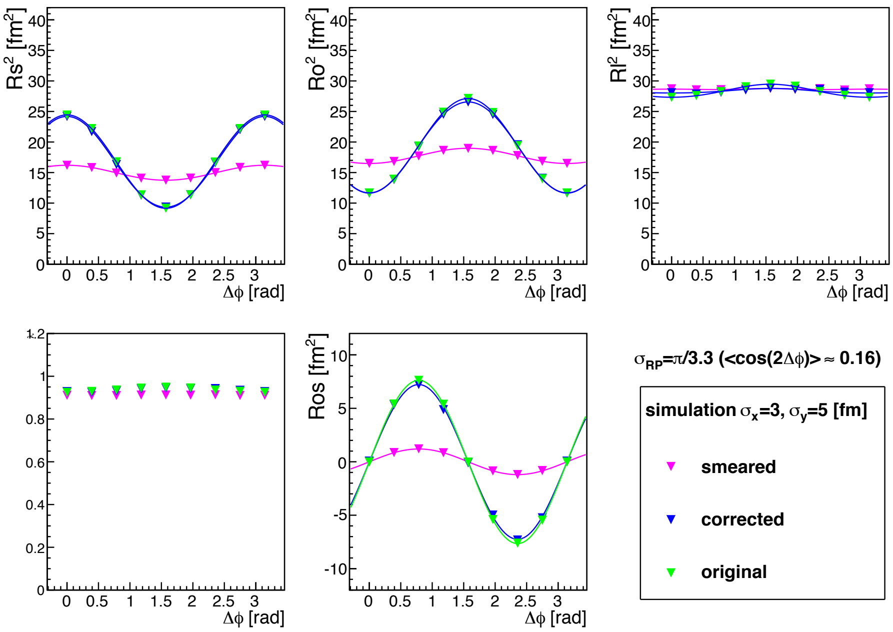

Figure 4.23: Corrected and uncorrected 3D HBT radii as a function of azimuthal pair angle relative to Ψ_2 ($\Delta\phi$) in HBT simulation with a bad event plane resolution.

In this thesis, we also measure azimuthal dependence of HBT radii with respect to 3rd-order event plane. Therefore we checked the feasibility of the above resolution correction method for 3rd-order event plane. The source shape in the transverse plane is controlled to be triangular using Woods-Saxon distribution (Details are described in Sec. 6.4.2). Figure 4.24 shows 3D HBT radii as a function of azimuthal pair angle with respect to 3rd-order event plane. Different marker colors correspond to different event plane resolution. The worse the event plane resolution becomes, the smaller the amplitude of the oscillation become due to smearing effect. Figure 4.25 shows corrected 3D HBT radii using Eq. (4.42). After the correction, the smeared radii are recovered to be the case of an ideal event plane resolution for all event plane resolutions. As shown in Fig. 4.22, the 3rd-order event plane measured by the north or south RXNP is about 0.2. Therefore this correction method is applicable in this analysis when the statistics is enough.

Figure 4.26 shows the extracted HBT radii of charged pions as a function of azimuthal pair angle relative to Ψ_2 ($\Delta\phi$) with and without the correction of the event plane resolution with Eq. (4.42)

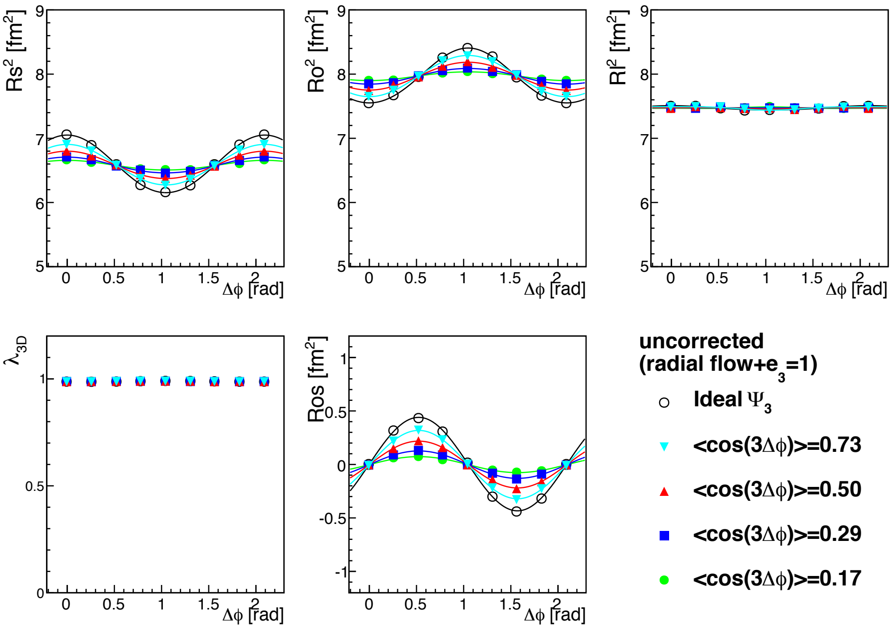

Figure 4.24: Uncorrected 3D HBT radii as a function of azimuthal pair angle relative to Ψ_3 ($\Delta\phi$) for different event plane resolution in HBT simulation.

using the 2$^{\text{nd}}$-order event plane shown in Figure 4.22. The above correction doesn't change the average of radii, but only the oscillation.

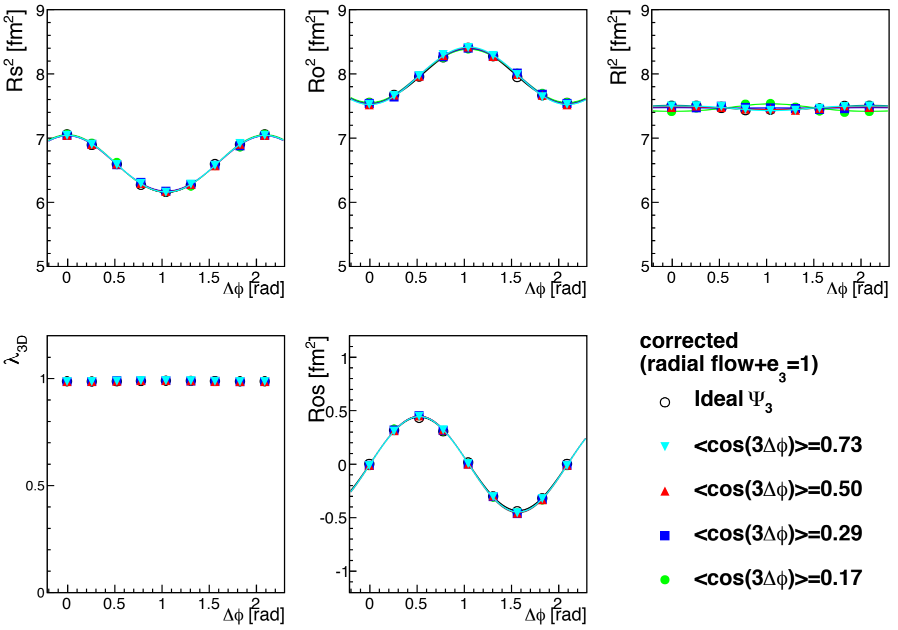

Figure 4.25: Corrected 3D HBT radii as a function of azimuthal pair angle relative to Ψ_3 ($\Delta\phi$) for different event plane resolution in HBT simulation.

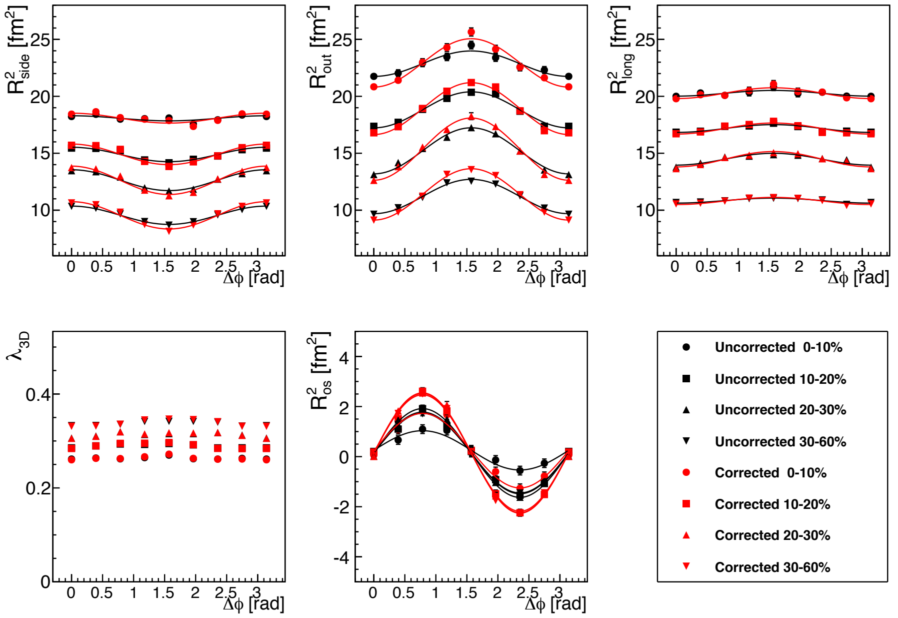

Figure 4.26: Corrected and uncorrected 3D HBT radii of charged pions as a function of azimuthal pair angle relative to Ψ_2 ($\Delta\phi$) in Au+Au collisions at $\sqrt{s_{\mathrm{NN}}}$ = 200 GeV.

4.5.6 Fitting Procedure

A usual χ^2 method is inappropriate for fitting correlation functions because the ratio of two Poisson distributions is not itself Poisson distributed. A log-likelihood minimization function is used in this analysis. We assume that relative momentum distributions for real (A) and mixed (B) pairs follow the Poisson probability distribution with means given by μ and ν. The correlation function is defined as the ratio of those means by imposing a δ-function constraint on the conditional probability for a correlation function when A and B are given:

$$\begin{aligned} P(C|A,B) &= \int d\mu d\nu \left(\frac{\mu^A e^{-\mu}}{A!} \frac{\nu^B e^{-\nu}}{B!} \delta(C - \mu/\nu) \right), && (4.46) \\ &= \int d\nu \nu^{A+B+1} e^{-(c+1)\nu}, && (4.47) \\ &= \frac{C^A}{A!B!} \frac{1}{(C+1)^{A+B+2}} \Gamma(A+B+2), && (4.48) \end{aligned}$$

where since A and B are positive integer, the Gamma function can be replaced by the relation of $\Gamma(n) = (n-1)!$. Therefore $P(C|A,B)$ is rewritten as the following equation:

$$P(C|A,B) = \frac{C^A}{A!B!} \frac{(A+B+1)!}{(C+1)^{A+B+2}}. \tag{4.49}$$

Then taking the negative of the twice the log and collecting leading order terms in A and B leads to the principal of maximum likelihood minimization function:

$$\chi^2 = -2 \left[A \ln \left(\frac{C(A+B)}{A(C+1)} \right) + B \ln \left(\frac{A+B}{B(C+1)} \right) \right]. \tag{4.50}$$

Equation (4.50) approaches χ^2 distribution in the limit of large A and B. Equation (4.50) is obtained from the assumption of Poisson distribution for A and B and the log-likelihood method. That is why this minimization function may be more accurate for fit of A and B with low statistics. The minimization process is performed by using the MINUIT package in CERN Program Library [58].

4.6 Initial Spatial Anisotropy

Azimuthal angle dependence of HBT radii provides us the information on the source shape at final state. In order to study the space-time evolution of the system, initial geometrical information is needed to be evaluated. Therefore Monte-Carlo Glauber calculation has been performed to get quantities at initial state such as the number of participant (N_{part}), initial eccentricity (ε_2), and initial triangularity (ε_3).

4.6.1 Monte-Carlo Glauber Simulation

The Glauber model [9] is often introduced to describe the collision geometry as mentioned in Sec. 1.2.2. The model is based on a geometrical picture of a nucleus-nucleus collisions and allows us to associate centrality determined experimentally with more useful quantities, such as N_{part}, ε_2, by which we can understand a event intuitively. In the Monte-Carlo calculation [10], the nucleons composing two nuclei are generated in space coordinate according to Woods-Saxon parameterization as the density distribution. An impact parameter b is chosen randomly. We assume that a nucleon-nucleon collision takes place if their distance d in the transverse plane satisfies

$$d < \sqrt{\sigma_{nn}/\pi}, \tag{4.51}$$

where σ_{nn} is the total inelastic nucleon-nucleon cross section.

For gold nuclei, the parameters in Woods-Saxon distribution are set to be $R = 6.38$ fm and $a = 0.54$ fm. The total inelastic nucleon-nucleon cross section of $\sigma_{nn} = 42$ mb is used for a center of mass energy of $\sqrt{s_{\mathrm{NN}}} = 200$ GeV.

Glauber Monte-Carlo simulations have been performed in PHENIX so far [59, 60, 10], where the initial geometrical quantities in the Glauber simulation are connected to experimental data assuming that the charge sum measured by the BBC is proportional to the number of participants. In the official calculations in PHENIX, the detector efficiency is also taken into account. In this simulation, we don't include the effect of detector efficiency because there is no significant difference between PHENIX official values and our calculations for N_{part} and the eccentricity as shown in Fig. 4.28. The number of participants distribution is used to determine the event centrality class (0-100% by 10% step). Figure 4.27 shows the number of participants and impact parameter distributions in this simulation. Each distributions for each centrality classes are plotted together. Figure 4.28 shows the number of participant (Left) and initial eccentricity as a function of centrality. Two types of spatial eccentricities explained in the next section are plotted in the right of the figure. PHENIX official values [60] simulated for Run7 are compared. Our simulation results are quite consistent with PHENIX calculations except most peripheral event class. Small difference in most peripheral event class would be caused by the effect of the detector efficiency. In this analysis we discuss over 60% centrality and don't need to take care of the difference.

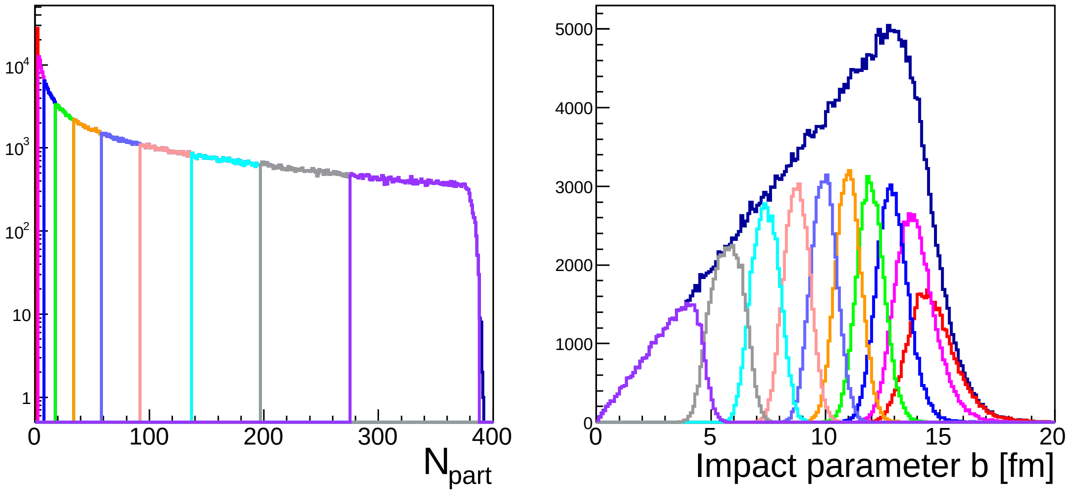

Figure 4.27: (Left) The number of participants distribution and that for each divided centrality classes. (Right) Impact parameter distribution and that for each divided centrality classes.

4.6.2 Initial Spatial Anisotropy

Azimuthal anisotropy in momentum space is related to the initial shape of the overlap region in nucleus-nucleus collisions because the geometrical anisotropy leads to the different pressure gradient

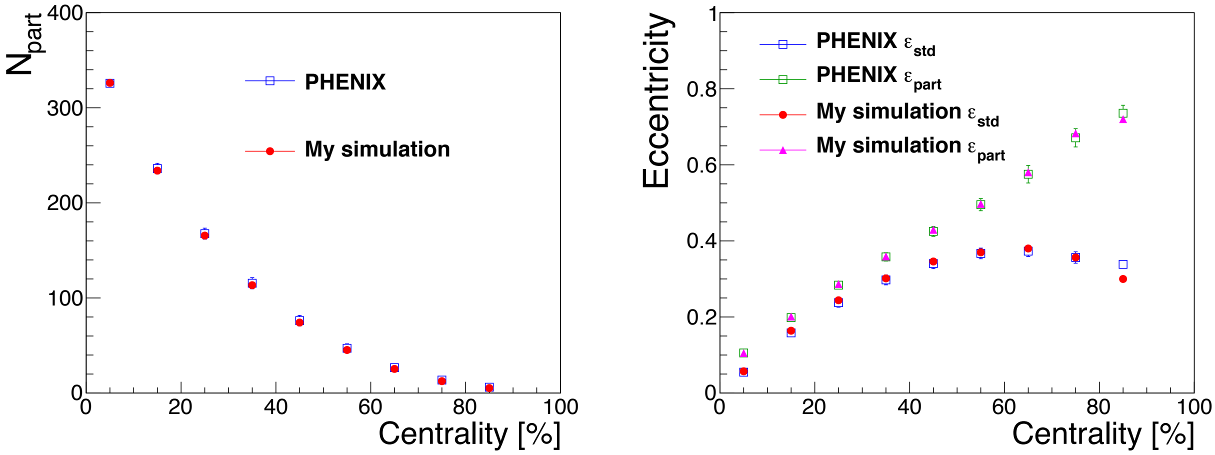

Figure 4.28: (Left) N_{part} as a function of centrality in Glauber simulation. PHENIX official values in Run7 are compared. (Right) Eccentricity as a function of centrality. Standard and participant eccentricity in PHENIX and my simulation are shown.

in the different direction, which results in causing the anisotropic flow like v_2. Therefore it is necessary to characterize such initial shape.

Eccentricity is typically used to quantify the shape because the overlap of two nuclei is like ellipse and defined as

$$\begin{aligned} \varepsilon &= \frac{\langle y^2\rangle - \langle x^2\rangle}{\langle y^2\rangle + \langle x^2\rangle}, \\ &= \varepsilon_{std}, \end{aligned} \tag{4.52}$$

where x and y is the spatial positions of participant nucleons. $\langle\cdots\rangle$ represents an average taken over all participating nucleons in a single collision event. We call it the standard eccentricity ε_{std} here. In the system of finite number of participants, the plane formed by the participants themselves (participant plane) is not consistent with reaction plane due to the fluctuations. Thus the eccentricity calculated relative to the participant plane is defined as

$$\varepsilon_{part} = \frac{\langle y'^2\rangle - \langle x'^2\rangle}{\langle y'^2\rangle + \langle x'^2\rangle}, \tag{4.53}$$

$$= \frac{\sqrt{(\sigma_y^2 - \sigma_x^2)^2 + 4\sigma_{xy}^2}}{\sigma_y^2 + \sigma_x^2}, \tag{4.54}$$

$$= \frac{\langle r^2 \cos[2(\phi - \Psi)]\rangle}{\langle r^2\rangle}, \tag{4.55}$$

$$\Psi = \frac{1}{2}\left[\tan^{-1}\left(\frac{\langle r^2 \sin(2\phi)\rangle}{\langle r^2 \cos(2\phi)\rangle}\right) + \pi\right], \tag{4.56}$$

where x' and y' is the spatial positions in the frame which is shifted to the center of mass of the participants ($\langle x\rangle = \langle y\rangle = 0$) and rotated relative to the reaction plane by an angle Ψ. The participant plane angle Ψ is taken to maximize the eccentricity. We call ε_{part} the participant eccentricity here. Both eccentricities in the different definitions are compared in the right of Fig. 4.28. The standard eccentricity decrease with centrality going from mid-central to peripheral collisions, while the participant eccentricity goes to unity because the fluctuation becomes large. Azimuthal HBT measurement is performed with respect to the event plane which is determined for event by event using the signal coming from participant measured at the RXNP. Therefore the participant eccentricity including the event-by-event fluctuation is more meaningful than the standard eccentricity in this study.

Higher order spatial anisotropy ε_n can be written with the similar definition to the participant eccentricity:

$$\varepsilon_n = \frac{\langle r^2 \cos[n(\phi - \Psi_n)]\rangle}{\langle r^2 \rangle}, \tag{4.57}$$

$$\Psi_n = \frac{1}{n}\left[\tan^{-1}\left(\frac{\langle r^2 \sin(n\phi)\rangle}{\langle r^2 \cos(n\phi)\rangle}\right) + \pi\right]. \tag{4.58}$$

For $n = 3$, ε_3 means the triangular anisotropy, which is often called triangularity, for $n = 4$, ε_4 means the quadrangular anisotropy. Figure 4.29 shows the calculated spatial anisotropy for $n = 2, 3, 4$. For $n = 4$, ϵ_4 is calculated with respect to Ψ_2 and Ψ_4 by changing Ψ_n in the definition of Eq. (4.57). Systematic errors are estimated by changing the input parameters of the Glauber calculation. The detail about the estimation of the systematic error are explained in App. C. Triangularity ε_3 and quadrangularly ε_4 clearly have finite value.

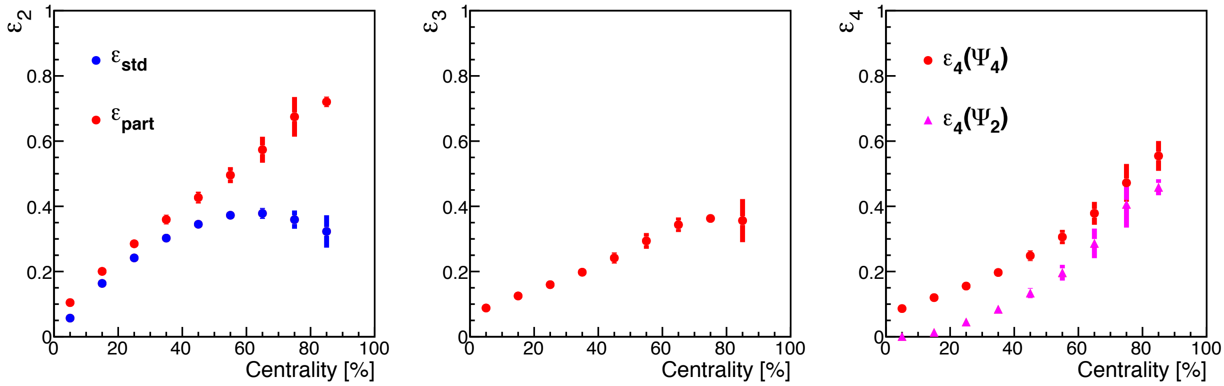

Figure 4.29: Initial higher order anisotropy as a function of centrality. ε_4 is calculated for both Ψ_2 and Ψ_4. Systematic errors are shown together.

4.7 Systematic Uncertainties

In this section, we explain the estimation of systematic uncertainties for extracted HBT radii. Systematic uncertainties have been estimated by changing the conditions of possible sources of them, such as single track selections, pair selections, event plane determination, and Coulomb correction. We present the result on HBT radii of charged pions with respect to Ψ_2 in this section, the result for charged kaons, and charged pions with respect to Ψ_3, are shown in App. B.

4.7.1 Uncertainties from Track and Pair Selection

To estimate systematic uncertainties derived from the track and pair selection, we have studied the HBT radii by changing the track matching cut, PID cut, and pair cuts. The differences from the values with default cut are calculated as systematic errors.

- track matching cut : 1.5σ, 2.0σ(default)
- PID cut : 1.5σ, 2.0σ(default)

In case of pair cuts, we apply tighter cuts than default cuts shown in Sec. 4.5.2. Both cuts for the DC and EMC are changed at the same time as shown in the followings:
For pion,

- $dz_{dc} < 5$ cm and $d\phi_{dc} > 0.105$ rad
- 5 cm $\leq dz_{dc} < 70$ cm and $d\phi_{dc} > 0.03$ rad
- $dz_{dc} \geq 70$ cm
- $dr_{emc} \geq 25.5$ cm

For kaon,

- $dz_{dc} < 4$ cm and $d\phi_{dc} > 0.05$ rad
- 5 cm $\leq dz_{dc} < 65$ cm and $d\phi_{dc} > 0.015$ rad
- $dz_{dc} \geq 65$ cm
- $\sqrt{(d\phi_{emc}/0.06)^2 + (dz_{emc}/19)^2} < 1.5$

The uncertainties from the track matching cut are $\sim$ 5% for R_s^2 and $\sim$ 6% for R_o^2 at most. The uncertainties from PID cuts are less than 1% for both R_s^2 and R_o^2.

4.7.2 Uncertainties from Event Plane Determination

We have evaluated the systematic error derived from the different event planes determined by the RXNP North or South or combined North and South (default). Figure 4.32 shows the centrality dependence of extracted pion HBT parameters measured with different event planes. The uncertainties from event plane determination are less than 2% for R_s^2 and R_l^2, 4% for R_o^2 at most.

4.7.3 Uncertainties from Coulomb Correction

As described in Sec. 4.5.3, the Coulomb correction procedure needs information on the source size. However this value is unknown and given by the extracted HBT radii. Therefore the iterative process is performed for the Coulomb correction. We have evaluated the difference of the extracted HBT radii with the Coulomb correction using the different input source size. HBT radii which are 1 fm less or larger than the extracted HBT radii are used as the input source size.

Figure 4.33 shows the centrality dependence of HBT parameters with different input source size for Coulomb correction. The uncertainties from event plane determination are less than 1% for R_s^2 and R_l^2, $\sim$2% for R_o^2 at most.

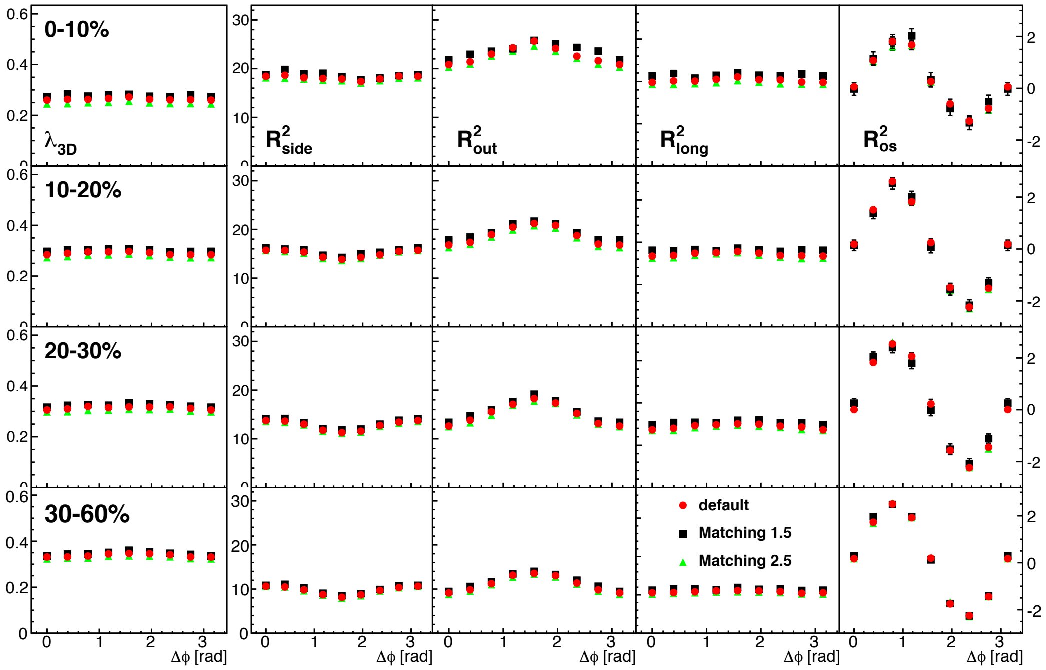

Figure 4.30: Squared HBT radii of charged pions with different conditions of track matching cut.

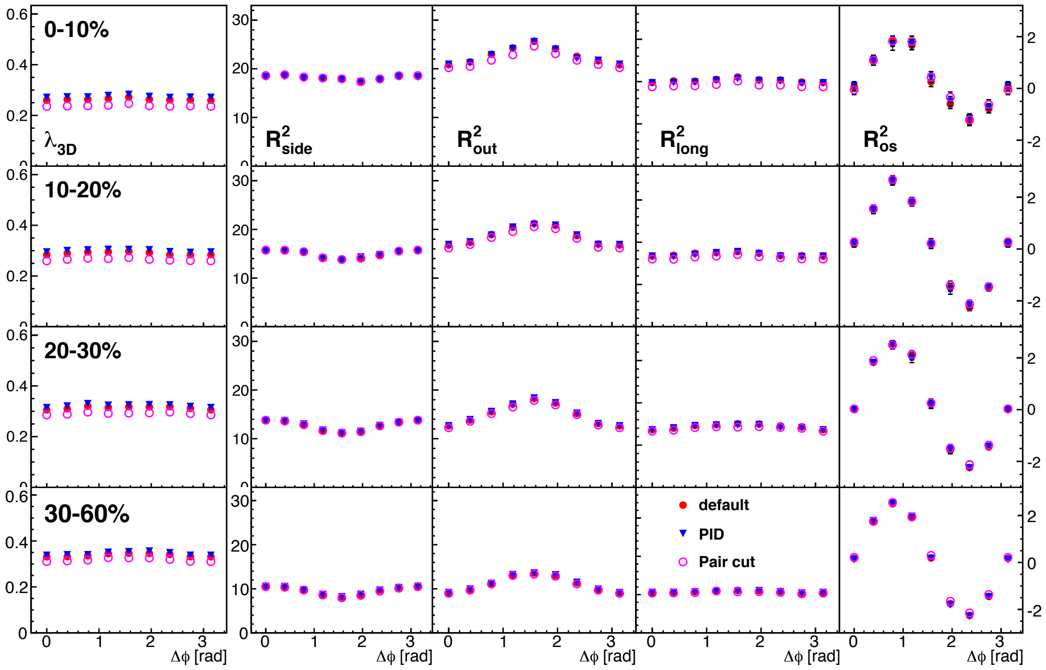

Figure 4.31: Squared HBT radii of charged pions with different conditions of PID cut and pair selection cut.

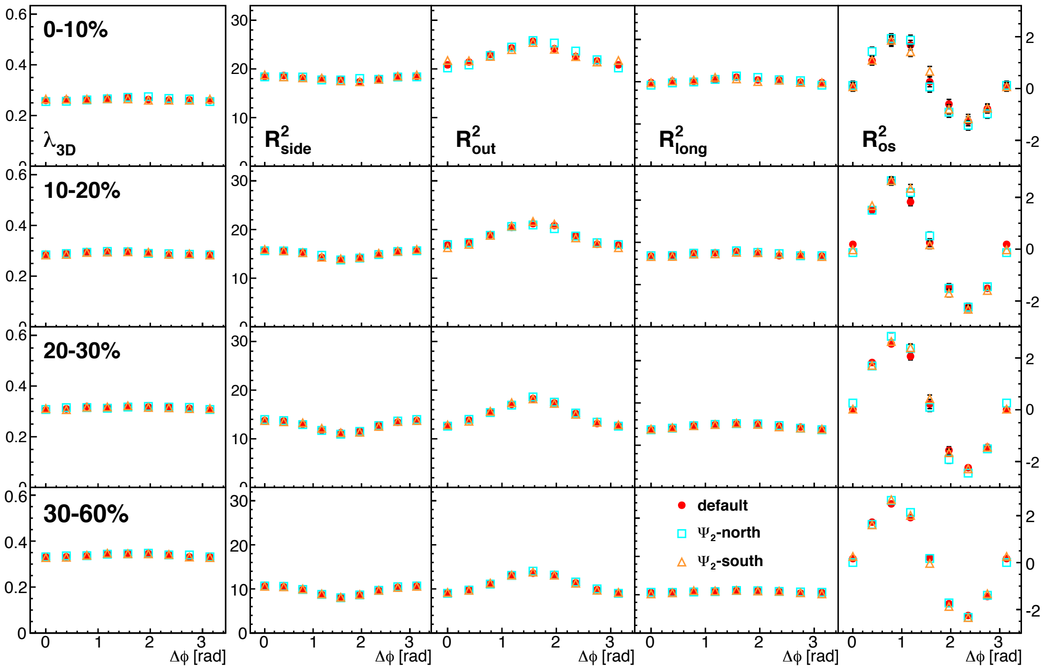

Figure 4.32: Squared HBT radii of charged pions measured with different event planes.

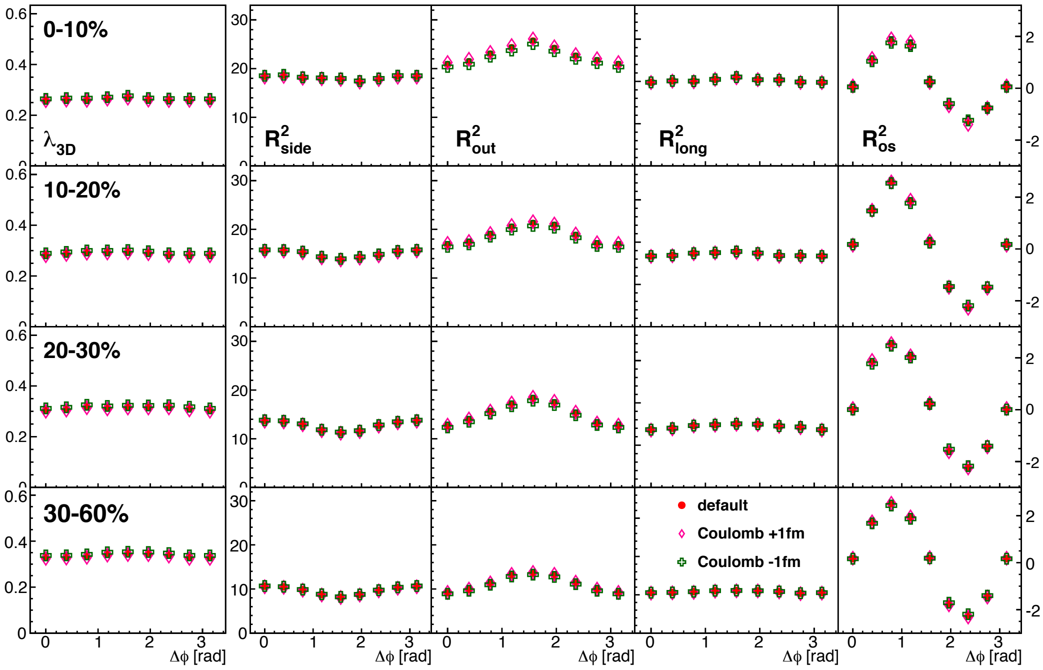

Figure 4.33: Squared HBT radii of charged pions with different input source size for Coulomb strength.

	λ				R_s^2			
0-10%								
$\Delta\phi$	0	$\pi/4$	$\pi/2$	$3\pi/4$	0	$\pi/4$	$\pi/2$	$3\pi/4$
Matching cut [%]	5.46	7.47	4.99	5.56	1.79	4.80	2.92	3.94
PID cut [%]	4.32	3.85	3.90	4.50	0.70	1.28	0.38	0.06
Pair cut [%]	9.28	9.94	9.49	10.04	0.92	0.66	0.90	0.57
Event plane [%]	1.88	1.55	0.52	0.14	1.05	1.46	0.66	1.01
Coulomb [%]	1.40	1.55	1.64	1.47	0.77	0.90	0.56	0.50
Total [%]	11.84	13.20	11.54	12.41	2.50	5.30	3.20	4.14
10-20%								
$\Delta\phi$	0	$\pi/4$	$\pi/2$	$3\pi/4$	0	$\pi/4$	$\pi/2$	$3\pi/4$
Matching cut [%]	4.34	4.56	3.53	4.10	1.65	1.61	2.12	2.32
PID cut [%]	3.78	3.67	2.76	3.32	0.98	0.21	0.46	1.29
Pair cut [%]	8.55	8.35	8.43	8.98	0.24	0.25	0.42	0.96
Event plane [%]	0.11	0.74	0.38	0.43	0.85	0.38	0.62	1.61
Coulomb [%]	1.66	1.73	1.84	1.71	0.67	0.72	0.74	0.79
Total [%]	10.44	10.37	9.74	10.57	2.22	1.83	2.41	3.35
20-30%								
$\Delta\phi$	0	$\pi/4$	$\pi/2$	$3\pi/4$	0	$\pi/4$	$\pi/2$	$3\pi/4$
Matching cut [%]	3.05	4.14	3.62	3.09	2.09	2.88	1.78	2.33
PID cut [%]	2.87	3.46	3.28	2.82	0.23	0.36	0.07	0.09
Pair cut [%]	6.57	7.04	7.18	7.45	0.43	0.05	1.07	0.95
Event plane [%]	1.22	1.32	1.10	0.77	0.84	0.87	1.39	1.78
Coulomb [%]	1.83	1.78	1.80	1.83	0.80	0.87	0.75	0.86
Total [%]	8.10	9.15	8.94	8.77	2.44	3.15	2.61	3.20
30-60%								
$\Delta\phi$	0	$\pi/4$	$\pi/2$	$3\pi/4$	0	$\pi/4$	$\pi/2$	$3\pi/4$
Matching cut [%]	1.90	2.66	2.63	2.45	1.00	2.87	3.16	2.35
PID cut [%]	1.95	2.44	1.36	1.80	0.85	0.06	0.89	0.22
Pair cut [%]	6.34	5.68	5.62	5.10	1.55	1.01	1.09	1.84
Event plane [%]	0.51	0.92	0.50	0.58	0.38	0.54	1.13	0.86
Coulomb [%]	1.95	1.82	1.90	1.83	0.87	0.71	0.80	0.98
Total [%]	7.19	7.03	6.65	6.24	2.24	3.17	3.73	3.27

Table 4.1: Summary of systematic errors for squared HBT radii of pions for four centralities. The errors at $\Delta\phi$=0, $\pi/4$, $\pi/2$, $3\pi/4$ are shown.

	R_o^2				R_l^2			
0-10%								
$\Delta\phi$	0	$\pi/4$	$\pi/2$	$3\pi/4$	0	$\pi/4$	$\pi/2$	$3\pi/4$
Matching cut [%]	3.58	4.65	2.14	1.88	4.95	6.43	3.27	4.27
PID cut [%]	0.45	0.82	0.55	0.69	0.46	1.80	1.12	0.98
Pair cut [%]	2.98	4.32	5.42	5.83	5.26	5.93	5.43	5.87
Event plane [%]	3.66	2.00	1.44	1.07	1.62	1.14	1.11	1.40
Coulomb [%]	2.17	2.41	1.93	2.12	0.15	0.23	0.44	0.04
Total [%]	6.32	7.12	6.33	6.60	7.42	9.01	6.54	7.45
10-20%								
$\Delta\phi$	0	$\pi/4$	$\pi/2$	$3\pi/4$	0	$\pi/4$	$\pi/2$	$3\pi/4$
Matching cut [%]	4.69	4.31	2.26	2.95	5.57	4.68	3.98	1.97
PID cut [%]	0.53	0.58	0.67	0.03	0.05	1.48	1.56	0.13
Pair cut [%]	3.67	2.53	3.21	4.43	4.24	5.43	5.10	4.74
Event plane [%]	1.89	1.11	0.65	1.09	0.62	0.63	0.63	1.33
Coulomb [%]	2.14	1.71	1.75	2.02	0.23	0.26	0.30	0.17
Total [%]	6.62	5.43	4.40	5.80	7.03	7.36	6.69	5.31
20-30%								
$\Delta\phi$	0	$\pi/4$	$\pi/2$	$3\pi/4$	0	$\pi/4$	$\pi/2$	$3\pi/4$
Matching cut [%]	3.56	5.09	3.40	2.16	5.06	6.70	4.33	2.80
PID cut [%]	0.17	0.58	0.22	0.11	0.45	0.32	0.29	0.83
Pair cut [%]	2.99	1.87	2.48	3.46	2.60	3.50	3.22	3.33
Event plane [%]	1.02	1.39	0.79	1.47	0.62	0.58	0.12	0.47
Coulomb [%]	1.89	2.08	1.70	1.92	0.43	0.62	0.35	0.40
Total [%]	5.13	6.00	4.61	4.74	5.76	7.62	5.42	4.48
30-60%								
$\Delta\phi$	0	$\pi/4$	$\pi/2$	$3\pi/4$	0	$\pi/4$	$\pi/2$	$3\pi/4$
Matching cut [%]	3.67	5.38	2.92	2.82	4.78	5.34	4.78	2.49
PID cut [%]	0.04	0.97	0.06	0.56	0.16	0.07	0.98	1.98
Pair cut [%]	1.86	1.50	1.08	1.02	1.55	1.60	2.50	1.23
Event plane [%]	1.07	1.26	0.93	0.32	1.93	0.56	1.54	1.48
Coulomb [%]	1.81	1.97	1.92	1.87	0.56	0.47	0.82	0.59
Total [%]	4.62	6.13	3.77	3.59	5.41	5.62	5.75	3.76

Table 4.2: Summary of systematic errors for squared HBT radii of pions for four centralities. The errors at $\Delta\phi$=0, $\pi/4$, $\pi/2$, $3\pi/4$ are shown.

	λ				R_s^2			
0-20%								
$\Delta\phi$	0	$\pi/4$	$\pi/2$	$3\pi/4$	0	$\pi/4$	$\pi/2$	$3\pi/4$
Matching cut [%]	1.25	1.25	1.25	1.25	12.57	6.89	7.15	10.67
PID cut [%]	1.86	1.86	1.86	1.86	1.62	5.57	4.19	3.23
Pair cut [%]	7.60	7.60	7.60	7.60	2.29	1.97	3.76	5.66
Event plane [%]	0.96	0.96	0.96	0.96	1.81	3.33	3.01	4.63
Coulomb [%]	8.73	8.73	8.73	8.73	2.18	1.98	2.20	2.33
Total [%]	11.80	11.80	11.80	11.80	6.61	11.83	6.76	8.74
20-60%								
$\Delta\phi$	0	$\pi/4$	$\pi/2$	$3\pi/4$	0	$\pi/4$	$\pi/2$	$3\pi/4$
Matching cut [%]	2.63	2.63	2.63	2.63	13.82	17.05	7.60	7.29
PID cut [%]	0.49	0.49	0.49	0.49	5.41	4.48	5.08	5.18
Pair cut [%]	5.66	5.66	5.66	5.66	2.90	2.42	5.25	2.00
Event plane [%]	0.81	0.81	0.81	0.81	0.56	3.29	6.06	5.02
Coulomb [%]	9.25	9.25	9.25	9.25	2.67	2.33	5.05	2.41
Total [%]	10.97	10.97	10.97	10.97	6.74	8.02	13.04	9.07

	R_o^2				R_l^2			
0-20%								
$\Delta\phi$	0	$\pi/4$	$\pi/2$	$3\pi/4$	0	$\pi/4$	$\pi/2$	$3\pi/4$
Matching cut [%]	5.38	5.73	6.04	8.78	4.85	7.06	11.46	4.64
PID cut [%]	8.77	5.70	11.03	14.03	9.72	3.42	9.37	16.66
Pair cut [%]	10.85	4.44	1.63	2.95	9.09	17.27	7.03	0.30
Event plane [%]	4.17	6.89	7.61	7.95	1.39	17.04	5.50	6.88
Coulomb [%]	4.78	5.78	6.96	5.43	3.00	3.18	2.68	2.69
Total [%]	16.25	12.40	15.86	18.28	13.76	25.05	16.32	18.23
20-60%								
$\Delta\phi$	0	$\pi/4$	$\pi/2$	$3\pi/4$	0	$\pi/4$	$\pi/2$	$3\pi/4$
Matching cut [%]	15.36	2.61	8.39	5.97	9.18	3.72	1.87	8.54
PID cut [%]	8.03	0.66	0.64	1.42	6.19	8.74	8.59	9.64
Pair cut [%]	8.16	6.58	2.19	2.35	8.89	11.04	3.59	7.99
Event plane [%]	2.82	5.11	4.13	3.66	3.38	3.58	6.15	4.95
Coulomb [%]	3.55	5.23	5.60	5.77	3.00	2.49	2.61	3.50
Total [%]	15.62	11.04	8.45	7.70	13.65	14.94	11.73	17.43

Table 4.3: Summary of systematic errors for squared HBT radii of kaons for four centralities. The errors at $\Delta\phi$=0, $\pi/4$, $\pi/2$, $3\pi/4$ are shown.

4.8 Summary of Cut Conditions

Event and Track selection	
zvertex	$\mid zvertex \mid < 30$ cm
quality cut	31 $\parallel$ 63
zed cut	$\mid zed \mid < 75$ cm
p_T	$p_T \geq 0.2$ GeV/c (0.3 GeV/c for kaon)
momentum	mom ≤ 2.0 GeV/c
temc	temc < 50 ns
PC3 matching cut	$\sqrt{\Delta\phi^2 + \Delta z^2} < 2\sigma$ (3σ for kaon)
EMC matching cut	$\sqrt{\Delta\phi^2 + \Delta z^2} < 2\sigma$ (3σ for kaon)
EMC energy cut	ecent > 0.1
RICH veto cut	n0 < 4
PID cut	2σ cut from pion (kaon) peak and 2σ veto cut from kaon (pion) and proton peaks
Pair selection (pion)	
Drift Chamber	$dz_{dc} < 5$ cm && $d\phi_{dc} > 0.07$ rad $dz_{dc} < 70$ cm && $d\phi_{dc} > 0.02$ rad $dz_{dc} > 70$ cm
EMC	$dr_{emc} > 17$ cm used only pairs from different towers
Pair selection (kaon)	
Drift Chamber	$dz_{dc} < 4$ cm && $d\phi_{dc} > 0.04$ rad $dz_{dc} < 65$ cm && $d\phi_{dc} > 0.01$ rad $dz_{dc} > 65$ cm
EMC	$\sqrt{(d\phi_{emc}/0.06)^2 + (dz_{emc}/19)^2} < 1$ used only pairs from different towers

Table 4.4: Summary of cut conditions

Chapter 5

Results

5.1 Azimuthally Integrated Measurements

In this section, the experimental results on centrality and m_T dependence of HBT radii obtained from azimuthally integrated measurements are presented for charged pions and kaons.

5.1.1 Centrality and m_T Dependence for Charged Pions

Figure 5.1 shows the the m_T dependence of HBT radii for positive and negative pion pairs for four centrality bins, 0-10%, 10-20%, 20-40%, and 40-70%. The results of both charges show a good agreement in all centrality bins. The correlation functions are shown in App. A.1.

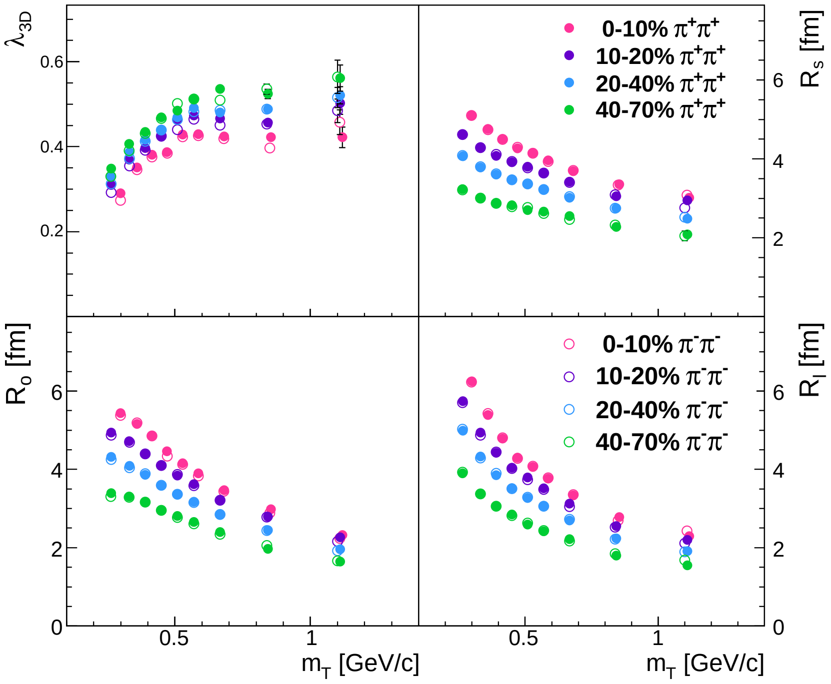

Figure 5.1: 3D HBT parameters of charged pions as a function of m_T for four centrality bins, where only the statistical errors are shown.

Consistency check with the previous result at the PHENIX experiment

We have performed the consistency check with the PHENIX result [36] with the same centrality bin as shown in Fig. 5.2. The R_s and R_o obtained in this analysis are quite consistent with the PHENIX result. The λ shows slightly smaller values compared to the PHENIX result, which is considered to be because of large background of electrons due to the photon conversion in the detector material newly installed in Run7. The R_l also shows slightly smaller values. But both are constant within the systematic uncertainties.

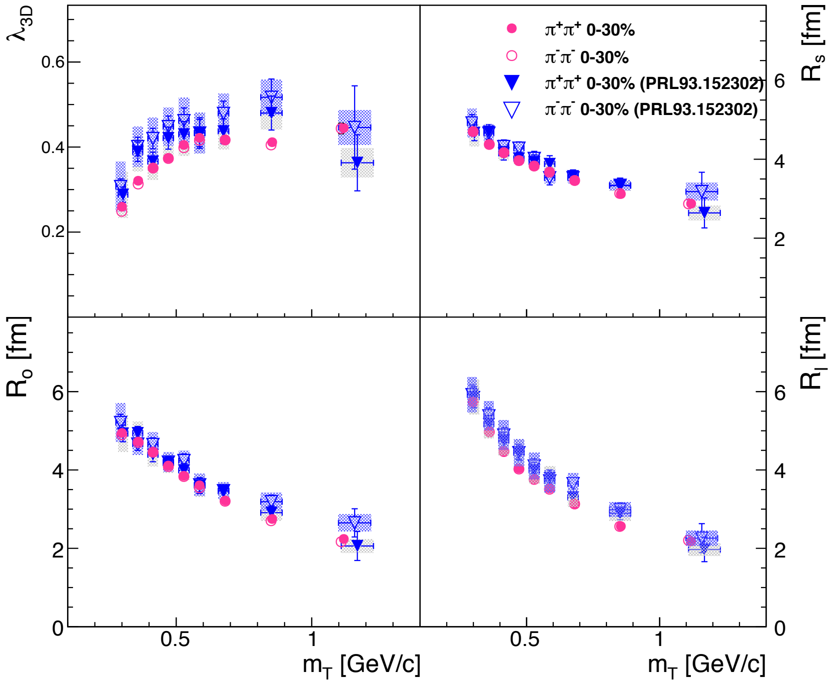

Figure 5.2: 3D HBT parameters of charged pions as a function of m_T in 0-30% with the comparison of the PHENIX result [36].

Comparison with the result from the STAR experiment

We have also compared our results with the result from the STAR experiment [62]. In 0-10%, 10-20%, both HBT radii are consistent. In peripheral collisions, although the centrality bins used in the STAR are not exactly the same as our bins, the trend of the m_T dependence show a good agreement. One can see the difference of the λ, which is similar trend to the difference in the comparison with the PHENIX result and would be the same reason described in the previous section.

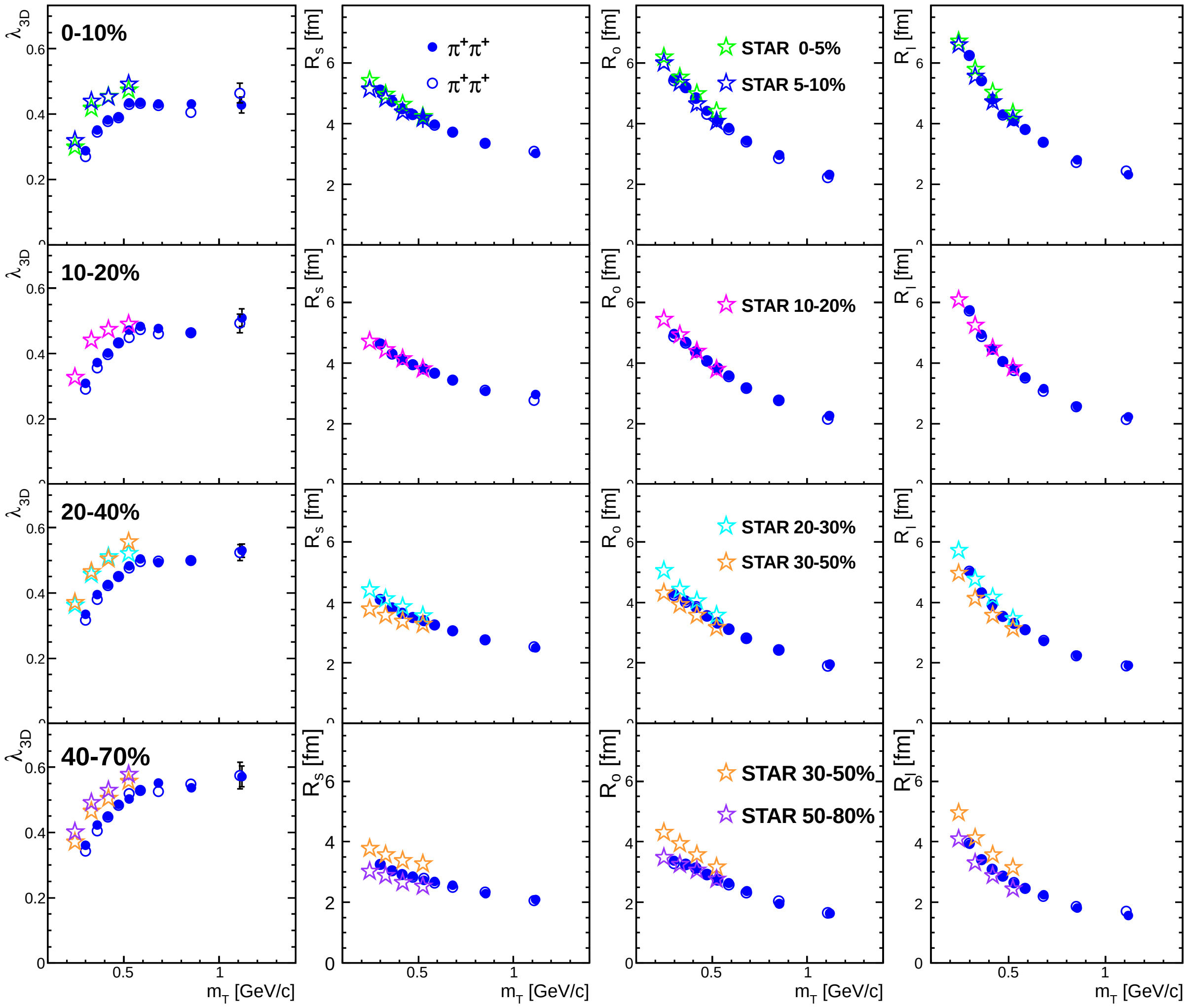

Figure 5.3: Comparison of the m_T dependence of 3D HBT parameters of charged pions with the STAR result [62].

5.1.2 Centrality and m_T Dependence for Charged Kaons

Figure 5.4 shows the m_T dependence of HBT radii for positive and negative kaon pairs for four centrality bins, where the systematic uncertainties are shown as color boxes. Both charges does not show any significant difference, but there seems to be small difference for λ and R_l in 0-10% centrality. Figure 5.5 shows the same plot for charge combined kaons. Figure 5.6 and Figure 5.7 are for four k_T and two centrality bins. The correlation functions are shown in App. A.2.

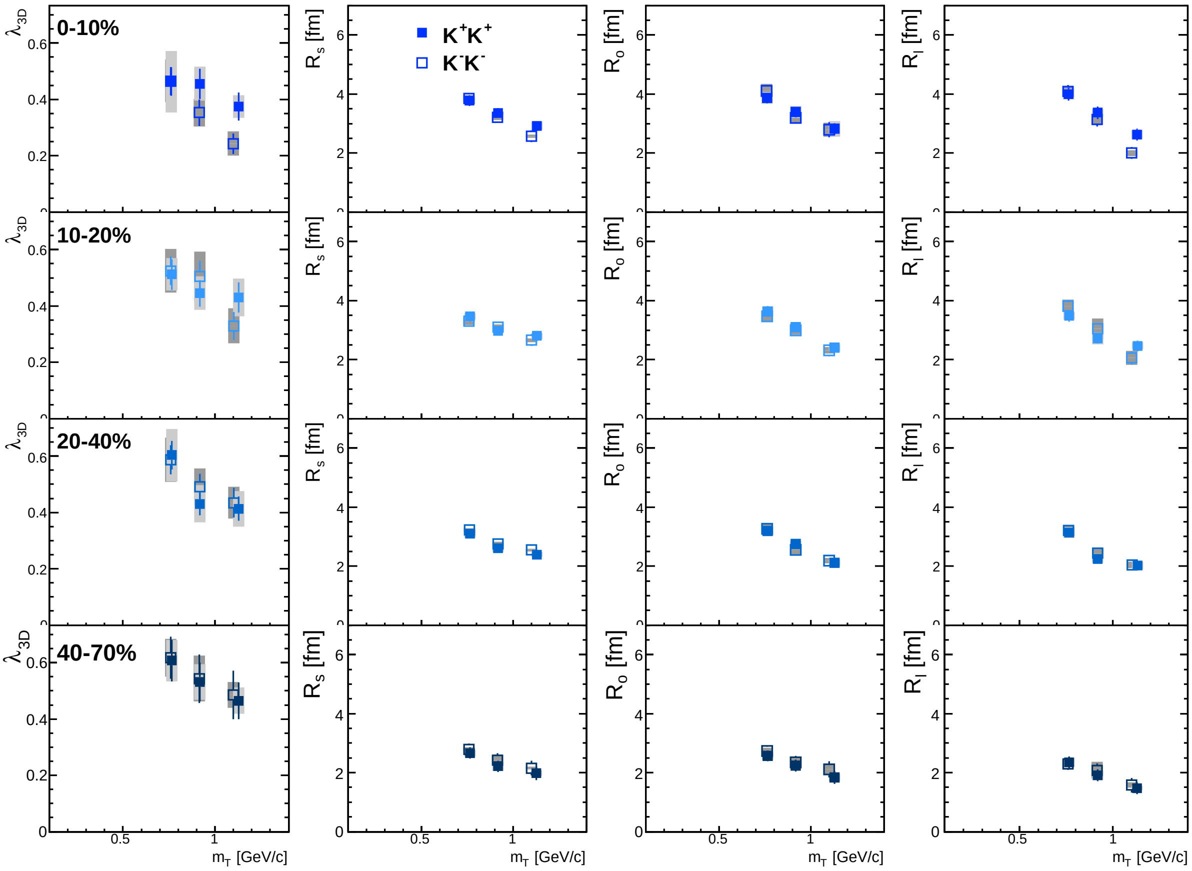

Figure 5.4: 3D HBT parameters of positive and negative kaon pairs as a function of m_T for four centrality bins.

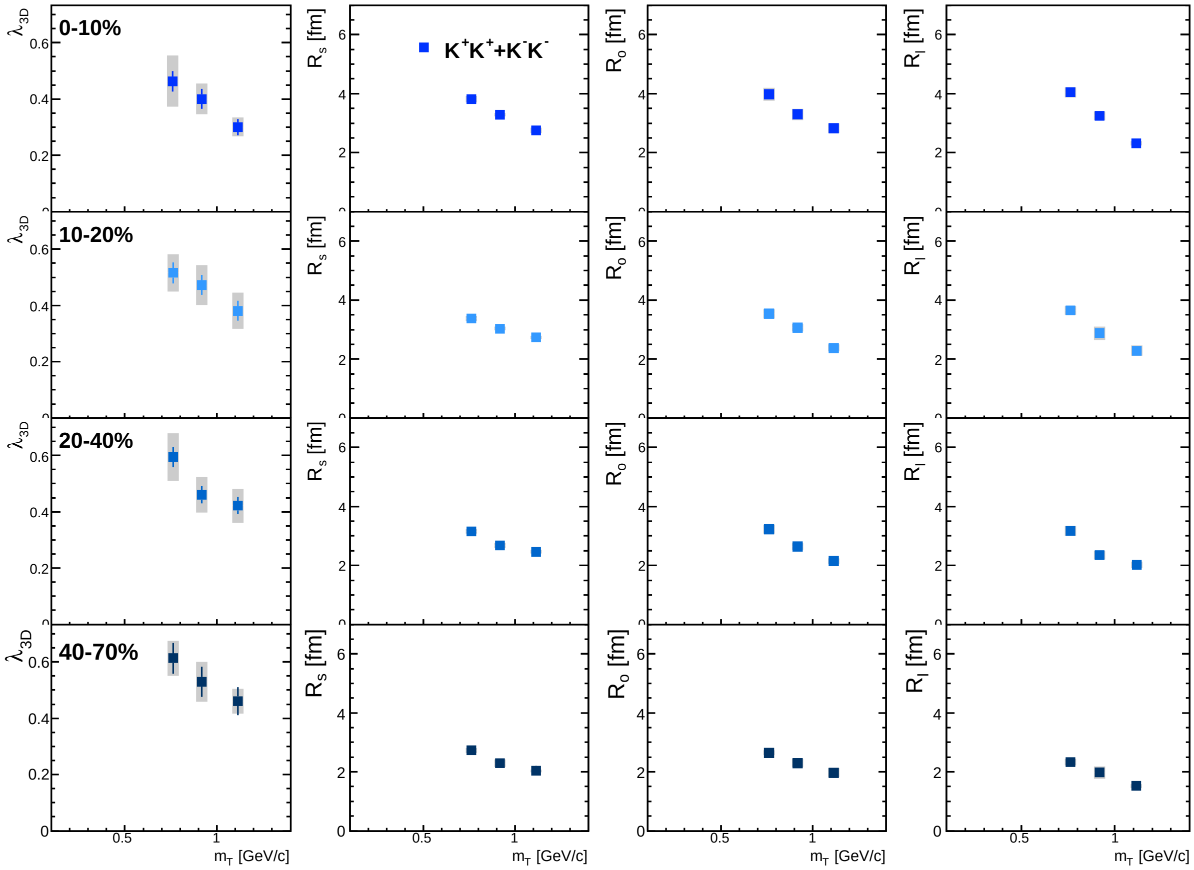

Figure 5.5: 3D HBT parameters of charged kaons as a function of m_T for four centrality bins, where positive and negative kaon pairs are combined.

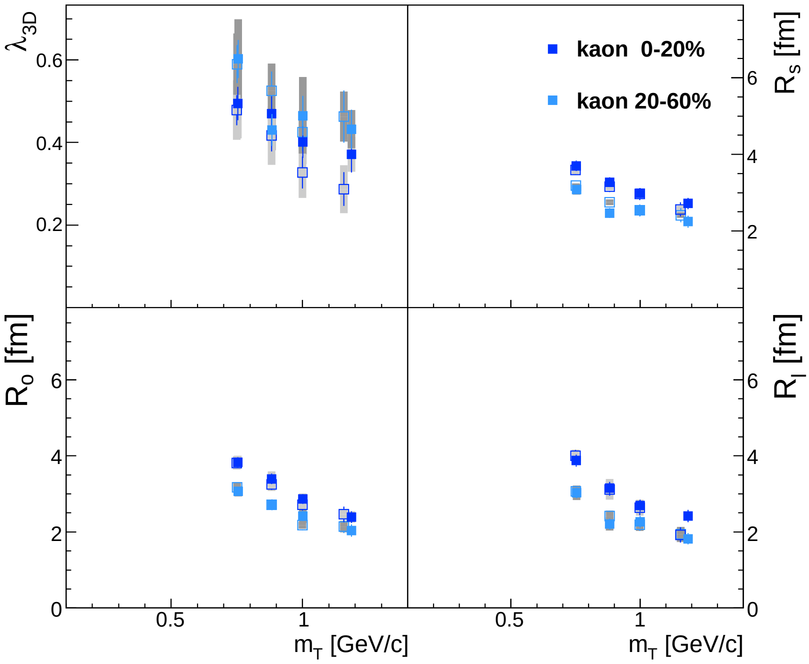

Figure 5.6: 3D HBT parameters of positive and negative kaon pairs as a function of m_T for two centrality bins.

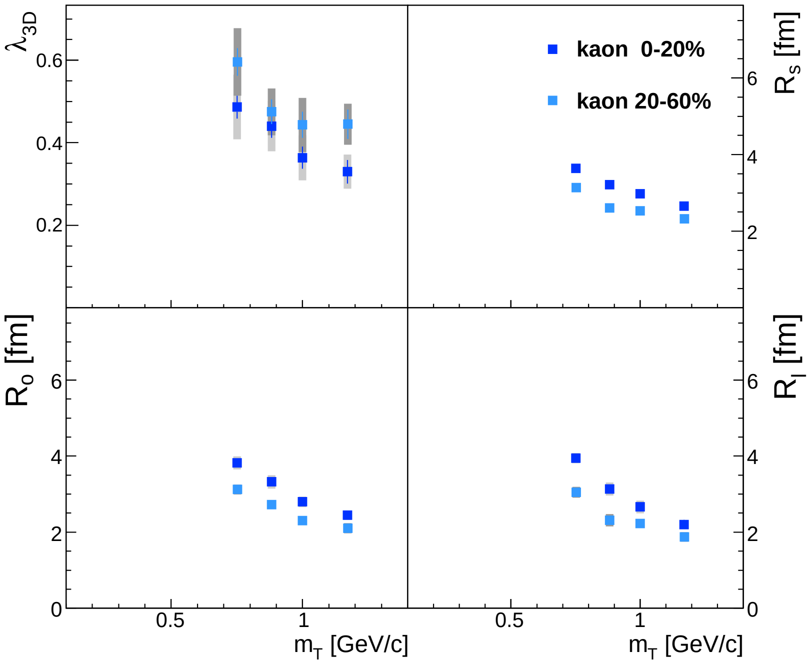

Figure 5.7: 3D HBT parameters of charged kaons as a function of m_T for two centrality bins, where positive and negative kaon pairs are combined.

5.2 Azimuthal HBT Measurement with respect to 2^{nd}-order Event Plane

5.2.1 Centrality Dependence of HBT Radii for Charged Pions

Figure 5.8 shows correlation functions of charged pions measured for $0.2 < k_T < 2.0$ GeV/c and eight azimuthal bins at four centrality bins, 0-10%, 10-20%, 20-30%, and 30-60%, without the correction of event plane resolution. These correlation functions as functions of q parameters are projections of the 3-dimensional correlation functions to each q direction, and those in the in-plane ($\Delta\phi$=0) and out-of-plane ($\Delta\phi$=$\pi/2$) directions are compared. Solid lines show the fit function with Eq. (4.36), which is also projected to each q direction. One can see the small difference of the correlation functions between the in-plane and out-of-plane directions, and the difference become clearer with centrality going from central to peripheral collisions. This difference corresponds to the different source size by azimuthal angles. The difference for R_o between the in-plane and out-of-plane directions is opposite to R_s The correlation functions with the correction of the event plane resolution are shown in Fig. A.3.1 in Appendix A.

Figure 5.10, 5.9 show the extracted 3D HBT radii of charged pions as a function of azimuthal pair angle with respect to 2^{nd}-order event plane Φ_2 for four different centralities with and without systematic uncertainties. Open symbols at $\phi - \Psi_2 = \pi$ are the same values with those at $\phi - \Psi_2 = 0$. The oscillations of R_s^2, R_o^2, and R_{os}^2 are clearly seen. For a boost-invariant system, the azimuthal angle dependence of HBT radii is expressed with the cosine and sine series functions [67]:

$$\begin{aligned} R_\mu^2(\Delta\phi) &= R_{\mu,0}^2 + 2\sum_n R_{\mu,n}^2(\Delta\phi)\cos(n\Delta\phi) \\ R_{os}^2(\Delta\phi) &= 2\sum_n R_{os,n}^2(\Delta\phi)\sin(n\Delta\phi) \end{aligned} \tag{5.1}$$

where $R_{\mu,n}^2$ is the n^{th}-order Fourier coefficients, μ denotes each direction in the Bertsch-Pratt parameterization (μ= o, s, l), and $\Delta\phi = \phi - \Psi_2$. The sums over n run from $n = 2$ for even values. The $R_{\mu,0}$ represents the average of HBT radius which should be the same as the radius obtained by the azimuthally integrated analysis.

The oscillation strength of R_s^2 increases with increasing centrality, which corresponds to the change of elliptical shape of the spatial distribution of participants with centrality going from central to peripheral collisions. In all centrality region, the oscillation strength of R_o^2 seems to be larger than that of R_s^2. Especially in centrality 0-10%, R_s^2 is almost flat, while R_o^2 has a strong oscillation.

As we already discussed, R_o contains the terms of the flow and the emission duration in addition to the geometrical term as shown in Eq. (2.20) and Eq. (2.37). Therefore this can be understood as the effect of the emission duration or flow anisotropy on R_o^2. The detailed discussions are described in the next chapter.

5.2.2 Centrality Dependence of HBT Radii for Charged Kaons

Figure 5.11 shows correlation functions of charged kaons for $0.3 < k_T < 2.0$ GeV/c in two centrality bins. Three dimensional correlation functions are projected over the lowest 50 MeV/c along the orthogonal directions. Solid lines show fit functions with Eq. (5.1). Correlation function measured at in-plane and out-of-plane directions are compared in this figure. Although the statistical uncertainties are large, the small difference of the width for both correlation functions can be seen.

The correlation function with the correction of the event plane resolution are shown in Fig. A.18 in Appendix A. Figure 5.12 shows the extracted 3-dimensional HBT radii of charged kaons as a function of azimuthal pair angle with respect to 2^{nd}-order event plane. In order to make the fit stable, we follow the technique used in [62]. The λ parameter is determined in the first fit for each azimuthal bin and averaged over azimuthal bins, then the fitting is performed again with the fixed λ value.

As well as charged pions, the oscillation can be seen for R_s^2, R_o^2, and R_{os}^2. In 0-20%, the oscillation amplitude of R_o^2 seems to be larger than that of R_s^2 though the systematic uncertainty of R_o is large, which is the same trend as charged pions. However the average of R_o^2 seems to be equal to or less than that of R_s^2 unlike the result of charged pions. In 20-60%, the oscillation of R_s^2 seems to be larger than that of R_o^2. Detailed comparison between charged pions and kaons is discussed in the next section.

5.2.3 k_T Dependence of HBT Radii for Charged Pions

As well as the centrality dependence of HBT radii, the k_T dependence have been studied for charged pions with six k_T bins and two centrality bins. The azimuthal angle is divided to four bins. Figure 5.13 shows the squared HBT radii as a function of $\phi - \Psi_2$ with the systematic uncertainties shown as open bands of two solid lines. Figure 5.14 also shows the squared HBT radii with fit lines by Eq. (5.1).

5.2.4 Comparison with Previous Results

In order to make sure the consistency of this analysis and published results, we have compared our results with results from the PHENIX experiment. Figure 5.15 shows the 3D HBT parameters as a function of $N_{part}^{1/3}$ calculated by Glauber model, where the circle symbols show the average of azimuthally Ψ_2 dependent HBT parameters for charged pions and kaon shown in Fig. 5.9 and Fig. 5.12. The square symbols show the results of azimuthally integrated analysis for both species published from the PHENIX experiment [36, 66]. The filled band shows those systematic uncertainties. The radii obtained in this analysis show good agreements with PHENIX results. The parameter λ obtained in this analysis seems to be slightly smaller than that in PHENIX experiment. It is known that the λ parameter is sensitive to the ratio of signal and background in identical particle pairs. The smaller value of the λ will be due to the increase of background like electrons from the conversion in Run7 data compared to in Run2 data which is used in [36].

Figure 5.16 shows the 3D HBT radii as a function of average m_T for two centrality regions, where the radii are the average of azimuthally Ψ_2 dependent HBT radii shown in Fig. 5.13. The results from azimuthally integrated analysis in STAR experiment [62] are compared. Because the centrality regions in both analysis are different, the absolute values of radii are different, but the slopes of m_T dependence in this analysis show the same as those in the result of STAR experiment.

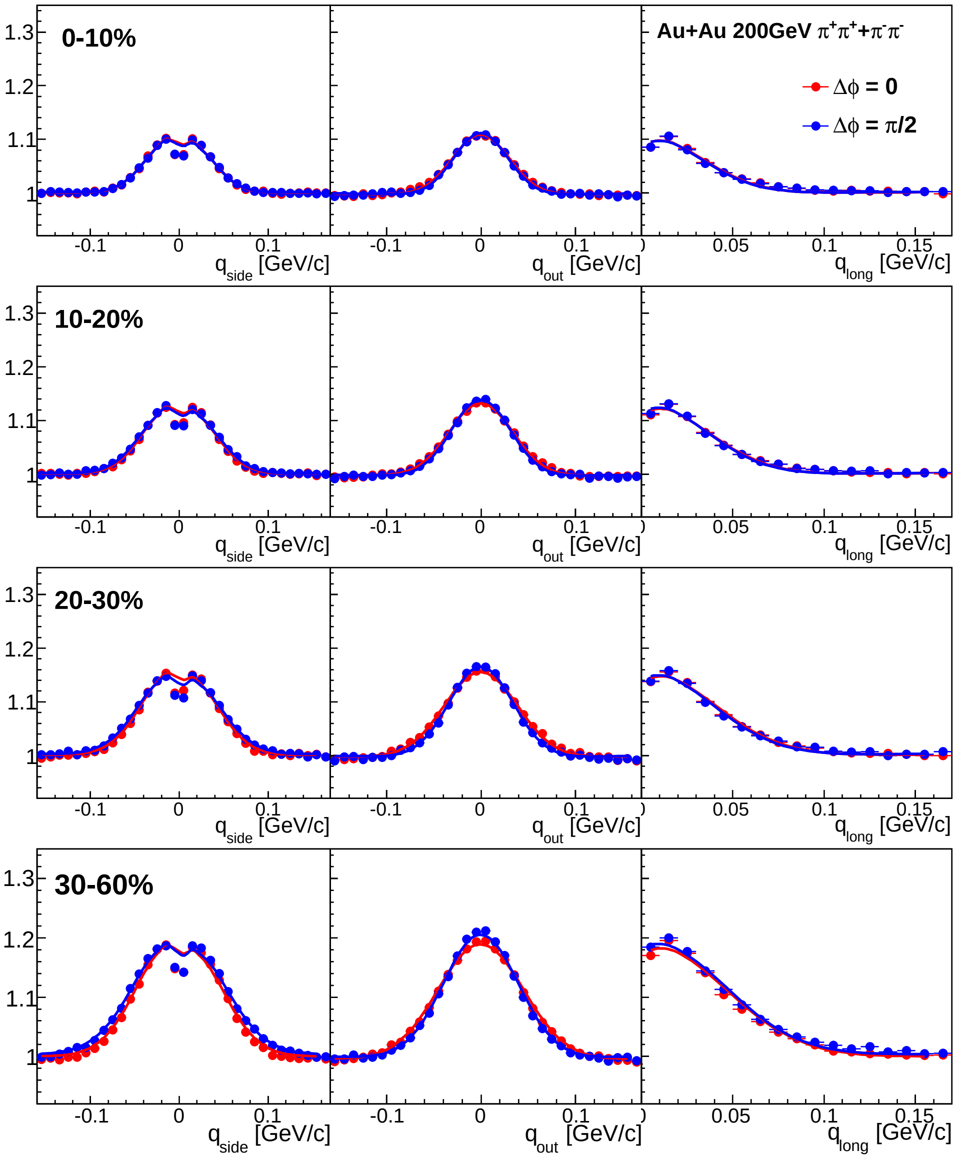

Figure 5.8: Projected 3D correlation functions of charged pion pairs in $0.2 < k_T < 2.0$ GeV/c at four centrality bins without the correction of the event plane resolution. Correlation functions at $\Delta\phi = 0$ (red symbol) and $\Delta\phi = \pi/2$ (blue symbol) are shown. Correlation functions are projected along each q directions with $q_{other} < 50$ [MeV/c]. Solid lines show the fit functions by Eq. (4.36), which is also projected in the same way.

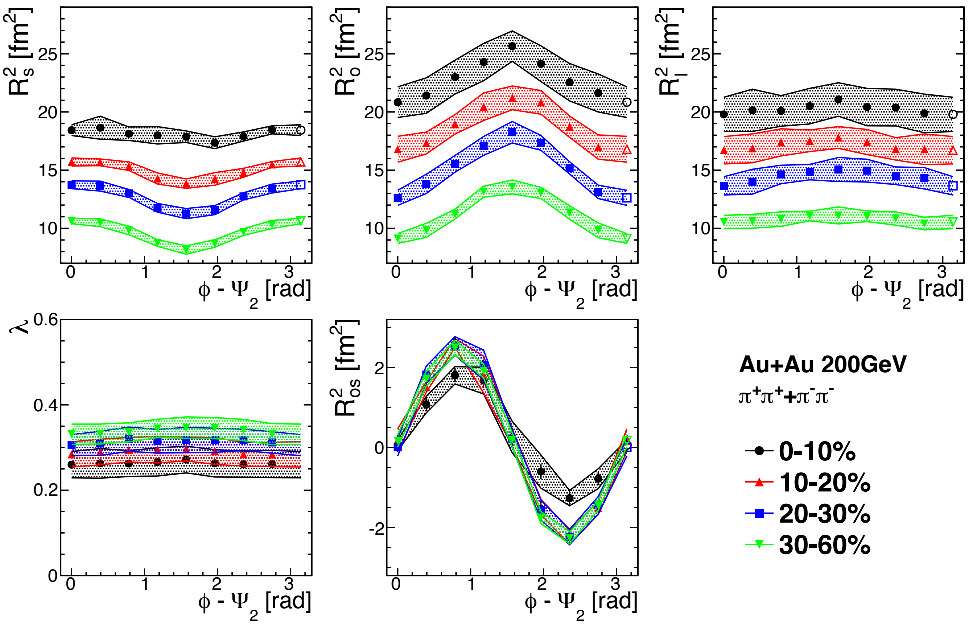

Figure 5.9: Extracted HBT parameters of charged pions in $0.2 < k_T < 2.0$ GeV/c as a function of azimuthal pair angle with respect to 2$^{\text{nd}}$-order event plane for four centrality bins with systematic uncertainties (shaded bands). The data point at $\Delta\Phi = \pi$ is the same value as the data at $\Delta\Phi = 0$.

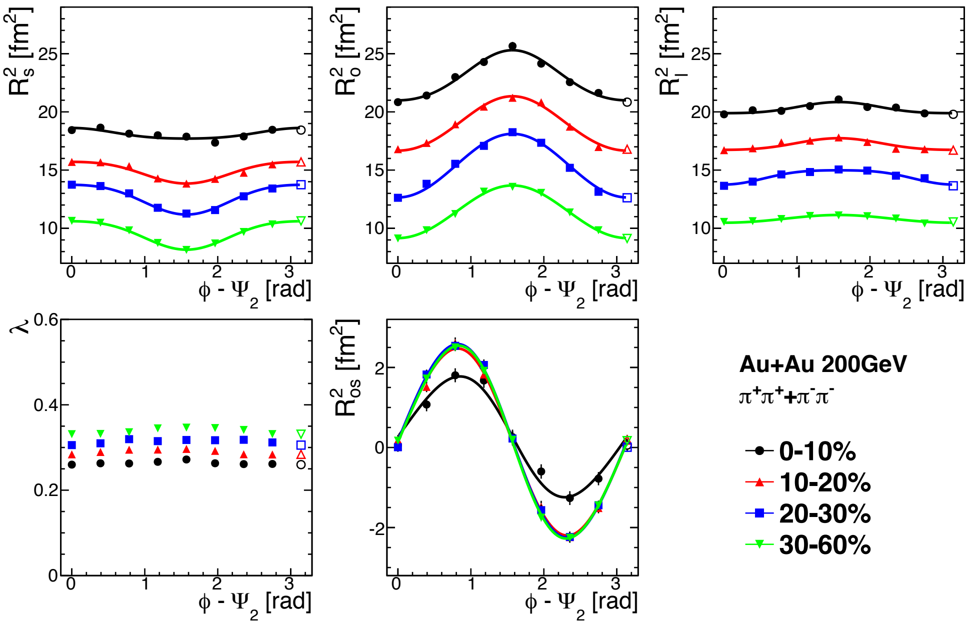

Figure 5.10: Extracted HBT parameters of charged pions in $0.2 < k_T < 2.0$ GeV/c as a function of azimuthal pair angle with respect to 2$^{\text{nd}}$-order event plane for four centrality bins. The data point at $\Delta\Phi = \pi$ is same value at $\Delta\Phi = 0$. Solid lines depict fit functions by Eq. (5.1).

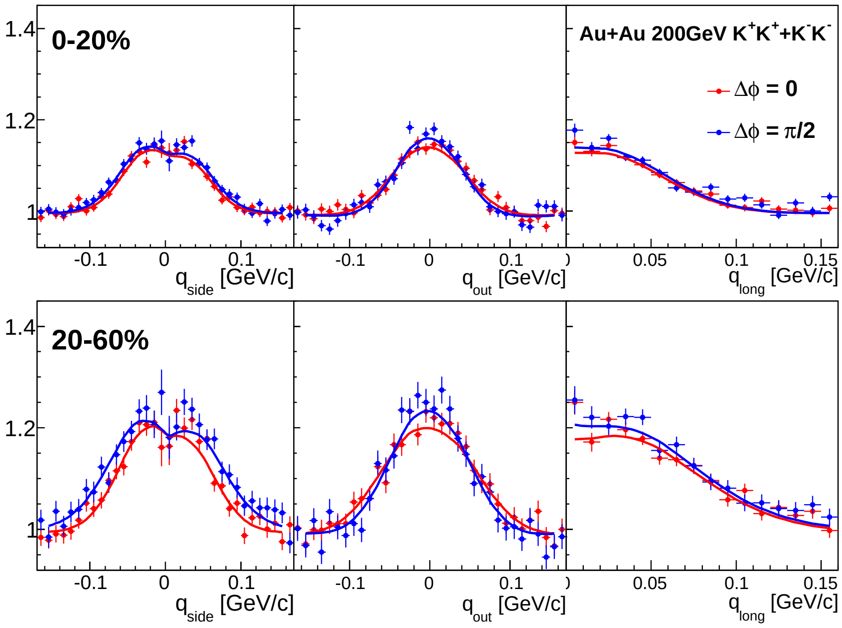

Figure 5.11: Projected 3D correlation functions of charged kaon pairs in $0.3 < k_T < 2.0$ GeV/c at 0-20% and 20-60% centrality without the correction of the event plane resolution. Correlation functions at $\Delta\phi = 0$ (red symbol) and $\Delta\phi = \pi/2$ (blue symbol) are shown. Correlation functions are projected along each q directions with $q_{other} < 50$ [MeV/c]. Solid lines show the fit functions.

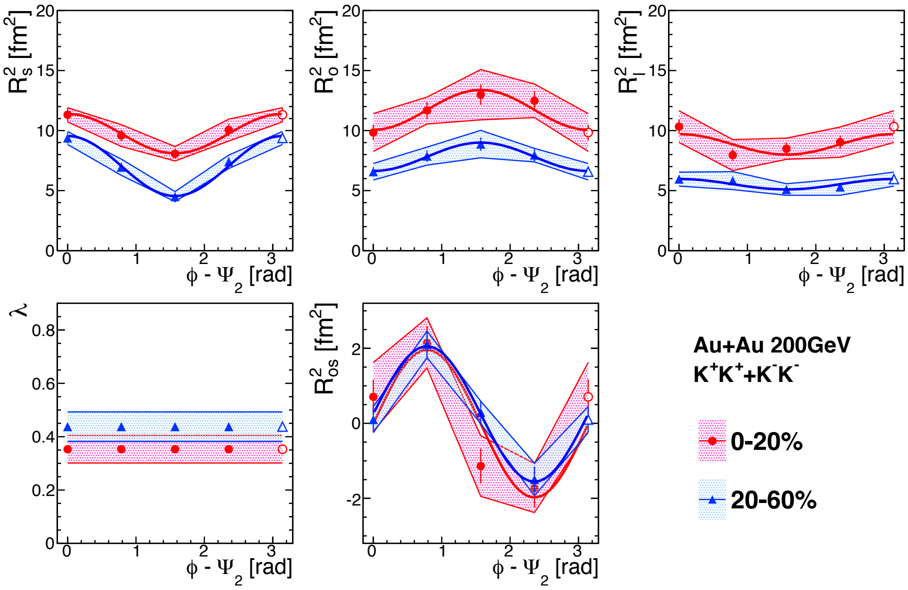

Figure 5.12: Extracted HBT parameters of charged kaons in $0.3 < k_T < 2.0$ GeV/c as a function of azimuthal pair angle with respect to 2^{nd}-order event plane in two centrality bins, where shaded bands show the systematic uncertainties. The data point at $\Delta\Phi = \pi$ is the same value at $\Delta\Phi = 0$. Solid lines depict the fit function by Eq. (5.1)

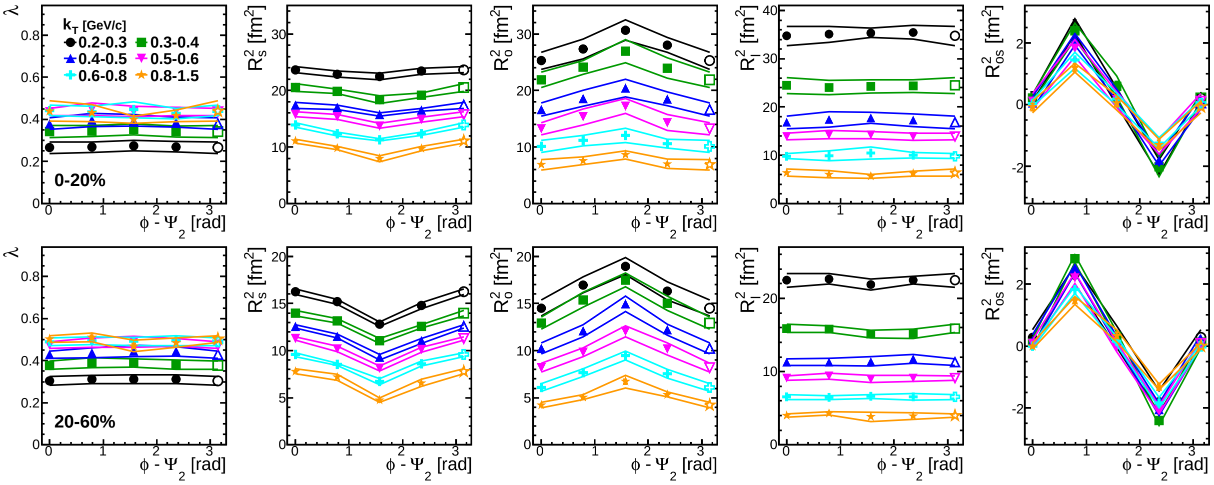

Figure 5.13: Extracted HBT parameters of charged pions as a function of azimuthal pair angle with respect to 2$^{\mathrm{nd}}$-order event plane for six k_T bins. Solid band lines represent systematic uncertainties. The data point at $\Delta\Phi = \pi$ is the same value at $\Delta\Phi = 0$.

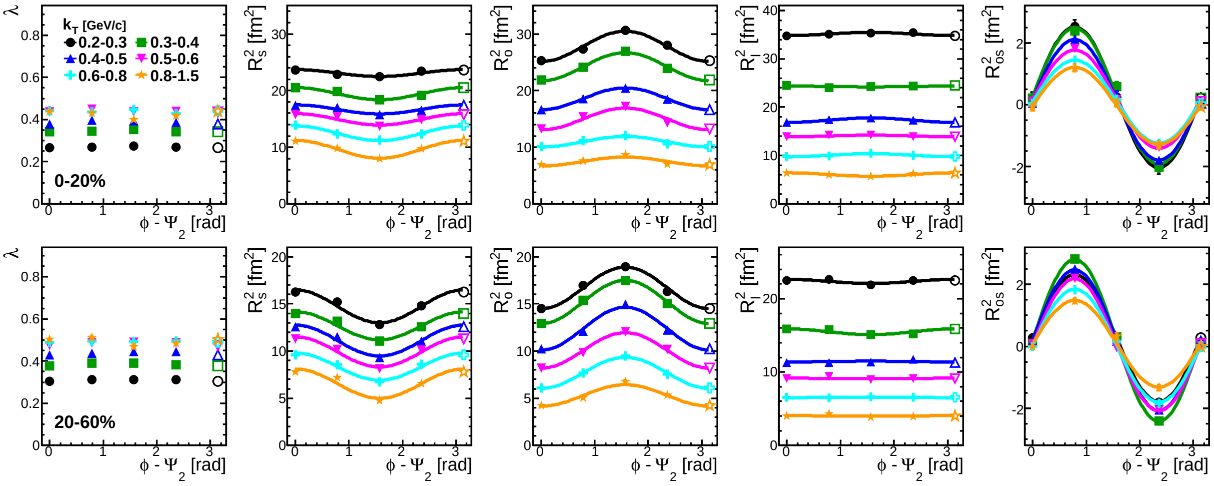

Figure 5.14: Extracted HBT parameters of charged pions as a function of azimuthal pair angle with respect to 2$^{\mathrm{nd}}$-order event plane for six k_T bins with fit functions by Eq. (5.1). The data point at $\Delta\Phi = \pi$ is the same value at $\Delta\Phi = 0$.

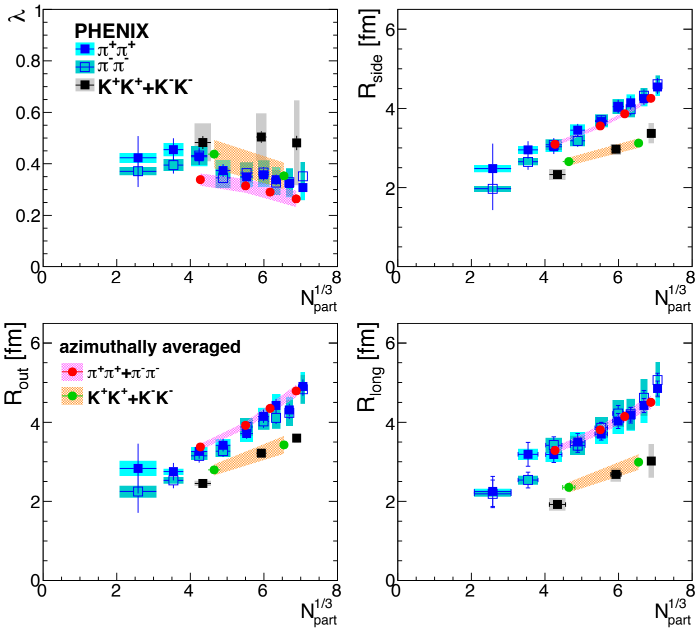

Figure 5.15: 3D HBT parameters of charged pions and kaons as a function of $N_{part}^{1/3}$. Averages of HBT parameters measured in different azimuthal angle with respect to Ψ_2 are compared with the results of azimuthally integrated analysis published in the PHENIX experiment [36, 66], where color bands represent the systematic uncertainties.

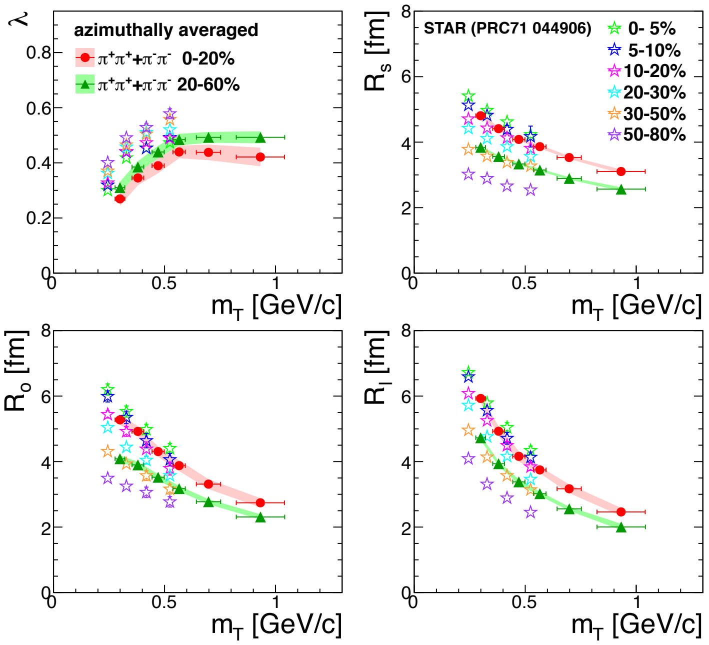

Figure 5.16: 3D HBT parameters as a function of average m_T. Averages of HBT parameters measured in different azimuthal angle with respect to Ψ_2 are compared with the results of azimuthally integrated analysis published in the STAR experiment [62], where color bands represent the systematic uncertainties.

5.3 Azimuthal HBT Measurement with respect to $3^{\rm rd}$-order Event Plane

5.3.1 Centrality Dependence of HBT Radii for Charged Pions

Figure 5.17 shows the extracted squared HBT radii as a function of $\phi - \Psi_3$, where the color bands represent the systematic uncertainties. Data points at $\phi - \Psi_3$=$2\pi/3$ is the same as data points at $\phi - \Psi_3$=0. Solid lines show fit functions by Eq. (5.1), where $\Delta\phi$=$\phi - \Psi_3$ and the summation over n takes $n = 3, 6$. Although R_o^2 seems to be asymmetry with respect to $\phi - \Psi_3 = \pi/3$ and the systematic uncertainties are large, they seem to have a peak around $\phi - \Psi_3 = 1.3$ in all centralities, which results in finite values of $R_{o,3}^2$. On the other hand, R_s^2s show almost non-oscillation or a slightly small oscillation with the same sign as R_o^2 unlike Ψ_2 dependence. Detailed discussion about their amplitudes is described in the next chapter. The correlation functions at $\phi - \Psi_3$=0, $\pi/3$ without and with the correction of the event plane resolution are shown in Fig. A.19 and Fig.A.19 in Appendix A.

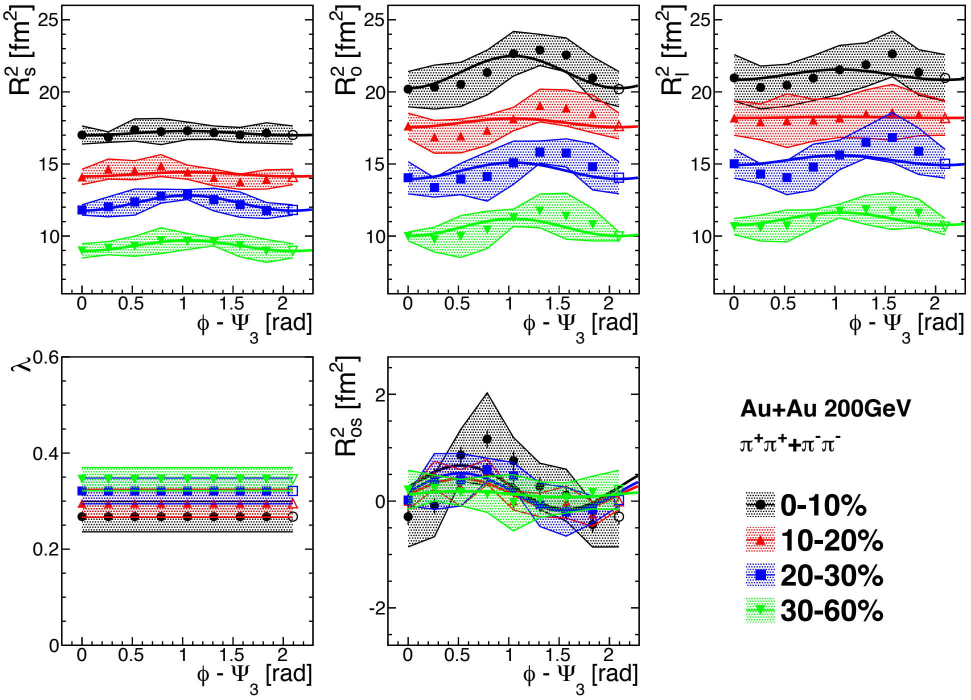

Figure 5.17: Extracted HBT parameters of charged pions in $0.2 < k_T < 2.0$ GeV/c as a function of azimuthal pair angle with respect to $3^{\rm rd}$-order event plane for four centrality classes, where shaded bands show the systematic uncertainties. The data point at $\phi - \Phi = 2\pi/3$ is same value at $\phi - \Phi = 0$. The solid lines depict the fit functions by Eq. (5.1).

5.3.2 k_T Dependence of HBT Radii for Charged Pions

Figure 5.18 shows squared 3D HBT radii as a function of azimuthal pair angle with respect to $3^{\rm rd}$-order event plane for five k_T bins and two centrality bins. Left four panels show the result for 0-20% centrality, and right panels for 20-60% centrality. R_s^2 does not show any significant k_T dependence for both centralities, while R_o^2 seems to have a small oscillation with the same sign in all k_T bins for both centralities. As well as the study of azimuthal HBT measurement for kaons, the λ is fixed by twice iterative fits for the stability of the fit. The values of λ are shown in Fig. 5.19.

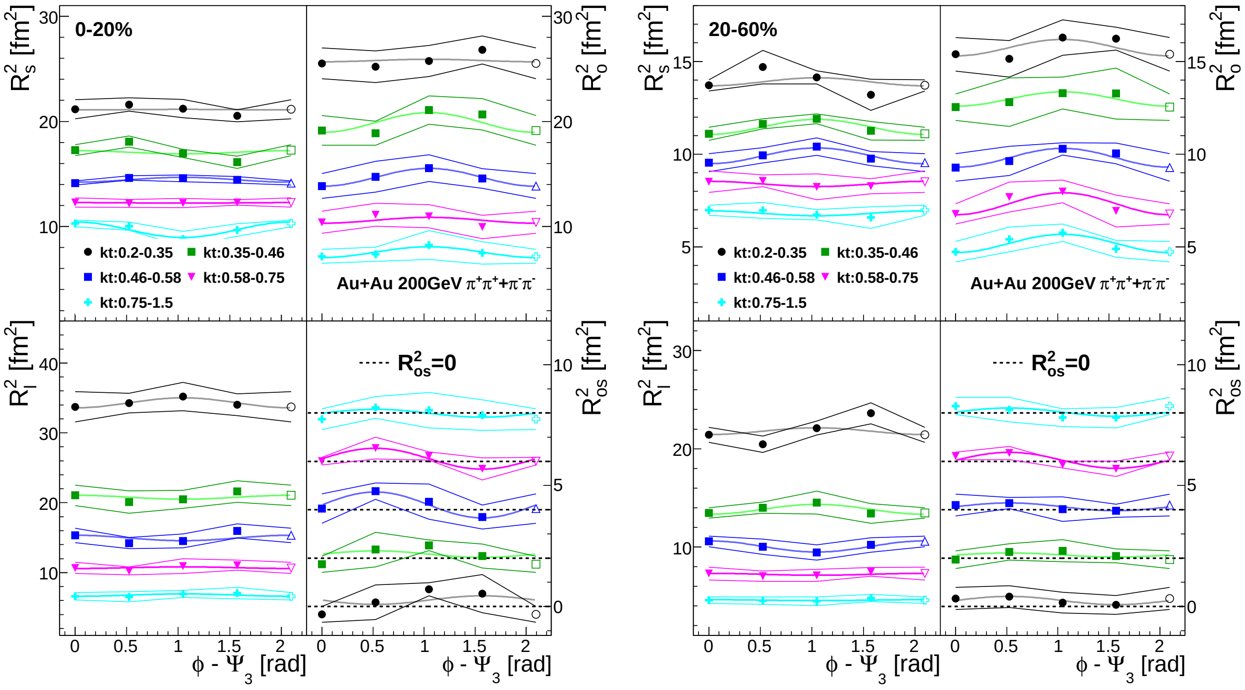

Figure 5.18: 3D HBT radii of charged pions as a function of azimuthal pair angle with respect to 3^{rd}-order event plane for five k_T bins and two centrality bins, 0-20% (Left) and 20-60% (Right). The data point at $\phi - \Phi = 2\pi/3$ is the same value at $\phi - \Phi = 0$. Band consisting of two thin lines represent the systematic uncertainties and normal solid lines depict the fit functions by Eq.(5.1). The R_{os}^2 is plotted with respect to the base line of R_{os}^2=0 (dashed lines).

5.3.3 Comparison with Previous Results

Although the HBT radii have been measured with respect to Ψ_3, the average of the radii should be the same as the azimuthally integrated analysis as well as the Ψ_2 dependence. We have compared the average HBT parameters from our result of Ψ_3 dependence, with the previous result from PHENIX experiment which is obtained from azimuthally integrated analysis [36] . Figure 5.19 shows the comparison of both results. As well as the comparison in Fig. 5.15, both are consistent within systematic uncertainties.

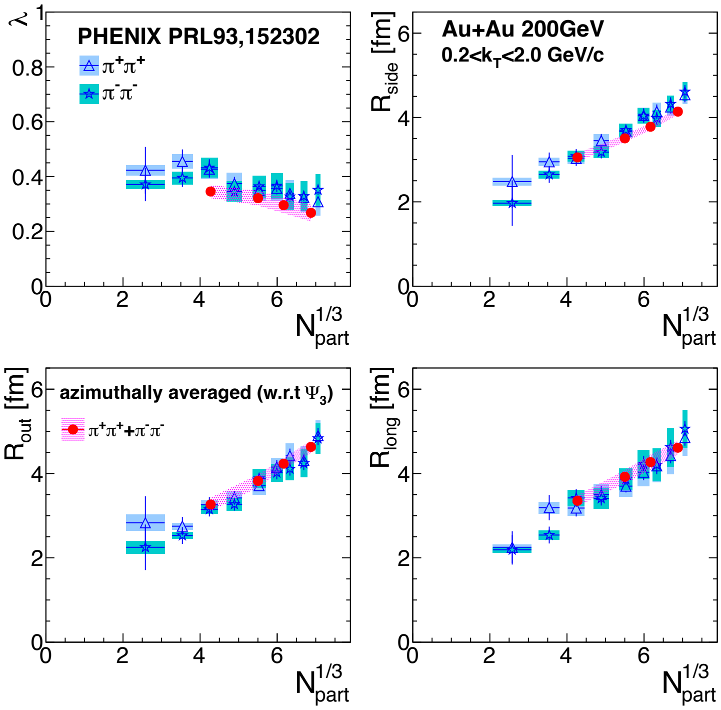

Figure 5.19: 3D HBT radii of charged pions as a function of $N_{part}^{1/3}$. Averages of azimuthally Ψ_3 dependent radii are compared with the results of azimuthally integrated analysis published in PHENIX [36]. Color bands show the systematic uncertainties.

Chapter 6

Discussion

6.1 Particle Species Dependence of HBT Radii

It is known that charged pions are much affected by the rescattering among hadrons and the decay of long-lived particles, while charged kaons have less interaction cross section and less affected by the decay particles. Therefore kaons may carry purer information on the particle emitting source and could be a probe of earlier stage of the collisions compared to pions. In the past study at the PHENIX experiment, there was no significant difference of HBT radii between charged pions and kaons [66]. However, there seems to have been small difference of R_o/R_s. Although it was difficult to study the centrality and m_T dependence of charged kaons in detail due to limited statistics, the Run-7 data set allows us to achieve such systematic study for charged kaons.

Figure 6.1 shows the comparison of m_T dependence of HBT radii between charged pions and kaons for four centrality bins. The R_s shows a good agreement between pions and kaons, while R_o and R_l of kaons show slightly larger values than those of pions. The difference increases with centrality going from peripheral to central collisions. R_o contain information on the emission duration, and R_o and R_l are also related to the freeze-out time under the hydrodynamic model as shown in Eq. (2.37), (2.38). Therefore this results may intuitively indicate that those temporal quantity during the system evolution is different between pions and kaons. Figure 6.2 shows the ratio of R_o and R_s, which is used as a quantity to roughly see the emission duration. There is no significant centrality dependence for both species, but the values of kaons are larger than those of pions in all centrality bins.

As shown in Fig. 5.4, there is no significant difference between positive and negative kaons. It is known that positive kaons have less the interaction cross section on nucleons by a factor of 4 compared to negative kaons (σ_{total} ~10 mb for positive kaons and ~40 mb at p = 0.5 GeV/c [63]). Therefore the difference of HBT radii between pions and kaons may not be due to the different hadronic cross section.

A recent theoretical model called the hydrokinetic model (HKM) [65] expects that the R_o and R_l of kaons are larger than those of pions at lower m_T. The HKM incorporates more realistic conditions such as, the initial condition like the Glauber model, the pre-thermal flow, the crossover transition, microscopic transport, and the effect of viscosity. The m_T dependence of pion HBT radii is reproduced by that model. In that calculation, some of kaons leave the system later than pions at the same m_T, which may indicate a longer emission duration of kaons. However it is still unclear by what that effect is driven.

The comparison of pions and kaon is discussed further in the context of a Blast-wave model study in Sec. 6.3.

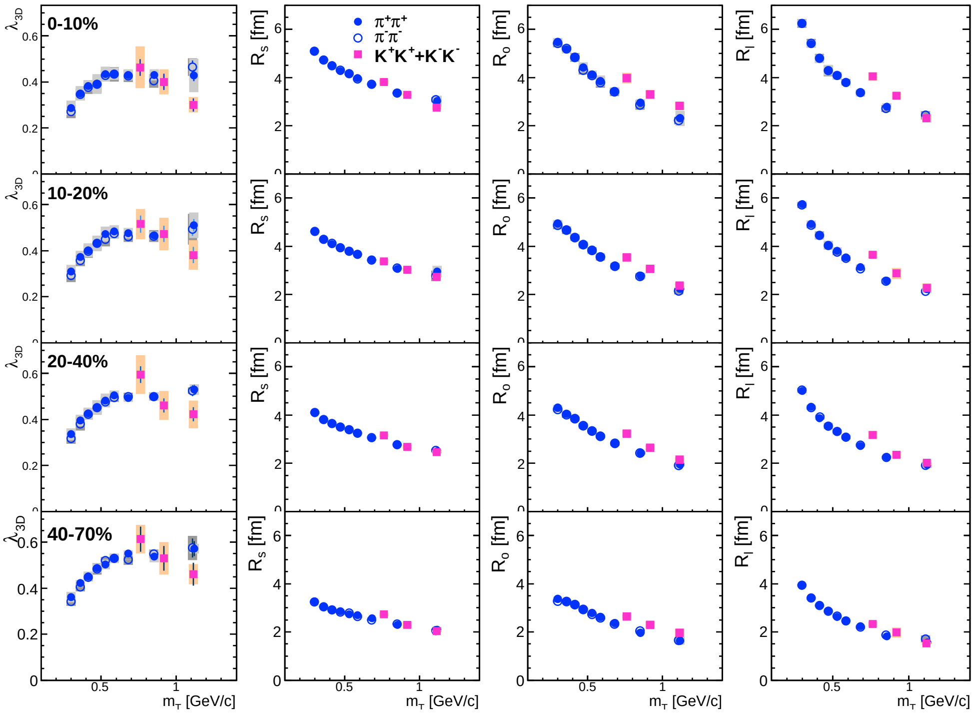

Figure 6.1: Comparison of m_T dependence of HBT radii between charged pions and kaons for four centrality bins.

6.2 Final Source Eccentricity

It is important to study the relation between final freeze-out eccentricity and initial spatial eccentricity in order to understand the space-time evolution in heavy ion collisions. We use the initial eccentricity $\varepsilon_{initial}$ obtained by a Monte-Carlo Glauber simulation as the quantity which indicates the elliptical shape of the source in initial state. Final eccentricity is extracted from the oscillation amplitude of HBT radii relative to 2^{nd}-order event plane by the Blast-wave model approach [67]. That model suggests that in case of vanishing space-momentum correlations, that is in static source, the eccentricity is given by

$$\varepsilon = 2\frac{R_{s,2}^2}{R_{s,0}^2} = -2\frac{R_{o,2}^2}{R_{s,0}^2} = 2\frac{R_{os,2}^2}{R_{s,0}^2}, \tag{6.1}$$

where $R_{\mu,n}$ is the Fourier coefficients in Eq. (5.1) and obtained by fitting the azimuthal angle dependence of HBT radii with Eq. (5.1). Especially $R_{s,n}$ is more suitable for the estimation of final eccentricity because R_s doesn't include any temporal information unlike R_o, R_{os}. We need to note that in more realistic case when there is collective expansion of the source, the final eccentricity $\varepsilon_{final} \approx 2R_{s,2}^2/R_{s,0}^2$ has about 30% uncertainties evaluated in [67] because the source size extracted by the HBT measurement does not represent the whole size but the homogeneity length of the source. This approximation would be more appropeate at lower k_T because HBT radii become the whole source size in the limit of $k_T = 0$ within the hydrodynamics.

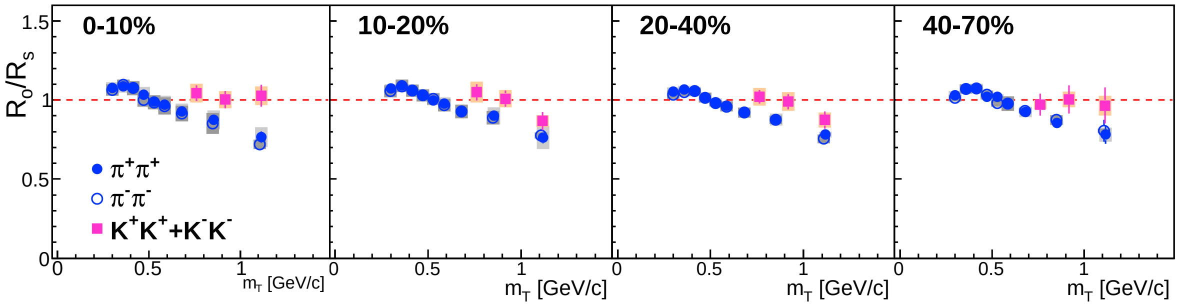

Figure 6.2: Comparison of R_o/R_s between charged pions and kaons.

6.2.1 Initial Eccentricity vs Final Eccentricity

Figure 6.3 shows final eccentricity of charged pions and charged kaons as a function of initial eccentricity. Result for charged pions in this analysis is consistent with the result from the STAR [64] experiment within systematic uncertainties. In this analysis the pion pairs in $0.2 < k_T < 2.0$ GeV/c ($\langle k_T \rangle \approx 0.54$ GeV/c) are analyzed to get more statistics. In the analysis of [64], the final eccentricity was determined as the average of three k_T bins ($0.15 < k_T < 0.25$, $0.25 < k_T < 0.35$, $0.35 < k_T < 0.60$ GeV/c). The consistency with the STAR experiment would indicate that our result is dominated by the pairs with lower k_T ($\sim$0.54 GeV/c) and the approximation of final eccentricity is held in our analysis. Final eccentricity of charged pions increases with increasing initial eccentricity, that is, with centrality going from central collision to peripheral one, while the final eccentricity is about half of initial eccentricity. It indicates that the source expands to in-plane direction with the large elliptic flow, while it still has elliptical shape at freeze-out because the final eccentricity has finite value. In other words, it indicates that the expansion time is not long enough to vanish the initial eccentricity. On the other hand, final eccentricity of charged kaons is larger than that of charged pions and close to initial eccentricity.

Here we need to note that the average k_T of kaons is larger than that of pions. The HBT radius has k_T dependence as shown in the previous section and the emission region of pairs with higher k_T corresponds to the region closer to the surface of the source under the picture of the radial flow. Therefore the ε_{final} also depends on the k_T. To make it clear whether the difference is due to the different average k_T between both particle species, we discuss the difference by comparing the ε_{final} for both species at the same m_T in the next section.

Figure 6.4 shows the oscillation amplitudes for several combinations of HBT radii for charged pions and kaons following the similar definitions of Eq. (6.1) as a function of the initial eccentricity. Left top panel is the same as Fig. 6.3. These oscillation amplitudes other than $2R_{s,2}^2/R_{s,0}$ would also reflect the spatial eccentricity at final state, and would additionally contain the temporal information and more sensitive contribution from the collective flow compared to R_s (e.g. see Eq. (2.37)). There is no significant difference between both species except R_s and R_l. The amplitudes including the temporal information, such as R_o and R_{os}, show the similar trends that the values in all central regions are larger than the values of R_s for pions. Especially in most central collisions, the amplitudes of R_o has finite value with although the ε_{final} is almost close to zero from R_s. Under the assumption that R_o and R_s have the same spatial information, that result may indicate that spatial eccentricity is quite small, but the emission duration of particles has azimuthal dependence or the flow anisotropy makes the oscillation only for R_o and R_{os} because R_o explicitly has those

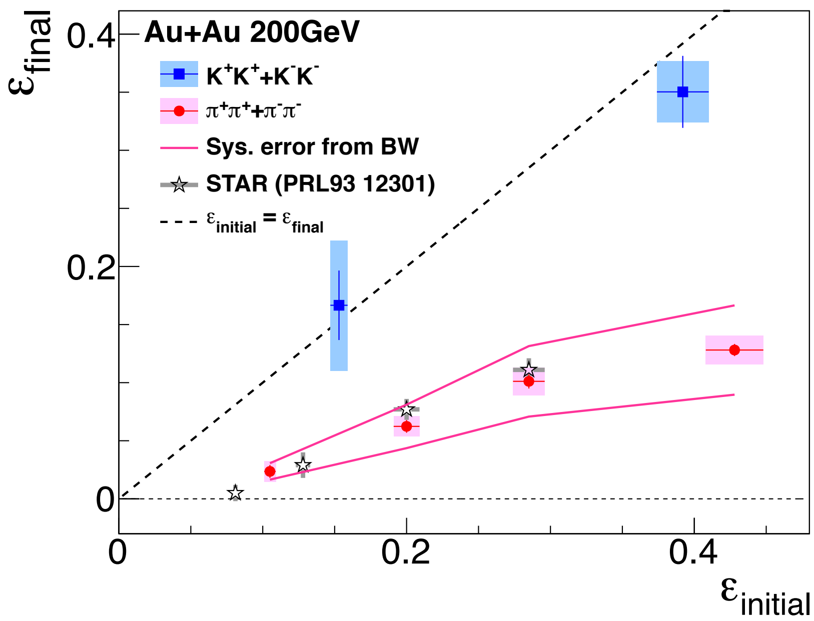

Figure 6.3: Initial eccentricity vs final eccentricity for charged pions and kaons. The k_T ranges are $0.2 < k_T < 2.0$ GeV/c for pions and $0.3 < k_T < 2.0$ GeV/c for kaons. The initial eccentricity is calculated by a Monte-Carlo Glauber simulation, where color bands shows the systematic uncertainties. A band consisting of two solid lines represents the 30% systematic uncertainties derived from the definition of the final eccentricity [67]. Result for pions measured by STAR [64] experiment is also shown. Dashed line shows $\varepsilon_{initial} = \varepsilon_{final}$.

dependence as shown in Eq. (2.20) and Eq. (2.37).

6.2.2 m_T Dependence of Final Eccentricity

As shown in the previous section, it has been found that the ε_{final} of kaons is larger than that of pions and almost the same as the initial eccentricity. The HBT radii does not represent the whole source size, but the size of emission region for a expanding source. Under the picture of the collective radial flow, all particles have a common transverse velocity at the same spatial position and it is expected that particles being closer to the source surface get larger velocity. Therefore the measured length decreases with increasing the transverse momentum of pairs (k_T). At the presence of such a radial flow effect, the m_T scaling needs to be tested for the comparison of both species.

Figure 6.5 shows the relative amplitude of the azimuthal HBT radii for charged pions and kaons as a function of m_T in two centrality bins, where the centrality regions of pions and kaons are set to be the same. The left top panel corresponds to the ε_{final}. The relative amplitudes of R_s and R_o show monotonic increases with m_T, except for R_o in 0-20%. These increases will be basically due to the variation of the emission region and qualitatively agree with the results of an ideal hydrodynamic model [26] shown in Fig. 6.6, which are calculated for non-central Au+Au collisions at RHIC energy. In Fig. 6.6, the slope of k_T dependence of the relative aptitudes of R_o is steeper than that of R_s above ~0.15 GeV/c, which is due to the effect of flow. On the other hand, our results does not show such strong $k_T(m_T)$ dependence in R_o. We note that that model does not

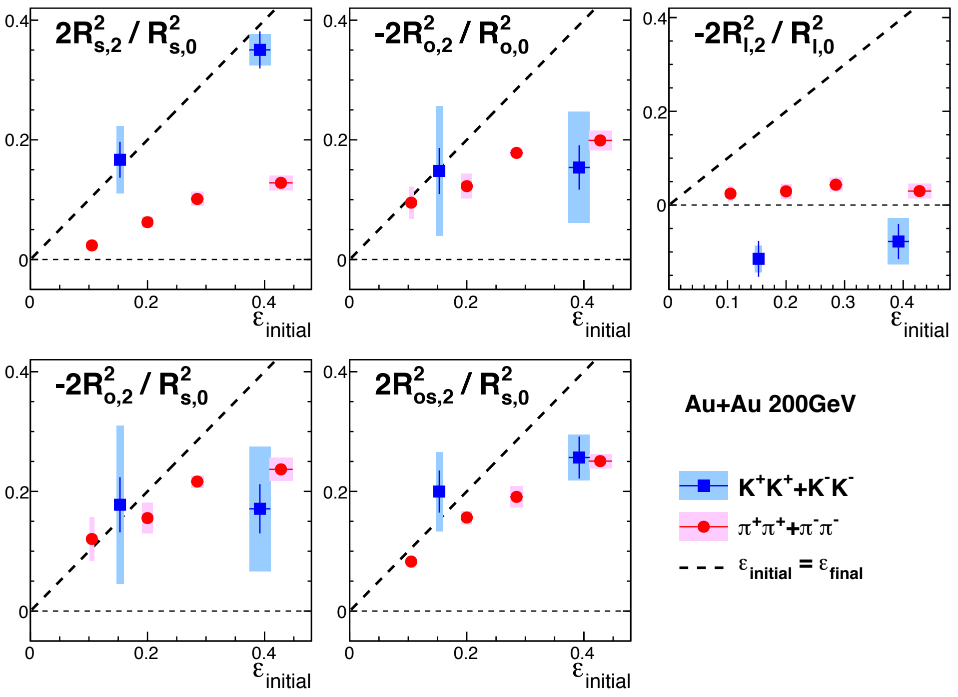

Figure 6.4: Relative amplitudes of azimuthal HBT radii for charged pions and kaons with respect to 2nd-order event plane, where color bands shows the systematic uncertainties. Dashed lines show the line of x-axis=y-axis.

incorporate the recent theoretical improvements described in Sec. 1.3.5, such as prethermal flow, stiffer equation of state, and viscosity.

The $-2R^2_{o,2}/R^2_{s,0}$ and $2R^2_{os}/R_{s,0}$ show similar trends to the $-2R^2_{o,2}/R^2_{o,0}$, which values in 0-10% seem to be independent of m_T. The R_o and R_{os} contain temporal information in addition to the geometrical information and may be different sensitivity to flow anisotropy due to the definition of the outward direction.

When we compare the results of charged pions and kaons, in 0-20% centrality both species are consistent at the same m_T, while in non-central collisions the relative amplitude of R^2_s of kaons is still larger than that of pions even at the same m_T. At higher m_T, the relative amplitude of R^2_s does not represent the whole source eccentricity, but would reflect the eccentricity. The relative amplitudes calculated by other HBT parameters do not show any significant difference between pions and kaons. On the other hand, for the average radii, the R_s shows a good agreement between pions and kaons, and the R_o and R_l show the difference in central and mid-cental collisions. It may be difficult to intuitively understand these data, and the average radii and the relative amplitudes representing the variation of the emission region between in-plane and out-of-plane directions would be at least different physics quantities. Further discussion is done in the context of the Blast-wave study in the following section.

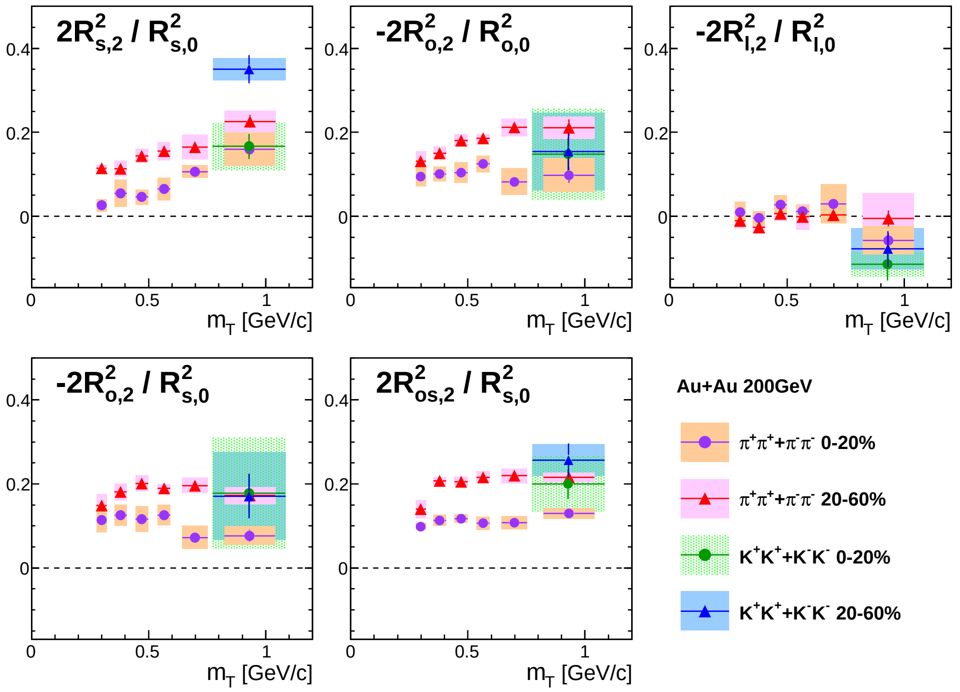

Figure 6.5: Relative amplitude of azimuthal HBT radii for charged pions and kaons with respect to 2$^{\text{nd}}$-order event plane as a function of m_T in two centrality bins in Au+Au 200 GeV collisions, where color bands shows the systematic uncertainties. The relative ratio of R_s shown in the left top panel corresponds to the ε_{final}.

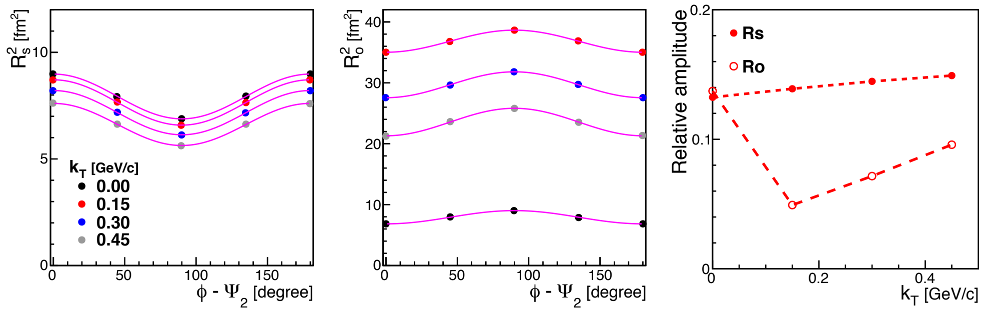

Figure 6.6: Azimuthal oscillations and relative amplitudes of the HBT radii calculated by an ideal hydrodynamic model [26] with b=7 fm Au+Au collisions at $\sqrt{s_{\text{NN}}}$=130 GeV, for 4 k_T values. Data points are read from the figures in [26].

6.3 Interpretation with Blast-wave Model

It is found that hydrodynamical calculations can reproduce the transverse momentum distributions (p_T spectra) and elliptic flow v_2 for identified particles in low p_T region described in Sec. 1.3. Although the results of HBT measurements have not been explained well by the hydrodynamical models until recently, one of the recent hydrodynamical calculation have successfully reproduced the k_T dependence of HBT radii at the same time as other observables, such as p_T spectra and v_2, described in Sec. 1.3. Therefore one might expect the azimuthal dependence of HBT radii can be also explained well by the same model. The comparison of measured azimuthal HBT results and the hydrodynamical model can give us further detailed description of the space-time evolution in heavy ion collisions.

In this section, we discuss the features at kinetic freeze-out and the evolution of the system in the heavy ion collisions by using the Blast-wave model expanded to the HBT correlation [67].

6.3.1 Blast-wave Model

Blast-wave model is based on a hydrodynamical model parameterized by the freeze-out parameters, such as the kinetic freeze-out temperature T_f and the transverse flow velocity β_T. Since the parameters are treated as free parameters, it is easy to handle the model and to compare with the data. It also helps us to intuitively understand the freeze-out configuration and system evolution.

The Blast-wave model assumes the local thermal equilibrium and boost-invariant longitudinal expansion. The expanded Blast-wave model suggested in [67] introduces additional parameters, such as the source size, the freeze-out time and the emission duration to take into account the HBT results. The followings are parameters used in that model:

1) T_f : Freeze-out temperature

2) ρ_0 : Transverse flow rapidity

3) ρ_2 : 2^{nd}-order modulation in the transverse flow

4),5) R_x, R_y : Transverse size of the source

6) a_s : Surface diffuseness of the source distribution

7) τ_0 : Freeze-out time

8) $\Delta\tau$: Emission duration

Here the transverse rapidity is defined as:

$$\rho(r, \phi_s) = (\rho_0 + \rho_2 \cos(2\phi_b))\, \tilde{r}, \tag{6.2}$$

$$\tilde{r} = \sqrt{(x/R_x)^2 + (y/R_y)^2}, \tag{6.3}$$

where x, y is space coordinate of particles, ϕ_s is the spatial azimuthal angle of particles given by $\phi_s = \tan^{-1}(y/x)$, ϕ_b is the azimuthal boost direction. This model assumes the radial boost direction is perpendicular to the elliptical subshell of the source. The relation of ϕ_s and ϕ_b is given by

$$\tan(\phi_s) = \left(\frac{R_y}{R_x}\right)^2 \tan(\phi_b). \tag{6.4}$$

The surface diffuseness a_s determines the shape of the spatial weighting function Ω, which is given by

$$\Omega = \frac{1}{1 + \exp[(\tilde{r} - 1)/a_s]}. \tag{6.5}$$

Therefore $a_s = 0$ gives a box profile as the density profile and $a_s = 0.3$ approximately gives a Gaussian shape. The freeze-out takes place at longitudinally proper time τ_0 with a Gaussian distribution of a width $\Delta\tau$ which means a finite emission duration.

Once a emission function, which describes the probability of emitting a particle with a certain momentum from a certain space-time point, is given, the shapes of p_T spectra, elliptic flow v_2, and HBT radii (R_s, R_o, R_l) are determined using the above eight parameters. The detailed formalism of the Blast-wave parameterization is described in Appendix E. The shape of p_T spectra is almost determined by T_f and ρ_0 (ρ_2 has much less sensitivity.), v_2 depends on the parameters 1) - 5), and HBT radii depend on all parameters, but R_s doesn't depend on the temporal parameters 7) and 8).

6.3.2 Fitting Results

To extract freeze-out parameters, we have performed the Blast-wave fit for p_T spectra and v_2 for charged hadrons, and HBT radii for charged pions. As described in previous section, there are eight parameters in this model. However each parameter has different sensitivities for each experimental observables. Therefore in order to effectively constrain the parameters, we determine T_f and ρ_0 by p_T spectra at first. After that, the simultaneous fit for v_2 and all HBT radii have been performed to obtain other parameters, ρ_2, R_x, R_y, τ, and $\Delta\tau$. As a default setup, a box profile ($a_s = 0$) as the spatial weighting function is used. The effect of the different profile is studied within the estimation of systematic uncertainties. The fit is performed for two different centrally classes 0-20% and 20-60%, but a slightly different centrality range (20-50%) is used only for v_2.

Figure 6.7 shows the fit results of spectra (left) and the χ^2 contour plot as functions of T_f and ρ_0. The data points of spectra are taken from [12] and results of positive and negative particles are combined. Results of the simultaneous fit for v_2 and HBT radii are shown in Fig. 6.8 and Fig. 6.9. The v_2 fit is performed for charged π, K, and $p(\bar{p})$, where the positive and negative particles are combined. The data points of v_2 are taken from [70]. The v_2 at low p_T is well described by the Blast-wave model. The fit for HBT radii is performed for all data measured with 6 k_T bins, where the data in each k_T bin is fitted simultaneously. Figure 6.10 shows the mean HBT radii as a function of m_T with the Blast-wave fit functions. The Blast-wave fit reproduce the m_T dependence of the mean HBT radii quite well. Figure 6.11 shows the χ^2 contour plots as functions of ρ_2 and R_y/R_x, and τ and $\Delta\tau$. The τ and $\Delta\tau$ have negative correlation, and the contour for them has two local minima. Under the assumption that the emission duration should be smaller than the freeze-out time, we apply the parameter limit of $\tau > \Delta\tau$ in the fit.

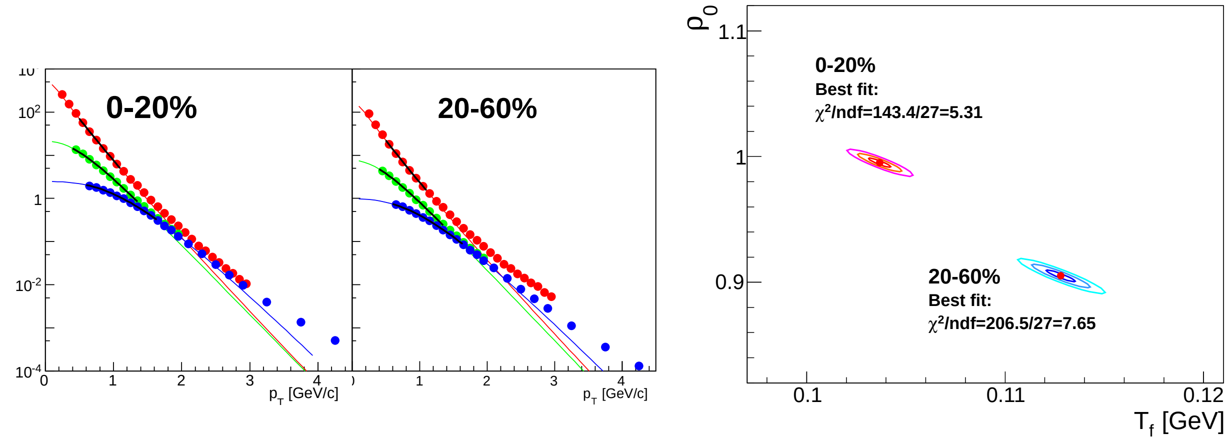

Figure 6.7: (Left) Blast-wave fit for p_T spectra of π, K, p in two centrality bins [12]. Solid black lines show the fit functions with the best fit parameters and actual fit range, and color lines shows the extended fit functions. (Right) χ^2 contour plot as functions of T_f and ρ_0. Solid lines show 1σ, 2σ, and 3σ contour lines and red points show the best fit parameters.

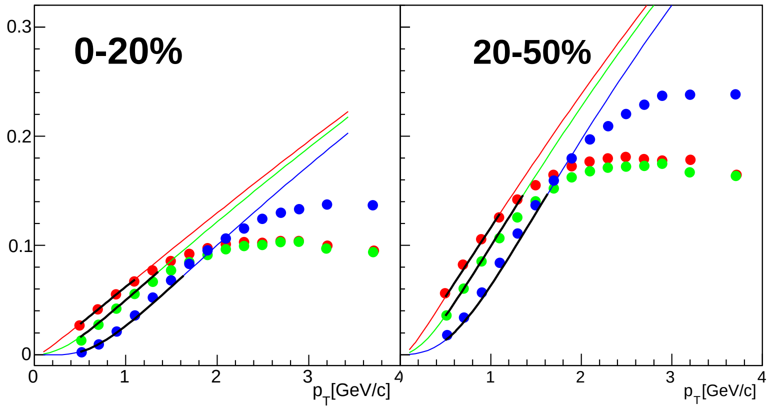

Figure 6.8: Blast-wave fit for v_2 of $\pi^+ + \pi^-$, $K^+ + K^-$, $p + \bar{p}$ [70]. Solid black lines show the fit functions with the best fit parameters and actual fit range, and color lines shows the extended fit functions.

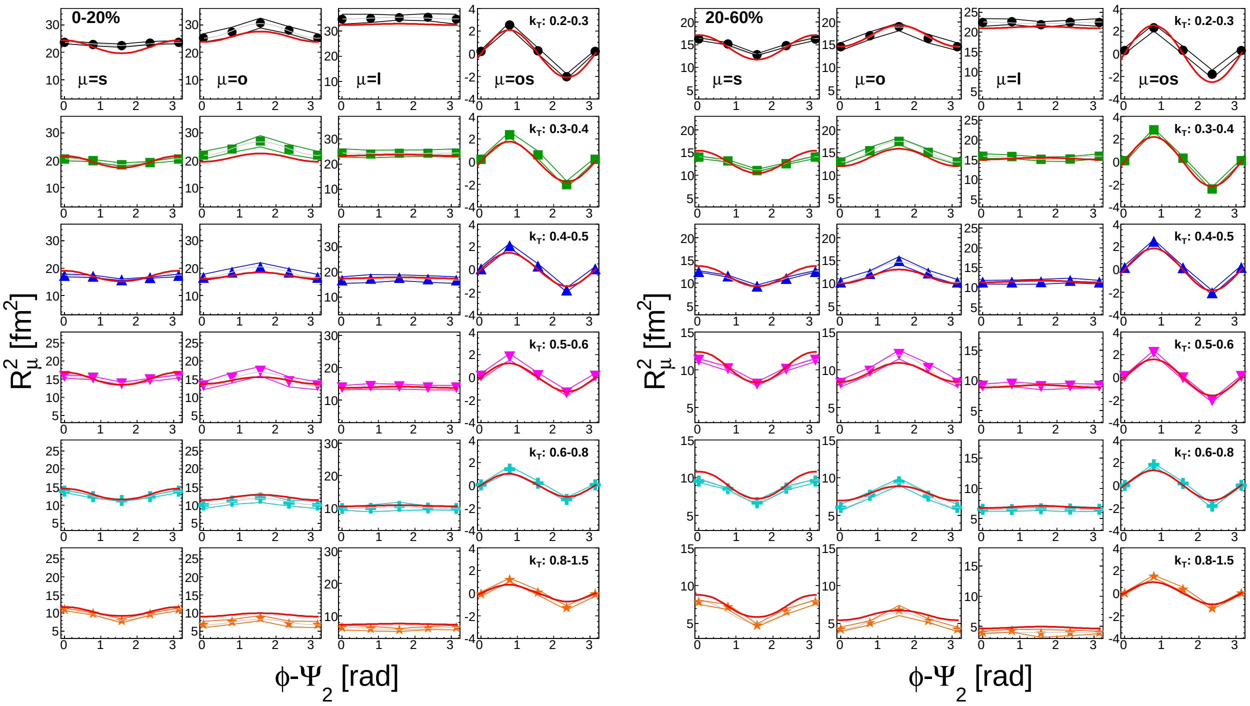

Figure 6.9: Blast-wave fit for pion HBT radii for 6 k_T bins and two centralities, 0-20%(Left) and 20-60%(Right). Red solid lines show the Blast-wave fit functions.

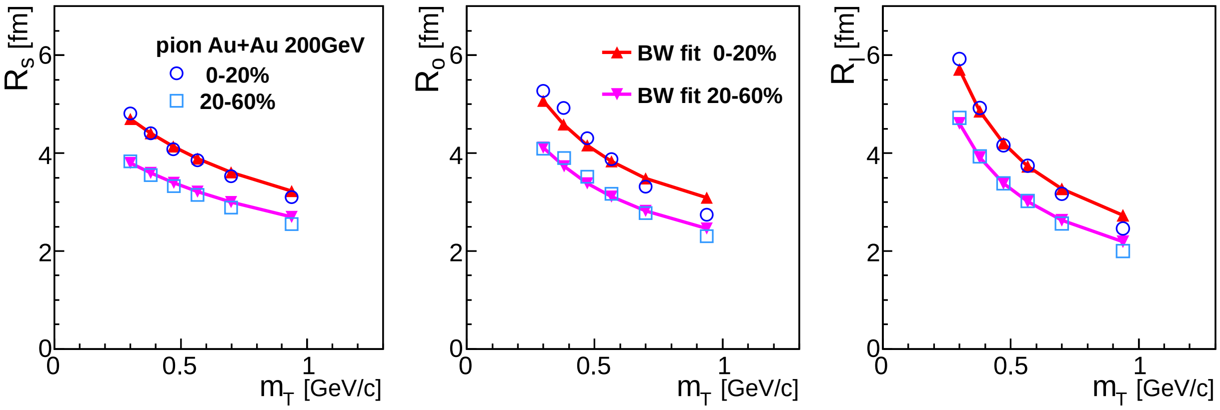

Figure 6.10: m_T dependence of the mean 3D HBT radii for charged pions with the Blast-wave fit lines, where the fit is applied for v_2 and azimuthal angle dependence of HBT radii using T_f and ρ_0 fixed by p_T spectra.

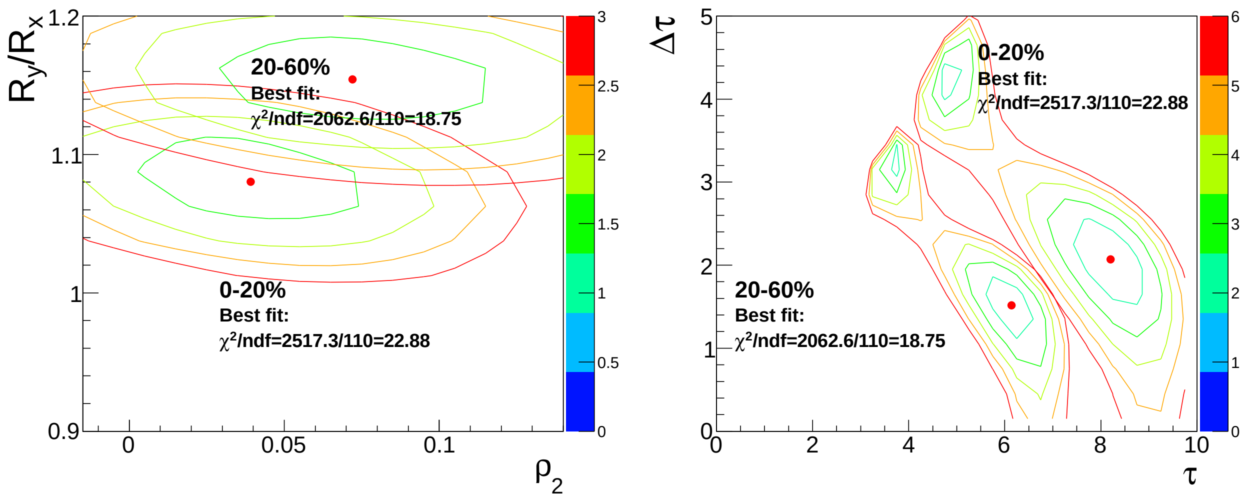

Figure 6.11: (Left) χ^2 contour plot as functions of ρ_2 and R_y/R_x. (Right) χ^2 contour plot as functions of τ and $\Delta\tau$. Red points show the best fit parameters.

6.3.3 Extracted Freeze-out Parameters

Figure 6.12 shows the extracted freeze-out parameters obtained by the Blast-wave fit for spectra, v_2 and azimuthal HBT radii. Table 6.1 shows a summary of the extracted parameters. One can see that χ^2 is not so good especially in the simultaneous fit of v_2 and HBT radii. It would be due to the inconsistency of the fit for the m_T dependence of oscillation amplitudes as described in the following discussion with Fig. 6.16. The parameter T_f and ρ_0 have a similar centrality dependence and values to the previous study [14, 62]. The parameter ρ_2 increases with decreasing N_{part}, which is qualitatively consistent with the centrality dependence of v_2. The freeze-out time τ and $\Delta\tau$ increase with centrality going from peripheral to central collisions, which are similar results to [62]. The extracted freeze-out time and the emission duration is comparable to the result from the 3-dimensional source imaging analysis [74] comparing with the Therminator model [73] (τ=8.55 fm/c and $\Delta\tau$=2 fm/c). The freeze-out time is also closer to a hydrodynamic model with resonance decays (~10 fm/c) than to the hydrodynamic model with hadronic rescattering (Hydro+RQMD) (~14 fm/c) [75].

Table 6.1: Extracted parameters by the Blast-wave fit. The T_f and ρ_0 are obtained by p_T spectra fit for π, K, p, and other parameters are obtained by a simultaneous fit for v_2 of π, K, p and pion HBT radii. The value inside () represents the systematic error.

Centrality [%]	T_f [MeV]	ρ_0	ρ_2	R_x [fm]	R_y/R_x	τ [fm/c]	$\Delta\tau$ [fm/c]	χ^2/NDF (spectra)	χ^2/NDF (v_2+HBT)
0-20	104	1.00	0.04	11.3	1.08	8.2	2.1	143.4/27	2517.3/110
	(5)	(0.06)	(0.001)	(0.5)	(0.006)	(0.8)	(0.8)	=5.3	=22.9
20-60	113	0.91	0.07	8.4	1.15	6.1	1.5	206.5/27	2062.6/110
	(8)	(0.06)	(0.008)	(0.7)	(0.025)	(0.6)	(0.5)	=7.7	=18.8

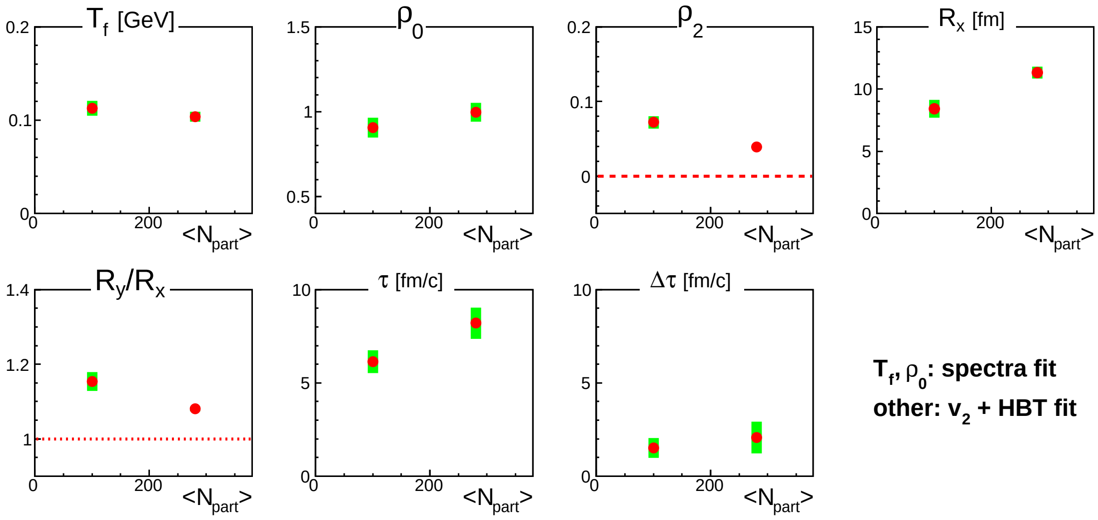

Figure 6.12: Extracted freeze-out parameters as a function of N_{part}. Color boxes show the systematic uncertainties.

Estimation of Systematic Uncertainties

In order to evaluate systematic uncertainties, the following checks have been performed:

- Changing the fit range for p_T spectra and v_2, and the k_T range of HBT radii used in the fit
- Changing the surface diffuseness to control the shape of the density profile in the source edge
- Changing the error values to determine the weight of each particle species in the fit

The extracted parameters for those systematic studies are shown in Fig. 6.14. The lower (higher) limit of the fit range is changed for p_T spectra and v_2 at the same time, where the k_T range of HBT radii is also changed. The fit range used in the Blast-wave fit is listed in Table 6.2. We have found that the fit range does not affect the extracted parameters so much. We assume the box profile for a spatial density profile as a default setup, but the realistic source would have a finite surface diffuseness. Therefore we have tested the fit using the weighting function with a_s=0.1 as shown in Fig. 6.13. The finite surface diffuseness results in slightly smaller values of T_f, ρ_0 and $\Delta\tau$, and slightly larger value of τ. The fits of p_T spectra and v_2 are performed for π, K and p simultaneously, but the fit results will be mainly constrained by pions because they have smallest statistic and systematic errors at low p_T, which region is mainly used for the Blast-wave fit. In this study, we set the errors of p_T spectra and v_2 to 10% and 8% of their values for all species. The change of the error values don't change the fitting results so much.

		p_T spectra	v_2	HBT
		p_T		k_T
default	π	0.5 - 1.13	0.5 - 1.13	0.2 - 1.5
	K	0.4 - 1.40	0.5 - 1.40	
	p	0.6 - 1.69	0.5 - 1.69	
range1	π	0.6 - 1.13	0.6 - 1.13	0.3 - 1.5
	K	0.5 - 1.40	0.6 - 1.40	
	p	0.7 - 1.69	0.6 - 1.69	
range2	π	0.5 - 1.03	0.5 - 1.03	0.2 - 0.8
	K	0.4 - 1.30	0.5 - 1.30	
	p	0.6 - 1.59	0.5 - 1.59	

Table 6.2: Fit range in the Blast-wave fit

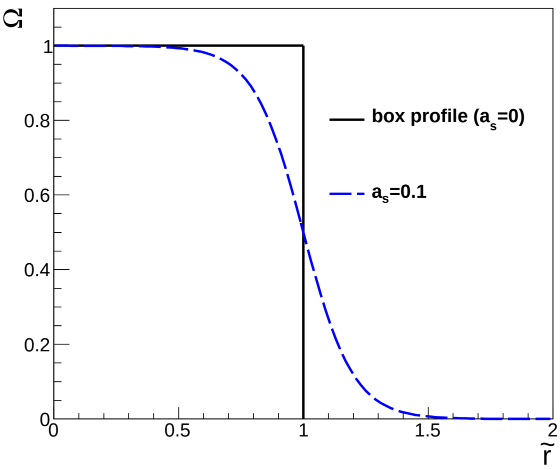

Figure 6.13: The spatial weighting function Ω for $a_s = 0$ (box profile) and a_s=0.1.

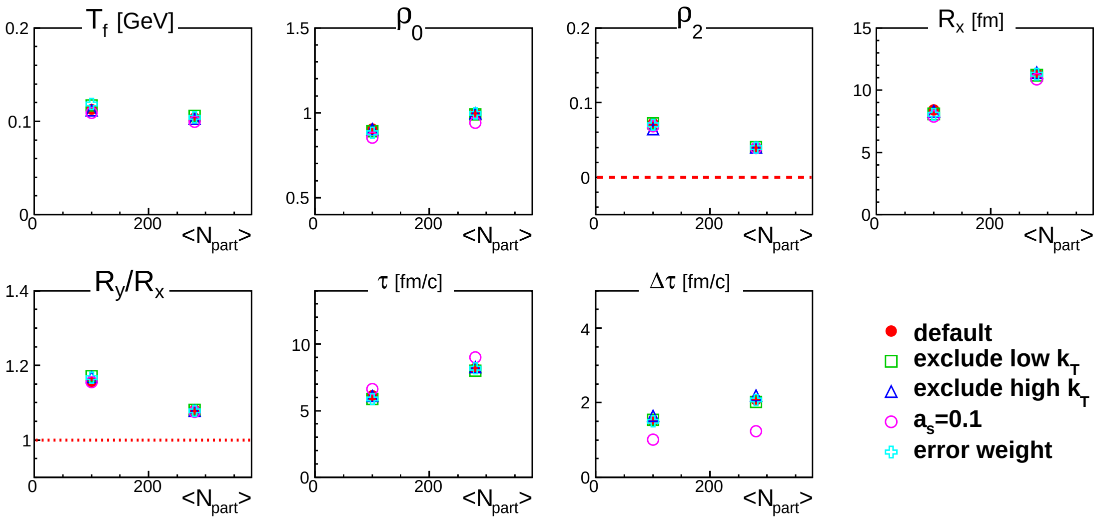

Figure 6.14: Extracted freeze-out parameters as a function of N_{part}.

Average HBT radii for π and K

Averages of 3D-HBT radii of pions are reproduced well by the Blast-wave parameterization as shown in Fig. 6.10. Under the assumption of the Blast-wave model, we can calculate the transverse momentum distribution, elliptic flow, and HBT radii for different hadrons. Figure 6.15 show the m_T dependence of HBT radii for kaons calculated by the Blast-wave model, where the model parameters shown in Table 6.1 are used. We note that the parameters in Table 6.1 are obtained by the transverse momentum distribution and elliptic flow of π, K, p, and HBT radii of π. Experimentally measured HBT radii of pions and kaons are also shown as open symbols. The Blast-wave model expects slightly larger R_s and R_o of kaons compared to pions at lower m_T, while both R_l almost fall on the same curve in the m_T dependence. This behavior is slightly different from the experimental results. One can see that the Blast-wave model calculation does not reproduce the measured HBT radii of kaons with the freeze-out parameters which reproduce the measured HBT radii of pions.

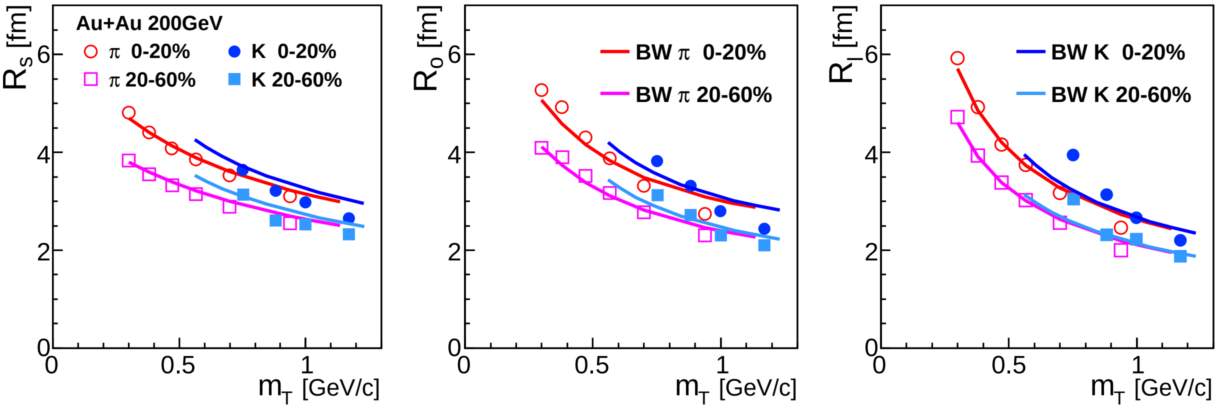

Figure 6.15: Average HBT radii of pions and kaons calculated by the Blast-wave model as a function of m_T, where the Blast-wave model parameters are obtained by the Blast-wave fit for spectra and v_2 of π, K, p and HBT radii of π.

m_T dependence of oscillation amplitudes for π and K

Although average 3D-HBT radii of pions are reproduced well by the Blast-wave parameterization as shown in Fig. 6.10 and Fig. 6.15, The oscillation strengths of R_s^2 and R_o^2 do not seem to match the data at lower and higher k_T as shown in Fig. 6.9. To see the m_T dependence of those amplitudes in detail, we have compared the values obtained by the Blast-wave function with the data in Fig. 6.16. One can see that the dependency on m_T calculated by the Blast-wave model is different with the experimental data for pions for both centrality regions. The m_T dependence of the oscillation amplitude of HBT radius reflects the variation of emission region, which would be related to the spatial density profile and velocity profile of emitting particles as well as the source eccentricity. Therefore this inconsistency may imply that the Blast-wave model used in this study has incompatible assumption with realistic case.

We have also calculated the relative amplitudes for kaons with the Blast-wave model using the parameters listed in Table 6.1, which are obtained by the fit for p_T spectra and v_2 of π, K, p, and HBT radii of π. When we compare the Blast-wave calculations for pions and kaons in Fig. 6.16, the values of kaons are slightly larger than those of pions. However it is not large enough to explain the experimental data of kaons. The Blast-wave model assumes that the freeze-out takes place at the same time for all hadrons. Therefore if the freeze-out time of kaons is faster than that of pions, the data will not be explained by this model.

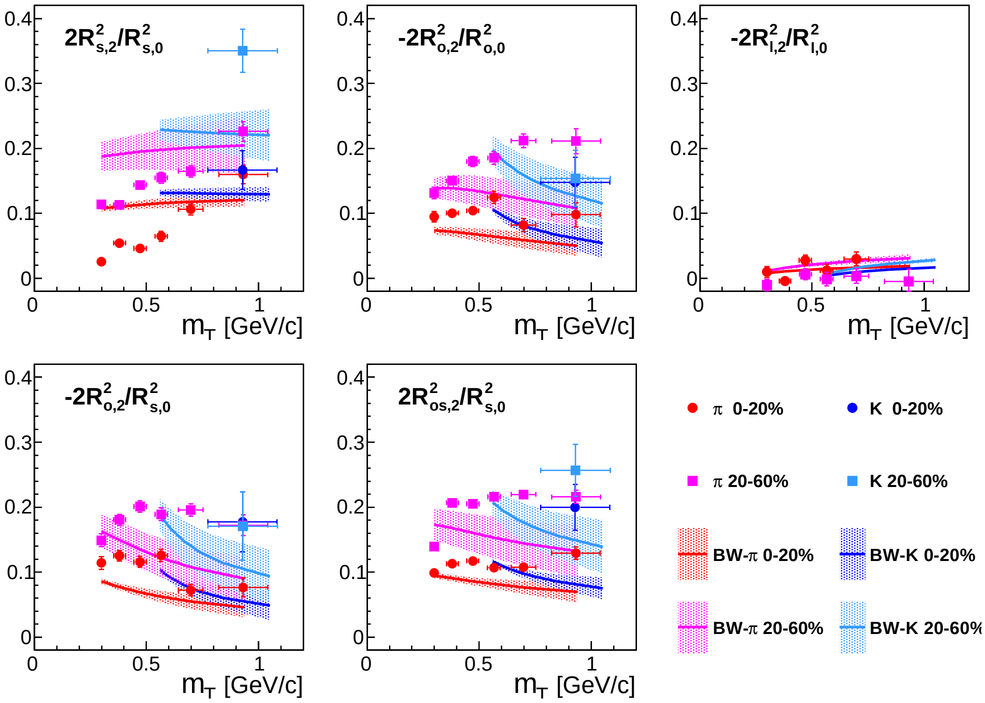

Figure 6.16: Comparison of the data and Blast-wave model calculations using fit results for the m_T dependence of relative amplitudes in two centrality regions. Blast-wave model calculations of kaons using the extracted parameters by spectra, v_2 and pion HBT.

6.3.4 Systematic Study of the Blast-wave Fit

In the previous section, we have performed the Blast-wave fit for the p_T spectra and v_2 of $\pi^+ + \pi^-$, $K^+ + K^-$, $p + \bar{p}$ and HBT radii of $\pi^+ + \pi^-$. However the azimuthal HBT result of $K^+ + K^-$ is also available for the Blast-wave fit though it is measured for the inclusive k_T. In this section, we present the results of the Blast-wave fit using the HBT radii of $K^+ + K^-$. We have performed the following tests (A-D) to investigate how the extracted parameters vary:

A. Fit for p_T spectra of π, K and p to obtain T_f and ρ_0. Simultaneous fit for v_2 of π, K and p and HBT radii of pions to obtain other parameters (already presented).

B. Fit for p_T spectra of π, K and p to obtain T_f and ρ_0. Simultaneous fit for v_2 of π, K and p and HBT radii of K to obtain other parameters.

C. Using only pion data. Fit for p_T spectra of π to obtain T_f and ρ_0. Simultaneous fit for v_2 of π and HBT radii of π to obtain other parameters.

D. Using only kaon data. Fit for p_T spectra of K to obtain T_f and ρ_0. Simultaneous fit for v_2 of K and HBT radii of K to obtain other parameters.

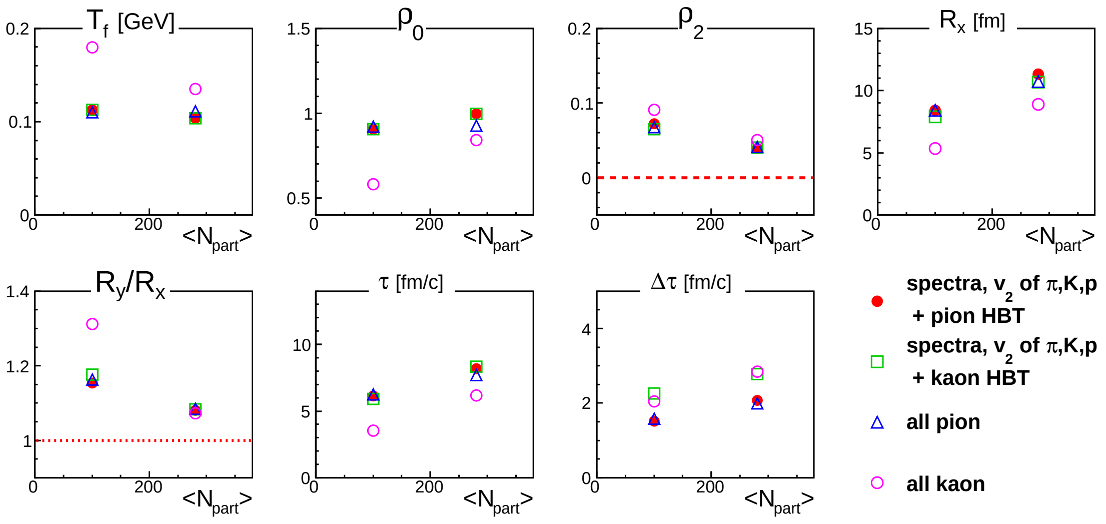

Figure 6.17: Extracted freeze-out parameters as a function of N_{part} for various combinations of observables used in the Blast-wave fit. The T_f and ρ_0 are obtained by p_T spectra fit, and other parameters are obtained by a simultaneous fit for v_2 and HBT radii.

Those fit results are shown in App. E.3. Figure 6.17 shows the results obtained by the above fits as a function of the number of participants (N_{part}) and Table 6.3 shows the summary of those parameters. If the freeze-out of all hadrons takes place at the same time, the extracted parameters should be the same between the fit A-D. However one can see that only the result of the fit D shows different values for the obtained parameters. In the result of the fit D, the T_f is larger, the system size R_x (R_y) is smaller, and the freeze-out time τ is smaller than the other fits. This result is consistent with the picture of faster freeze-out of kaons than pions. The R_y/R_x, which corresponds to the final eccentricity, is also larger than the other fits in peripheral collisions. The emission duration ($\Delta\tau$) in the fit B and D where the kaon HBT radii are used shows slightly larger values compared to the fit result using pion HBT radii although the freeze-out time (τ) shows smaller values. One may think that the smaller R_x in the fit D is inconsistent with the result in Fig. 6.1. However the smaller values of ρ_0 lead to the larger HBT radii (not whole source size) within the Blast-wave model.

Table 6.3: Summary of extracted parameters of the Blast-wave model for different fit conditions. The T_f and ρ_0 are obtained by p_T spectra fit, and other parameters are obtained by a simultaneous fit for v_2 and HBT radii. The value inside () represents the systematic error.

Centrality [%]	T_f [MeV]	ρ_0	ρ_2	R_x [fm]	R_y/R_x	τ [fm/c]	$\Delta\tau$ [fm/c]	χ^2/NDF (spectra)	χ^2/NDF (v_2+HBT)
Fit B									
0-20	104	1.00	0.04	10.7	1.08	8.3	2.8	143.4/27	52.2/30
	(5)	(0.06)	(0.006)	(0.7)	(0.01)	(0.8)	(0.5)	=5.3	=1.7
20-60	113	0.91	0.07	7.9	1.18	5.9	2.3	206.5/27	43.2/30
	(8)	(0.06)	(0.009)	(0.6)	(0.01)	(0.8)	(0.5)	=7.7	=1.4
Fit C									
0-20	111	0.93	0.04	10.7	1.08	7.7	2.0	53.1/6	2541.4/99
	(42)	(0.31)	(0.01)	(3.8)	(0.02)	(5.1)	(2.0)	=8.9	=25.7
20-60	110	0.92	0.07	8.4	1.16	6.2	1.6	70.3/6	2013.5/99
	(42)	(0.30)	(0.01)	(2.9)	(0.04)	(4.1)	(1.6)	=11.7	=20.3
Fit D									
0-20	135	0.84	0.05	8.9	1.07	6.2	2.8	21/10	46.8/21
	(29)	(0.10)	(0.02)	(1.1)	(0.07)	(2.2)	(0.6)	=2.1	=2.2
20-60	180	0.58	0.09	5.4	1.31	3.5	2.0	27.1/10	23.2/21
	(8)	(0.03)	(0.02)	(0.3)	(0.02)	(0.8)	(0.5)	=2.7	=1.1

6.4 Final Source Triangularity

Fluctuations of the initial geometry in the heavy ion collisions, which are considered to be the origin of higher harmonic flow, may be preserved at the end of the system evolution, referred to as kinetic freeze-out. Triangular flow, v_3, shows a weak centrality dependence as we introduced in Fig. 1.10, while the initial spatial triangularity calculated within a Monte-Carlo Glauber model has a pronounced centrality dependence as shown in Fig. 4.29. The magnitude of the final source triangularity will depend on the strength of the initial triangularity, the flow profile, the expansion time, and the viscosity of the QGP.

6.4.1 Centrality and m_T Dependence

Centrality dependence comparing with 2nd-order

We have again plotted R_s^2 and R_o^2 for charged pions as functions of azimuthal angle with respect to 2nd and 3rd-order event planes in Fig. 6.18. The filled symbols show the extracted HBT radii, and the open symbols are the same data points symmetrized from -π to π. The solid lines depict the fit functions with Eq. (5.1) setting n=2 or n=3. The systematic uncertainties are shown as upper and lower line bands. In most central events, the values of R_s^2 show a very weak oscillation with respect to both Ψ_2 and Ψ_3, while R_o^2 clearly exhibits finite oscillations for both event planes. In mid-central events, both clear oscillations of R_s^2 and R_o^2 with respect to Ψ_2 have the opposite sign, which reflects the elliptical shape of the particle emitting source viewed from the in-plane to the out-of-plane direction. On the other hand, both R_s^2 and R_o^2 with respect to Ψ_3 show the same sign. Figure 6.19 shows the relative amplitudes of HBT parameters for both event planes following the same manner as the definition of the ε_{final}, as a function of $\varepsilon_{n,initial}$ which is calculated by the Monte-Carlo Glauber simulation presented in Sec. 4.6. The relative $R_{s,3}^2$ is less than or equal to be zero, as noted in the oscillation in Fig. 6.18, while the relative $R_{o,3}^2$ is larger than or equal to be zero. For all amplitudes, the values of for 3rd-order are small compared to those for 2nd-order.

m_T dependence

We cannot conclude that the source has or does not have a triangular shape at final state only by those small oscillation amplitude of HBT radii with respect to Ψ_3 seen in different centrality bins. Because there is no 3rd-order harmonic anisotropy in the Gaussian approximation for a static source with a triangular shape [27]. However, it is known that HBT radii are influenced by the presence of dynamical correlations between momentum and spatial distribution at freeze-out, which leads to smaller HBT radii because the length of the homogeneity region around the source surface is measured. In case of the source with a triangular shape and no anisotropy in flow field, the spatial extents of the base and vertex of the triangle may be measured from 0° and 60° relative to Ψ_3, which of course depends on the flow profile, and momentum. Therefore it is important to see m_T dependence of the 3rd-order oscillation amplitudes of HBT radii. Figure 6.20 shows the m_T dependence of the 3rd-order relative amplitudes. The $R_{o,3}^2/R_{o,0}^2$ seems to increase with m_T, while $R_{s,3}^2/R_{s,0}^2$ does not show a significant m_T dependence.

Comparison with a hydrodynamic model

A recent hydrodynamic model including 3rd-order hydrodynamic flow and spatial anisotropy [71] provides a possible explanation of the result for 3rd-order event plane dependence of HBT radii in central collisions. That model focuses on two extreme cases:

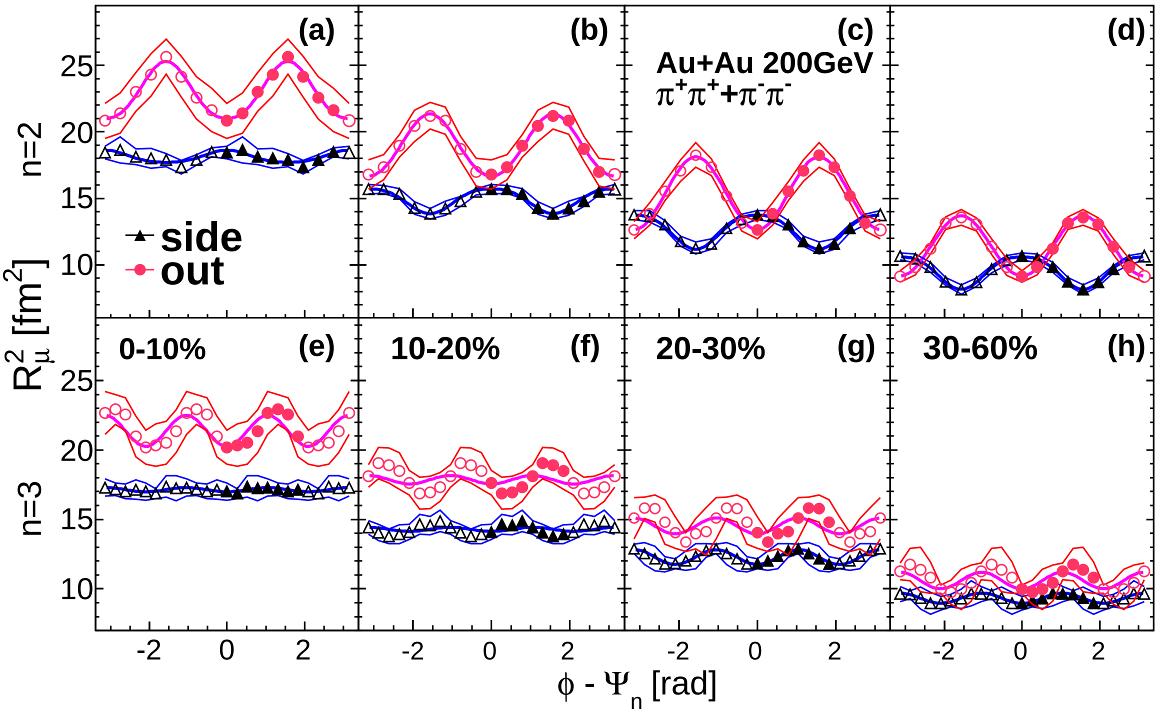

Figure 6.18: The azimuthal angle dependence of R_s^2 and R_o^2 for charged pions with respect to $2^{\rm nd}$ and $3^{\rm rd}$-order event plane in Au+Au collisions at $\sqrt{s_{\rm NN}}$=200 GeV. Filled symbols show the extracted HBT radii and open symbols are the same data symmetrized from $-\pi$ to π rad as filled symbols. Color bands consisting of two thin lines represent the systematic uncertainties.

- “flow-dominated-source”: source with a triangular flow and without a triangular spatial anisotropy
- “geometry-dominated-source”: source without a triangular flow and with a triangular spatial anisotropy

For both cases, oscillations of R_s^2 and R_o^2 as a function of Ψ_3 are shown in the left panel of Fig. 6.21, which are taken from [71]. The finite oscillation of R_o^2 with very weak oscillation of R_s^2 seen in central collisions (Fig. 6.18 (e)) is qualitatively consistent with the “flow-dominated-source”. The model also suggests that m_T dependence of the oscillation amplitudes would be a key observable to substantiate this picture. The right panel of Fig. 6.21 shows k_T dependence of the $3^{\rm rd}$-order oscillation amplitudes of R_s^2 and R_o^2 for the “flow-dominated-source” and “geometry-dominated-source”. One of features of this plot is the sign flip of R_s^2 at $k_T \approx 0.6$ GeV/c for the “flow-dominated-source”. In Fig. 6.22, we compare our result with that model, where the results of model calculations are scaled by 0.3 to see the trend of the m_T dependence. Experimental result of $R_{o,3}^2$ shows a similar trend to the “flow-dominated-source”, while $R_{s,3}^2$ does not show the sign flip seen in Fig. 6.21 (b). Experimental result of $R_{s,3}$ would rather show the opposite sign flip as Fig. 6.21 (b), that is, the $R_{s,3}^2$ shows a slight negative value at $m_T \approx 0.5$ GeV/c and goes up at higher m_T (m_T>0.8 GeV/c).

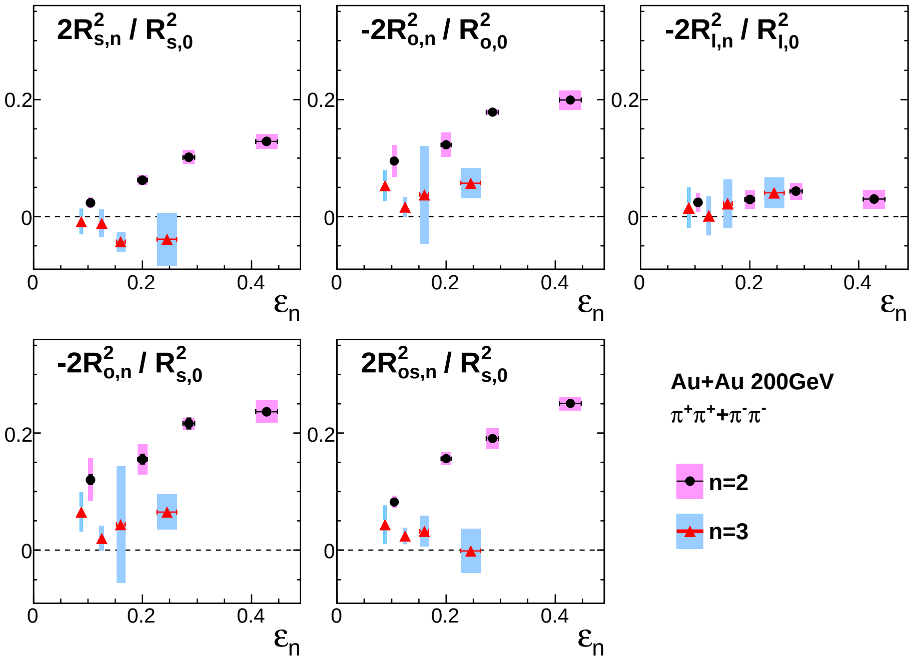

Figure 6.19: Relative amplitudes of squared HBT radii with respect to 2nd and 3rd-order event planes as a function of initial ε_n, where the initial ε_n is calculated by a Monte-Carlo Glauber model. Color boxes represent the systematic uncertainties.

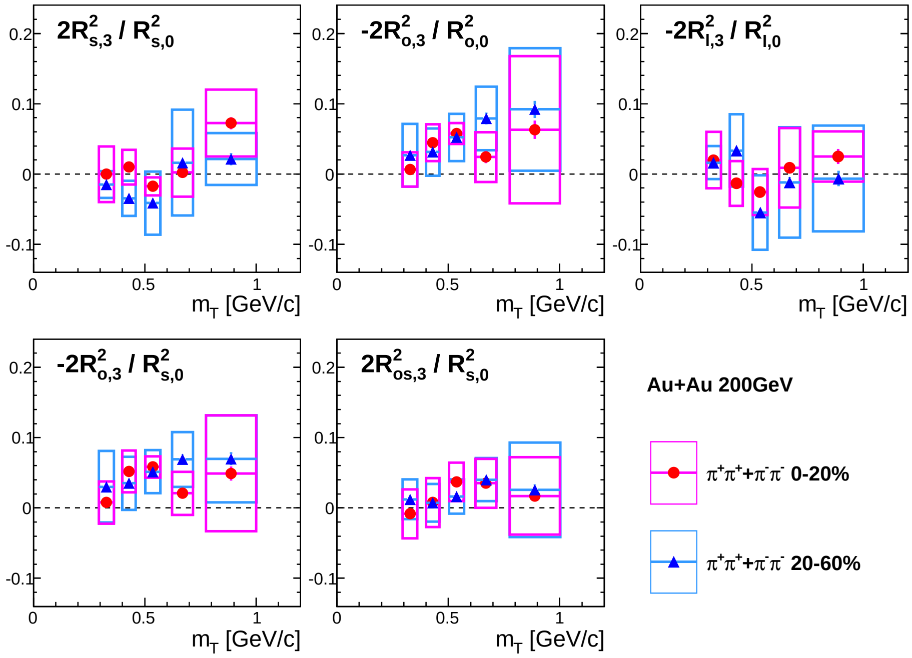

Figure 6.20: Relative amplitudes of squared HBT radii with respect to 3rd-order event plane as a function of m_T for two different centrality bins, where color boxes represent the systematic uncertainties.

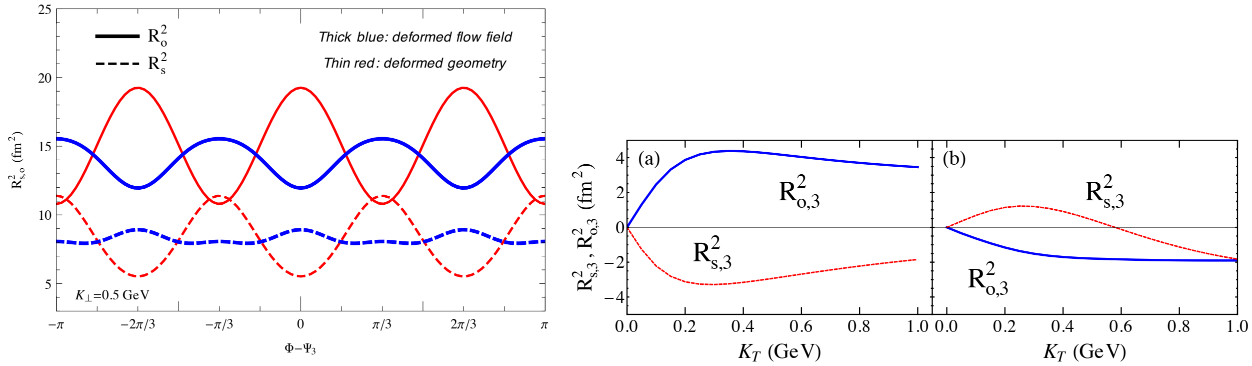

Figure 6.21: R_s^2 and R_o^2 as a function of emission angle Φ with respect to Ψ_3 (Left) and k_T dependence of the 3$^{\rm rd}$-order oscillation amplitudes of R_s^2 and R_o^2 (Right) for the "geometry-dominated-source" (thin red lines or (a)) and "flow-dominated-source" (thick blue lines or (b)) calculated by a hydrodynamic model with a simple Gaussian source. These figures are taken from [71].

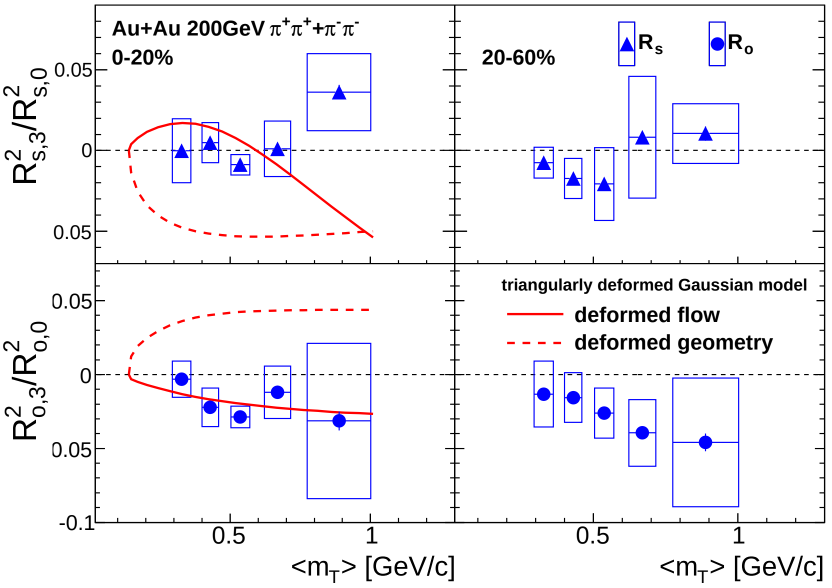

Figure 6.22: m_T dependence of the 3$^{\rm rd}$-order oscillation amplitudes of R_s^2 and R_o^2 with the comparison of a hydrodynamic model with a simple Gaussian source [71].

6.4.2 Interpretation with a Monte-Carlo Simulation

Main sources to make the azimuthal angle dependence of HBT radii will be the spatial anisotropy of particle emitting source and the flow anisotropy as described in the previous studies [26, 67]. Dynamical correlations between momentum and spatial distributions at the end of the system evolution have a large effect on the 3$^{\text{rd}}$-order dependence [71].

In order to disentangle the contributions of the spatial and flow anisotropy to azimuthal angle dependence of HBT radii, we have performed a Monte-Carlo simulation including the effects form both spatial and flow anisotropy with simple assumptions, which is similar to those adopted in the Blast-wave model. In this simulation, we don't include the Coulomb interaction, viscosity and source opacity for simple case.

Simulation Setup

Basic information of the simulation is described in App. D. The spatial distribution of particles in transverse plane follows the Woods-saxon distribution. To control the source shape, we introduce a parameter e_n into the radius parameter R in the definition of Woods-saxon distribution $\Omega(r)$:

$$\Omega(r) = \frac{1}{1+\exp(\frac{r-R}{a})}, \tag{6.6}$$

$$R = R_0\,(1-2e_n\cos(n\phi)). \tag{6.7}$$

Figure 6.23 shows generated particles with different e_n, which controls elliptical (n=2) and triangular (n=3) shapes of the source, and a parameter a is set to 0.54. We have already mentioned that the transverse momentum distribution of produced hadrons at kinetic freeze-out follows the exponential function with the inverse slope T_f as shown in Sec. 1.3.2. Therefore m_T distribution in this simulation is made to follow the same manner. In addition to the thermal motion, the experimental data show the existence of the collective expansion called the radial flow. To take it into account in this simulation, generated particles with their thermal motion are boosted toward

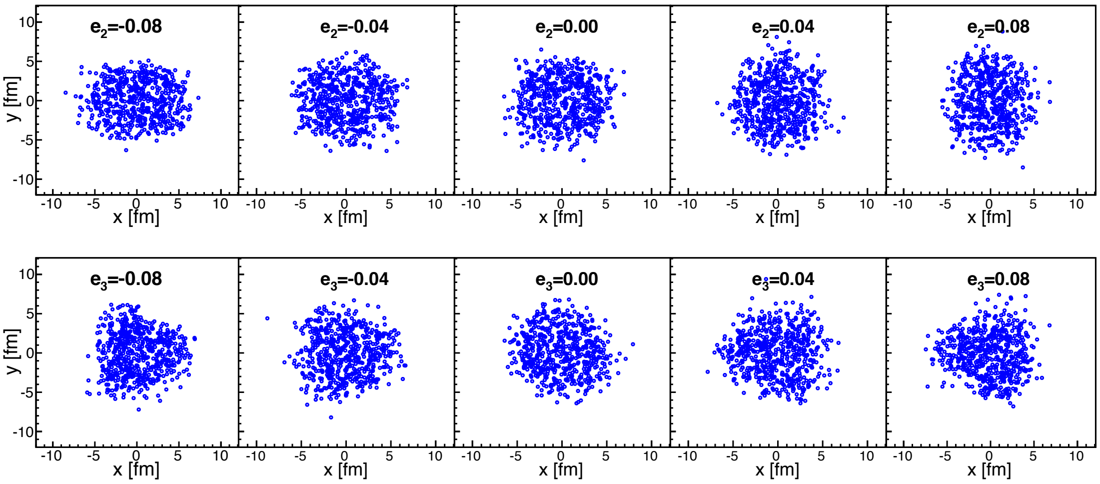

Figure 6.23: Scatter plots of generated particles in $x-y$ plane for elliptical (n=2) and triangular (n=3) source, where R_0 = 5 fm, a = 0.54.

the outside of the source with a velocity β_T which is proportional to the distance from the center of the source. We use the similar definition used in the Blast-wave model [67, 68] for the radial flow velocity:

$$\begin{aligned} \beta_T(r) &= \tanh[\rho(r)], \quad (6.8) \\ \rho(r) &= \left(\frac{r}{R}\right) \cdot \tanh^{-1}[\beta_0(1 + 2\beta_n \cos(n\phi))], \quad (6.9) \end{aligned}$$

where $\rho(r)$ is transverse flow rapidity, β_0 represents the strength of radial flow and β_n is used to control the anisotropy in the momentum space. Figure 6.24 shows a example of the transverse velocity β_T plotted as a function of r/R. To boost particles, we need the assumption about the direction to which the particles are boosted. In this study, we have tested two case of boost angles as shown in Fig. 6.25. One is the most simple case, where particles are boosted to the radial direction from the center of the source to their spatial positions (black lines in Fig. 6.25. We call it “radial boost” here). Another one is the same assumption as Eq. (6.4) adopted in the Blast-wave model, which means that the boost angle of the particle is perpendicular to the surface of the source (magenta lines in Fig. 6.25. We call it “perpendicular boost”).

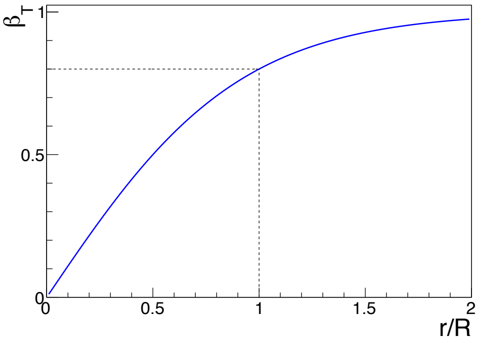

Figure 6.24: Transverse velocity with $\beta_0 = 0.8$ and $\beta_n = 0$.

Since there are several parameters in this simulation, other parameter except for e_n and β_n, such as the average radius R_0, the strength of radial flow β_0, the freeze-out temperature T_f and the emission duration $\Delta\tau$, have been tuned so that the observables reproduce the experimental data. The T_f and β_0 have been tuned by comparing with the m_T distributions published from PHENIX [12]. Figure 6.26 shows the inverse slope parameter in the m_T distribution as a function of particle mass, where experimental results are compared with simulation results for different β_0 and T_f. Although the mass dependence in our simulation seems to be slightly different from the experimental results, the strength of radial flow shows similar values. Since the emission duration affects R_o, but not R_s, we have tuned $\Delta\tau$ in addition to R_0 for each centralities so that the average of R_s^2 and R_o^2 are reproduced. Table 6.4 shows the summary of tuned parameters. Figure 6.27 shows the tuned R_s^2 and R_o^2 as a function of azimuthal angle to which the particle are emitted, where e_2 and β_2 are set to 0.03 and 0 respectively. We note that the k_T dependence of the mean R_o is much affected by $\Delta\tau$ as shown in Fig. 6.28. Slopes of R_s show the similar trend to the experimental result, while slopes of R_o are not reproduced well and the experimental results favor $\Delta\tau$=1 fm/c instead of $\Delta\tau$=3.5 fm/c. In later study, when we focus on the k_T (m_T) dependence, $\Delta\tau$=1 is used to see the m_T dependences, however for cantrality dependent studies, we have used the parameters listed in the Table 6.4 in order to get the absolute value of R_o right about the experimental value.

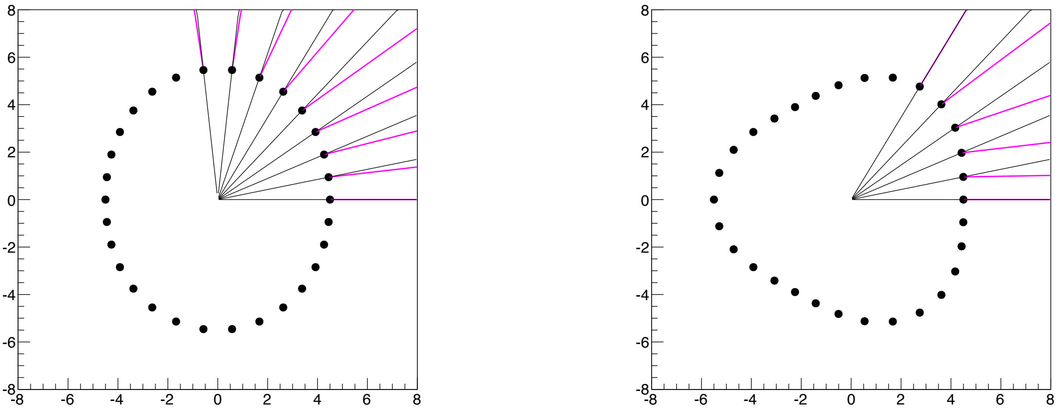

Figure 6.25: Boost angle of simulated particles ((Left)elliptical source (Right)triangular source). Dots represent particle elements consisting of the source, black lines show the radial direction from the center of the source, and magenta lines show the perpendicular direction to the surface of the source.

Table 6.4: Summary of simulation parameters

centrality	T_f	β_0	R_0	τ	$\Delta\tau$
0-10%	0.143	0.75	9.5	10	3.5
20-30%	0.149	0.69	7.5	10	2.7

m_T dependence of Oscillation Amplitudes for 3$^{\text{rd}}$-order Event Plane

We have calculated the m_T dependence of the 3$^{\text{rd}}$-order oscillation amplitudes, and results of R_s^2 and R_o^2 for two sets of e_3 and β_3 are shown as open symbols with dotted or dashed lines in Fig. 6.29 with the experimental results.

In both centrality bins, different values of β_3 for fixed e_3 (e_3=0 (-0.02) for 0-20% or (20-60%)) are used to see the effect of the flow anisotropy, where $\Delta\tau$ is fixed at 1 fm/c so that the mean R_o has a similar m_T dependence to the data. The result for e_3=0 and β_3=0.02 qualitatively agrees with the result shown in the right panel of Fig. 6.21. Finite β_3 seems to be needed to reproduce the m_T dependence of $R_{o,3}^2$. For $2R_{s,3}^2/R_{s,0}^2$, negative e_3 leads to negative values at moderate m_T, but does not reproduce the slightly positive values at larger m_T.

χ^2 minimization for e_n and β_n

We have performed the χ^2 minimization for e_n and β_n by varying their values and comparing the simulation and experimental results of centrality dependence. In order to keep the consistency with the experimental data, HBT radii in this simulation are measured relative to the event plane, not the direction of β_n plane. Event plane is determined by Eq. (4.9), where p_T is used as a weight in calculating the flow vectors. Also, the k_T range is set to $0.2 < k_T < 2.0$ GeV/c. We note that our simulation cannot reproduce the behavior of the 3$^{\text{rd}}$-order oscillation amplitudes at higher m_T, but the experimental result integrated over k_T is primarily influenced by pairs with lower k_T. The elliptic and triangular flow are also calculated in the simulation. The search ranges and steps of e_n

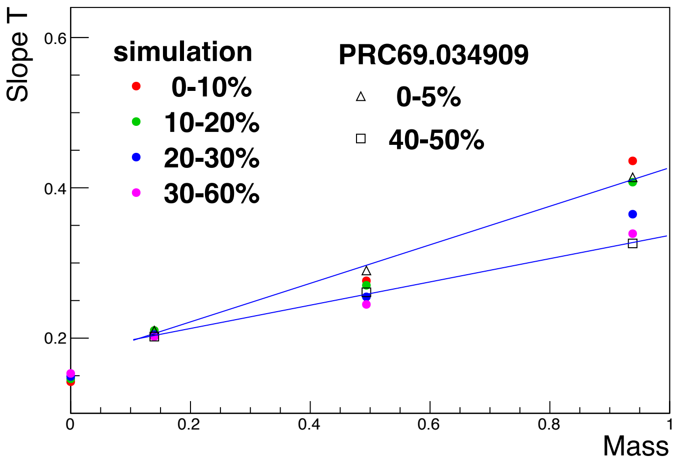

Figure 6.26: Inverse slope parameter as a function of particle mass. Simulation and experimental results are compared.

and β_n are shown in Table 6.5 and the parameters shown in Table 6.4 are used.

Table 6.5: Search conditions of e_n and β_n

parameter	range	step
e_n	$-0.05 \leq e_n \leq 0.08$	0.005
β_n	$0 \leq \beta_n \leq 0.17$	0.005

Figure 6.30 and Figure 6.31 show the calculated relative amplitudes with different β_n as a function of e_n for n=2 and n=3 for the radial boost. Relative amplitudes basically increase with increasing e_n. In both orders, the relative amplitudes for positive e_n and small β_n deviate from the global trend and have opposite sign, which is introduced by the sign change of the event plane relative to the flow (β_n) plane. In case of $\beta_n = 0$, more particles are emitted to the direction to which the source elongates because of the density profile and the assumption of the radial boost. Therefore the event plane is not necessarily aligned with β_n plane. For elliptical source, both amplitudes are sensitive to β_2. On the other hand, for triangular source, the relative amplitude of R_s^2 is insensitive to β_3, while that of R_o^2 is affected by β_3. Figure 6.32 and Figure 6.33 are the calculated relative amplitudes for the perpendicular boost. One can see the similar trend that the relative amplitude of R_s^2 is insensitive to β_3. Figure 6.34 and 6.35 show v_2 and v_3 calculated in this simulation for the radial boost. One can see finite values of v_n for finite e_n and $\beta_n = 0$, which means that the spatial anisotropy causes finite momentum anisotropy because of the assumption of density profile in this simulation. The similar trend can be seen for the perpendicular boost as shown in Figure 6.36 and 6.37.

Figure 6.38 and Figure 6.39 show the contour plots of χ^2 calculated from the difference of relative amplitudes of R_s^2 and R_o^2, and v_n between data and simulation for 2^{nd}- and 3^{rd}-order event planes for the radial and perpendicular boost respectively, where the v_n of charged pions is taken from [70]. Shaded bands represent the areas of 2-σ (1-σ) contours for 2^{nd} (3^{rd}) order. For 2^{nd}-order,

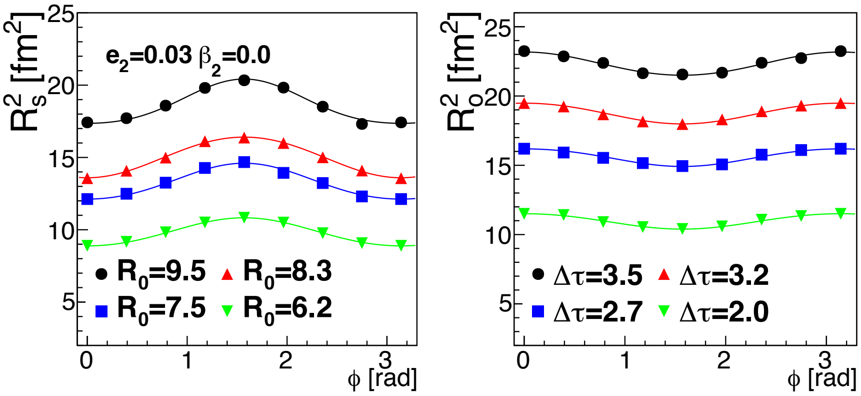

Figure 6.27: Tuned R_s^2 and R_o^2 as a function of azimuthal angle with respect to 2nd-order event plane, where the parameter R_0 and $\Delta\tau$ are tuned.

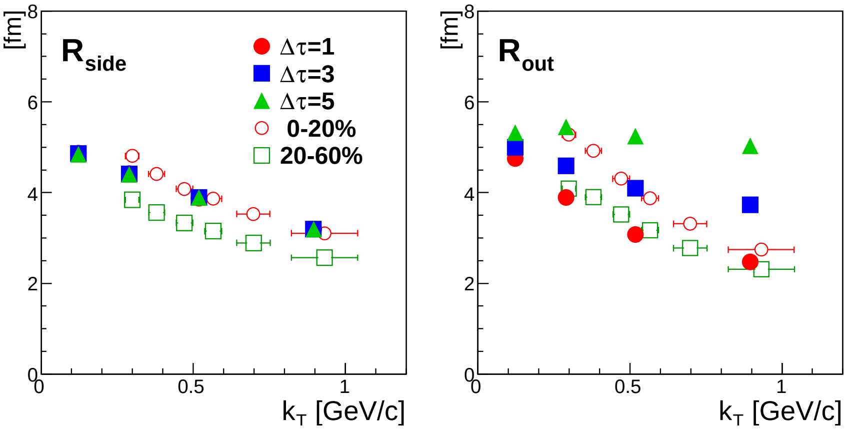

Figure 6.28: k_T dependence of the mean R_s and R_o with the parameters of 0-10% shown in Table 6.4, where resuls using three different $\Delta\tau$ are shown. Experimental results are also shown.

there is no region where the relative amplitudes of R_s and R_o, and v_2 match with each of them. Even if we focus on R_s and R_o, they do not show the overlap region in mid-central events. It may mean that the assumptions used in this simulation do not match well to the realistic conditions. But if we focus on R_s and v_2, the e_2 and β_2 in the overlap increase with going from most-central to mid-central collisions ($e_2 \approx 0$, $\beta_2 \approx 0.02$ in 0-10%, $e_2 \approx 0.02$, $\beta_2 \approx 0.09$ in 20-30%), which seems to be consistent with the picture of the final eccentricity and momentum anisotropy driven by initial elliptical shape of the source.

For 3rd-order, the relative amplitude of R_s is not much affected by β_3 compared to the case of 2nd order in both centralities. In 0-10%, the shaded area of R_s is located on $e_3 \approx 0$, and the overlap with R_o or v_3 shows finite β_3. This result means that the oscillation of R_o mainly comes from finite β_3, and is consistent with the picture that the R_o oscillation is dominated by the triangular flow, but not by spatial anisotropy as suggested in [71]. In 20-30%, the e_3 constrained by R_s seems to show zero or slightly negative value. On the other hand, R_o cannot give any strong constraint on these parameters. The initial triangularity calculated by the Glauber model clearly shows finite values

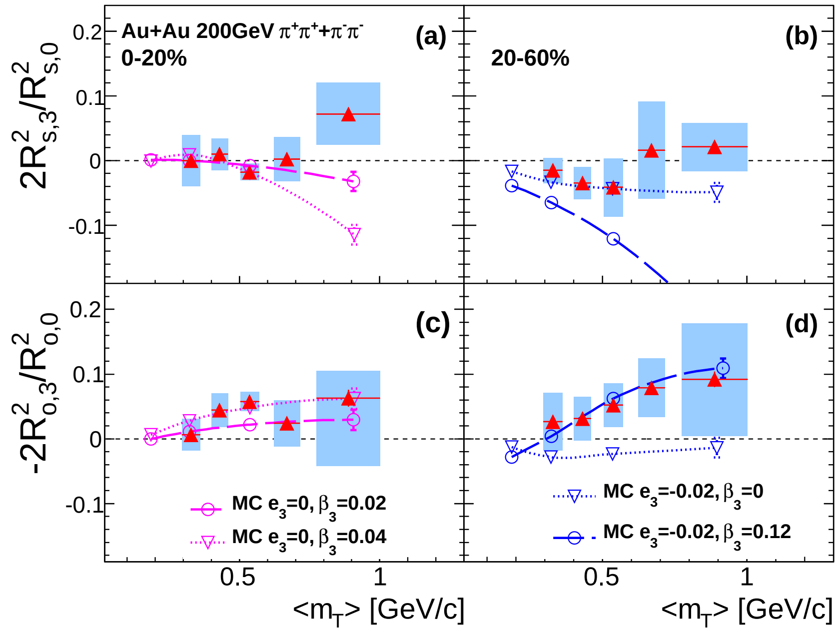

Figure 6.29: Transverse mass (m_T) dependence of the relative R_s and R_o for 3rd-order event plane in two centrality bins. Open symbols with dotted and dashed lines are calculated by MC-simulation.

at mid-central to peripheral collisions as shown in Fig 4.29. Therefore this result may indicate that the initial triangular shape is significantly reduced and potentially reversed at the end of time evolution.

These results would depend on the assumptions and parameters in the simulation. Therefore we need a more realistic model such as event-by-event hydrodynamic model for a full understanding of these results. It is remarkable that even with rather different boost assumptions, the general trends are consistent in terms of extracted optimum (e_2, β_2) and (e_3, β_3) combinations. In a recent hydrodynamic model [76], the time evolution of the spatial anisotropy is calculated. In that calculation, the sign of triangular spatial anisotropy turns over at ~7 fm/c faster than elliptic spatial anisotropy. This also seems to support the result of our simulation.

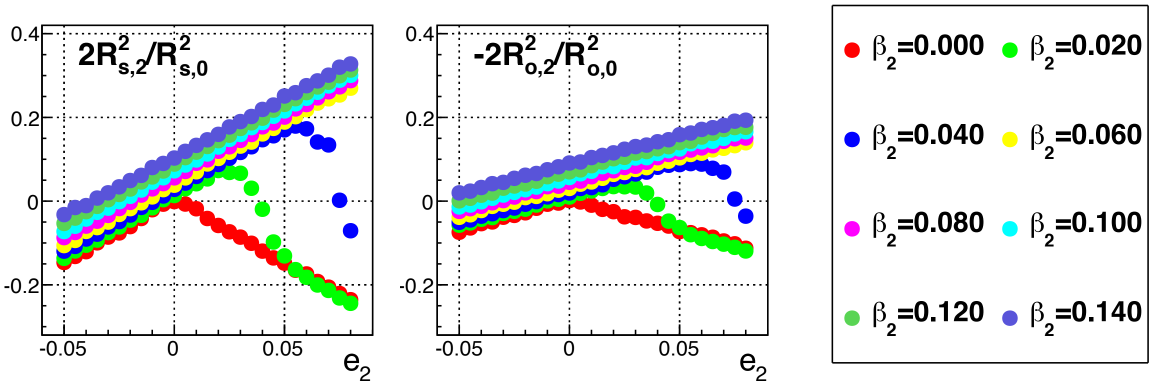

Figure 6.30: Relative amplitudes of R_s^2 and R_o^2 as a function of e_2 for various β_2 for the radial boost, where the parameters for 0-10% shown in Table 6.4 are used.

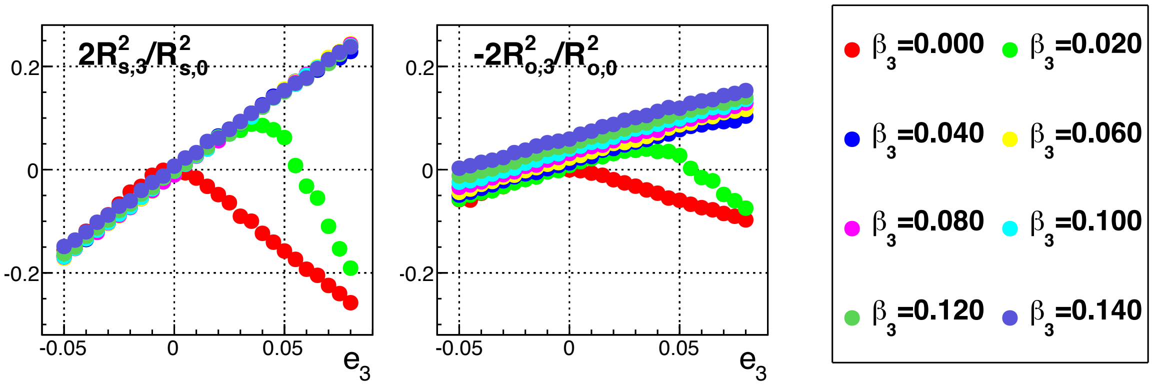

Figure 6.31: Relative amplitudes of R_s^2 and R_o^2 as a function of e_3 for various β_3 for the radial boost, where the parameters for 0-10% shown in Table 6.4 are used.

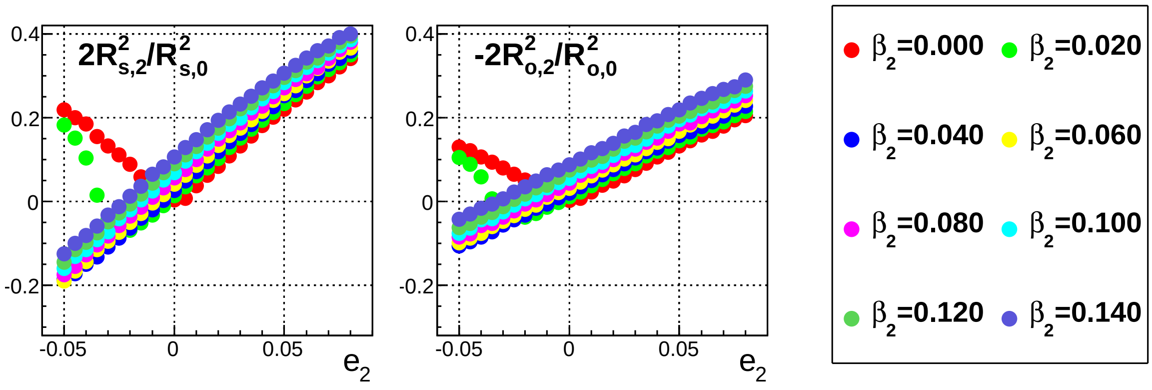

Figure 6.32: Relative amplitudes of R_s^2 and R_o^2 as a function of e_2 for various β_2 for the perpendicular boost, where the parameters for 0-10% shown in Table 6.4 are used.

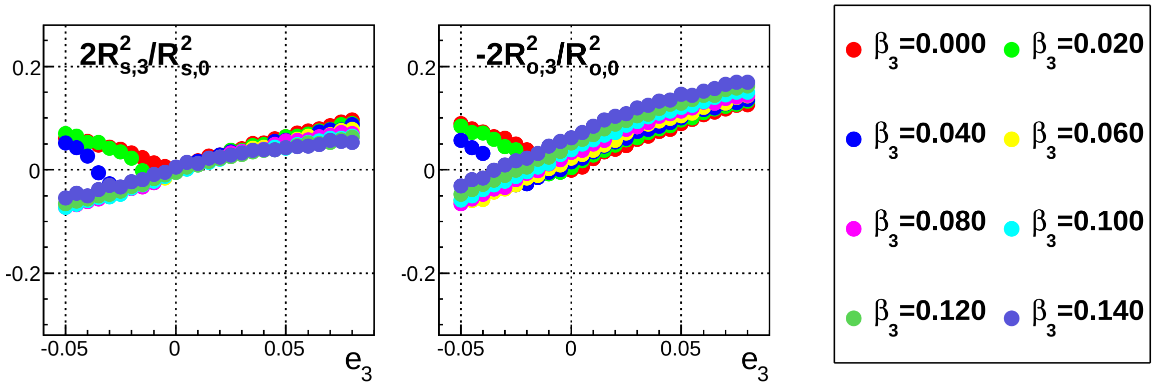

Figure 6.33: Relative amplitudes of R_s^2 and R_o^2 as a function of e_3 for various β_3 for the perpendicular boost, where the parameters for 0-10% shown in Table 6.4 are used.

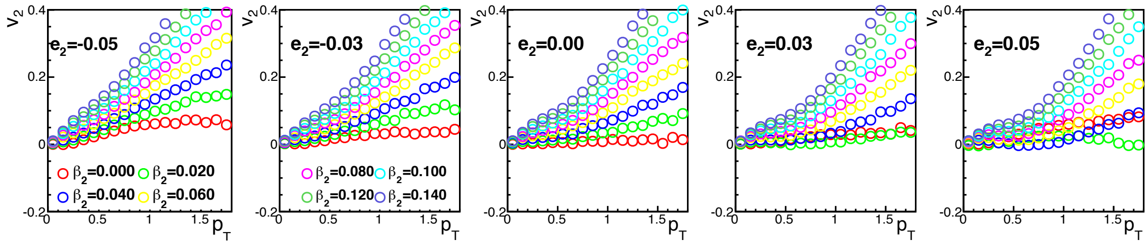

Figure 6.34: v_2 as a function of p_T for different e_2 and β_2 for the radial boost, where the parameters for 0-10% shown in Table 6.4 are used.

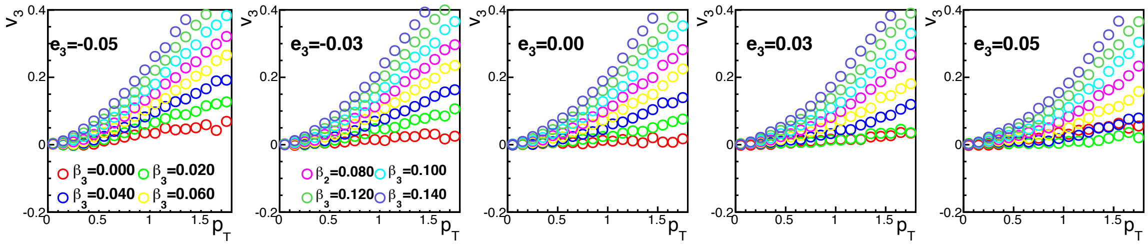

Figure 6.35: v_3 as a function of p_T for different e_3 and β_3 for the radial boost, where the parameters for 0-10% shown in Table 6.4 are used.

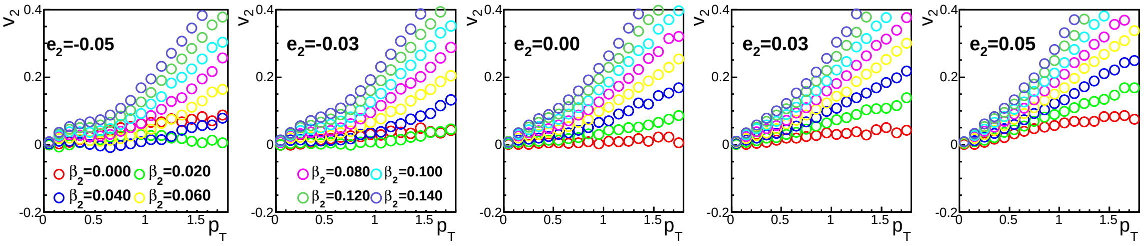

Figure 6.36: v_2 as a function of p_T for different e_2 and β_2 for the perpendicular boost, where the parameters for 0-10% shown in Table 6.4 are used.

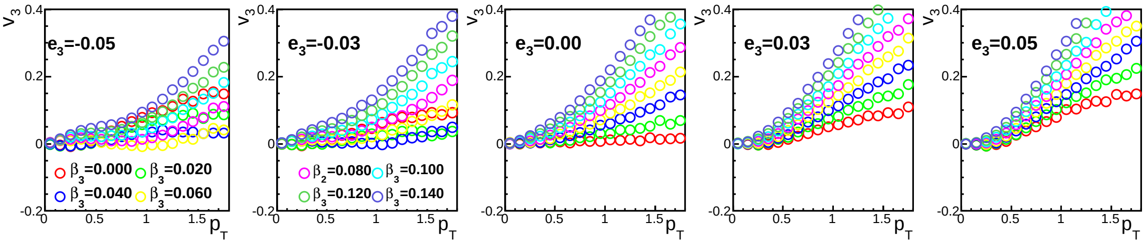

Figure 6.37: v_3 as a function of p_T for different e_3 and β_3 for the perpendicular boost, where the parameters for 0-10% shown in Table 6.4 are used.

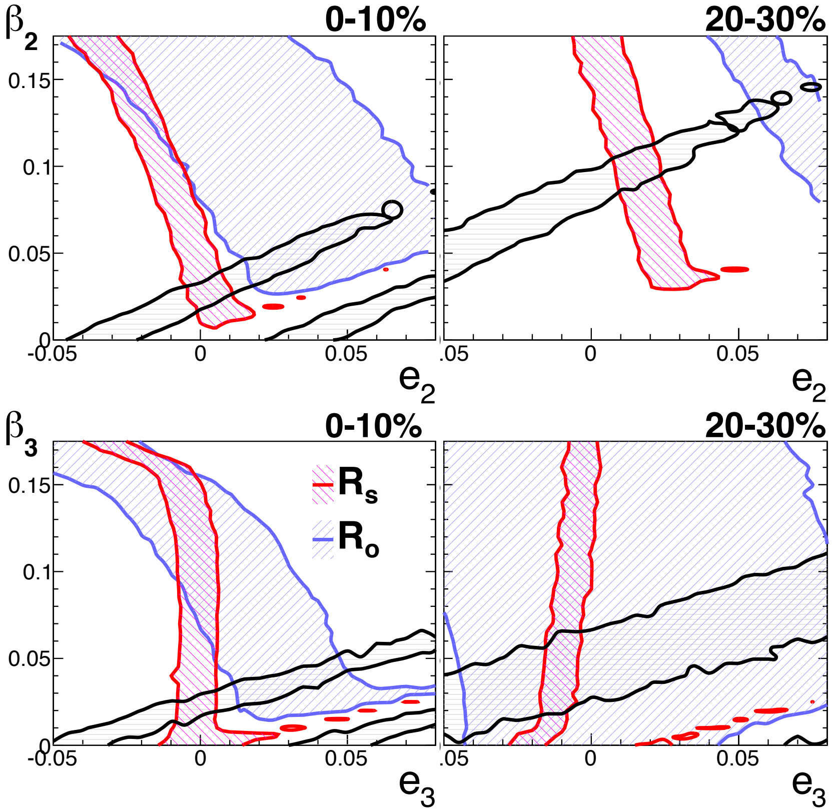

Figure 6.38: Contour map of χ^2 between data and simulation for 2nd- and 3rd-order, where the χ^2 is calculated from the relative amplitudes of R_o and R_s, and v_n. Shaded areas represent the regions within 2-σ contour for 2nd-order HBT and 1-σ contour for 3rd-order HBT, and 4-σ contour for v_n.

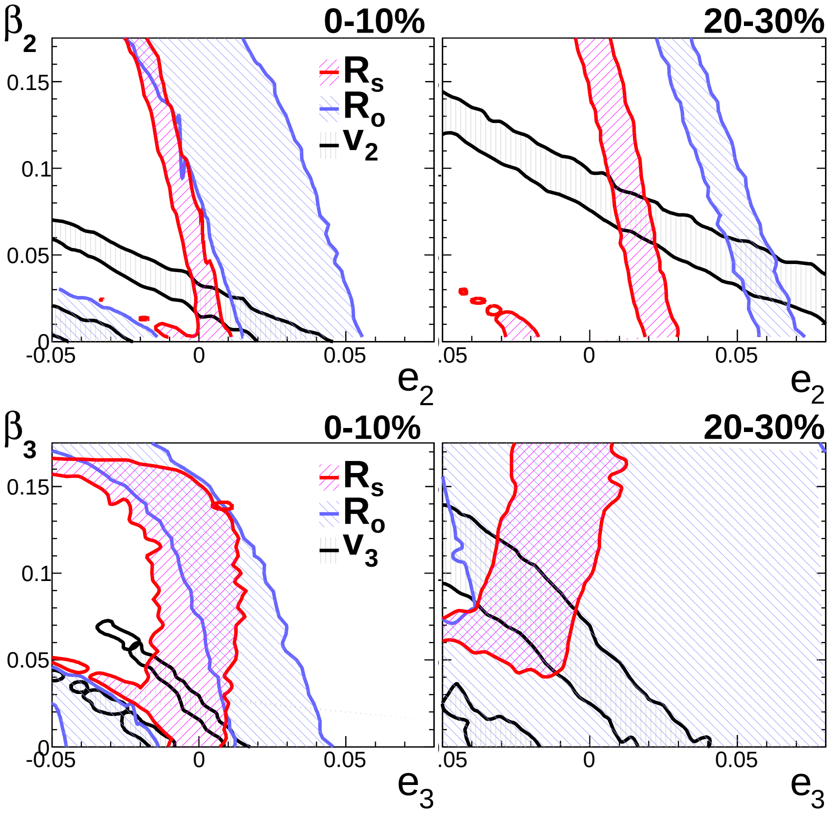

Figure 6.39: Contour map of χ^2 between data and simulation for 2nd- and 3rd-order, where the χ^2 is calculated from the relative amplitudes of R_o and R_s, and v_n. Shaded areas represent the regions within 2-σ contour for 2nd-order HBT and 1-σ contour for 3rd-order HBT, and 4-σ contour for v_n.

6.5 Quardrangular Component of Final Source Shape

It is known that there is a correlation between 2^{nd} and 4^{th}-order order event planes as presented in [18, 72]. The v_4, quadrangular (4^{th}-order) flow, was also measured with respect to 2^{nd}-order event plane. Therefore the quadrangular component of the source shape in addition to elliptical one may be measured with respect to 2^{nd}-event plane. In this section, we discuss the 4^{th}-order component of the source shape at final state using the azimuthal angle dependence of HBT radii with respect to 2^{nd}-order event plane.

Figure 6.40 (a)-(c) show azimuthal angle dependence of R_s^2 and R_o^2 with respect to 2^{nd}-order event plane for three centrality bins after applying the correction to 4^{th}-order ($n_{bin}/2{=}4$) by Eq. (4.42), where solid red lines depict the fit functions by Eq. (5.1). Panels (d)-(f), (g)-(i) in Figure 6.40 show the Fourier decomposition of R_s^2 and R_o^2 in Fig.6.40a-c respectively. One can see small 4^{th}-order component of R_s^2 and R_o^2. In mid∼peripheral collisions, the $R_{s,4}^2$ and $R_{o,4}^2$ shows the same sign. The relative oscillations of these 4^{th}-order component are shown in Fig. 6.41 as a function of $\varepsilon_4(\Psi_2)$ following a similar definition to the final eccentricity. The $\varepsilon_4(\Psi_2)$ represents the initial quadrangularity relative to Ψ_2 and calculated by the Monte-Carlo Glauber simulation described in Sec. 4.6. They seems to have finite values beyond their systematic uncertainties.

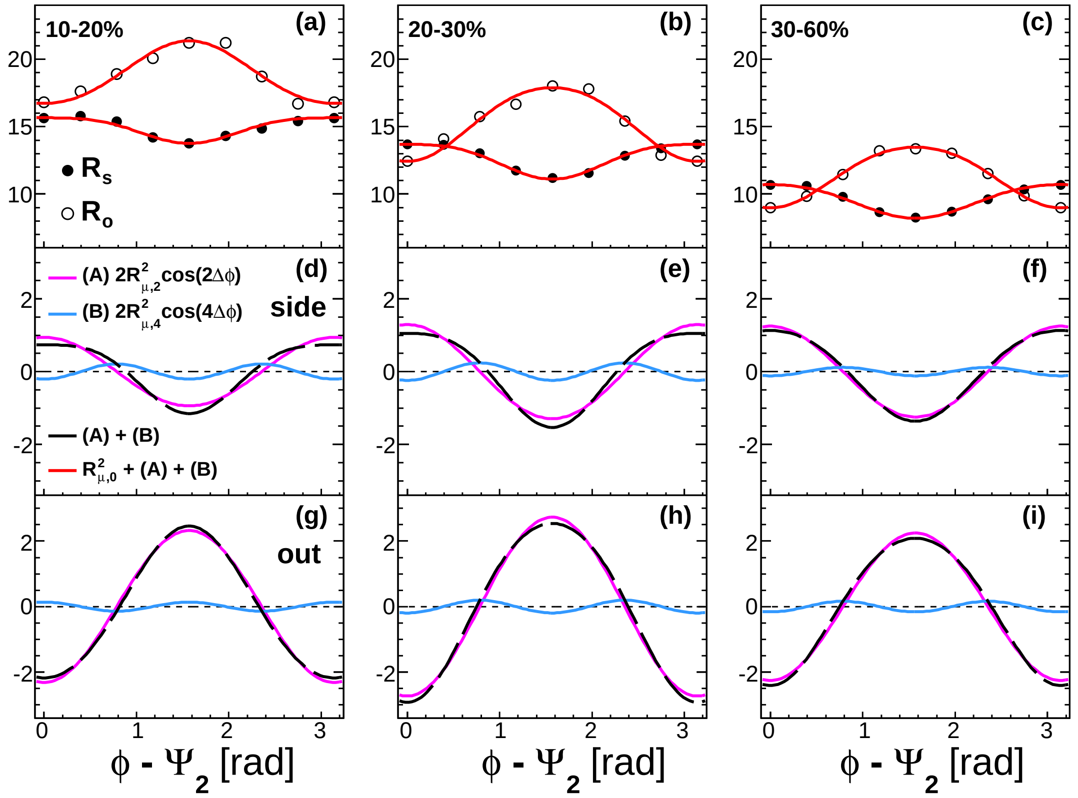

Figure 6.40: Fourier decompositions of R_s^2 and R_o^2 relative to 2^{nd}-order event plane for charged pions.

It may be difficult to conclude whether the source at freeze-out has a 4th-order fluctuation in shape and to determine its sign because these oscillation also consist of the contributions from the spatial and flow anisotropy in 4th-order. It will be also affected by the variation of the emission region. If we apply the same picture as the 3rd-order event plane dependence suggested in [71], R_o^2 is much affected by the flow anisotropy in case of the spherical source, where the thickness of the emission region corresponding to R_o decrease in the direction of the triangular flow. In Fig. 6.40 (h)-(i), R_o^2 decrease at the direction of $\Psi_2 \approx \Psi_4$. It indicate that the 4th-order component of R_o^2 may be driven by the quadrangular flow. On the other hand, R_s^2 also decrease at that direction. It seems to be a similar behavior to 3rd-order dependence. For further discussion on tho topic, the measurement with respect to Ψ_4 with a better event plane resolution and theoretical model including the effect of event-by-event fluctuation are needed.

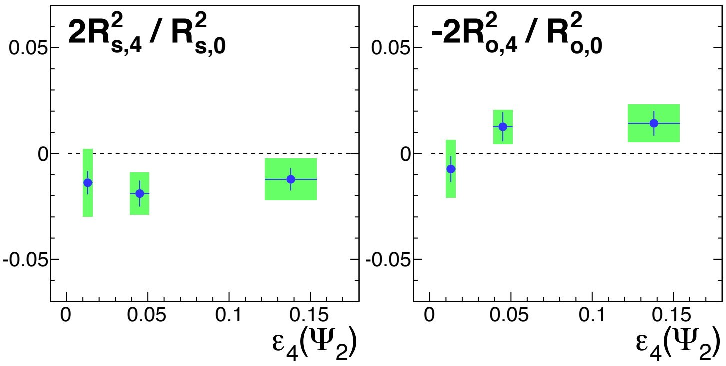

Figure 6.41: Relative 4th-order Fourier coefficients of R_s^2 and R_o^2 as a function of initial $\varepsilon_4(\Psi_2)$ calculated by a Monte-Carlo Glauber simulation.

Chapter 7

Conclusion

The quark-gluon plasma is a state of nuclear matter where quarks and gluons are deconfined in hadrons. A unique tool to study the QGP on earth is the relativistic heavy ion collisions. After the QGP is formed by the collisions, the system expands and cools rapidly, and become hadronic state as predicted by Quantum Chromodynamics. Therefore it is important to reveal the space-time evolution of the created hot and dense matter for the comprehensive understanding of the characteristics of the QGP. The HBT interferometry is a powerful tool to study it.

We have measured the azimuthal dependence of HBT radii for charged pions and kaons with respect to 2^{nd} and 3^{rd}-order event planes in Au+Au collisions at $\sqrt{s_{\mathrm{NN}}} = 200$ GeV at RHIC-PHENIX. The Reaction Plane Detector installed prior to 2007 running period allowed us to measure event planes with good resolutions.

In the measurements of HBT radii relative to 2^{nd}-order event plane, the oscillations of both HBT radii for charged pions and kaons are clearly observed. Final eccentricity increases with centrality going from central to peripheral collisions for both species. Final eccentricity of charged pions is about the half of initial eccentricity calculated by a Monte-Carlo Glauber simulation, which indicates the source strongly expands to the in-plane direction. However since it still has finite value, the result suggests that particles are emitted from the source during a short time before the strong expansion overcomes the initial eccentricity of the source and before the out-of-plane shape change into in-plane expanded shape. On the other hand, final eccentricity of charged kaons is larger than that of charged pions even at the same transverse mass. It has also been observed that azimuthally average R_o and R_l of kaons are slightly larger than those of pions, and the difference increase with centrality going from peripheral to central collisions, while R_s shows a good agreement between both species. Since positive and negative kaons, which have different cross sections, do not show significant difference in HBT radii, the difference between pions and kaons may not be simply explained by the hadronic rescattering with different cross sections. These result suggest that charged pions and kaons may have different freeze-out mechanism.

In order to extract information on the freeze-out, we have performed the data fitting by the Blast-wave model. Results of transverse momentum distribution and elliptic flow v_2 as well as pion HBT results are used for the fit. Extracted parameters show the following features:

- 2^{nd}-order modulation in the flow field (ρ_2) increases with decreasing the number of participant (N_{part})
- Source size is about 7.5-11 fm for 0-60% centralities under the assumption of box profile as spatial distribution. Results indicate out-of-plane extended source.

- System lifetime τ and emission duration $\Delta\tau$ increase with centrality. Their values are ~8 fm/c and ~2 fm/c respectively in 0-20% centrality.

The freeze-out time obtained by this study is also closer to a prediction by the hydrodynamic calculation without the hadronic rescattering than the hydrodynamic calculation with the hadronic rescattering. That may suggest that the stage of the hadronic rescattering before the freeze-out is much short.

To investigate whether there is a difference between pions and kaons within the framework of Blast-wave model, we have calculated the m_T dependence of HBT radii and final eccentricity for both species using the freeze-out parameters obtained by the Blast-wave fit for pion HBT result. Although the Blast-wave calculation could reproduce the average of HBT radii for pions, it could not reproduce the average of kaon HBT radii and the m_T dependence of final eccentricity quantitatively for pions and kaons. The slopes of final eccentricity as a function of m_T sometimes show even opposite trend compared to the experimental data. Final eccentricity of kaons are slightly larger than that of pions in Blast-wave calculation, but it is not enough to explain the data. In the fit result using kaon HBT radii, larger $\Delta\tau$ is obtained. This also suggest the longer emission duration of koans than that of pions.

In the measurement of HBT radii relative to 3$^{\text{nd}}$-order event plane, we observe the significant oscillation of R_o and the zero or small oscillation of R_s with the same sign as R_o at mid-central event. Azimuthal angle dependence of HBT radii will be determined by the balance between spatial anisotropy and flow anisotropy. Therefore zero oscillation of HBT radii does not necessarily mean no spatial triangular component of the source.

We have performed a simple Monte-Carlo simulation to disentangle the contributions from spatial and flow anisotropy to azimuthal angle dependence of HBT radii. Parameters used in this simulation are spatial anisotropy e_n and flow anisotropy β_n, which should be main sources to make the azimuthal angle dependence of HBT radii. Simulations of HBT radii for 2$^{\text{nd}}$ and 3$^{\text{rd}}$-order event plane dependences are calculated in two-dimensional parameter space of (e_n,β_n) in order to make χ^2 maps defined by the difference between experimental data and simulation. Results for 2$^{\text{nd}}$-order event plane shows that the parameter e_2 constrained by R_s and v_2 increases with centrality going from central to peripheral collisions. It is consistent with centrality dependence of final eccentricity calculated by the R_s oscillation. On the other hand, it is difficult to explain both R_s and R_o oscillations with this simulation as seen in the result of the Blast-wave study. Results for 3$^{\text{nd}}$-order event plane shows that the parameter e_3 is primarily constrained by R_s and shows zero or slightly negative value. This result implies that the initial triangular deformation may be significantly reduced and potentially flipped the orientation by the triangular flow. However these results will be affected by simulation conditions and assumptions. Therefore comparisons with theoretical model with realistic conditions, such as an even-by-event hydrodynamics with fluctuating initial conditions including hadronic cascade before the kinetic freeze-out will be needed for a full understanding of the experimental data and further discussions on the details of the system evolution.

Appendix A

Correlation Functions

In this chapter, the 3-dimensional correlation function projected to each $q_\mu\,(\mu = s, o, l)$ direction without and with the correction of the event plane resolution are shown. The fit lines are also shown together.

A.1 Correlation Functions of Charged Pions in Azimuthally Integrated Analysis

A.2 Correlation Functions of Charged Kaons in Azimuthally Integrated Analysis

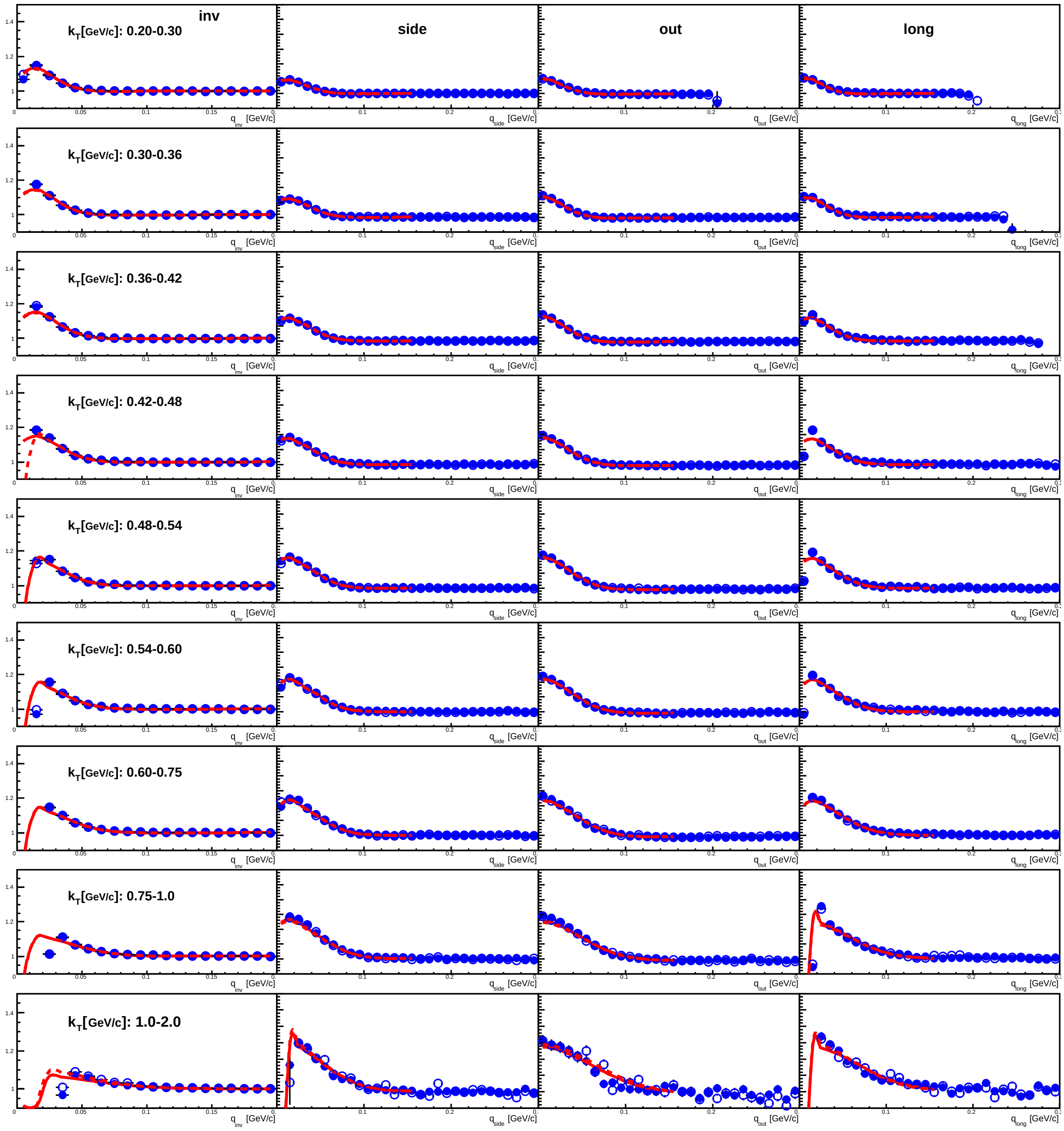

Figure A.1: Correlation functions of charged pion pairs in 0-10% centrality, where solid lines show the fit functions. Filled symbols show positive pion pairs and open symbols show negative pion pairs.

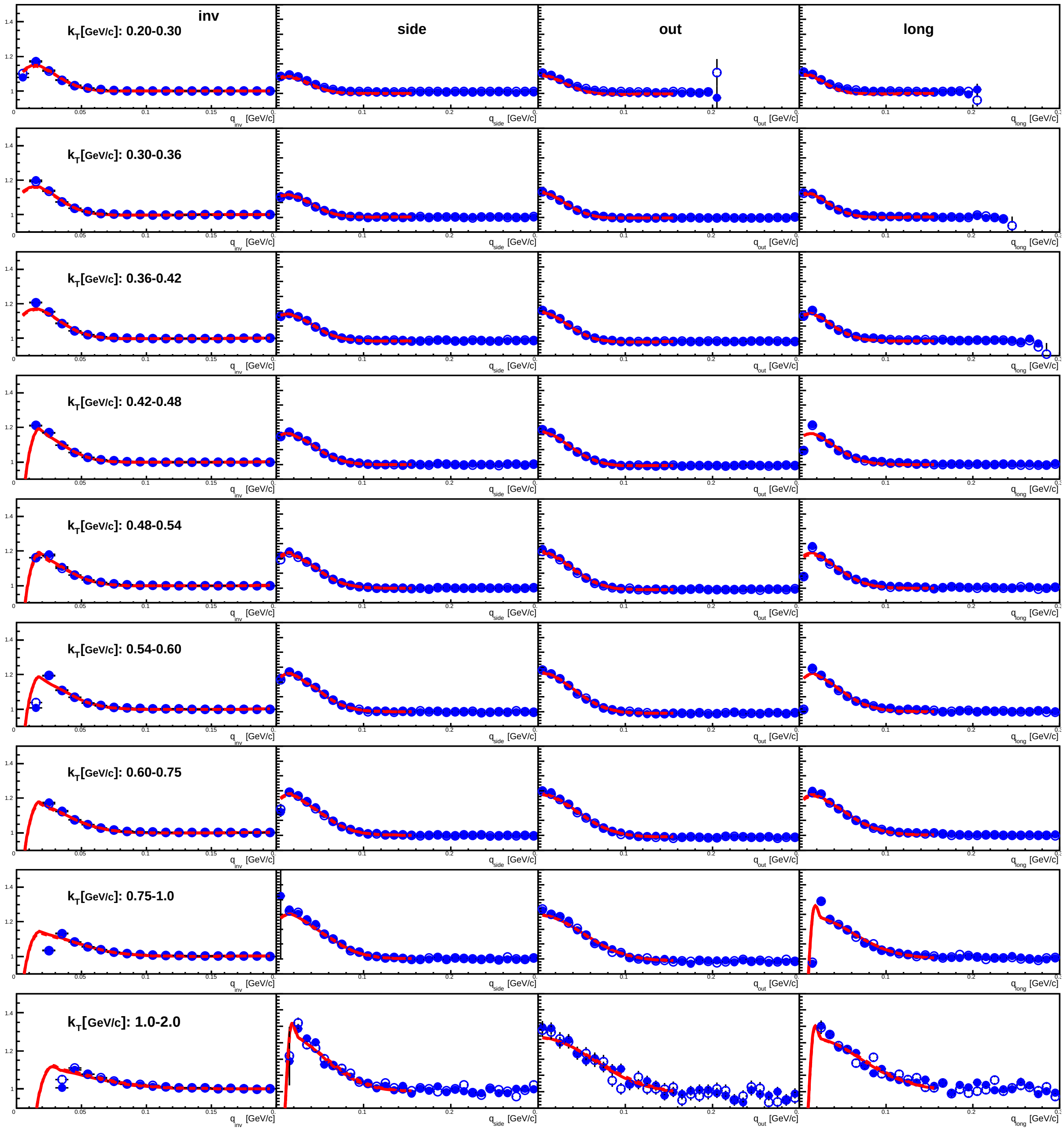

Figure A.2: Correlation functions of charged pion pairs in 10-20% centrality, where solid lines show the fit functions. Filled symbols show positive pion pairs and open symbols show negative pion pairs.

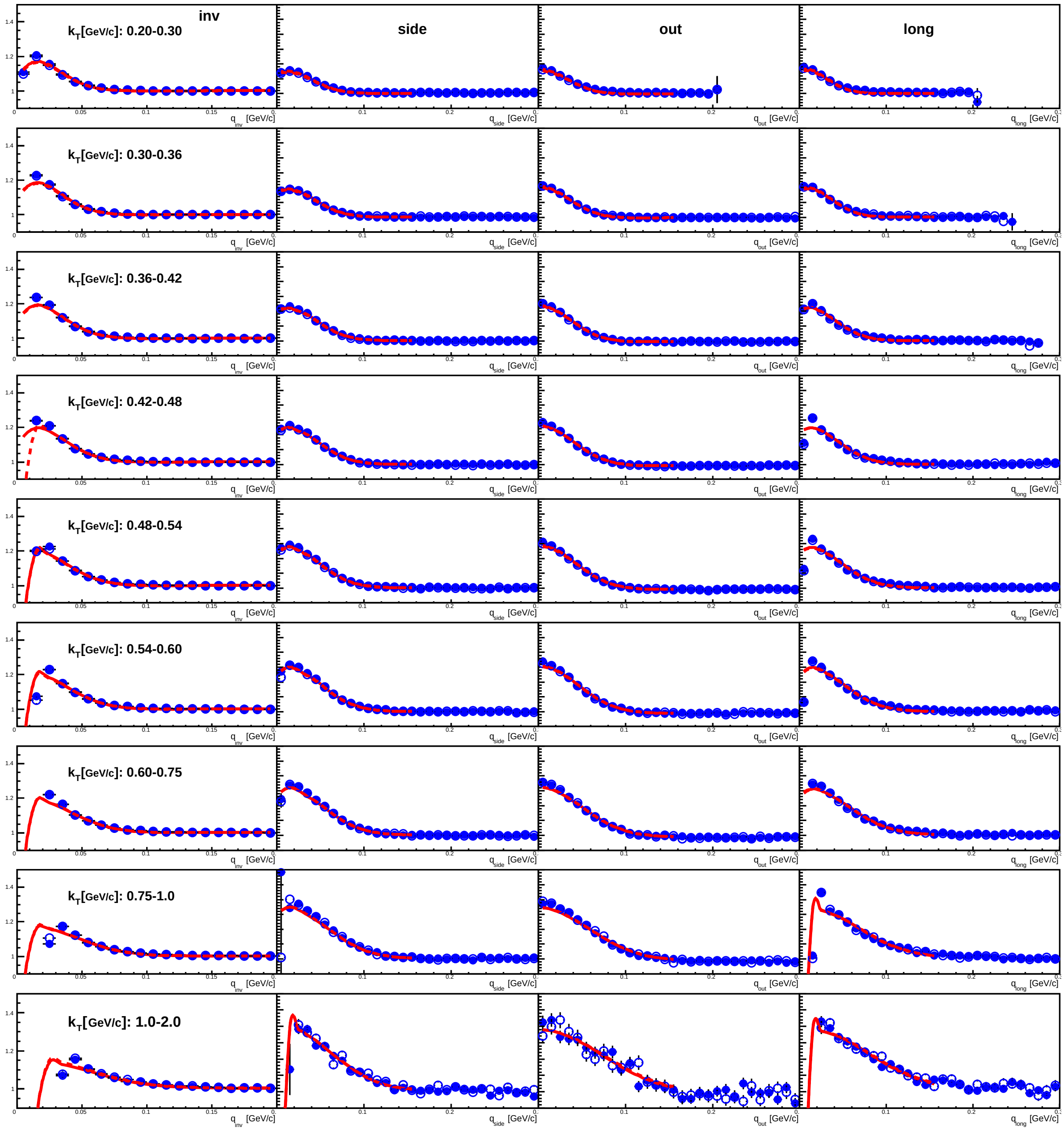

Figure A.3: Correlation functions of charged pion pairs in 20-40% centrality, where solid lines show the fit functions. Filled symbols show positive pion pairs and open symbols show negative pion pairs.

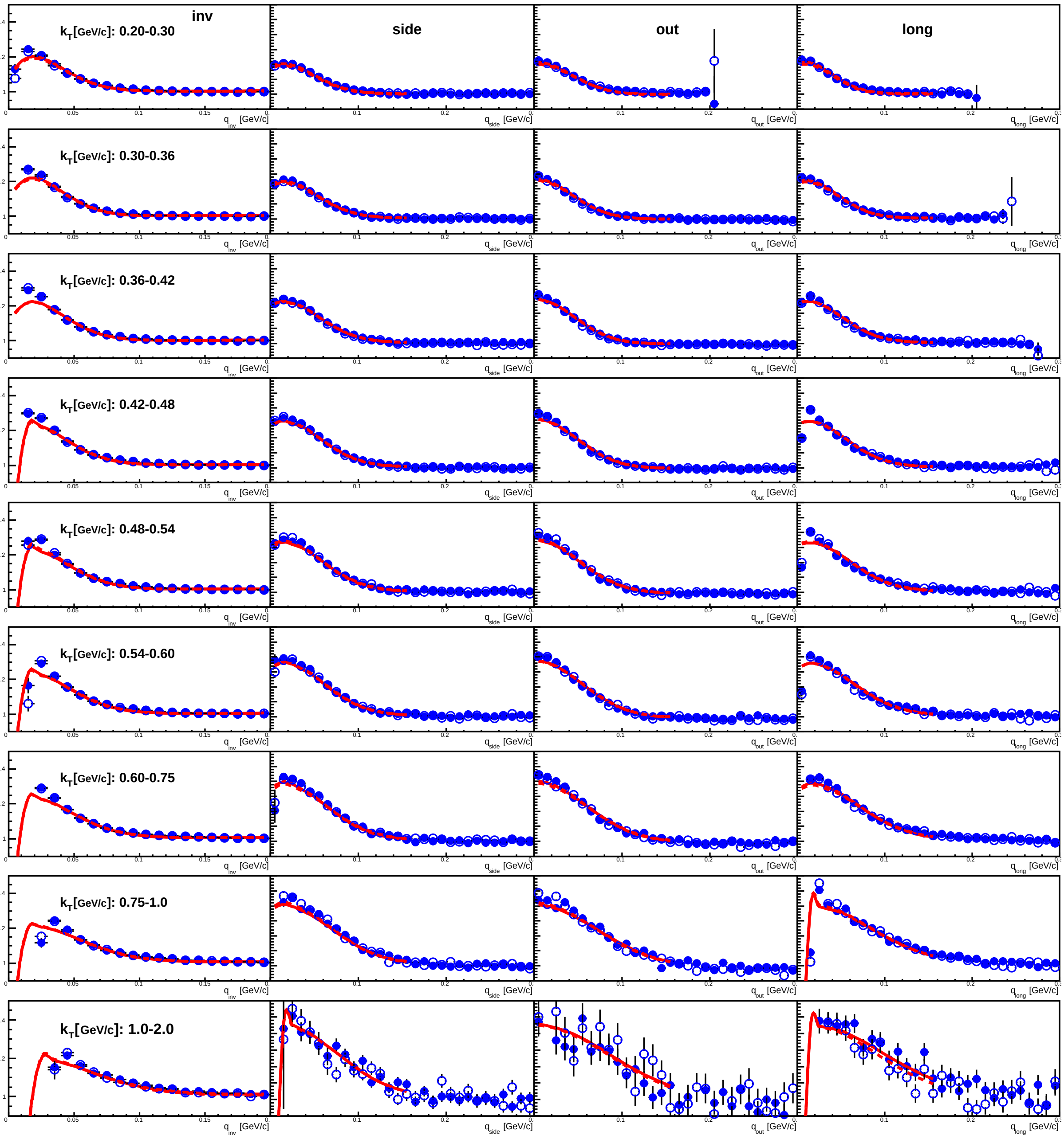

Figure A.4: Correlation functions of charged pion pairs in 40-70% centrality, where solid lines show the fit functions. Filled symbols show positive pion pairs and open symbols show negative pion pairs.

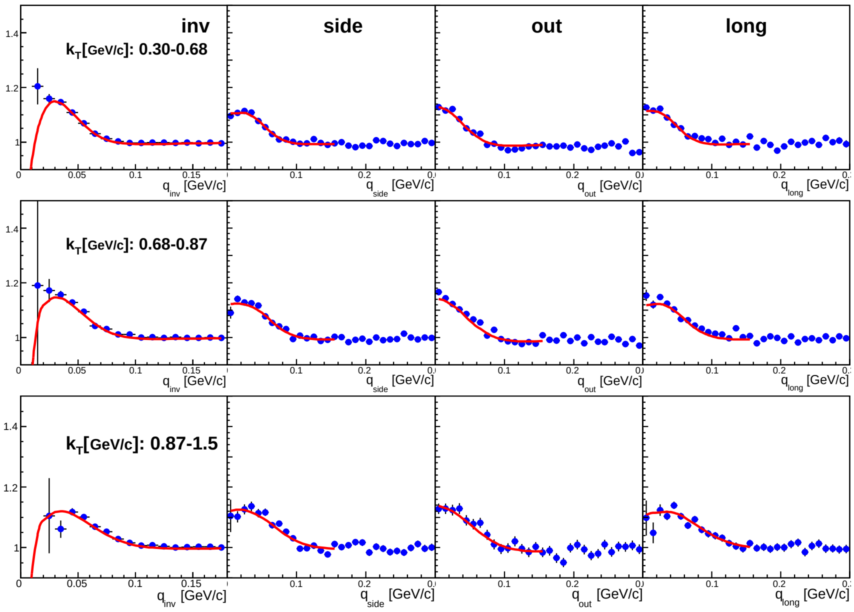

Figure A.5: Correlation functions of charge combined kaon pairs in 0-10% centrality, where solid lines show the fit functions.

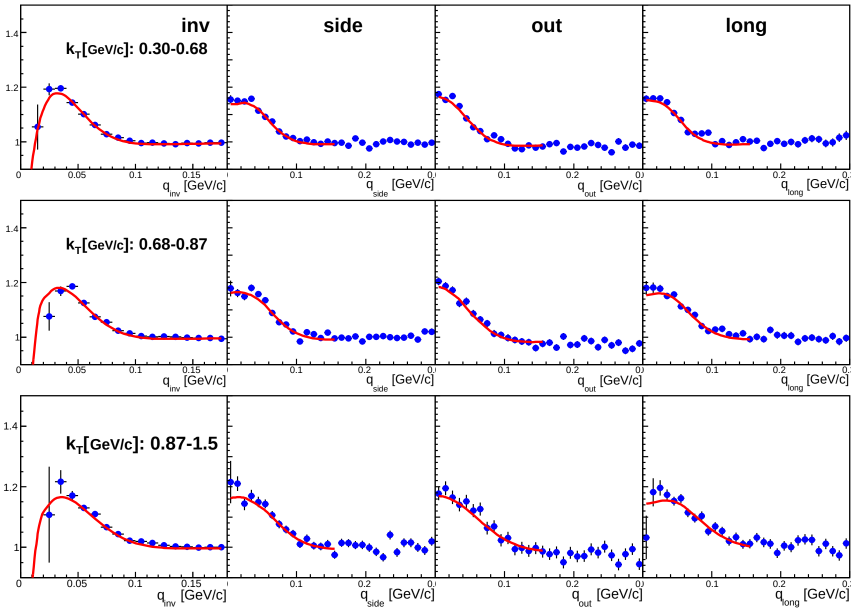

Figure A.6: Correlation functions of charge combined kaon pairs in 10-20% centrality, where solid lines show the fit functions.

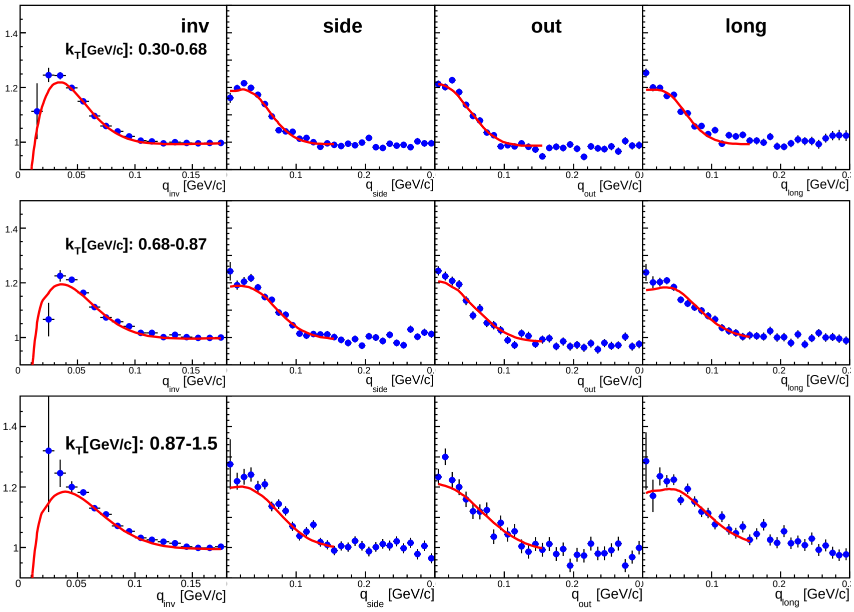

Figure A.7: Correlation functions of charge combined kaon pairs in 20-40% centrality, where solid lines show the fit functions.

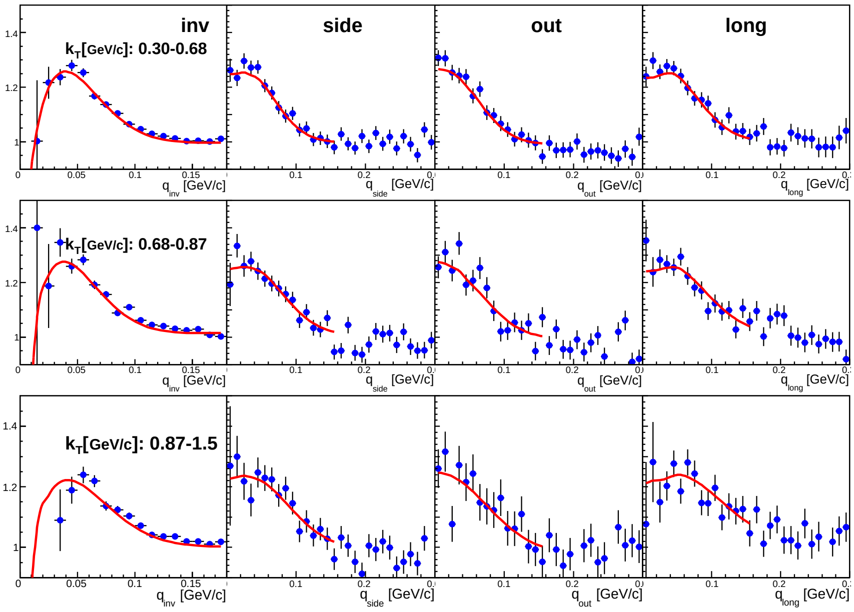

Figure A.8: Correlation functions of charge combined kaon pairs in 40-70% centrality, where solid lines show the fit functions.

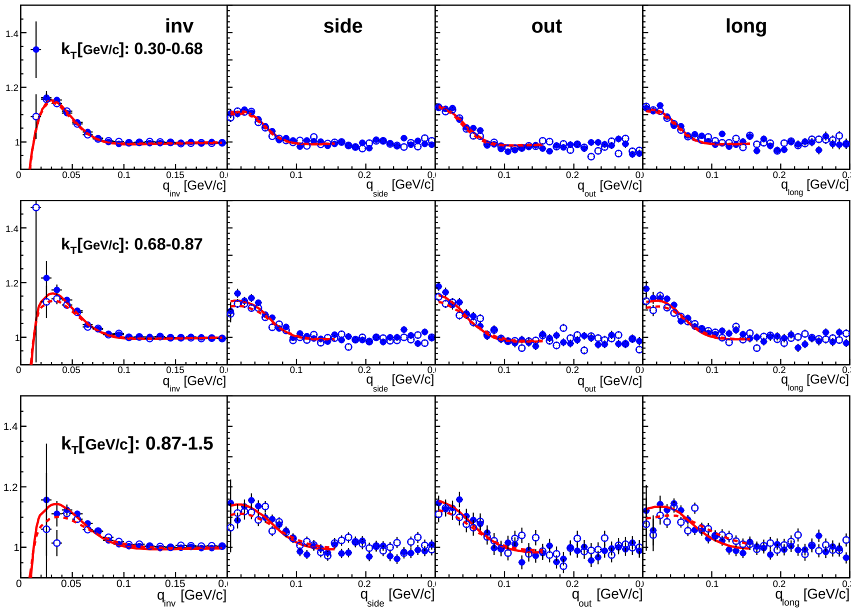

Figure A.9: Correlation functions of charged kaon pairs in 0-10% centrality, where solid lines show the fit functions

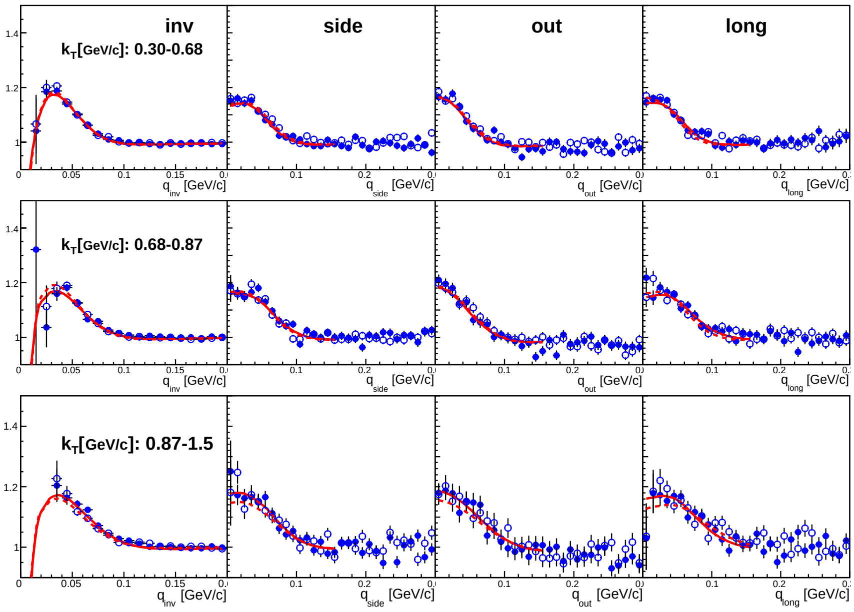

Figure A.10: Correlation functions of charged kaon pairs in 10-20% centrality, where solid lines show the fit functions.

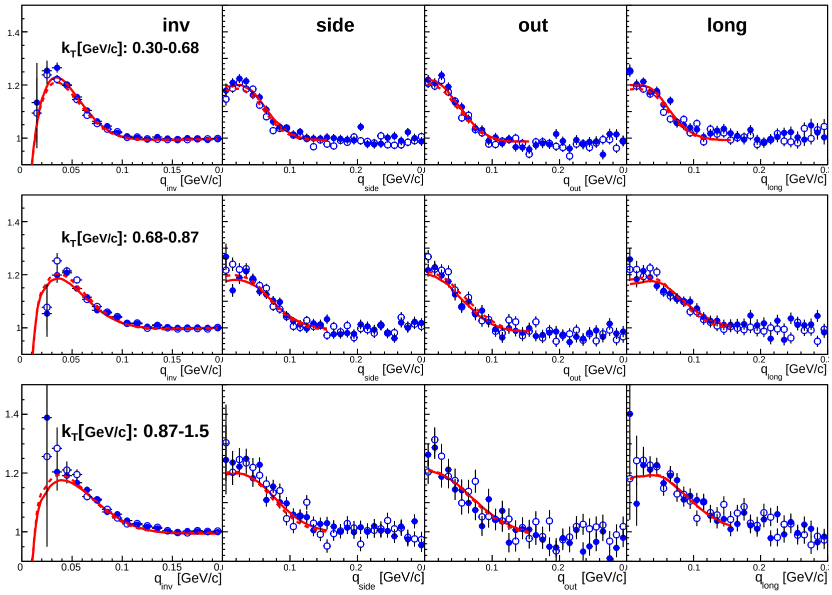

Figure A.11: Correlation functions of charged kaon pairs in 20-40% centrality, where solid lines show the fit functions.

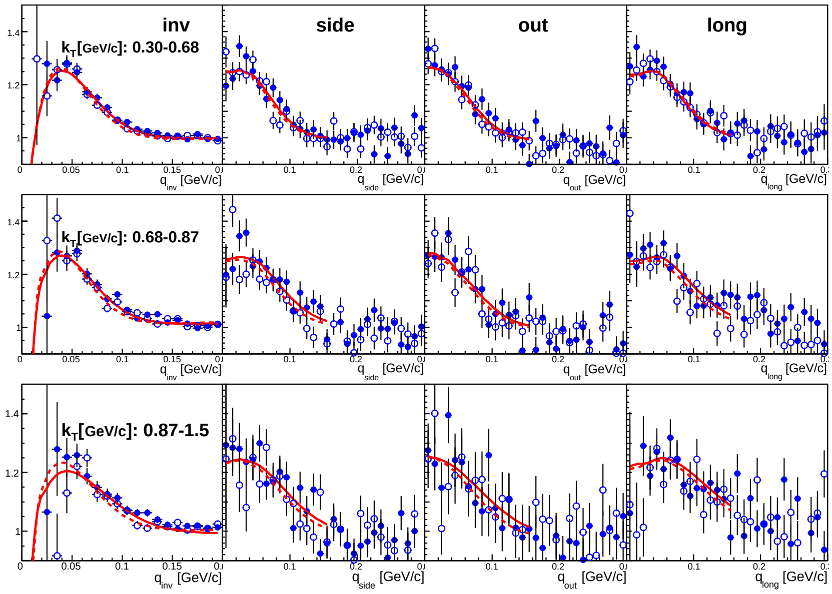

Figure A.12: Correlation functions of charged kaon pairs in 40-70% centrality, where solid lines show the fit functions.

A.3 Correlation Functions of Charged Pions with respect to 2nd-order Event Plane

A.3.1 Centrality Dependence

A.3.2 k_T Dependence

A.4 Correlation Functions of Charged Kaons with respect to 2nd-order Event Plane

A.5 Correlation Functions of Charged Pions with respect to 3rd-order Event Plane

A.5.1 Centrality Dependence

A.5.2 k_T Dependence

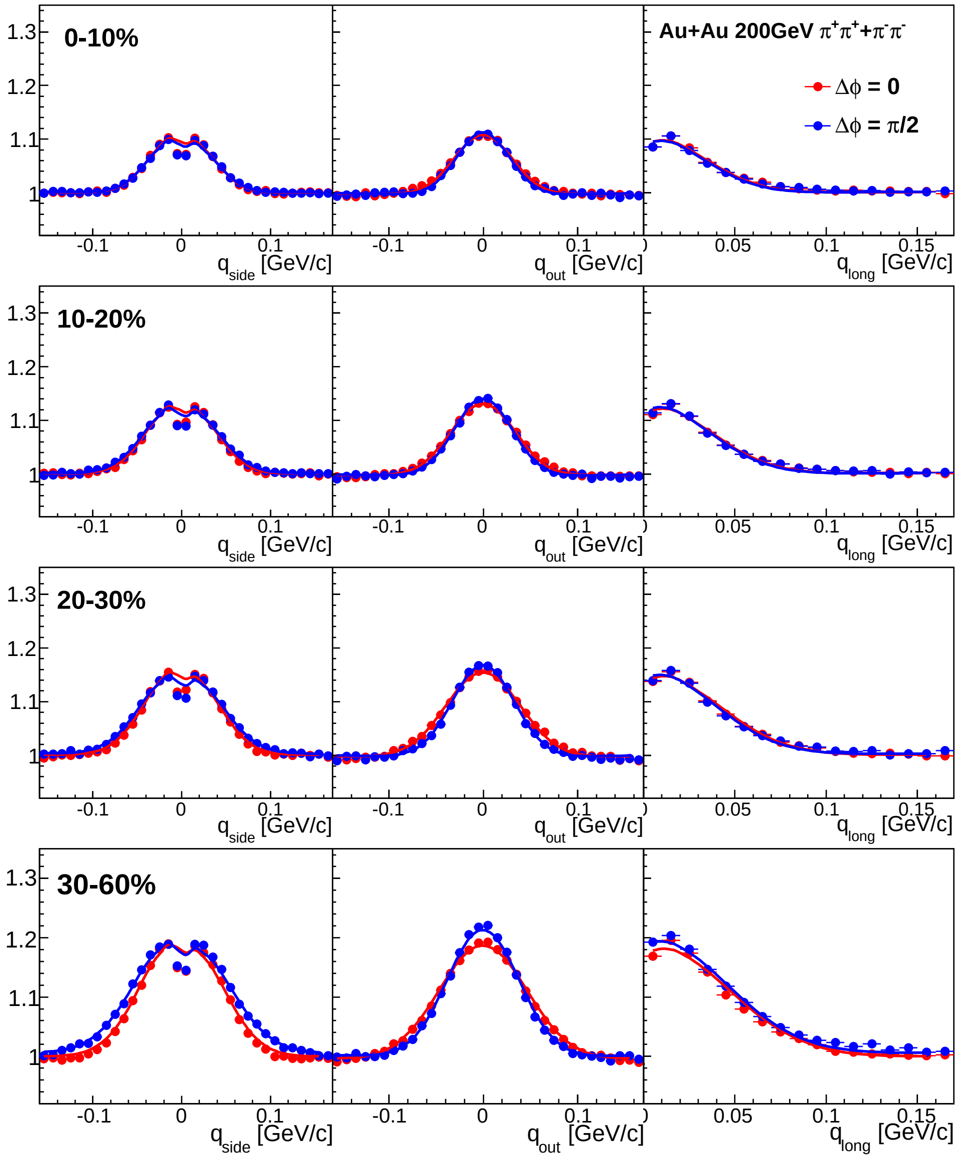

Figure A.13: Projected 3D correlation functions of charged pion pairs measured with respect to 2^{nd}-order event plane for $0.2 < k_T < 2.0$ GeV/c with the correction of the event plane resolution. Correlation functions at $\Delta\phi = 0$ (red symbol) and $\Delta\phi = \pi/2$ (blue symbol) are shown. Correlation functions are projected along each q directions with $q_{other} < 50$ [MeV/c]. Solid lines show the fit functions.

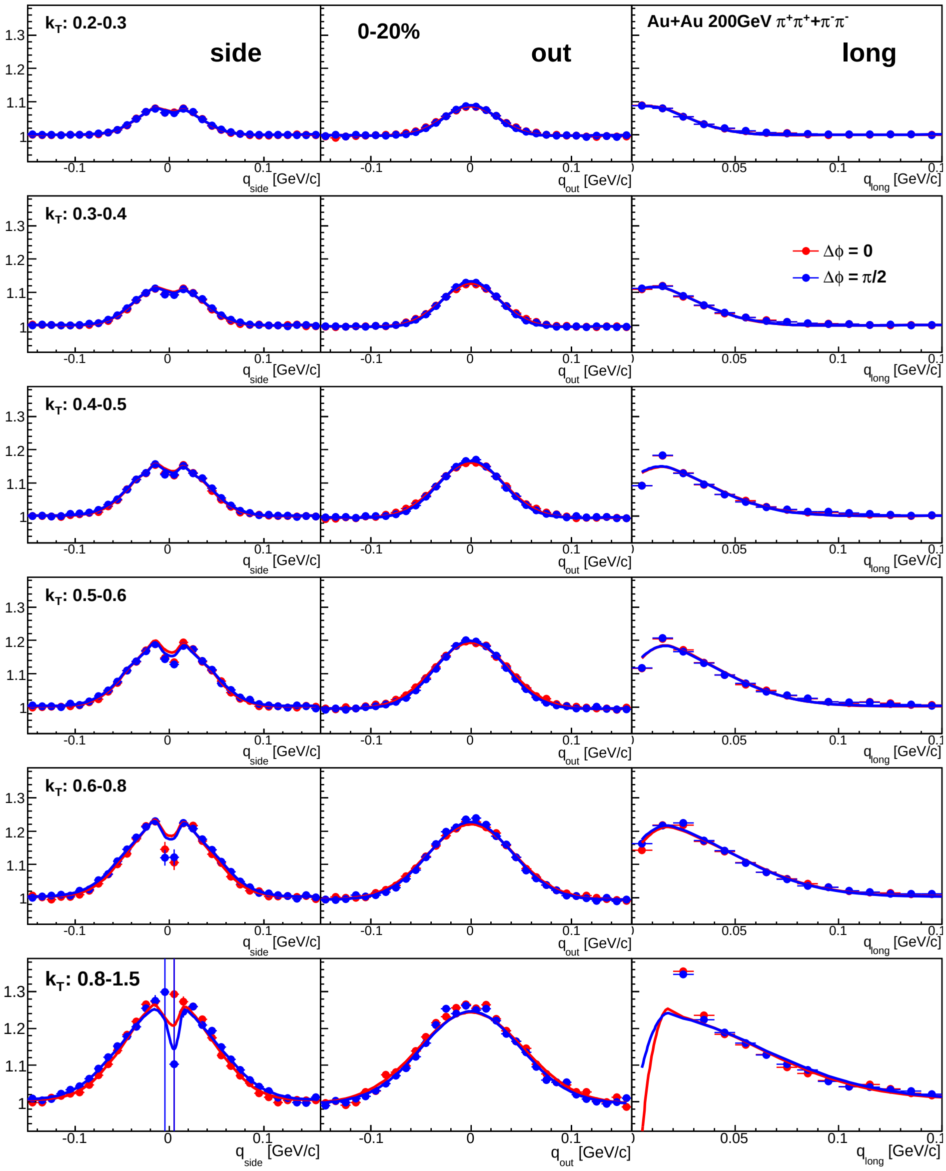

Figure A.14: Projected 3D correlation functions of charged pion pairs measured with respect to 2$^{\mathrm{nd}}$-order event plane for $0.2 < k_T < 2.0$ GeV/c at five k_T bins in 0-20% centrality bin without the correction of the event plane resolution. Correlation functions at $\Delta\phi = 0$ (red symbol) and $\Delta\phi = \pi/2$ (blue symbol) are shown. Correlation functions are projected along each q directions with $q_{other} < 50$ [MeV/c]. Solid lines show the fit functions.

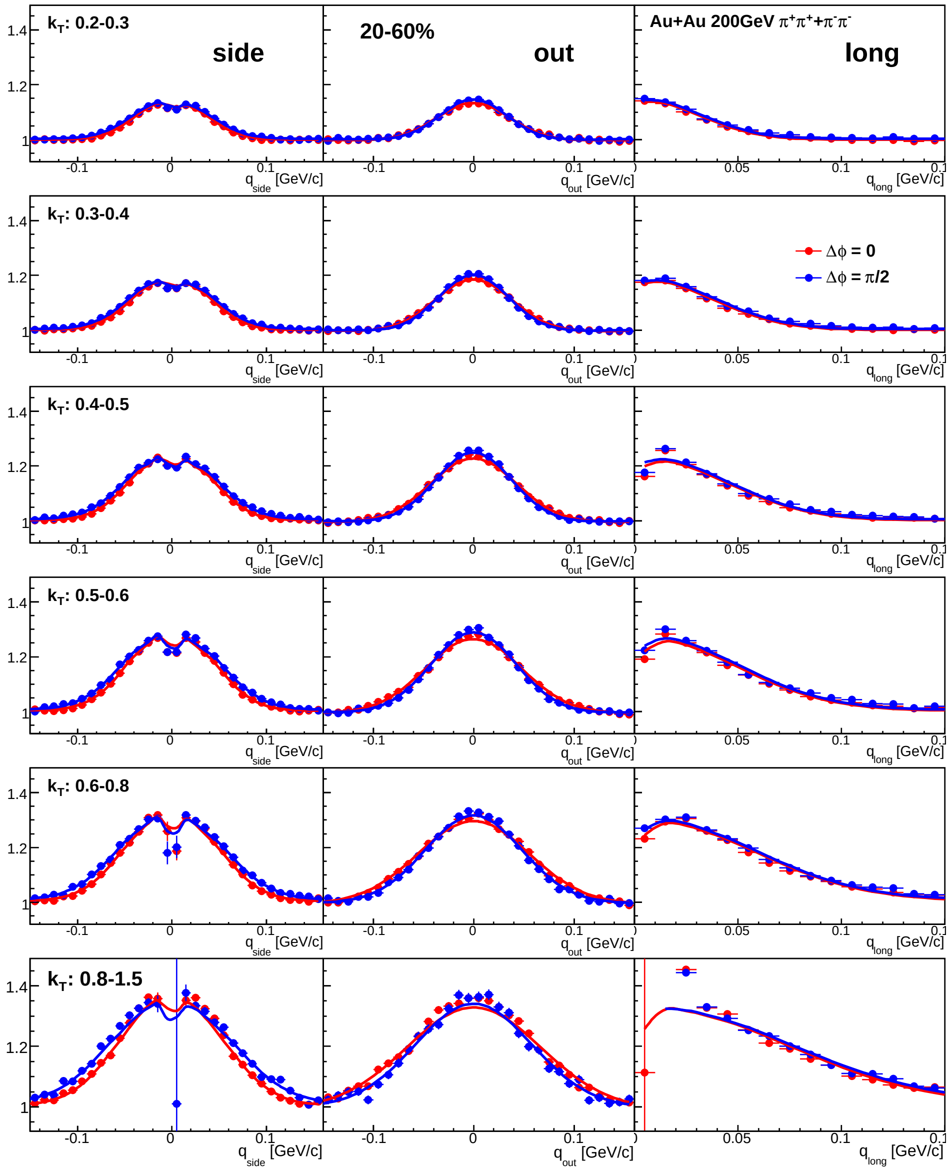

Figure A.15: Projected 3D correlation functions of charged pion pairs measured with respect to 2^{nd}-order event plane for $0.2 < k_T < 2.0$ GeV/c at five k_T bins in 20-60% centrality bin without the correction of the event plane resolution. Correlation functions at $\Delta\phi = 0$ (red symbol) and $\Delta\phi = \pi/2$ (blue symbol) are shown. Correlation functions are projected along each q directions with $q_{other} < 50$ [MeV/c]. Solid lines show the fit functions.

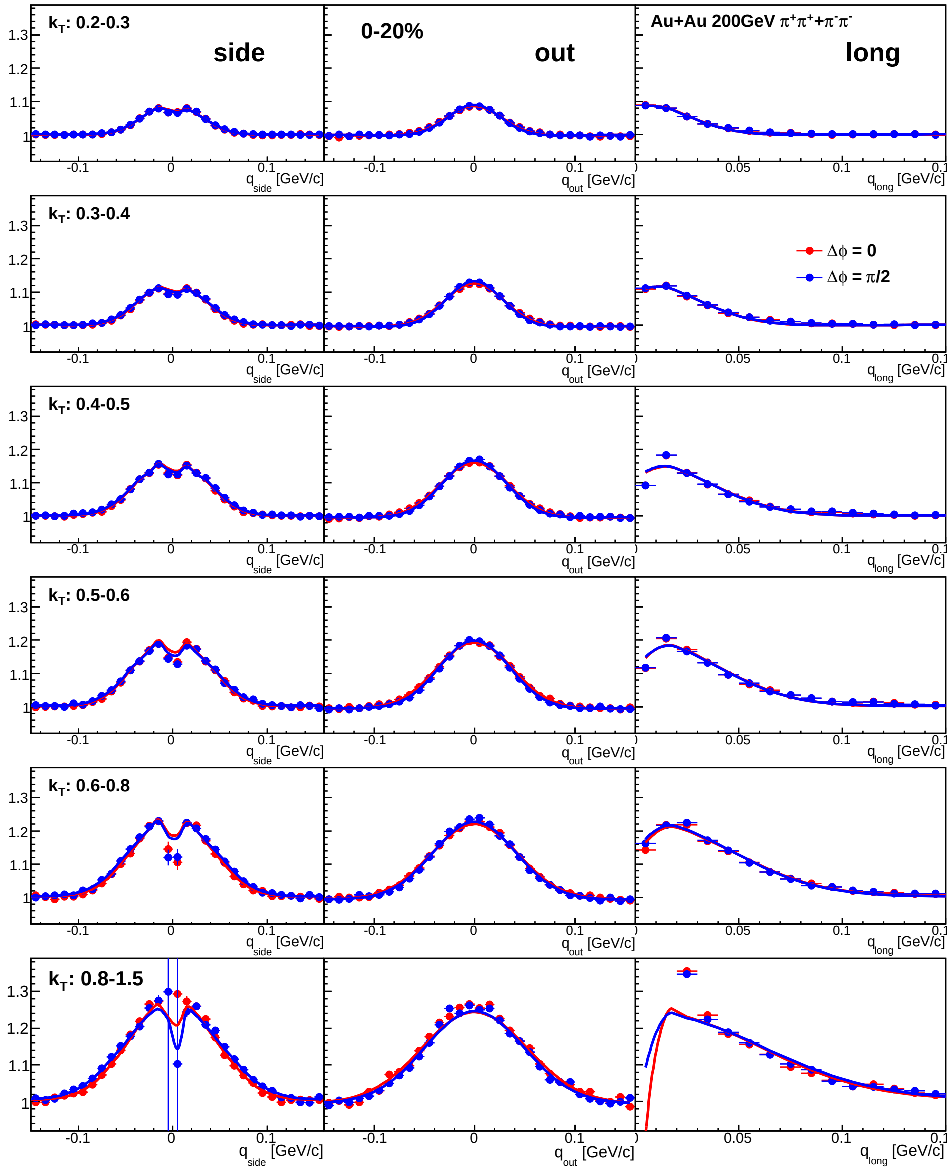

Figure A.16: Projected 3D correlation functions of charged pion pairs measured with respect to 2$^{\mathrm{nd}}$-order event plane for $0.2 < k_T < 2.0$ GeV/c at five k_T bins in 0-20% centrality bin with the correction of the event plane resolution. Correlation functions at $\Delta\phi = 0$ (red symbol) and $\Delta\phi = \pi/2$ (blue symbol) are shown. Correlation functions are projected along each q directions with $q_{other} < 50$ [MeV/c]. Solid lines show the fit functions.

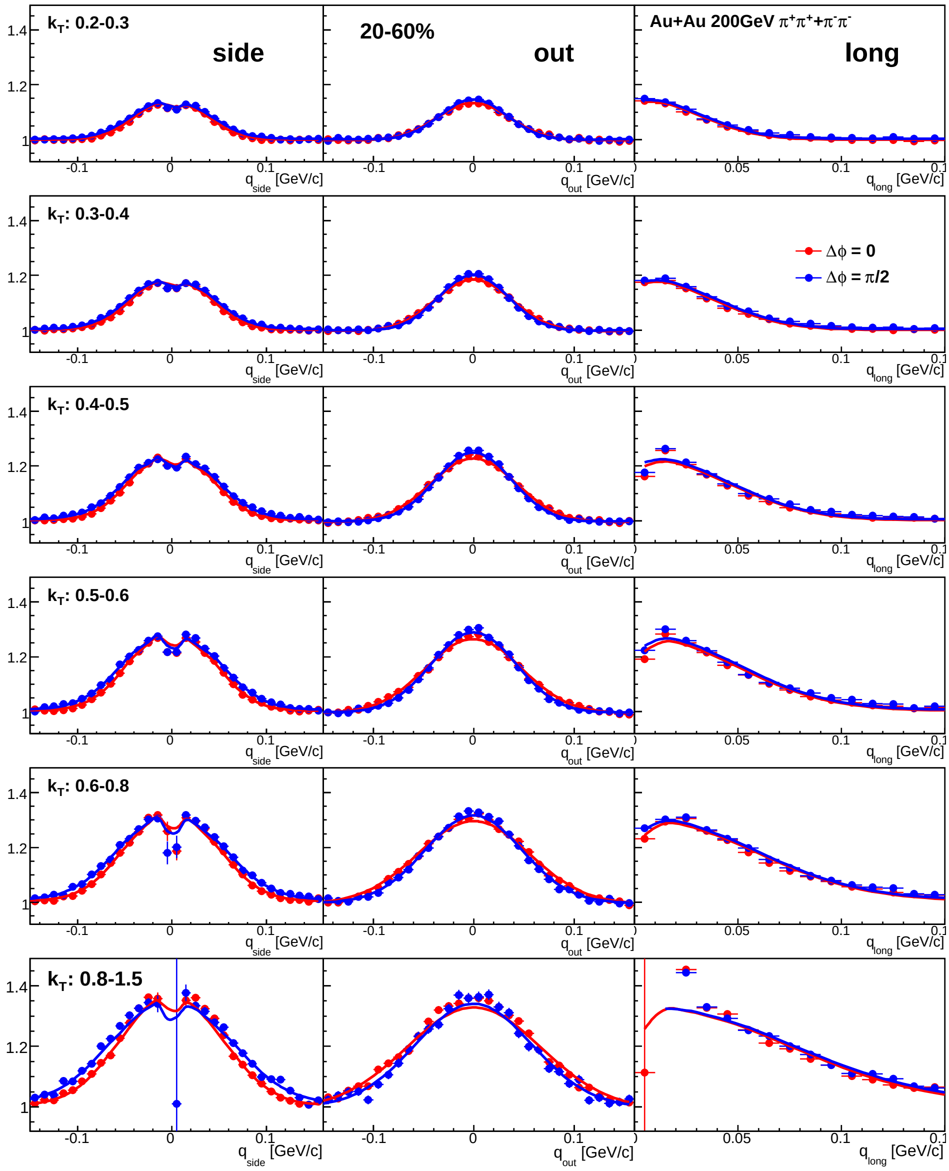

Figure A.17: Projected 3D correlation functions of charged pion pairs measured with respect to 2nd-order event plane for $0.2 < k_T < 2.0$ GeV/c at five k_T bins in 20-60% centrality bin with the correction of the event plane resolution. Correlation functions at $\Delta\phi = 0$ (red symbol) and $\Delta\phi = \pi/2$ (blue symbol) are shown. Correlation functions are projected along each q directions with $q_{other} < 50$ [MeV/c]. Solid lines show the fit functions.

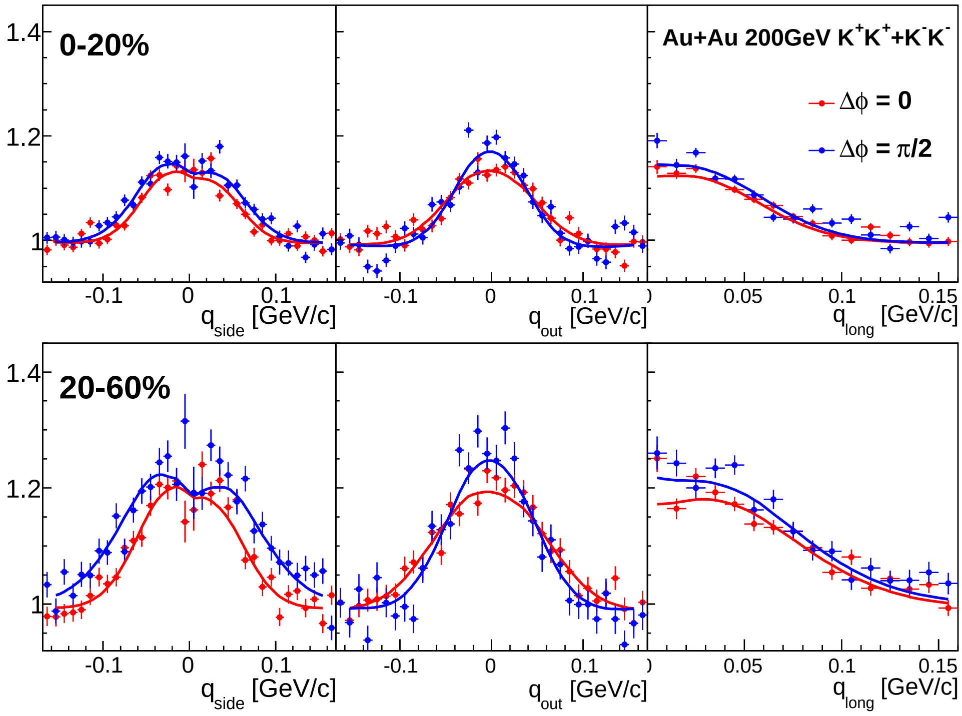

Figure A.18: Projected 3D correlation functions of charged kaon pairs measured with respect to 2^{nd}-order event plane for $0.3 < k_T < 2.0$ GeV/c at 0-20% centrality with the correction of the event plane resolution. Correlation functions at $\Delta\phi = 0$ (red symbol) and $\Delta\phi = \pi/2$ (blue symbol) are shown. Correlation functions are projected along each q directions with $q_{other} < 50$ [MeV/c]. Solid lines show the fit functions.

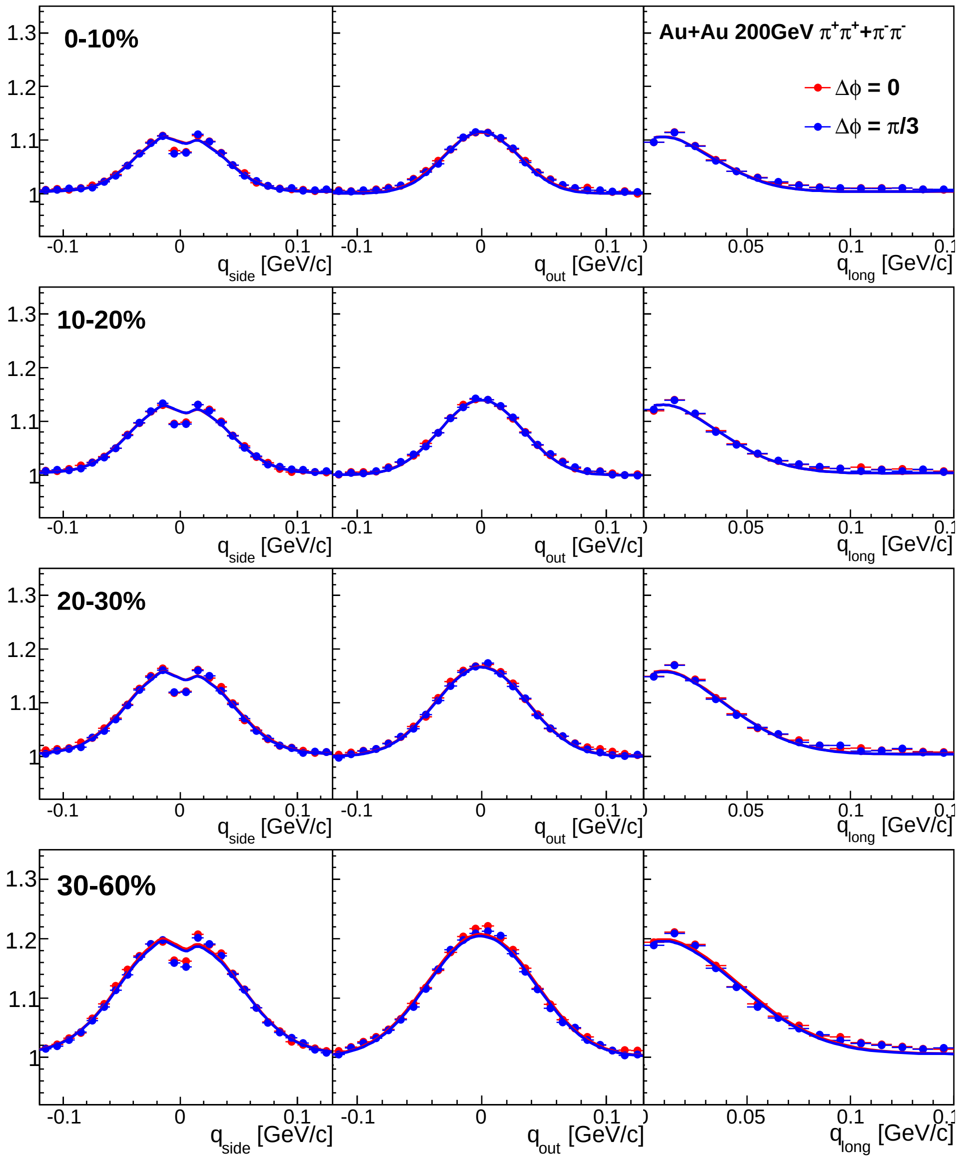

Figure A.19: Projected 3D correlation functions of charged pion pairs measured with respect to 3^{rd}-order event plane for $0.2 < k_T < 2.0$ GeV/c at four centrality bins without the correction of the event plane resolution. Correlation functions at $\Delta\phi = 0$ (red symbol) and $\Delta\phi = \pi/3$ (blue symbol) are shown. Correlation functions are projected along each q directions with $q_{other} < 50$ [MeV/c]. Solid lines show the fit functions.

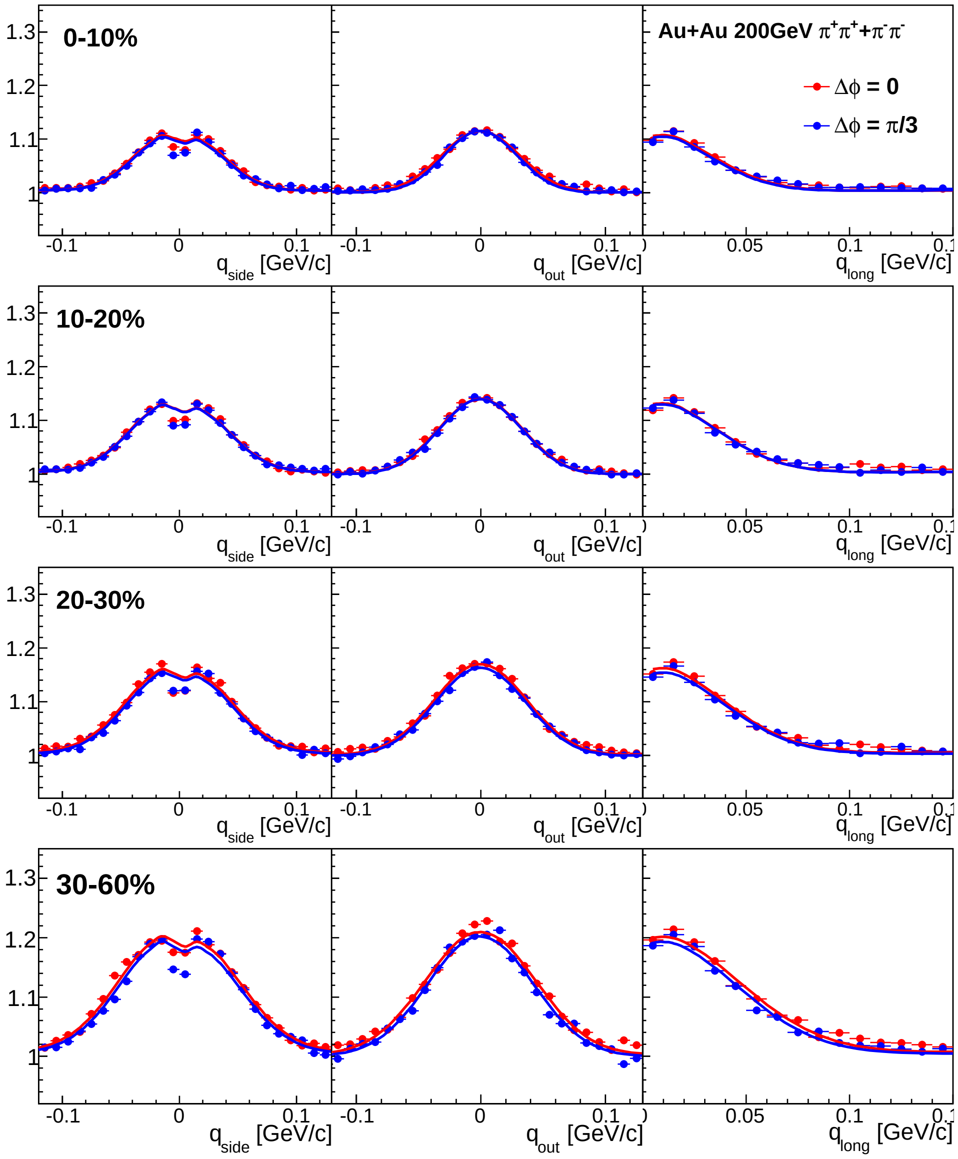

Figure A.20: Projected 3D correlation functions of charged pion pairs measured with respect to 3^{rd}-order event plane for $0.2 < k_T < 2.0$ GeV/c at four centrality bins with the correction of the event plane resolution. Correlation functions at $\Delta\phi = 0$ (red symbol) and $\Delta\phi = \pi/3$ (blue symbol) are shown. Correlation functions are projected along each q directions with $q_{other} < 50$ [MeV/c]. Solid lines show the fit functions.

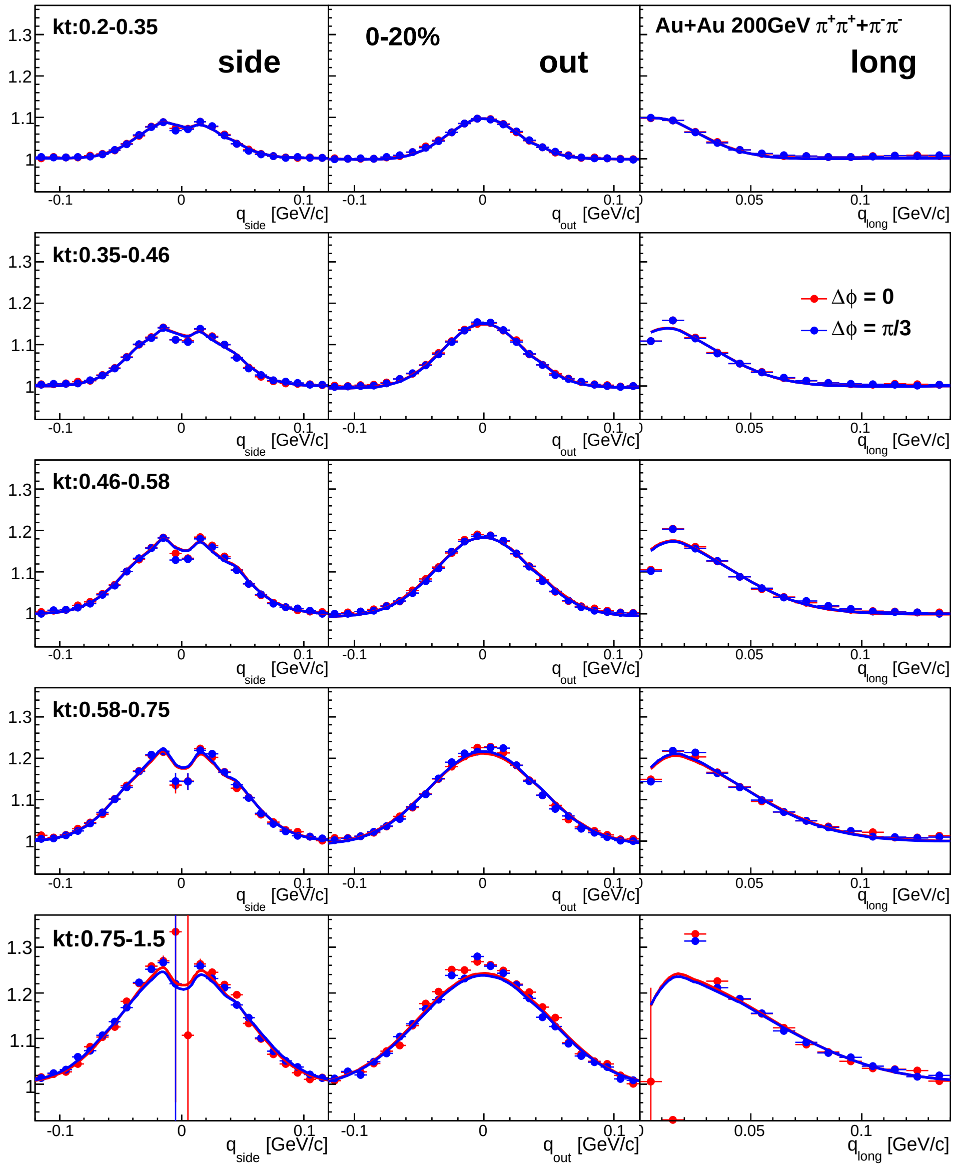

Figure A.21: Projected 3D correlation functions of charged pion pairs measured with respect to 3^{rd}-order event plane for $0.2 < k_T < 2.0$ GeV/c at five k_T bins without the correction of the event plane resolution. Correlation functions at $\Delta\phi = 0$ (red symbol) and $\Delta\phi = \pi/3$ (blue symbol) are shown. Correlation functions are projected along each q directions with $q_{other} < 50$ [MeV/c]. Solid lines show the fit functions.

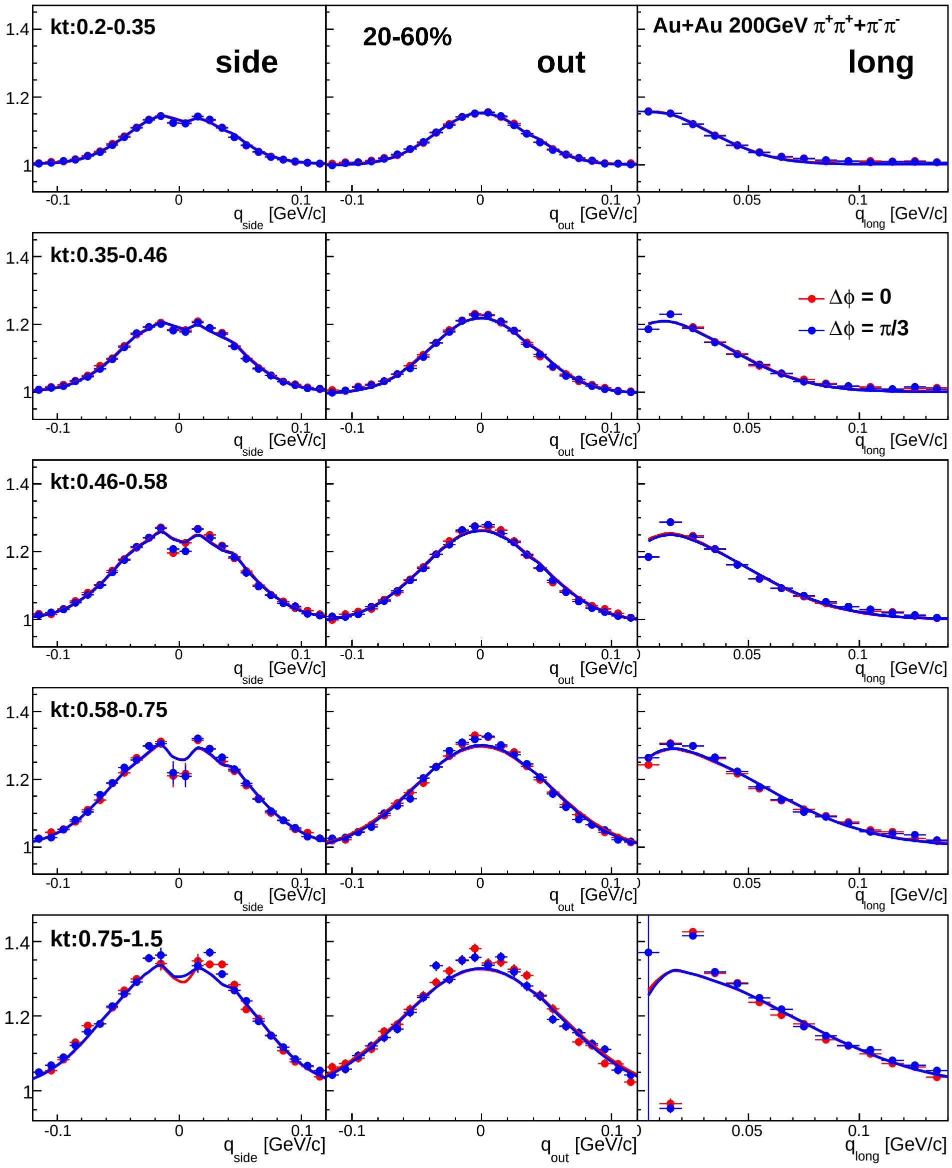

Figure A.22: Projected 3D correlation functions of charged pion pairs measured with respect to 3^{rd}-order event plane for $0.2 < k_T < 2.0$ GeV/c at five k_T bins without the correction of the event plane resolution. Correlation functions at $\Delta\phi = 0$ (red symbol) and $\Delta\phi = \pi/3$ (blue symbol) are shown. Correlation functions are projected along each q directions with $q_{other} < 50$ [MeV/c]. Solid lines show the fit functions.

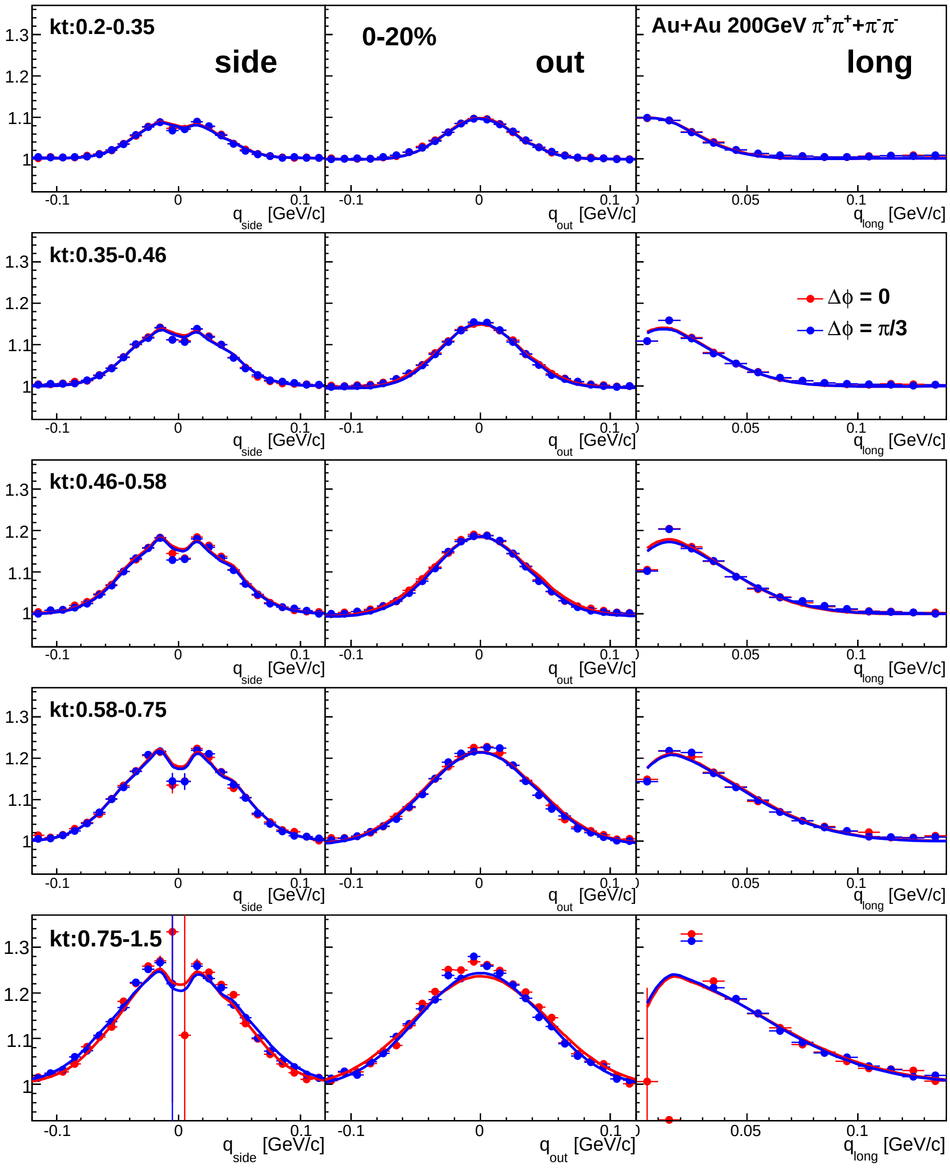

Figure A.23: Projected 3D correlation functions of charged pion pairs measured with respect to 3rd-order event plane for $0.2 < k_T < 2.0$ GeV/c at five k_T bins with the correction of the event plane resolution. Correlation functions at $\Delta\phi = 0$ (red symbol) and $\Delta\phi = \pi/3$ (blue symbol) are shown. Correlation functions are projected along each q directions with $q_{other} < 50$ [MeV/c]. Solid lines show the fit functions.

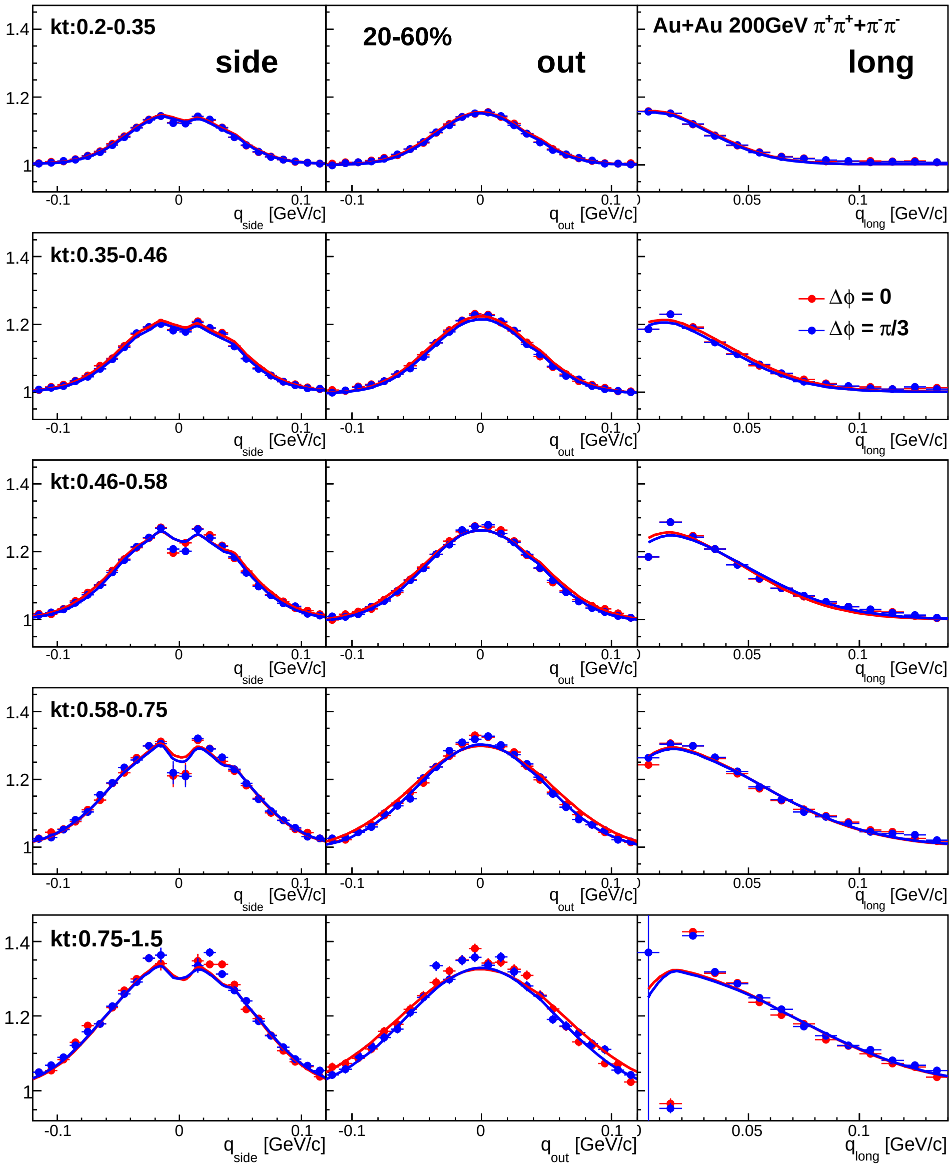

Figure A.24: Projected 3D correlation functions of charged pion pairs measured with respect to 3$^{\rm rd}$-order event plane for $0.2 < k_T < 2.0$ GeV/c at five k_T bins with the correction of the event plane resolution. Correlation functions at $\Delta\phi = 0$ (red symbol) and $\Delta\phi = \pi/3$ (blue symbol) are shown. Correlation functions are projected along each q directions with $q_{other} < 50$ [MeV/c]. Solid lines show the fit functions.

Appendix B

Systematic study of HBT radii

B.1 k_T Dependence of Pion HBT Radii with respect to 2$^{\mathrm{nd}}$-order Event Plane

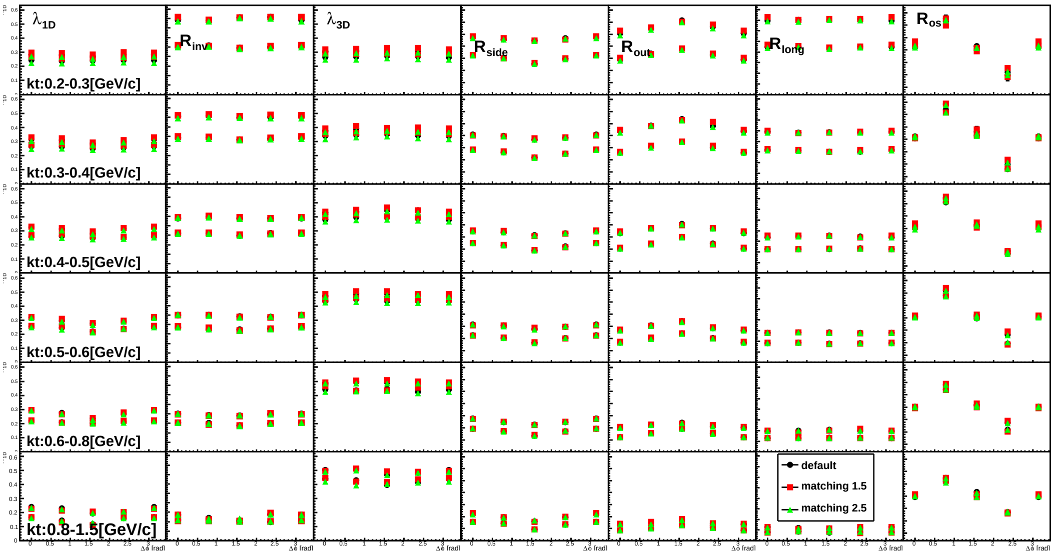

Figure B.1: HBT parameters of charged pions in $0.2 < k_T < 2.0$ GeV/c as a function of azimuthal pair angle with respect to 2$^{\mathrm{nd}}$-order event plane in six k_T and two centrality bins with different matching cuts.

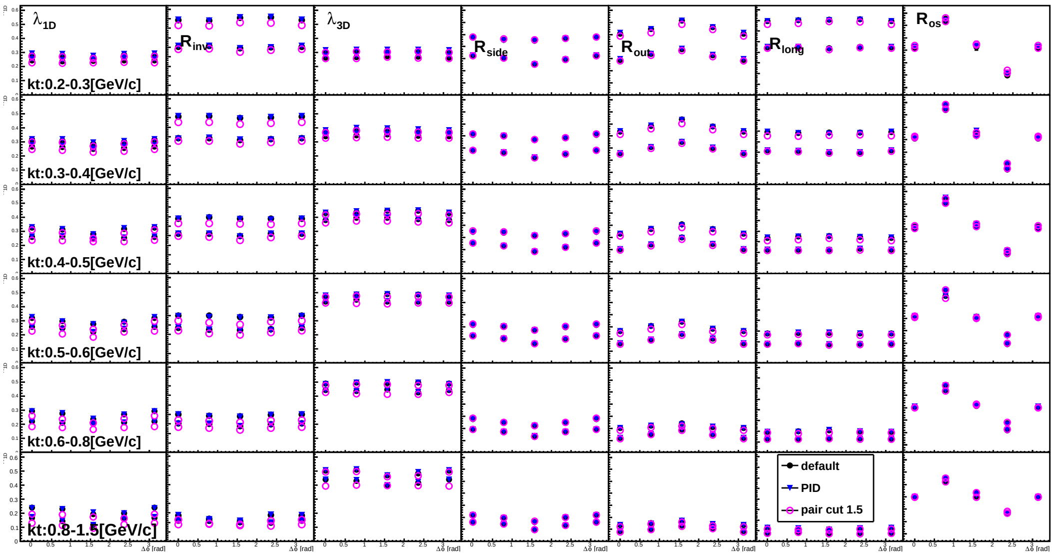

Figure B.2: HBT parameters of charged pions in $0.2 < k_T < 2.0$ GeV/c as a function of azimuthal pair angle with respect to 2^{nd}-order event plane in six k_T and two centrality bins with different PID cut.

B.2 Kaon HBT Radii with respect to 2^{nd}-order Event Plane

B.3 Centrality Dependence of Pion HBT Radii with respect to 3^{rd}-order Event Plane

B.4 k_T Dependence of Pion HBT Radii with respect to 3^{rd}-order Event Plane

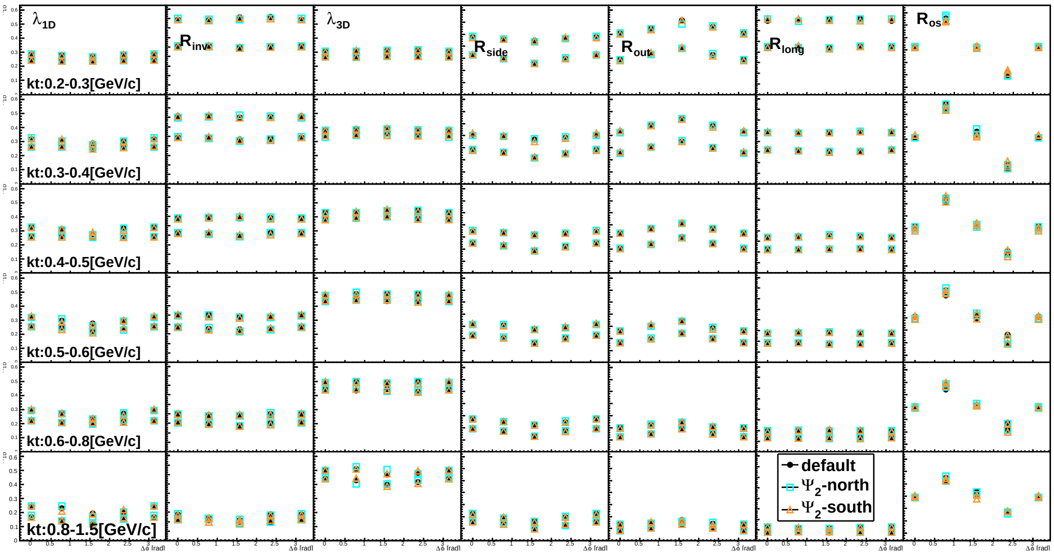

Figure B.3: HBT parameters of charged pions in $0.2 < k_T < 2.0$ GeV/c as a function of azimuthal pair angle with respect to 2$^{\text{nd}}$-order event plane in four k_T and two centrality bins with different event planes.

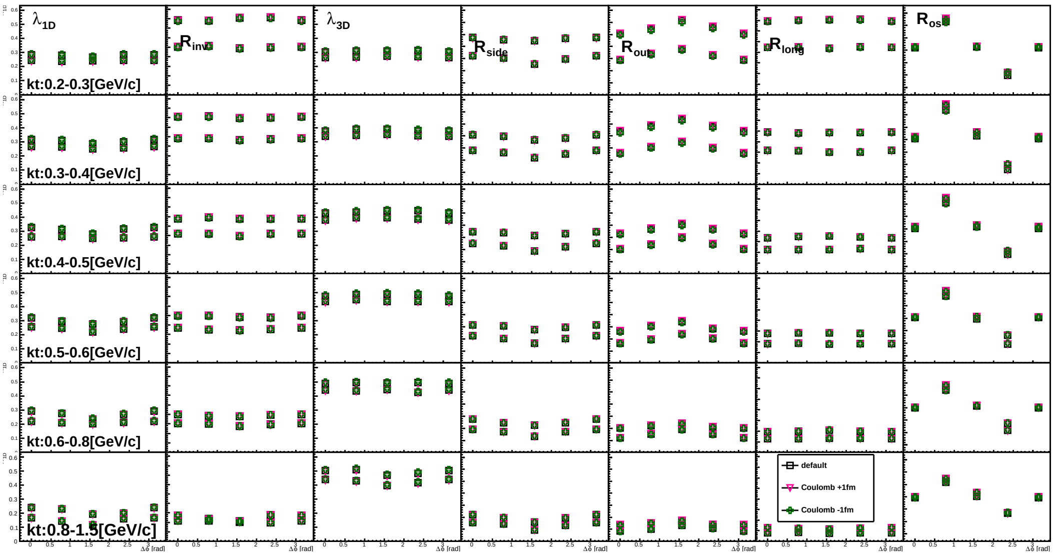

Figure B.4: HBT parameters of charged pions in $0.2 < k_T < 2.0$ GeV/c as a function of azimuthal pair angle with respect to 2$^{\text{nd}}$-order event plane in four k_T and two centrality bins with different input source size for the calculation of the Coulomb interaction.

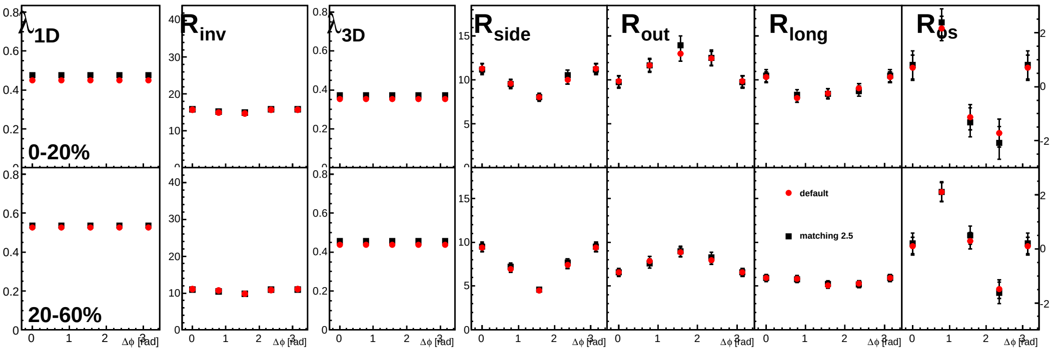

Figure B.5: HBT parameters of charged kaons in $0.3 < k_T < 2.0$ GeV/c as a function of azimuthal pair angle with respect to 2$^{\text{nd}}$-order event plane in two centrality bins with different matching cut.

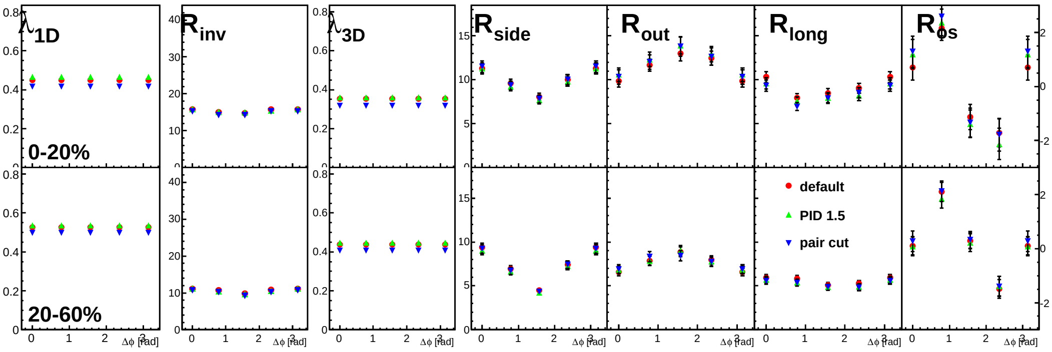

Figure B.6: HBT parameters of charged kaons in $0.3 < k_T < 2.0$ GeV/c as a function of azimuthal pair angle with respect to 2$^{\text{nd}}$-order event plane in two centrality bins with different PID cut.

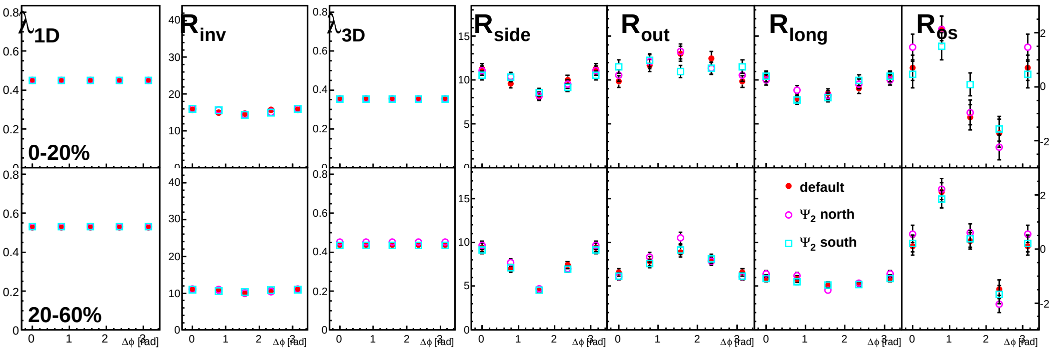

Figure B.7: HBT parameters of charged kaons in $0.3 < k_T < 2.0$ GeV/c as a function of azimuthal pair angle with respect to 2$^{\text{nd}}$-order event plane in two centrality bins with different event planes.

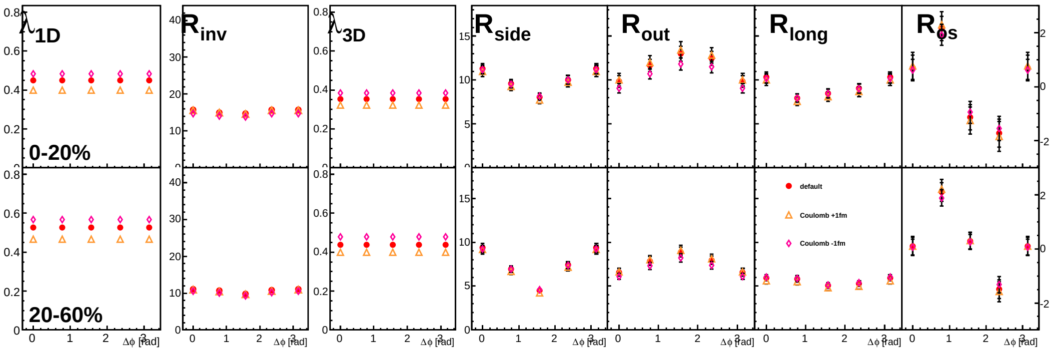

Figure B.8: HBT parameters of charged kaons in $0.3 < k_T < 2.0$ GeV/c as a function of azimuthal pair angle with respect to 2nd-order event plane in two centrality bins with different input source size for the calculation of the Coulomb interaction.

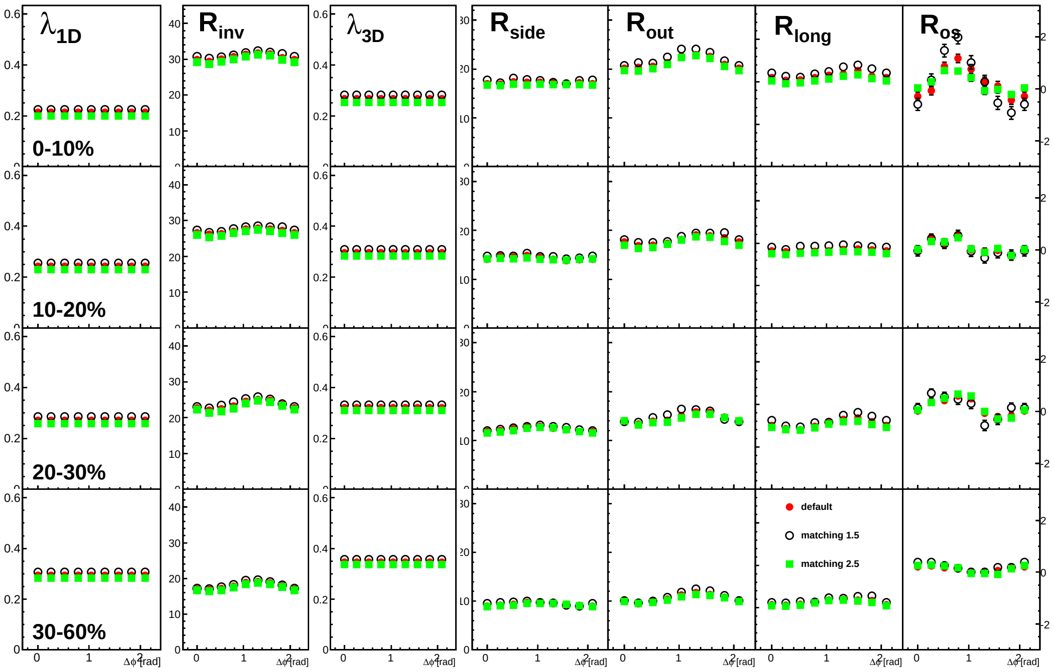

Figure B.9: HBT parameters of charged pions in $0.2 < k_T < 2.0$ GeV/c as a function of azimuthal pair angle with respect to 3rd-order event plane in four centrality bins with different matching cuts.

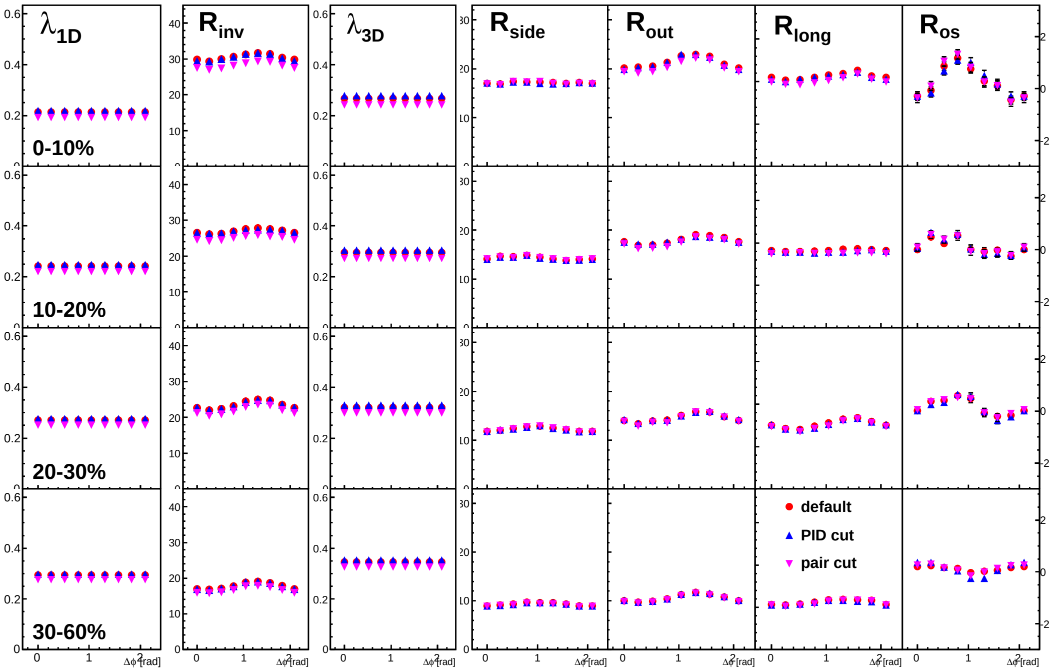

Figure B.10: HBT parameters of charged pions in $0.2 < k_T < 2.0$ GeV/c as a function of azimuthal pair angle with respect to 3rd-order event plane in four centrality bins with different PID cut.

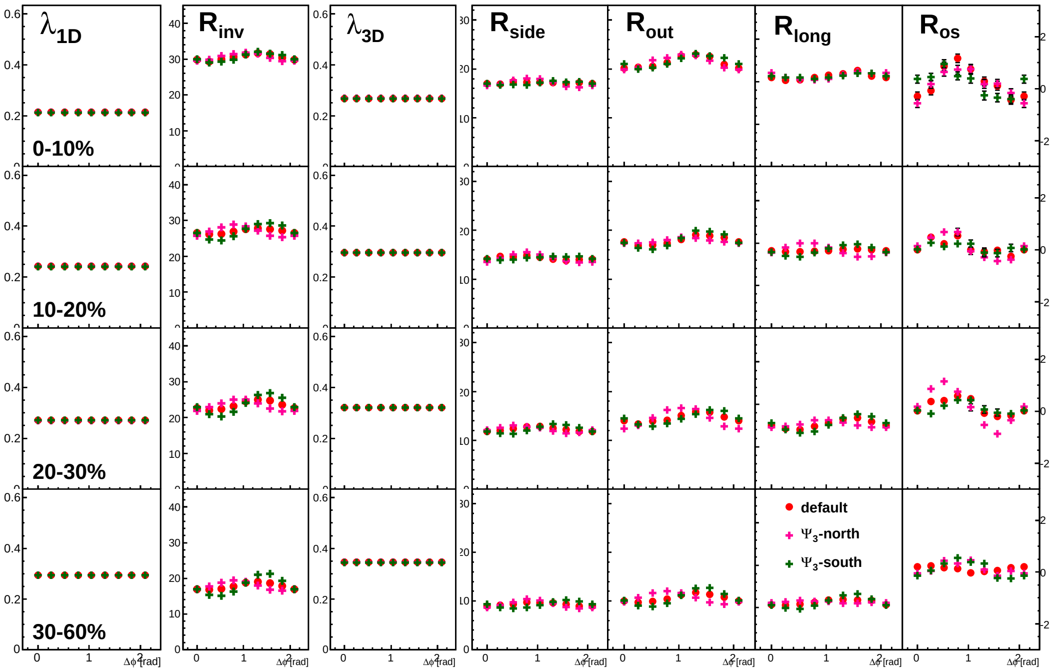

Figure B.11: HBT parameters of charged pions in $0.2 < k_T < 2.0$ GeV/c as a function of azimuthal pair angle with respect to 3rd-order event plane in four centrality bins with different event planes.

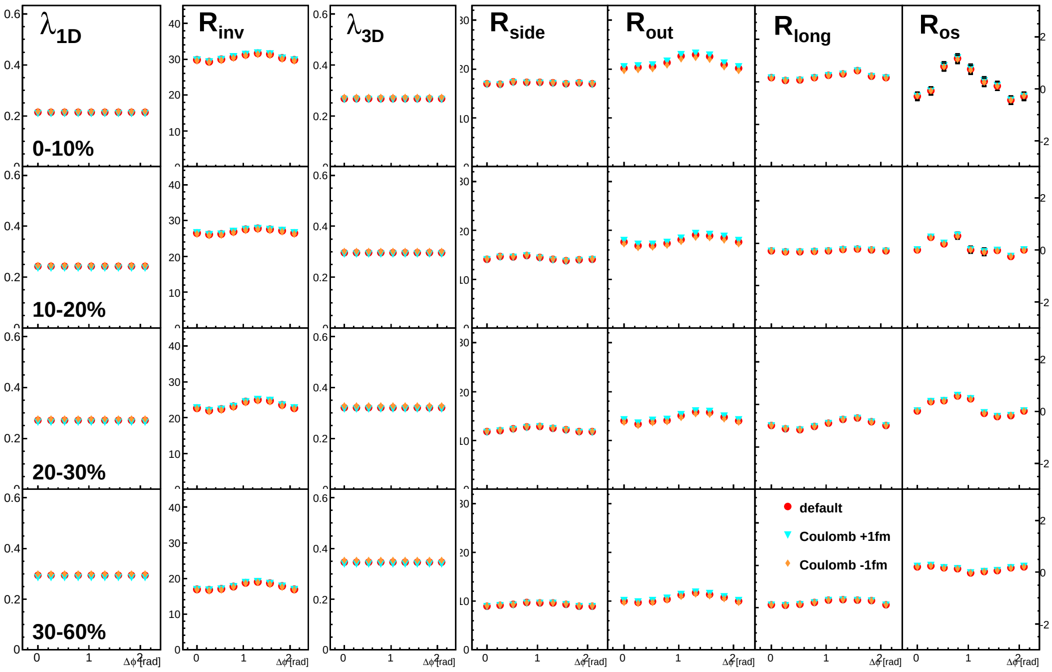

Figure B.12: HBT parameters of charged pions in $0.2 < k_T < 2.0$ GeV$/c$ as a function of azimuthal pair angle with respect to 3rd-order event plane in four centrality bins with different input source size for the calculation of the Coulomb interaction.

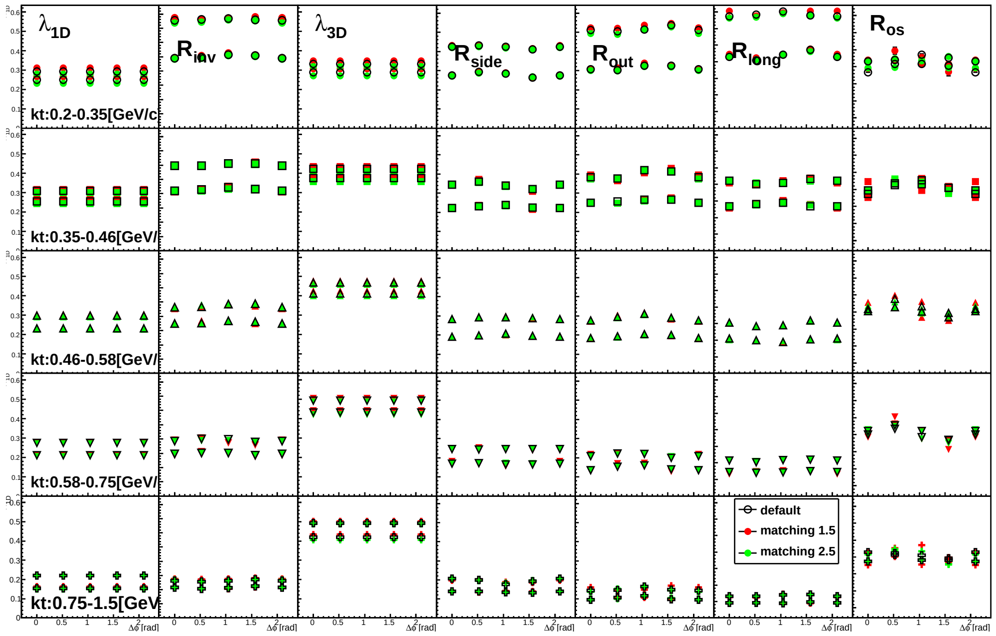

Figure B.13: HBT parameters of charged pions in $0.2 < k_T < 2.0$ GeV$/c$ as a function of azimuthal pair angle with respect to 3rd-order event plane in five k_T and two centrality bins with different matching cuts.

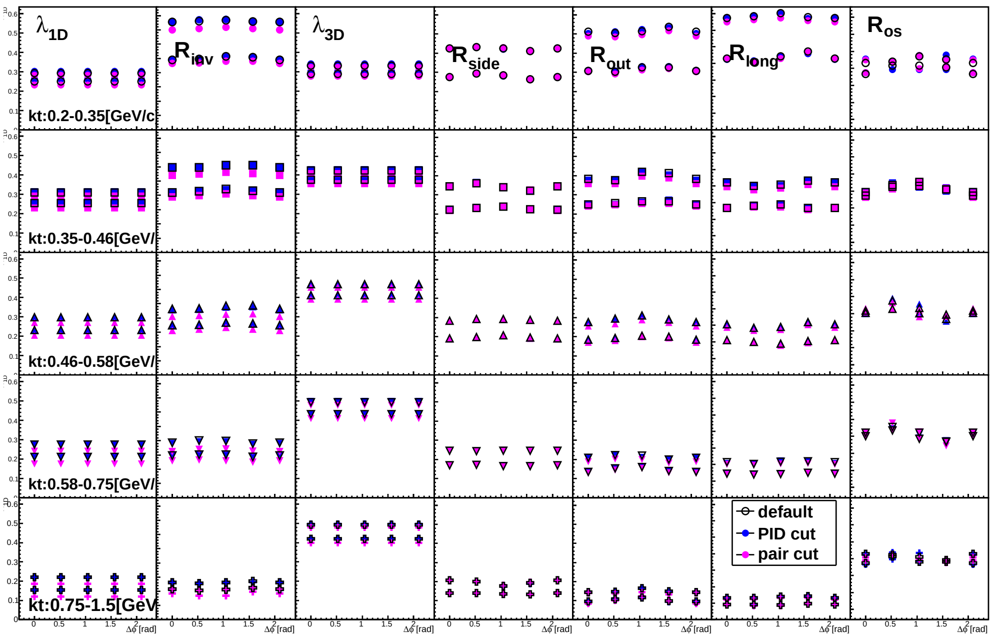

Figure B.14: HBT parameters of charged pions in $0.2 < k_T < 2.0$ GeV/c as a function of azimuthal pair angle with respect to 3rd-order event plane in five k_T and two centrality bins with different PID cut.

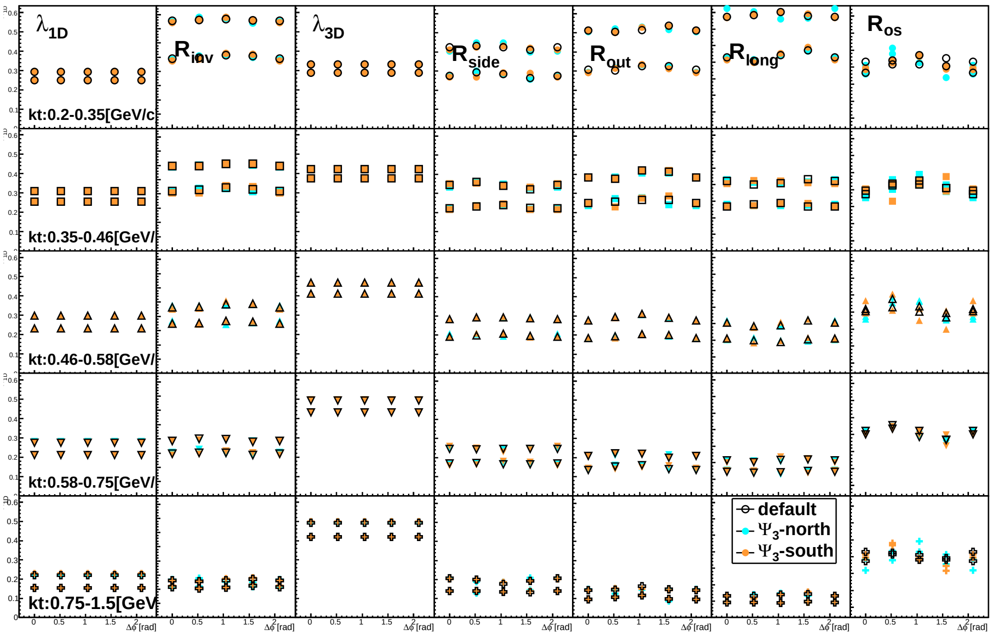

Figure B.15: HBT parameters of charged pions in $0.2 < k_T < 2.0$ GeV/c as a function of azimuthal pair angle with respect to 3rd-order event plane in five k_T and two centrality bins with different event planes.

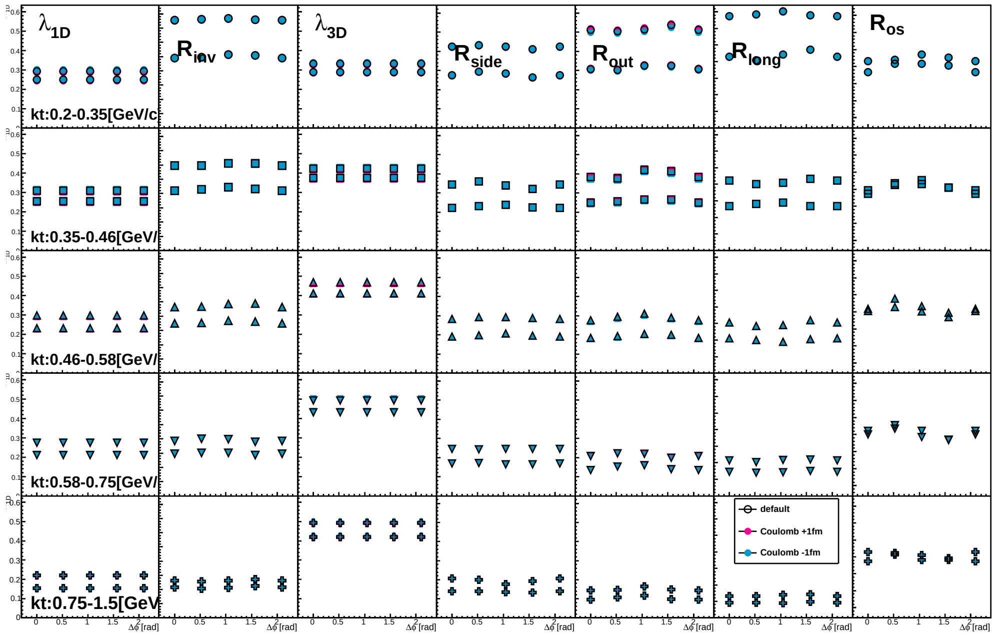

Figure B.16: HBT parameters of charged pions in $0.2 < k_T < 2.0$ GeV/c as a function of azimuthal pair angle with respect to 3^{rd}-order event plane in five k_T and two centrality bins with different input source size for the calculation of the Coulomb interaction.

Appendix C

Galuber Model

C.1 Spatial Eccentricity

Participant eccentricity is defined as:

$$\varepsilon_{part} = \frac{\{y'^2\} - \{x'^2\}}{\{y'^2\} + \{x'^2\}} \tag{C.1}$$

where x' and y' are the coordinates with respect to participant plane angle Ψ and given by

$$x' = r\cos(\phi - \Psi), \tag{C.2}$$
$$y' = r\sin(\phi - \Psi). \tag{C.3}$$

Participant eccentricity is rewritten by using Eq. (C.2), (C.3),

$$\begin{aligned} \varepsilon_{part} &= \frac{\sum r_i^2 \sin^2(\phi_i - \Psi) - \sum r_i^2 \cos^2(\phi_i - \Psi)}{\sum r_i^2}, \\ &= \frac{\sum r_i^2 \left(\sin^2(\phi_i - \Psi) - \cos^2(\phi_i - \Psi)\right)}{\sum r_i^2}, \\ &= \frac{-\sum r_i^2 \cos[2(\phi_i - \Psi)]}{\sum r_i^2}, \\ &= \frac{-\langle r^2 \cos[2(\phi - \Psi)]\rangle}{\langle r^2 \rangle}. \end{aligned} \tag{C.4}$$

The participant plane angle Ψ of a give event is chosen to maximize the eccentricity, therefore we require the following condition:

$$\frac{d\varepsilon_{part}}{d\Psi} = 0. \tag{C.5}$$

The Ψ is determined by solving Eq. (C.5),

$$\begin{aligned} \frac{d}{d\Psi}\left(\sum r_i^2 \cos[2(\phi_i - \Psi)]\right) &= \frac{d}{d\Psi}\left(\sum \left[r_i^2 \cos(2\phi_i)\cos(2\Psi) + r_i^2 \sin(2\phi_i)\sin(2\Psi)\right]\right), \\ &= \sum \left[-2r_i^2 \cos(2\phi_i)\sin(2\Psi) + 2r_i^2 \sin(2\phi_i)\cos(2\Psi)\right], \\ &= 0. \end{aligned}$$

Therefore Ψ is given by

$$\begin{aligned} \tan(2\Psi) &= \frac{\sum r_i^2 \sin(2\phi_i)}{\sum r_i^2 \cos(2\phi_i)}, \\ &= \frac{\langle r^2 \sin(2\phi)\rangle}{\langle r^2 \cos(2\phi)\rangle}. \end{aligned} \tag{C.6}$$

In Eq. (C.4)) we replace Ψ to $\Psi + \pi/2$ so that the eccentricity has positive value.

$$\varepsilon_{part} = \frac{\langle r^2 \cos[2(\phi - \Psi)]\rangle}{\langle r^2\rangle}, \tag{C.7}$$

$$\Psi = \frac{\arctan\left(\langle r^2 \sin(2\phi)\rangle / \langle r^2 \cos(2\phi)\rangle\right) + \pi}{2}. \tag{C.8}$$

Drawing an analogy to the eccentricity, we can express the Eq. (C.9), (C.10) in general forms:

$$\varepsilon_n = \frac{\langle r^2 \cos[n(\phi - \Psi)]\rangle}{\langle r^2\rangle}, \tag{C.9}$$

$$\Psi_n = \frac{\arctan\left(\langle r^2 \sin(n\phi)\rangle / \langle r^2 \cos(n\phi)\rangle\right) + \pi}{n}, \tag{C.10}$$

where in case of $n = 3$ the ε_3 represents triangular anisotropy of participants called triangularity.

C.2 Systematic Uncertainties

Systematic errors are estimated by changing the cross section and the parameters for Woods-Saxon function. The change of parameters is based on the previous study[59, 60, 61]. The list of conditions we have checked are followings:

- default: R=6.38 fm, a= 0.535 fm, σ_{nn}=42 mb
- sys1: change σ_{nn} to 39 mb
- sys2: change σ_{nn} to 45 mb
- sys3: change the Woods-Saxon parameters (R=6.65 fm, a=0.55 fm)
- sys4: change the Woods-Saxon parameters (R=6.25 fm, a=0.53 fm)

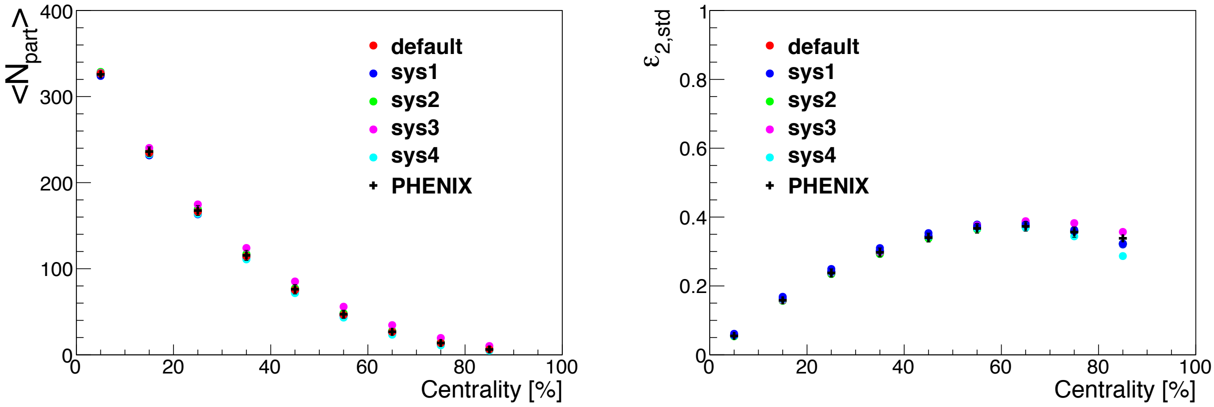

Figure C.1: N_{part} (left) and ε_{std} calculated with different input parameters of Glauber simulation are plotted as a function of centrality. PHENIX official values in Run7 are compared.

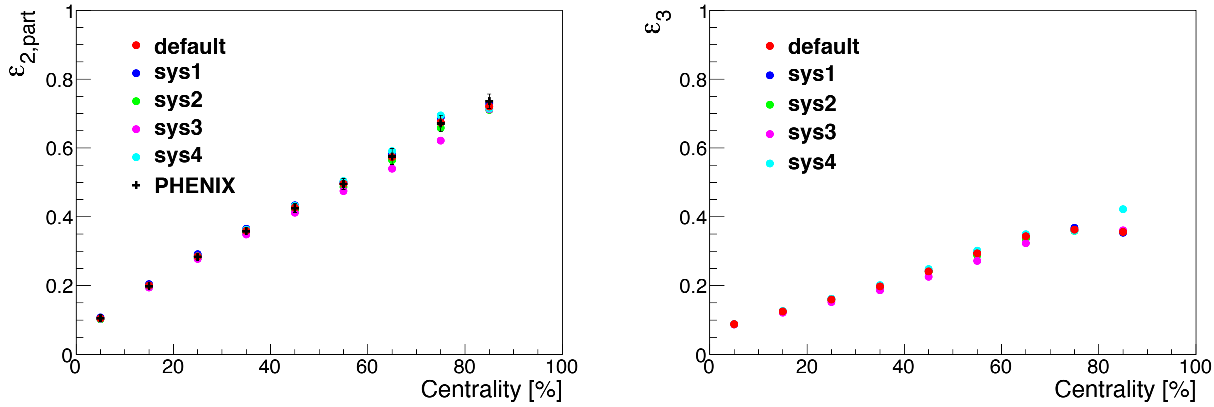

Figure C.2: ε_{part} (left) and ε_3 calculated with different input parameters of Glauber simulation are plotted as a function of centrality. PHENIX official values in Run7 are compared for ε_{part}.

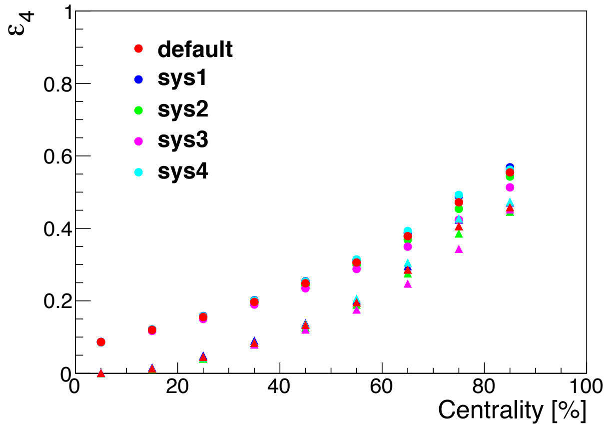

Figure C.3: ε_4 calculated with different input parameters of Glauber simulation are plotted as a function of centrality, where ε_4 is calculated for both Ψ_2 and Ψ_4.

C.3 Data Table of Monte-Carlo Glauber Simulation

Centrality	$\langle N_{part} \rangle$	$\langle \varepsilon_{std} \rangle$	$\langle \varepsilon_2 \rangle$	$\langle \varepsilon_3 \rangle$	$\langle \varepsilon_4(\Psi_4) \rangle$	$\langle \varepsilon_4(\Psi_2) \rangle$
0-10%	326.7	0.057	0.105	0.088	0.086	0.001
	(3.5)	(0.005)	(0.004)	(0.001)	(0.002)	(0.001)
10-20%	234.4	0.163	0.200	0.125	0.120	0.013
	(7.2)	(0.010)	(0.009)	(0.004)	(0.004)	(0.003)
20-30%	166.1	0.242	0.285	0.16	0.155	0.045
	(9.9)	(0.011)	(0.011)	(0.008)	(0.007)	(0.006)
30-40%	114.4	0.302	0.359	0.198	0.197	0.084
	(11)	(0.013)	(0.015)	(0.012)	(0.010)	(0.009)
40-50%	75.2	0.345	0.427	0.241	0.248	0.134
	(10.9)	(0.011)	(0.018)	(0.017)	(0.016)	(0.016)
50-60%	46.3	0.373	0.496	0.294	0.306	0.196
	(10.3)	(0.012)	(0.025)	(0.024)	(0.022)	(0.024)
60-70%	26.4	0.378	0.574	0.343	0.378	0.286
	(8.8)	(0.017)	(0.04)	(0.022)	(0.035)	(0.045)
70-80%	13.5	0.359	0.675	0.363	0.472	0.406
	(6.7)	(0.028)	(0.061)	(0.007)	(0.058)	(0.071)
80-90%	6.2	0.323	0.720	0.356	0.555	0.458
	(4.2)	(0.050)	(0.016)	(0.066)	(0.046)	(0.025)
0-20%	280.4	0.111	0.153	0.107	0.103	0.007
	5.3)	(0.008)	(0.006)	(0.003)	(0.003)	(0.002)
20-60%	100.4	0.316	0.392	0.224	0.227	0.115
	10.7)	(0.012)	(0.018)	(0.016)	(0.014)	(0.013)
0-30%	242.4	0.154	0.197	0.124	0.121	0.020
	(6.7)	(0.009)	(0.008)	(0.004)	(0.004)	(0.003)
30-60%	78.6	0.340	0.428	0.245	0.251	0.138
	(10.8)	(0.012)	(0.020)	(0.018)	(0.016)	(0.016)

Table C.1: The number of participants and initial eccentricity with respect to higher-order participant plane angle calculated by Monte-Carlo Glauber simulation

Appendix D

Simulation

As decried in Sec. 4.5.5, a simple simulation for HBT was performed to make sure the validity of the correction of the event plane resolution. Here we explain the detail of the simulation.

D.1 Generation of Particles

In this simulation, particles with certain 4-dimensional momenta and spatial coordinates are generated by random number. The 4-dimensional momenta are basically given by the following conditions:

- p_T distribution of particles at freeze-out follows the Boltzmann distribution.

  $$\frac{dN}{p_T dp_T} \propto \exp(-\frac{p_T}{T_f}), \tag{D.1}$$

  where T_f is freeze-out temperature.
- Rapidity distribution is uniform within $-1 < y < 1$.
- Azimuthal distribution is uniform within $0 < \phi < 2\pi$.

The spatial coordinates are also determined by giving spatial density distribution such as Gaussian and Woods-saxon distribution.

D.2 HBT Correlation

We need to add HBT correlation between two particles by hand in this simulation. As shown in Eq. (2.3), the strength of the HBT correlation is given by

$$|\Psi_{12}(p_1, p_2)|^2 \propto [1 + \cos(\Delta x \cdot q)] \, . \tag{D.2}$$

The two relative momentum distributions are made using all possible particle pairs which are weighted and not weighted with the strength calculated by Eq. (D.2). The correlation function in this simulation is defined as the ratio of those two distributions.

Appendix E

Blast wave Model

E.1 p_T Spectra and Elliptic Flow

In the blast-wave parameterization suggested in [67], a emission function is given by

$$\begin{aligned} S(r,\phi_s,\tau,\eta) = m_T\cosh(\eta-y)\Omega(r,\phi_s)e^{-(\tau-\tau_0)^2/(2\Delta\tau^2)}, \\ \times\sum_{n=1}^{\infty}(\mp)^{n+1}e^{n\alpha\cos(\phi_b-\phi_p)}e^{-n\beta\cosh(\eta-y)}, \end{aligned} \tag{E.1}$$

where η is the space-time rapidity given by

$$\eta = \frac{1}{2}\ln\left[\frac{t+z}{t-z}\right], \tag{E.2}$$

and p_T is the transverse momentum, m_T is the transverse mass, y is rapidity, ϕ_p is azimuthal angle of particle momentum, and α and β are defined as

$$\alpha = \frac{p_T}{T}\sinh\rho(r,\phi_s), \tag{E.3}$$

$$\beta = \frac{m_T}{T}\cosh\rho(r,\phi_s). \tag{E.4}$$

Since the HBT measurement is usually performed in the longitudinally co-moving system (LCMS), we can simplify Eq. (E.1) by setting y=0.

Observables we want to know, such as spectra, v_2, and HBT radii, are obtained by performing the integral of the emission function Eq. (E.1) over phase space weighted with certain quantity B:

$$\int d^4x\,S(x,K)B(x,K) = \int_0^{2\pi}d\phi_s\int_0^{\infty}rdr\int_{-\infty}^{\infty}d\eta\int_{-\infty}^{\infty}\tau d\tau S(r,\phi_s,\tau,\eta)B(x,K). \tag{E.5}$$

Azimuthally integrated p_T spectra is obtained by integrating over ϕ_p for Eq. (E.5) setting $B(x,K)$=1.

$$\frac{dN}{p_Tdp_T} = \int d\phi_p\int d^4xS(x,K), \tag{E.6}$$

$$\begin{aligned} &= \int d\phi_p\int_0^{2\pi}d\phi_s\int_0^{\infty}rdr\int_{-\infty}^{\infty}d\eta\int_{-\infty}^{\infty}\tau d\tau, \\ &\times\ m_T\cosh(\eta)\Omega(r,\phi_s)e^{-(\tau-\tau_0)^2/(2\Delta\tau^2)},\times\sum_{n=1}^{\infty}(\mp)^{n+1}e^{n\alpha\cos(\phi_b-\phi_p)}e^{-n\beta\cosh(\eta)}. \end{aligned} \tag{E.7}$$

The integral over τ can be calculated as

$$\int_{\infty}^{\infty} d\tau\,\tau e^{-(\tau-\tau_0)^2/2\Delta\tau^2} = \sqrt{2\pi}\,\tau_0\Delta\tau. \tag{E.8}$$

If we assume Boltzmann distribution for all particles, only the first term in the summation in Eq. (E.1) is used. As a result, Eq. (E.7) is rewritten as the following:

$$\begin{aligned} \frac{dN}{p_T dp_T} &= \sqrt{2\pi}\,\tau_0\Delta\tau \int_0^{2\pi} d\phi_p \int_0^{2\pi} d\phi_s \int_0^{\infty} r dr \int_{-\infty}^{\infty} d\eta, \\ &\times\ m_T \cosh(\eta)\Omega(r,\phi_s) \times e^{\alpha\cos(\phi_b-\phi_p)} e^{-\beta\cosh(\eta)}, \\ &= 2\sqrt{2\pi}\,\tau_0\Delta\tau \int_0^{2\pi} d\phi_p \int_0^{2\pi} d\phi_s \int_0^{\infty} r dr\, m_T\Omega(r,\phi_s)\, e^{\alpha\cos(\phi_b-\phi_p)} K_1(\beta), \end{aligned} \tag{E.9}$$

where $K_n(\beta)$ is the modified Bessel function of the second kind, which is defined as

$$K_n(z) = \frac{1}{2}\int_{-\infty}^{\infty} dt \cosh(nt) e^{-z\cosh(t)}. \tag{E.10}$$

Here we replace $\phi_b - \phi_p$ as ϕ', and the range of the integral over ϕ' is from ϕ_b to $\phi_b - 2\pi$. Then the range can be replaced from 0 to 2π because the integrand is the periodic function with 2π. Finally, Eq. (E.9) is rewritten as

$$\frac{dN}{p_T dp_T} = 2(2\pi)^{3/2}\,\tau_0\Delta\tau m_T \int_0^{2\pi} d\phi_s \int_0^{\infty} r dr\, \Omega(r,\phi_s)\, I_0(\alpha) K_1(\beta), \tag{E.11}$$

where I_n is the modified Bessel function of the first kind given by

$$I_n(z) = \frac{1}{2\pi}\int_0^{2\pi} dt \cos(nt) e^{-z\cos(t)}. \tag{E.12}$$

Elliptic flow $v_2$is calculated as

$$v_2(p_T, m) = \frac{\int d\phi_p \int d^4x\ \cos(2\phi_p) S(x,K)}{\int d\phi_p \int d^4x\, S(x,K)}. \tag{E.13}$$

The denominator is the same expression with Eq. (E.11). The numerator can be calculated by a similar way to derive the p_T spectra.

$$\begin{aligned} &\int d\phi_p \int d^4x\ \cos(2\phi_p) S(x,K), \\ &= 2\sqrt{2\pi}\,\tau_0\Delta\tau \int_0^{2\pi} d\phi_p \int_0^{2\pi} d\phi_s \int_0^{\infty} r dr\, m_T\Omega(r,\phi_s)\ \cos(2\phi_p) e^{\alpha\cos(\phi_b-\phi_p)} K_1(\beta), \\ &= 2\sqrt{2\pi}\,\tau_0\Delta\tau \int_0^{2\pi} d\phi_p \int_0^{\infty} r dr\, m_T\Omega(r,\phi_s) K_1(\beta)\cos(2\phi_b) \int_0^{2\pi} d\phi' \cos(2\phi_,) e^{\alpha\cos(\phi')}, \\ &= 2(2\pi)^{3/2}\,\tau_0\Delta\tau m_T \int_0^{2\pi} d\phi_p \int_0^{\infty} r dr\, \Omega(r,\phi_s) K_1(\beta)\cos(2\phi_b) I_2(\alpha). \end{aligned} \tag{E.14}$$

Finally, the elliptic flow is expressed as

$$v_2(p_T, m) = \frac{\int_0^{2\pi} d\phi_p \int_0^{\infty} r dr\, \Omega(r,\phi_s) K_1(\beta)\cos(2\phi_b) I_2(\alpha)}{\int_0^{2\pi} d\phi_s \int_0^{\infty} r dr\, \Omega(r,\phi_s)\, I_0(\alpha) K_1(\beta)}. \tag{E.15}$$

E.2 HBT Radii

In the Bertsch-Pratt parameterization described in Sec. 2.2.2, four HBT radii are related to space-time variance as [67]

$$\begin{aligned}
R_s^2 &= \frac{1}{2}(\langle \tilde{x}^2\rangle + \langle \tilde{y}^2\rangle) - \frac{1}{2}(\langle \tilde{x}^2\rangle - \langle \tilde{y}^2\rangle)\cos(2\phi_p) - \langle \tilde{x}\tilde{y}\rangle \sin(2\phi_p), && \text{(E.16)}\\
R_o^2 &= \frac{1}{2}(\langle \tilde{x}^2\rangle + \langle \tilde{y}^2\rangle) + \frac{1}{2}(\langle \tilde{x}^2\rangle - \langle \tilde{y}^2\rangle)\cos(2\phi_p) + \langle \tilde{x}\tilde{y}\rangle \sin(2\phi_p), &&\\
&\quad -2\beta_T(\langle \tilde{t}\tilde{x}\rangle \cos\phi_p + \langle \tilde{t}\tilde{y}\rangle \sin\phi_p) + \beta_T^2\langle \tilde{t}^2\rangle, && \text{(E.17)}\\
R_{os}^2 &= \langle \tilde{x}\tilde{y}\rangle \cos(2\phi_p) - \frac{1}{2}(\langle \tilde{x}^2\rangle - \langle \tilde{y}^2\rangle)\sin(2\phi_p) + \beta_T(\langle \tilde{t}\tilde{x}\rangle \sin\phi_p - \langle \tilde{t}\tilde{y}\rangle \cos\phi_p), && \text{(E.18)}\\
R_l^2 &= \langle \tilde{z}^2\rangle - 2\beta_l\langle \tilde{t}\tilde{z}\rangle + \beta_l^2\langle \tilde{t}^2\rangle, &&\\
&= \langle \tilde{z}^2\rangle, && \text{(E.19)}
\end{aligned}$$

where

$$\begin{aligned}
\langle f(x)\rangle &= \frac{\int d^4x f(x) S(x,K)}{\int d^4x S(x,K)}, && \text{(E.20)}\\
\tilde{x}^\mu &= x^\mu - \langle x^\mu\rangle, && \text{(E.21)}
\end{aligned}$$

and β_l vanishes in the LCMS frame and the terms including t and z depend on the proper time τ and emission duration of particles $\Delta\tau$. As shown in above equations, R_s depends only on the spatial extent of the source and azimuthal angle ϕ_p, while R_o, R_{os} is sensitive to the temporal parameters, such as τ and $\Delta\tau$ as well as the spatial extent.

E.3 Fit Results

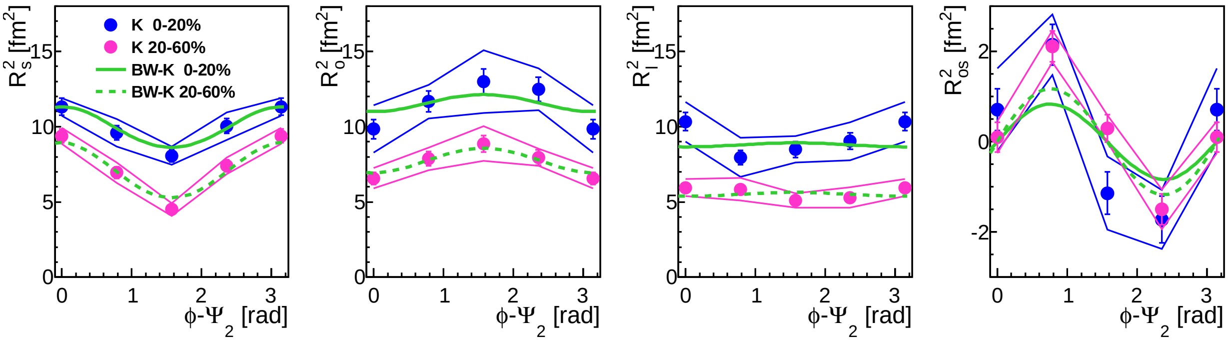

Figure E.1: Blast-wave fit of HBT radii in the fit B.

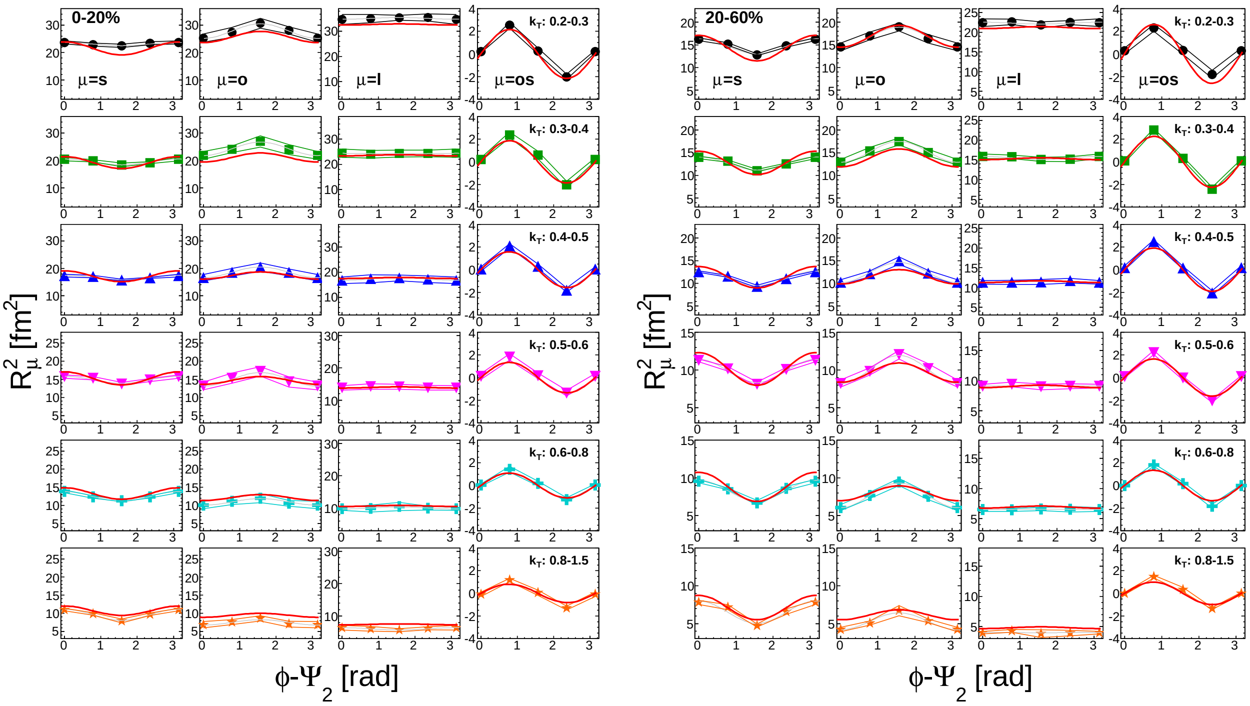

Figure E.2: Blast-wave fit of HBT radii in the fit C, 0-20%(Left) and 20-60%(Right).

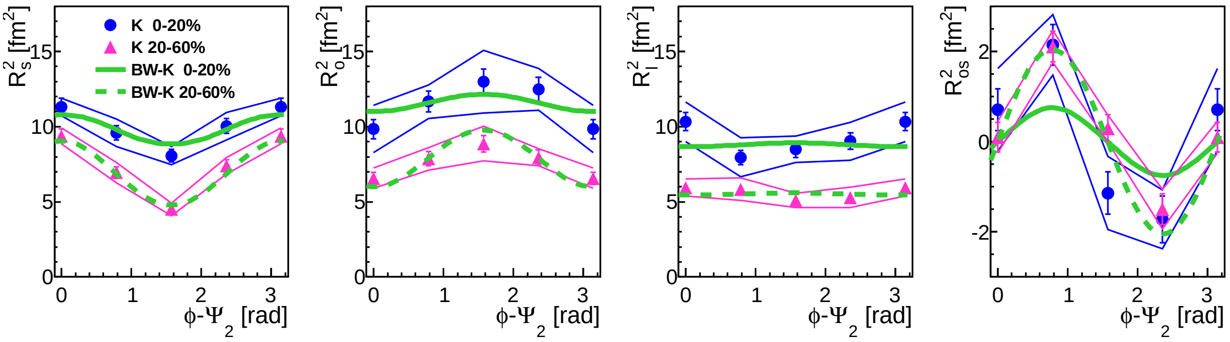

Figure E.3: Blast-wave fit of HBT radii in the fit D.

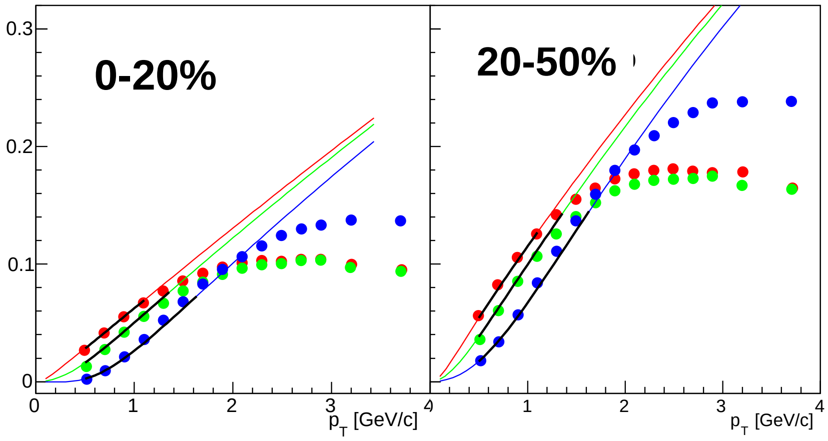

Figure E.4: Blast-wave fit of v_2 in the fit B.

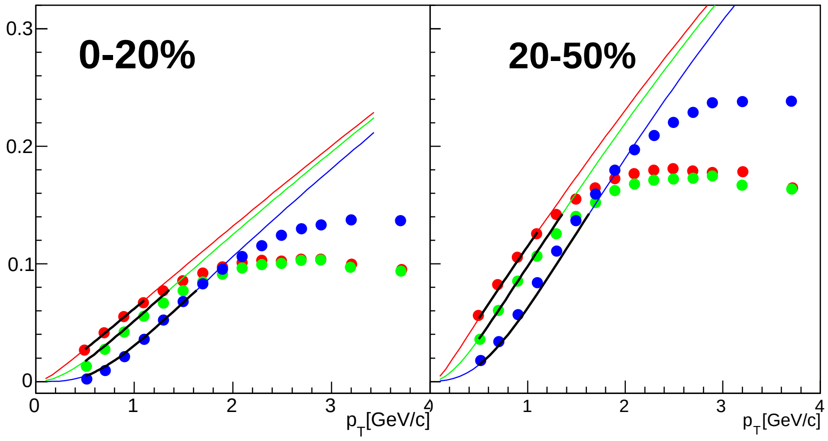

Figure E.5: Blast-wave fit of v_2 in the fit C.

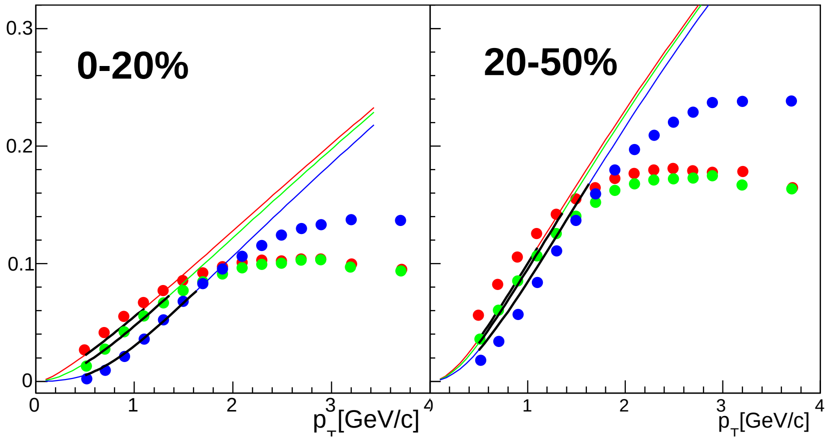

Figure E.6: Blast-wave fit of v_2 in the fit D.

Bibliography

[1] K. YAGI, T. HATSUDA and Y. MIAKE, *Quark-Gluon Plasma*, CAMBRIDGE UNIVERSITY PRESS (2005)

[2] S. Bethke, "The 2009 World Average of α_s", *Eur. Phys. J.* **C64**, 689 (2009)

[3] F. Karsch, "Lattice QCD at high temperature and density", *Lect. Notes Phys.* **583**, 209 (2002)

[4] J. D. Bjorken, "Highly relativistic nucleus-nucleus collisions: The central rapidity region", *Phys. Rev.* **D27**, 140 (1983)

[5] T. Matsui, "Dynamical evolution of the quark-gluon plasma and phenomenology", *Nucl. Phys.* **A461**, 27 (1987)

[6] L. McLerran and R. Venugopalan, "Gluon distribution functions for very large nuclei at small transverse momentum", *Phys. Rev.* **D49**, 3352 (1994)

[7] L. McLerran, "The Color Glass Condensate and Small-x Physics", *Lect. Notes Phys.* **583**, 291 (2002), hep-ph/0104285 (2001)

[8] X.-N. Wang, "A pQCD-based approach to parton production and equilibration in high-energy nuclear collisions", Phys. Rept. **280**, 287 (1997)

[9] R. J. Glauber, G. Matthiae, "High-Energy Scattering of Protons by Nuclei", *Nucl. Phys.* **B21** 135 (1970)

[10] M. L. Miller, K. Reygers, S. J. Sanders, P. Steinberg, "Glauber Modeling in High Energy Nuclear Collisions", *Ann. Rev. Nucl. Part. Sci.* **57**, 205 (2007)

[11] S. S. Adler *et al.*, "Systematic studies of the centrality and $\sqrt{s_{\rm NN}}$ dependence of the $dE_T/d\eta$ and $dN_{ch}/d\eta$ in heavy ion collisions at midrapidity", *Phys. Rev.* **C71**, 034908 (2005)

[12] S. S. Adler *et al.*, "Identified charged particle spectra and yields in Au+Au collisions at $\sqrt{s_{\rm NN}}$ = 200 GeV", *Phys. Rev.* **C69**, 034909 (2004)

[13] K. Guettler *et al.*, "Inclusive Production of Low-Momentum Charged Pions at x=0 at the CERN Intersecting Storage Rings", *Phys. Lett.* **B64**, 111 (1976)

[14] S. S. Adler *et al.*, "Production of *phi* at midrapidity in $\sqrt{s_{\rm NN}} = 200$ GeV Au+Au collisions at relativistic energies", *Phys. Rev.* **C72**, 014903 (2005)

[15] S. S. Adler *et al.*, "Elliptic Flow of Identical Hadrons in Au+Au Collisions at $\sqrt{s_{\rm NN}} = 200$ GeV", *Phys. Rev. Lett.* **91**, 182301 (2003)

[16] R. J. Fries, B. Müller, C. Nonaka and S. A. Bass, "Hadron production in heavy ion collisions: Fragmentation and recombination from a dense parton phase", *Phys. Rev.* **C68**, 044902 (2003)

[17] S. Afanasiev *et al.*, "Elliptic flow for ϕ Mesons and (Anti)deuterons in Au+Au Collisions at $\sqrt{s_{\mathrm{NN}}} = 200$ GeV", *Phys. Rev. Lett.* **99**, 052301 (2007)

[18] A. Adare *et al.*, "Measurements of Higher Order Flow Harmonics in Au+Au Collisions at $\sqrt{s_{\mathrm{NN}}} = 200$ GeV", *Phys. Rev. Lett.* **107**, 252301 (2011)

[19] S. V. Akkelin and Yu. M. Sinyukov, "The HBT-interferometry of expanding sources" *Phys. Lett.* **B356**, 525 (1995)

[20] M. Lisa, S. Pratt, R. Soltz, and U. Wiedemann, "Femtoscopy in Relativistic Heavy Ion Collisions: Two Decades of Progress", *Ann. Rev. Nucl. Part. Sci.* **55**, 357 (2005)

[21] T. Hirano and K. Tsuda, "Collective flow and two-pion correlations from a relativistic hydrodynamic model with early chemical freeze-out", *Phys. Rev.* **C66**, 054905 (2002)

[22] U. Heinz and P. F. Kolb, "Two RHIC puzzles: Early thermalization and the HBT problem", arXiv:hep-ph/024061 (2002)

[23] D. Zschiesche, H. Stocker and W. Greiner, "Space-time evolution and Hanbury Brown-Twiss analysis of relativistic heavy ion collisions in a chiral SU(3)×SU(3) model", *Phys. Rev.* **C65**, 064902 (2002)

[24] Y. Aoki, G. Endrodi, Z. Fodor, S. D. Katz, K. K. Szabo, "The order of the quantum chromodynamics transition predicted by the standard model of particle physics", *Nature* **443**, 675 (2006)

[25] S. Pratt, "Resolving the Hanbury Brown-Twiss Puzzle in Relativistic Heavy Ion Collisions", *Phys. Rev. Lett.* **102**, 232301 (2009)

[26] U. Heinz and P. F. Kolb, "Emission angle dependent pion interferometry at RHIC and beyond", *Phys. Lett.* **B542**, 216 (2002)

[27] S. Voloshin, "Femtoscopy of the system shape fluctuations in heavy", *J. Phys. G: Nucl. Part. Phys.* **38**, 124097 (2011)

[28] R. Hanbury Brown and R. Q. Twiss, "A test of a new type of stellar interferometer on Sirius", *Nature*, **178**, 1046 (1956)

[29] G. Goldhaber, S. Goldhaber, W. Lee, and A. Pais "Influence of Bose-Einstein Statistics on the Antiproton-Proton Annihilation Process", *Phys. Rev.* **120**, 300 (1960)

[30] Sandra S. Padula, "HBT Interferometry: Historical Perspective", *Braz. J. Phys*, **35**

[31] Scott Pratt, "Coherence and Coulomb effects on pion interferometry", *Phys. Rev.* **D33**, 72 (1986)

[32] G. Bertsch, M. Gong, and M. Tohyama, "Pion interferometry in ultra relativistic heavy-ion collisions", *Phys. Rev.* **C37**, 1896 (1988)

[33] M. G. Bowler, "Extended sources, final state interactions and Bose-Einstein correlations", *Z. Phys.* **C39**, 81 (1988)

[34] W. A. Zajc*at el.*, “Two-pion correlations in heavy ion collisions”, *Phys. Rev.* **C29**, 2173 (1984)

[35] U. A. Wiedemann, P. Scotto, and U. Heinz, “Transverse momentum dependence of Hanbury-Brown-Twiss correlation radii”, *Phys. Rev.* **C53**, 918 (1996)

[36] S. S. Adler *et al.*, “Bose-Einstein Correlations of Charged Pion Pairs in Au+Au Collisions at $\sqrt{s_{\mathrm{NN}}} = 200$ GeV”, *Phys. Rev. Lett.* **93**, 152302 (2004)

[37] S.H.Aronson *et al.*, “PHENIX Magnet System,” *Nucl. Instrum. Meth.* **A499**, 480 (2003)

[38] M.Allen *et al.*, “PHENIX Inner Detectors,” *Nucl. Instrum. Meth.* **A499**, 549 (2003)

[39] C. Adler *et al.*, “The RHIC zero degree calorimeters,” *Nucl. Instrum. Meth.* **A470**, 488 (2001)

[40] Alexei Denisov, PHENIX internal web page, RUN4 Subsystem tutorials (`https://www.phenix.bnl.gov/WWW/run/04/subsys_tutorials/zdc/zdc_tutorial.ppt`)

[41] E. Richardson *et al.*, “A reaction plane detector for PHENIX at RHIC”, *Nucl. Instrum. Meth.* **A636**, 99 (2011)

[42] K. Adcox *et al.*, “PHENIX central arm tracking detectors”, *Nucl. Instrum. Meth.***A499**, 489 (2003)

[43] K. Adcox *et al.*, “Construction and performance of the PHENIX pad chambers”, *Nucl. Instrum. Meth.***A497**, 263 (2003)

[44] M. Aizawa *et al.*, “PHENIX central arm particle ID detectors”, *Nucl. Instrum. Meth.***A499**, 508 (2003)

[45] J. Velkovska *et al.*, “Multi-gap Resistive Plate Chambers: Time-Of-Flight system of the PHENIX high-p_T Detector”, Conceptual Design Report (PHENIX internal) (2005)

[46] L. Aphecetche *et al.*, “PHENIX calorimeter”, *Nucl. Instrum. Meth.***A499**, 521 (2003)

[47] S. S. Adler *et al.*, “PHENIX on-line systems”, *Nucl. Instrum. Meth.***A499**, 560 (2003)

[48] J. Barrette *et al.*, “Proton and pion production relative to the reaction plane in Au+Au collisions at 11A GeV/c”, *Phys. Rev.* **C56**, 3254 (1997)

[49] J. T. Mitchell *et al.*, “Event reconstruction in the PHENIX central arm spectrometers”, *Nucl. Instrum. Meth.* **A482**, 491 (2002)

[50] A. Adare *et al.*, “Deviation from quark number scaling of the anisotropy parameter v_2 of pions, kaons, and protons in Au+Au collisions at $\sqrt{s_{\mathrm{NN}}} = 200$ GeV”, *Phys. Rev.* **C85**, 064914 (2012)

[51] A. Enokizono, “Space-time evolution of hot and dense matter probed by Bose-Einstein correlation in Au+Au collisions at $\sqrt{s_{\mathrm{NN}}} = 200$ GeV”, PhD thesis, Hiroshima University (2004)

[52] M. A. Lisa *et al.*, “Bombarding Energy Dependence of π^- Interferometry at the Brookhaven AGS”, *Phys. Rev. Lett.* **84**, 2798 (2000)

[53] C. Adler *et al.*, “Pion Interferometry of $\sqrt{s_{\mathrm{NN}}} = 130$ GeV Au + Au Collisions at RHIC”, C. Adler *et al.*, *Phys. Rev. Lett.* **87**, 082301 (2001)

[54] M. G. Bowler, “Coulomb corrections to Bose-Einstein corrections have greatly exaggerated”, *Phys. Lett.* **B270**, 69 (1991)

[55] Y. M. Sinyukov *et al.*, “Coulomb corrections for interferometry analysis of expanding hadron systems”, *Phys. Lett.* **B432**, 248 (1998)

[56] R. Averbeck, A. Dress, Y. Akiba and T. Hachiya, “An electron cocktail for central and peripheral Au+Au collisions at $\sqrt{s_{\mathrm{NN}}} = 130$ GeV”, PHENIX Analysis Note 089 (2001)

[57] U. Heinz, A. Hummel, M. A. Lisa and U. A. Wiedemann “Symmetry constraints for the emission angle dependence of Hanbury-Brown-Twiss radii”, *Phys. Rev.* **C66**, 044903 (2002)

[58] F. James, “MINUIT”, CERN Program Library Long Writeup D506, http://wwwasdoc.web.cern.ch/wwwasdoc/minuit/minmain.html

[59] K. Reygers, “Glauber Monte-Carlo Calculations for Au+Au Collisions at $\sqrt{s_{NN}} = 200$ GeV”, PHENIX Analysis Note 169 (2003)

[60] R. Wei, R. Lacy, A. Taranenko, J. Jia, M. Shimomura, S. Esumi and A. Milov, “Glauber Calculations of Centrality Dependent Variables in Au+Au collisions at $\sqrt{s_{NN}} = 200$ GeV”, PHENIX Analysis Note 768, (2009)

[61] M. Shimomura, “Systematic Study of Azimuthal Anisotropy for Charged Hadron in Relativistic Nucleus-Nucleus Collisions at RHIC-PHENIX”, PhD thesis, University of Tsukuba (2009)

[62] J. Adams *et al.*, “Pion Interferometry in Au+Au Collisions at $\sqrt{s_{\mathrm{NN}}} = 200$ GeV”, *Phys. Rev.* **C71**, 044906 (2005)

[63] J. Beringer *et al.* (Particle Data Group), “Review of Particle Physics”, *Phys. Rev.* **C86**, 010001 (2012)

[64] J. Adams *et al.*, “Azimuthally Sensitive Hanbury Brown-Twiss Interferometry in Au+Au Collisions at $\sqrt{s_{\mathrm{NN}}} = 200$ GeV”, *Phys. Rev. Lett.* **93**, 012301 (2004)

[65] I. A. Karpenko and Y. M. Sinyukov, “Kaon and pion femtoscopy at the highest energies available at the BNL Relativistic Heavy Ion Collider (RHIC) in a hydrokinetic model”, *Phys. Rev.* **C81**, 054903 (2010)

[66] S. Afanasiev *et al.*, “Charged Kaon Interferometric Probes of Space-Time Evolution in Au+Au Collisions at $\sqrt{s_{\mathrm{NN}}} = 200$ GeV”, *Phys. Rev. Lett.* **103**, 142301 (2009)

[67] F. Retière and M. A. Lisa, “Observable implications of geometrical and dynamical aspects of freeze-out in heavy ion collisions”, *Phys. Rev.* **C70**, 044907 (2004)

[68] A. Kiyomichi, “Study of Identified Hadrons Spectra and Yields at Mid-rapidity in $\sqrt{s_{\mathrm{NN}}} =$ 200 GeV Au+Au Collisions”, PhD thesis, University of Tsukuba (2005)

[69] U. A. Wiedemann, “Two-particle interferometry for non central heavy-ion collisions”, *Phys. Rev.* **C57**, 266 (1998)

[70] Y. Gu, “PHENIX Measurements of Higer-order Flow Harmonics for Identified Charged Hadrons in Au+Au collisions at $\sqrt{s_{\mathrm{NN}}} =$ 39-200 GeV”, *Nucl. Phys. A*, 904-905, 353c (2013)

[71] C. J. Plimberg, C. Shen and U. Heinz, "HBT interferometry relative to the triangular flow plane in heavy-ion collisions", arXiv:1306.1485 [nucl-th] (2013)

[72] The ATLAS Collaboration, "Measurement of reaction plane correlations in Pb-Pb collisions at $\sqrt{s_{\rm NN}}$=2.76 TeV", ATLAS Note, ATLAS-CONF-2012-049 (2012)

[73] A. Kisiel, T. Taluc, W. Broniowski, W. Florkowski, "Therminator: Thermal heavy-Ion generator", *Comput. Phys. Commun.* **174**, 669 (2006)

[74] S. Afanasiev *et al.*, "Source Breakup Dynamics in Au+Au Collisions at $\sqrt{s_{\rm NN}}$ =200 GeV via Three-Dimensional Two-Pion Source Imaging", *Phys. Rev. Lett* **100**, 232301 (2008)

[75] D. Teaney, J. Lauret, and E. V. Shuryak, "A Hydrodynamic Description of Heavy Ion Collisions at the SPS and RHIC", arXiv:nucl-th/0110037 (2001)

[76] D. Teaney and L. Yan, "Triangularity and dipole asymmetry in relativistic heavy ion collisions", *Phys. Rev.* **C83**, 064904 (2011)